A LOWER CRUSTAL PERSPECTIVE ON THE STABILIZATION AND REACTIVATION OF CONTINENTAL LITHOSPHERE IN THE WESTERN CANADIAN SHIELD

by

Rebecca M. Flowers

B.S. Geology
College of William & Mary, 1998

M.Sc., Geology
University of Utah, 2000

SUBMITTED TO THE DEPARTMENT OF EARTH ATMOSPHERIC AND PLANETARY SCIENCES IN PARTIAL FULFILLMENT OF THE REQUIREMENTS FOR THE DEGREE OF
[Doctor of Science]
DOCTOR OF PHILOSOPHY
AT THE
© MASSACHUSETTS INSTITUTE OF TECHNOLOGY

SEPTEMBER 2005

Signature of Author: ___
Department of Earth, Atmospheric, and Planetary Sciences
July 19, 2005

Certified by: ___
Samuel A. Bowring
Professor of Geology
Thesis Supervisor

Accepted by: ___
Maria T. Zuber
E.A. Griswold Professor of Geophysics and Planetary Science
Department Head

A LOWER CRUSTAL PERSPECTIVE ON THE STABILIZATION AND REACTIVATION OF CONTINENTAL LITHOSPHERE IN THE WESTERN CANADIAN SHIELD

by

Rebecca M. Flowers

Submitted to the Department of Earth Atmospheric and Planetary Sciences at the
Massachusetts Institute of Technology on June 30, 2005 in Partial Fulfillment of the
Requirements for the Degree of Doctor of Philosophy in Geology

ABSTRACT

New geochronological, thermochronological, geological and isotopic data from an extensive (> 20,000 km^2) exposure of high-pressure granulites (0.8 to > 1.5 GPa, >750 °C) in the East Lake Athabasca region of the Snowbird tectonic zone provide important constraints on the stabilization, reactivation and exhumation of continental lithosphere in the western Canadian Shield. The exhumed lower crust of this craton comprises several disparate domains that preserve a complex record of tectonic, magmatic and metamorphic processes from formation to exhumation.

U-Pb zircon geochronology documents two episodes of metamorphic zircon growth at 2.55 Ga and 1.9 Ga, linked with two high-pressure granulite facies assemblages preserved in Chipman domain mafic granulites. The intervening 650 m.y. of relative quiescence implies a period of lithospheric stability during which the granulites continued to reside in the deep crust. Disruption of the stable Archean craton at 1.9 Ga broadly coincides with the assembly of the Laurentian supercontinent. The correlation of 1.9 Ga mafic magmatism and metamorphism in the Chipman domain with contemporaneous mafic magmatism along > 1200 km strike-length of the Snowbird tectonic zone indicates that regional asthenospheric upwelling was an important aspect of this reactivation event.

U-Pb (titanite, apatite, rutile), $^{40}Ar/^{39}Ar$ (hornblende, muscovite, apatite) and (U-Th)/He (zircon, apatite) thermochronometry documents the cooling history of domains in the East Lake Athabasca region during the 200 m.y. multistage history of unroofing following 1.9 Ga metamorphism. Linkage of reconstructed temperature-time histories with existing pressure-temperature-deformation paths reveals spatial and temporal heterogeneity in exhumation patterns, with domain juxtaposition during episodes of unroofing separated by intervals of crustal residence. Low temperature (U-Th)/He zircon and apatite dates are the oldest reported for terrestrial rocks, and confirm the protracted residence of rocks at shallow (≤ 2 km) crustal depths following the re-attainment of a stable lithospheric configuration in the western Canadian shield at ca. 1.7 Ga.

Thesis Supervisor: Samuel A. Bowring
Title: Professor of Geology

ACKNOWLEDGEMENTS

During the last five years, there have been many people who have contributed to the completion of my PhD. First, I must thank my advisor, Sam Bowring. Sam has generously provided me with an extraordinary number of opportunities, a large degree of freedom in my research, and support on a variety of levels during my time at MIT. I have learned much from the very large scale at which Sam is always thinking about science, and am continually amazed by his boundless enthusiasm for a huge array of scientific problems. The very high standards Sam sets for research, teaching and mentorship will continue to influence the quality I strive for in those areas in the future.

It has been a fantastic experience to work in the Snowbird tectonic zone for my PhD thesis. Mike Williams has been central in this research effort. I have been fortunate to learn from his exceptional skills in the field, as well as to obtain valuable feedback from him regarding, ideas, papers and talks throughout the course of this project. It was excellent to interact with Julie Baldwin, Kevin Mahan, Greg Dumond, and Philippe Goncalves during our efforts to integrate geochronological, structural and metamorphic information from these complex rocks. Special thanks to Alexis Ault for hard work, good company, and exceptional enthusiasm that were central to the success of my two field seasons, despite black flies, bad weather and bear-induced tent destruction. I also appreciate the opportunities I've had to interact with and obtain feedback from individuals at the Geological Survey of Canada, including Simon Hanmer, Sally Perhrsson, and Rob Berman.

Thanks to Kip Hodges for the opportunity to obtain data in the Ar lab and to Tim Grove for helpful discussions regarding the petrology of Snowbird rocks. I appreciate Wiki Royden's advising of my thermal modeling second generals project that has given me a more complete understanding of the lithospheric scale implications of geo- and thermochronological datasets. Also, thanks to Pete Reiners for the recent opportunity to visit and obtain (U-Th)/He data in his lab at Yale.

The members of the TIMS lab maintain a supportive, always interesting and dynamic lab environment, and thanks go to Dan Condon, Jim Crowley, Danny MacPhee, Jenny Matzel, Noah McLean, Jahan Ramezani, and Blair Schoene. Special thanks to Frank Dudas, who has been my primary source of knowledge regarding chemistry and analysis in the non-zircon world of TIMS isotope geochemistry. I also appreciate Pat Walsh's refreshingly direct manner of handling the administrative aspects of the TIMS lab. Malcolm Pringle provided much knowledgeable help during acquisition of Ar data and was patient answering my questions regarding Ar analysis. Lindy Elkins-Tanton was my first office mate at MIT, and her balancing of work and personal life had an important influence on my own decisions regarding how to attain that balance. Thanks to all the G&G students who I've overlapped with for the supportive and productive environment in this department.

Most importantly, I thank my family. My parents are responsible for instilling in me a curiosity about the natural world, and a belief that hard work and perseverance make all things possible. Debbie, my sister, has a down-to-earth and very upbeat approach to life that I always find motivating. Kevin has been an unwavering source of support and balance in my life throughout the last five years. Thanks.

TABLE OF CONTENTS

INTRODUCTION

Rare exposures of lower continental crust exert a tremendous influence on our understanding of deep crustal processes, because these terranes offer the best opportunity to directly examine this generally inaccessible level of continents. These regions allow scrutiny of the rock types and structural relationships commonly imaged by seismic techniques in the deep crust, provide a critical in situ context for more robust interpretation of the record contained in lower crustal xenolith samples, and allow more thorough evaluation of models for the rheological, metamorphic and chemical evolution of the deep portions of continents. The character and behavior of the deep crust has an important impact on how this signal is manifested as magmatism, deformation and/or metamorphism at higher levels of the crustal column. Because the lower crust retains the most direct crustal signature of activity within the underlying mantle, this region can also yield essential insights into mantle dynamics. Thus, constraining the tectonic and thermal evolution of the lower crust is necessary for a more comprehensive understanding of the evolution of the continents.

The East Lake Athabasca region in the western Canadian Shield contains vast tracts (>20,000 km^2) of high-pressure (HP) (1.0 to >1.5 GPa) granulites that represent one of the largest and best-preserved exposures of lower continental crust on the planet. This area spans the Snowbird tectonic zone, a ~2800 km long gravity and magnetic anomaly that separates the Rae and Hearne crustal provinces of the western Churchill Province. This dramatic geophysical feature has alternatively been interpreted as a Paleoproterozoic suture (Hoffman, 1989) and as an Archean intracratonic shear zone that was reactivated in the Paleoproterozoic (Hanmer, 1997). Deciphering the complex record of repeated HP granulite facies metamorphic events, overprinted by the unroofing history, has posed the central problem in the ongoing controversy over the formation and maturation of this cratonic region. This thesis focuses on constraining the tectonic and thermal evolution of continental lithosphere in the western Canadian Shield by deconvolving this complex record using a variety of geochronological, thermochronological, and isotopic techniques. The following chapters sequentially translate the deep crustal record into an interpreted history of 1) lithospheric stabilization in the Archean, 2) dramatic lithospheric reactivation in the Proterozoic, 3) subsequent multistage exhumation and juxtaposition of HP granulite domains, and 4) re-attainment of a stable lithospheric configuration responsible for the long-term preservation of this portion of the continental lithosphere.

Chapter 1 highlights the exceptional value of zircon for deciphering complex metamorphic records in deep crustal rocks. This study uses an integrated U-Pb TIMS, ion microprobe, and imaging effort to determine the timing of two distinct HP granulite facies events preserved in rocks of the East Lake Athabasca region. Thermobarometric analysis of mafic granulites in the Chipman domain has revealed two granulite facies metamorphic assemblages that record conditions of ~1.3 GPa, 850 °C and ~1.0 GPa, 800 °C (Mahan et al., 2005). Our analysis of metamorphic zircon grains from mafic and felsic granulite gneisses documents a dominant population of ca. 2.55 Ga zircon that is linked with the first HP assemblage. The U-Pb systematics of these metamorphic zircon grains show a complex response to a perturbation at 1.9 Ga, with limited new zircon growth at this time. Independent documentation of HP granulite facies metamorphism in the Chipman domain at 1.9 Ga (Chapter 2) is consistent with the conditions preserved in the second granulite assemblage of the mafic gneisses. Together, these results provide strong evidence for subjection of the Chipman domain to two HP granulite facies events separated by 650 m.y. This dataset is used to argue for extended residence of the granulites in the deep crust between 2.55 Ga and 1.9 Ga HP granulite facies metamorphic events, during a 650 m.y. period of relative quiescence and lithospheric stability. This implies an event of fundamental importance was required to disrupt this stable Archean craton in the Proterozoic.

Chapter 2 examines the nature and significance of lithospheric destabilization at 1.9 Ga. This record contrasts dramatically with the stability of most preserved Archean cratons following assembly. High precision U-Pb TIMS zircon geochronology, in conjunction with whole rock Sm-Nd isotopic data, whole rock geochemistry data, and field observations, are used to constrain the timescales and intensity of HP granulite facies metamorphism and anatexis during 1.9 Ga lithospheric reactivation. Mafic dike anatexis during syntectonic and synmetamorphic intrusion of Chipman mafic dikes at 1.0-1.2 GPa, ~ 800 °C conditions (Williams et al., 1995) occurred at 1896.2 ± 0.3 Ma, and was followed by the protracted maintenance of elevated temperatures for 5-15 m.y.

Limited melting of the host rocks during high temperatures at this time is attributed to their dehydrated character owing to previous metamorphism in the Archean. Chipman domain mafic magmatism is correlated with contemporaneous focused mafic intrusive activity along > 1200 km strike-length of the Snowbird tectonic zone. These data provide compelling evidence for a regional episode of asthenospheric upwelling associated with the destabilization of this Archean craton that coincided with the assembly of the Laurentian supercontinent.

Chapter 3 explores the tempo, duration and rates of exhumation of disparate domains in the East Lake Athabasca region following 1.9 Ga lithospheric reactivation. The nature and rates of processes that juxtapose and exhume crustal domains are of central importance for understanding the significance and representativeness of lower crustal exposures, and for evaluating the degree of lower crustal terrane modification during transport to the Earth's surface. A ~200 m.y. interval for exhumation of lower crustal rocks in the East Lake Athabasca region is constrained by the timing of 1.9 Ga HP granulite facies metamorphism, and the subsequent ca. 1.7 Ga deposition of Athabasca basin sediments over the exhumed granulites. High-resolution U-Pb (titanite, apatite, rutile) and ^{40}Ar/^{39}Ar (hornblende, muscovite, biotite) thermochronometry, linked with existing thermobarometric and structural data, reveals an exhumation history characterized by multiple pulses of unroofing at different rates separated by intervals of crustal residence for variable durations. The convergence of domainal thermal histories places constraints on the timing of domain juxtaposition relative to regional unroofing. The temporally and spatially heterogeneous patterns of lower crustal exhumation in the East Lake Athabasca region may be a common feature of the unroofing histories of HP granulite terranes.

Chapter 4 evaluates the history of vertical continental motions in the East Lake Athabasca region following the apparent re-attainment of a stable lithospheric configuration at ca. 1.7 Ga. Although the preservation of ancient continental crust testifies to the extreme stability of some portions of the continents, evidence suggests that even these regions undergo episodes of epeirogenic uplift and subsidence in response to changing mantle dynamics. (U-Th)/He thermochronometry is widely utilized to constrain uplift histories in areas of active or recent tectonism, but the application of this technique to assess vertical motions in regions of apparent tectonic stability has been limited. This study presents the Earth's oldest reported (U-Th)/He zircon and apatite dates that document the residence of rocks in the East Lake Athabasca region at temperatures ≤ 30 °C at depths of ≤ 2km for 1.0-1.7 b.y. These data are exploited to generate a suite of viable models for the low temperature thermal history of these rocks that may reflect low amplitude vertical motions within this continental interior. This study highlights the promise of using low temperature thermochronometers to constrain the history of cratonic subsidence and uplift and thereby gain insight into the stability of continents and mantle dynamics.

REFERENCES

Hanmer, S., 1997, Geology of the Striding-Athabasca mylonite zone, northern Saskatchewan and southeastern District of Mackenzie, Northwest Territories: Geological Survey of Canada Bulletin, v. 501, pp.1-92.

Hoffman, P.F., 1988, United Plates of America, the birth of a craton: Early Proterozoic assembly and growth of Laurentia: Annual Reviews of Earth and Planetary Science Letters, v. 16, p.545-603.

Mahan, K.H., 2005, Exhumation of exposed deep continental crust, western Canadian Shield: Integrating structural analysis, petrology, and in situ geochronology: PhD thesis, University of Massachusetts, Amherst, Massachusetts.

Williams, M.L., Hanmer, S., Kopf, C. and Darrach, M., 1995, Syntectonic generation and segregation of tonalitic melts from amphibolite dikes in the lower crust, Striding-Athabasca mylonite zone, northern Saskatchewan: Journal of Geophysical Research, v.100(B8), p.15,717-15,734.

Chapter 1

Complex U-Pb zircon systematics induced by repeated high-pressure, high-temperature metamorphic events, Snowbird tectonic zone, Canada

ABSTRACT

U-Pb TIMS zircon and monazite data, combined with ion microprobe zircon analysis and detailed imaging studies, are used to decipher the complex polymetamorphic history preserved in high-pressure granulites in the East Lake Athabasca region of the western Canadian Shield. Mafic and felsic granulites contain a dominant population of 2.55 Ga metamorphic zircon that show an unusual response to high temperature metamorphism at 1.9 Ga. The complex U-Pb zircon systematics are attributed to Pb redistribution and/or zircon recrystallization during this event. The primary population of 2.55 Ga zircon is linked with the first high-pressure granulite facies assemblage (~1.3 GPa, 850 °C) preserved in the mafic granulite gneisses. Limited new zircon growth at 1.9 Ga, and the perturbed zircon systematics, are correlated with a second episode of high-pressure granulite facies metamorphism (1.0-1.2 GPa, ~800 °C) independently dated at 1.9 Ga by zircon in migmatitic Chipman mafic granulite dikes. The similarity in metamorphic conditions preserved in the Chipman dikes to a second granulite facies assemblage (~1.0 GPa, 800 °C) in the mafic granulite gneisses, suggests their coeval development at 1.9 Ga. These data provide compelling evidence for two episodes of high-pressure granulite facies metamorphism in the Chipman domain. Limited melting of the Chipman domain during subjection to 1.9 Ga high temperatures is consistent with little retrogression following dehydration in the Archean. The recurrence of metamorphism at high-pressure conditions implies that the granulites resided in the deep crust between 2.55 and 1.9 Ga during a period of relative quiescence. Chemically diverse monazite populations of variable ages are interpreted to represent fluid mediated growth and/or recrystallization during this interval. These data suggest a ~650 m.y. period of lithospheric stability initially heralded by 2.55 Ga metamorphism and dramatically terminated by significant reactivation in the Proterozoic during assembly of the Laurentian supercontinent.

INTRODUCTION

The lower continental crust preserves a record of lithospheric perturbation by the underlying asthenosphere, manifested as repeated episodes of high-grade metamorphism, deformation, mafic magmatism, and melting. Lower crustal rocks thus have the potential to yield unique insights into crust-mantle coupling during lithospheric evolution. However, deciphering the cumulative product of a complex history preserved in multiply deformed polymetamorphic rocks can be a challenging problem. Linking accessory mineral geochronological data with metamorphic assemblages is critical for deconvolving such histories.

U-Pb zircon geochronology is key to deciphering complex metamorphic records, owing to the robust character of this mineral that allows it to retain chronological information through most P-T conditions encountered in the crust. However, this same property contributes to the structural, morphological, and isotopic complexity of zircon crystals that have experienced dynamic histories. In addition to multicomponent mixtures of inherited, magmatic, and/or metamorphic zircon that can exist within single crystals, isotopic resetting of zircon grains via recrystallization and fluid-alteration processes can occur at high grade conditions (e.g. Pidgeon et al., 1998; Hoskin and Black, 2000; Carson et al., 2002), and subsequent low temperature Pb loss in radiation damaged crystals can further complicate the U-Pb systematics (e.g. Silver and Deutsch, 1963; Cherniak et al., 1991). Understanding the behavior of zircon during multiple periods of metamorphism is essential for exploiting the isotopic record preserved within these crystals. This, in turn, is crucial for providing timing constraints on discrete metamorphic, melting and deformation events preserved in deep crustal rocks that can profoundly influence the interpretation of tectonic histories.

We provide an example of these complexities by using an integrated U-Pb TIMS, ion microprobe, and imaging study of metamorphic zircon grains from mafic and felsic granulites to determine the timing of two distinct high-pressure, high temperature (HP-HT) metamorphic events preserved in rocks of the East Lake Athabasca region, along the Snowbird tectonic zone, in the western Canadian Shield. Although previous U-Pb TIMS metamorphic zircon analysis has been interpreted to date ca. 1.9 Ga HP granulite assemblages in several areas (Flowers, Chapter 2; Baldwin et al., 2004), the earlier history of these Archean rocks has been difficult to decipher. Mafic granulite gneisses described in this study preserve two metamorphic assemblages that yield conditions of ~1.3 GPa, 850 °C, and ~ 1.0 GPa, 800 °C (Mahan et al., 2005). The latter are consistent with 1.0-1.2 GPa, 750-850 °C conditions dated at 1896.2 ± 0.3 Ma based on zircon in migmatitic Chipman mafic granulite dikes in this domain (Williams et al., 1995; Flowers, Chapter 2). In the current study, our analysis of zircon from mafic and felsic granulite gneisses reveals a dominant population of 2.55 Ga metamorphic zircon that we link with the first HP granulite assemblage in this rock. The 2.55 Ga zircon show a complex response to the second HP granulite facies metamorphism at 1.9 Ga documented in the Chipman mafic dikes. The data provide strong evidence for two HP granulite facies episodes in the Chipman domain separated by 650 m.y. These results allow us to consider 1) the significance of U-Pb systematics in metamorphic zircon subjected to protracted high-temperature conditions, and 2) the tectonic implications for extended deep crustal residence, continental stability, and lithospheric reactivation processes.

GEOLOGICAL SETTING

The western Canadian Shield is an amalgamation of Archean cratons that were welded in the Paleoproterozoic. The western Churchill Province within this region is bounded by the Thelon orogen (2.02-1.90 Ga) to the northwest and the Trans-Hudson orogen (1.85-1.80 Ga) to the southeast (Figure 1). The Snowbird tectonic zone is a dramatic, northeast-trending linear gravity anomaly that separates the Rae and Hearne crustal provinces of the western Churchill Province, extending ~2800 km from the coast of the Hudson Bay to the Canadian Cordillera (Goodacre et al., 1987; Hanmer et al., 1995). This feature has been interpreted as a Paleoproterozoic intercontinental suture (Hoffman, 1988; Ross et al., 1995, 2000), a Paleoproterozoic intracontinental transform (Lewry and Sibbald, 1980) and an Archean intracontinental strike-slip shear zone (Hanmer et al., 1995, 1997).

The East Lake Athabasca region spans the central segment of the Snowbird tectonic zone, and includes an extensive tract of granulite facies rocks with peak metamorphic conditions from 1.0 to > 1.5 GPa, >750 °C (Figure 2). This region contains deep crustal rocks within the East Athabasca mylonite triangle along the trace of the

Snowbird tectonic zone, deep crustal rocks in the Rae domain to the west, as well as shallower level amphibolite facies rocks within the Hearne domain to the east. To the south the rocks are overlain by sediments of the ca. 1.7 Ga Athabasca basin. The East Athabasca mylonite triangle has been subdivided into three distinct tectonically bounded domains. The Chipman domain is dominated by heterogeneous > 3.0 Ga Chipman tonalitic gneisses, contains lenses of mafic and felsic granulites, and preserves the deep levels of the Chipman mafic dike swarm that intruded across the entire domain and records metamorphism at conditions of 1.0-1.2 GPa, 750-850 °C (Williams et al., 1995; Flowers, Chapter 2) (Figure 3). The northwestern domain is composed of ca. 2.6 Ga mafic to felsic plutonic rocks, interpreted to have been emplaced and metamorphosed at ~1.0 GPa, 900 °C (Williams et al., 2000). The southern domain contains felsic and mafic granulites with minor eclogite, recording peak conditions ≥ 1.5 GPa, 900-1000 °C (Snoyenbos et al., 1995; Kopf, 1999; Baldwin et al., 2003, 2004).

The complex record of both Archean and Paleoproterozoic metamorphic events along the Snowbird tectonic zone, including the East Athabasca mylonite triangle, is largely responsible for the ongoing controversy over the tectonic significance of this profound structure. In the Chipman domain, HP granulite facies metamorphism (1.0-1.2 GPa, 750-850 °C) has been dated at 1896.2 ± 0.3 Ma using zircon from migmatitic mafic granulite dikes. Peak conditions in the southern domain have been interpreted at 1904.0 ± 0.3 Ma based on metamorphic zircon in eclogite, although these same rocks also contain a record of earlier metamorphic zircon growth at ca. 2.55 Ga (Baldwin et al., 2004). The ca. 2.6 Ga Mary granite in the northwestern domain underwent metamorphism at ~1.0 GPa, 900 °C with subsequent isobaric cooling inferred to have occurred shortly after the emplacement of these rocks in the Archean (Williams et al., 2000). Felsic granulites within both the Chipman and southern domains are characterized by abundant garnets that exclusively contain an Archean population of ≥2.55 Ga monazite, with multiple comparably aged and younger populations distributed in the matrix, implying that the garnet in these rocks grew during an Archean metamorphic event (Mahan et al., in review, Baldwin et al., in review). A record of ca. 2.55 Ga and 1.9 Ga metamorphism has also been documented along the northern trace of the Snowbird tectonic zone, interpreted to date conditions of 0.5-0.6 GPa, 650-750 °C, and 0.9-1.1

GPa, 650-750 °C, respectively (Stern and Berman, 2000; Berman et al., 2002). In the East Athabasca mylonite triangle, mafic and felsic granulites occur in all three domains and may hold the greatest promise for unraveling the polymetamorphic history in this region. Although these lithologies are most abundant in the southern and northwestern domains, garnetiferous mafic and felsic granulites also occur as minor components in the western part of the Chipman domain. These units have not previously been targeted for U-Pb zircon geochronological analysis.

CHIPMAN DOMAIN MAFIC AND FELSIC GRANULITE GNEISSES

Mafic granulites crop out as deformed lenses meters to tens of meters wide, and up to hundreds of meters long, within > 3.0 Ga variably deformed heterogeneous Chipman tonalitic gneisses in western portions of the Chipman domain (Figure 3). Less common garnetiferous felsic granulites similarly occur and, when observed, were always associated with the mafic granulites, implying a genetic link. The western Chipman domain coincides with a dramatic anomaly visible in the total field magnetic map, suggesting that the mafic lithologies may increase in abundance at depth. The restriction of the mafic granulite lenses and associated magnetic anomaly to the western part of the domain, and the less common occurrence of anorthositic, gabbroic and ultramafic inclusions that are prevalent within Chipman tonalite further east, may reflect a somewhat different protolith character in eastern and western parts of the domain. Chipman mafic dikes that record 1.9 Ga granulite facies metamorphism intrude across the entire domain.

Chipman domain mafic granulites include both Grt+Cpx layers, and medium to very coarse-grained orthopyroxenite units. Study primarily focused on the former, because of the greater potential for deciphering the metamorphic history using the garnet-bearing assemblages. The dominant mineralogy of this lithology is Grt + Cpx + Pl + Opx + Qtz, with secondary hornblende, accessory ilmenite and apatite, and the presence of zircon and rutile in some samples (Figure 4A). Metamorphic analysis and thermobarometric study of Chipman domain mafic granulite samples by Mahan et al. (2005) documented 1) an early assemblage of Grt + Cpx that preserves conditions of ~1.3 GPa, 850 °C and is interpreted to have developed from an igneous opx-bearing assemblage, 2) retrogression to a Hbl-bearing matrix assemblage during rehydration, and 3) a second less pervasive granulite facies assemblage of Opx + Cpx that records conditions of ~ 1.0 GPa, 800 °C. Felsic granulite gneisses contain a Grt+Sil+Ksp+Pl+Qtz anhydrous peak assemblage, with abundant accessory zircon, monazite and rutile.

The petrographic setting of zircon was documented within mafic granulite sample 02M133A, the same sample on which much petrologic and thermobarometric analysis and U-Pb TIMS and ion microprobe studies also focused. Commonly 10-50 μm zircon crystals occur in the M1 garnet and clinopyroxene assemblage, as well as in matrix garnet, clinopyroxene, hornblende and plagioclase phases (Figure 4B). Cathodoluminescence images of in situ zircon revealed generally similar zonation patterns. Zircon grains typically contained darker unzoned or weakly zoned cores with bright overgrowths, with less common occurrence of darker overgrowths or homogeneous zircon lacking obvious overgrowths.

WHOLE ROCK GEOCHEMISTRY

Major and trace element concentrations were determined for five samples of Grt+Cpx bearing mafic granulites, five samples of orthopyroxenites, and three samples of garnet-rich felsic granulites from the Chipman domain by XRF and ICPMS at the University of Massachusetts, Amherst and at Activation Laboratories, respectively (Table 1). The Grt+Cpx bearing mafic granulites contain SiO_2 ranging from 47.9 to 52.9%, MgO from 7.0 to 10.6%, and lower Al_2O_3 from 11.0 to 16.8%. The orthopyroxene-rich granulites contain overlapping SiO_2 from 48.9 to 53.8%, higher MgO from 13.7 to 26.0%, and lower Al_2O_3 from 3.7 to 7.8%. Bulk compositions of felsic granulites are characterized by SiO_2 from 61.0 to 69.8%, MgO from 3.2 to 5.7%, and Al_2O_3 from 13.4 to 17.1%, with variability ascribed to heterogeneity in proportions of garnet, feldspar and quartz. Chipman domain felsic granulite major element data are within a similar range to that for southern domain felsic granulites (Baldwin et al., in review).

Rare earth element (REE) patterns for the Grt+Cpx bearing mafic granulite samples are variable (Figure 5A). They include negative and positive slopes, as well as generally flat patterns. In contrast, REE patterns for the orthopyroxene-rich granulites consistently have a negative slope, suggesting the presence of garnet in the source (Figure 5A). Most samples do not contain pronounced Eu anomalies that would imply the role of plagioclase fractionation during the generation or emplacement of the mafic protolith. The felsic granulite samples are characterized by enriched and negatively sloping LREEs and relatively flat HREE patterns, with two of three sample displaying positive Eu anomalies (Figure 5B). These patterns are similar to those reported for southern domain felsic granulites (Baldwin et al., in press), suggesting a similar genesis.

Whole rock Sm-Nd isotopic data were previously acquired for the same ten mafic granulite samples for which major and trace element data are reported in this study (Flowers, Chapter 2). Nine of the samples were characterized by time-integrated LREE enrichment and present-day ε_{Nd} values from –24.5 to –0.9. Sm-Nd data for one Grt+CPx granulite was characterized by time-integrated LREE depletion, consistent with its positively sloping REE pattern, with a present day ε_{Nd} value of 17.5. The ε_{Nd} values at 2.6 Ga ranged from –7.29 to 2.720 with depleted mantle model dates from 3.91 to 2.91 Ga.

U-Pb GEOCHRONOLOGY

Analytical Methods

Zircon and monazite grains were isolated from the samples by standard crushing, water table, heavy liquid, and magnetic separation techniques. To optimize the selection of crystals for TIMS analysis, representative grains were mounted in epoxy, polished to expose grain interiors, and imaged with cathodoluminescence (CL) and/or backscatter (BE) techniques to characterize internal structures. Several zircon grains were analyzed via TIMS following ion microprobe analysis, described further below. Electron microprobe Th, Ca, Y and U chemical maps were also acquired for a subset of monazite crystals.

Zircon and monazite grains were extracted from the grain-mount, photographed, and measured. Sizeable (> 100 micron) zircon and monazite crystals were broken into fragments for analysis, while smaller grains were analyzed in their entirety. Most zircon grains and fragments were air-abraded with pyrite after the method of Krogh (1982), and rinsed and ultrasonicated in 3 M HNO_3. Monazite grains were rinsed and ultrasonicated in high-purity water. A subset of zircon grains were subjected to a version of the chemical abrasion technique (Mattinson, 2005), in which zircon crystals were placed in quartz crucibles in a muffle furnace at ~900 °C for ~60 hours, loaded into Teflon FEP microcapsules and leached in 29 M HF at ~180 °C for 12 hours, then transferred to savillex beakers and prepared for dissolution according to standard procedures. A less aggressive leach step in 29 M HF at ~80 °C for 12-17 hours in savillex beakers on a hotplate was used for high U zircon grains that completely dissolved during the higher temperature chemical abrasion procedure. All fractions were loaded into savillex beakers, washed and ultrasonicated again in 3 M HNO_3 (zircon) or high-purity water (monazite), rinsed in distilled acetone and high-purity water, and loaded into Teflon FEP microcapsules in high-purity water. Samples were spiked with a mixed ^{205}Pb-^{233}U-^{235}U tracer. Zircon grains were dissolved in 29 M HF at 220 °C for 48-96 hours, and converted to 6 M HCl at 180 °C for 12-24 hours. Monazite crystals were dissolved in 12 M HCl at 180 °C for 48 hours. Pb and U were chemically separated using HCl anion exchange chemistry modified after Krogh (1973). Pb and U were loaded on single Re filaments with a silica gel 0.1 M H_3PO_4 emitter solution and analyzed on the Massachusetts Institute of Technology VG Sector 54 mass spectrometer. Pb isotopic ratios were measured either by peak jumping using an axial counting Daly detector, or dynamically with Faraday cups and the Daly detector, peak-jumping ^{205}Pb into the axial position to obtain a real-time Faraday-Daly gain calibration. U was measured as an oxide in static mode on three Faraday cups. U-Pb data and details regarding isotopic ratios corrections are provided in Table 2. Decay constant and U-Pb tracer calibration uncertainties are systematic errors not included in the cited dates, as these are unnecessary for comparison of data acquired within a single lab. Concordia diagrams for all zircon and monazite analyzed by TIMS are shown in Figures 6 through 10.

Zircon grains for SHRIMP U-Pb analysis were prepared in a 1-inch diameter, Au-coated, polished grain-mount. Spots within the zircon were selected using optical and CL imaging, and were analyzed on the SHRIMP II at the Australian National University using a 25 μm diameter, 3.5 nA, 10 kV, negative O_2 primary ion beam. Positive secondary ions were extracted at 10 kV and analyzed at mass resolution 5000 using a single ETP electron multiplier and magnetic field switching. Each analysis consisted of 5 scans through the isotopes of interest and took 8 minutes. The Pb isotopic compositions were measured directly. Pb/U and Pb/Th were determined relative to chips of zircon standards SL13 (U = 238 ppm) and FC1 (radiogenic $^{206}Pb/^{238}U = 0.1859$) using a power-law relationship between Pb^+/U^+ and UO^+/U^+ (Claoué-Long et al., 1995) and an exponent of 1.55. The standard also provided an estimate of Pb isotopic fractionation (2.5 ± 2.0 ‰/amu). Common Pb was corrected using ^{204}Pb assuming the composition of 2.5 Ga average crustal Pb (Cumming & Richards, 1975). Refer to Table 3 for analytical results and to Figure 11 for the ion microprobe zircon concordia diagram.

U-Pb TIMS Analytical Results

U-Pb TIMS data were acquired for zircon grains from three representative samples of Grt+Cpx+Opx mafic granulites and one sample of felsic granulite, and for monazite from the felsic granulite. Mafic granulite sample 02M133A was targeted due to its well-preserved reaction textures that also permitted detailed petrological and kinematic study (Mahan et al. 2005). The two other mafic samples were selected to obtain the widest spatial distribution of data over the observed extent of Chipman domain mafic granulite exposures. The felsic granulite sample was collected from a lens associated with mafic granulite sample 02M133A.

Sample 02M133A was collected from a mafic granulite body at Cora Lake (Figure 3). Zircon grains range in size from tens to hundreds of microns. The dominant population of zircon is characterized by cores and overgrowths (Figure 6) A secondary zircon population is homogeneous and bright in CL. Within the dominant population, three general groups can be distinguished based on differences in external morphology and CL-imaged internal structures (Figure 6). The first group is spherical to ovate, is dominated by zircon that dimly luminesces in CL, and has thin bright CL-imaged rims. The second group contains rounded to tabular ovate grains, sector and oscillatory-zoned cores that appear rounded and resorbed, and bright CL-imaged overgrowths with variable thicknesses (up to 100 μm). The third group is characterized by facetted spherical to ovate grains with sector and oscillatory-zoned cores of variable resorption, and similar sector zoned overgrowths that are not obviously resorbed (up to 200 μm). This dominant zircon population is characterized by Th/U ratios of 0.21-0.31, and U concentrations from 55-280 ppm. Ten abraded and one unabraded zircon fragments yielded a linear array with an upper intercept of 2554.5 ± 4.3 Ma and a lower intercept of 1896.0 ± 18 Ma (MSWD = 3.2) (Figure 6). The three fragments analyzed from the first group of zircons, characterized by the thinnest rims, yielded the most concordant analyses. One physically abraded fragment subsequently subjected to chemical abrasion (z5c) yielded a ^{207}Pb/^{206}Pb date older than a fragment of the same grain (z5b) analyzed by standard methods, but still plotted on the mixing array. Two zircon grains from the homogeneous, bright CL secondary population were chemically abraded and yielded ca. 1.9 Ga dates. These two grains had previously been analyzed by ion microprobe, with results discussed further below.

Sample 03-88A is from the interior of a medium-grained, banded mafic granulite body at Bompas Lake. Zircon grains are spherical to ovate, are typically < 150 μm in diameter, and compose two populations characterized by distinct internal structures visible in CL (Figure 7). The first population is dominated by zircon that is homogeneous and bright in CL, with 5-20 μm darker CL rims. The second, more abundant type of zircon is characterized by an oscillatory to irregularly zoned internal domain, irregular embayments on several grains suggesting possible resorption, and overgrowths of variable thickness. Zircon grains have Th/U ratios of 0.08 – 0.39 and U concentrations from 30-235 ppm. No dramatic difference in U-Pb systematics was detected between the two populations distinguished in CL. Five abraded single zircon grains, two unabraded single zircon grains, one unabraded zircon fragment, and one chemically abraded zircon fragment yielded a linear array with an upper intercept of ca. 2.56 Ga and a lower intercept of ca. 1.86 Ga (Figure 7). The chemically abraded zircon fragment (z8c) plotted at an older age on the mixing array than its unabraded counterpart analyzed by standard methods (z8a).

Sample 03-159A was collected from a ~50m wide layer of mafic granulite at Lytle Lake. Zircon grains are spherical to ovate, range in size from tens to hundreds of microns, and do not luminesce in CL (Figure 8). Zircon crystals have Th/U ratios of 0.20-0.32 and U concentrations of 340-690 ppm. The suppression of zircon CL is attributed to radiation damage from high U concentrations. Some grains display faint internal sector zoning in BE, and possible overgrowths. Three abraded fragments from two larger-sized zircons, two abraded single zircons, four unabraded single zircons, and two chemically abraded zircon fragments were analyzed. The five abraded fractions and one unabraded fraction yielded a poorly defined array with a ca. 2.55 Ga upper intercept and a Proterozoic lower intercept (Figure 8). One significantly older analysis is interpreted to contain a minor inherited component. Although the unabraded zircon fractions were intended to better define the lower intercept of the array by retaining the zircon overgrowths, these fractions show increased discordance likely caused by secondary Pb loss in the high U, radiation damaged rims. The two chemically abraded zircon fragments displayed significantly greater discordance than the other analyzed fractions.

Sample 03-175A is a partially retrogressed felsic granulite from Cora Lake characterized by cm-scale garnets. Zircon grains are abundant, spherical to ovate, typically < 100 μm (up to 150 μm in length), and do not luminesce in CL (Figure 9). Th/U ratios are 0.09-0.14. Radiation damage due to moderate U concentrations of 260-340 ppm is inferred to cause the suppression of zircon CL. In BE zircons show faint internal concentric zoning, with possible thin < 10 μm rims on some crystals. Five abraded, three unabraded, and three chemically abraded fractions of single zircon grains and fragments were analyzed. Five fractions yield a poorly defined array with an upper intercept at ca. 2.5 Ga and a Proterozoic lower intercept (Figure 9). The thin rims and low temperature Pb loss due to radiation damage are interpreted to contribute to data scatter and the poorly defined lower intercept date. Two of three chemically abraded zircon fractions, including a fragment with a counterpart analyzed by standard methods, displayed significantly greater discordance than the other analyses. In addition, eight monazite fragments were analyzed from six different monazite crystals interpreted to represent different populations. Imaged monazite grains were characterized by concentric and patchy zonation, as well as homogeneous textures, with widely varying Th, Ca, Y and U concentrations, and a broad range (0.5-75) of Th/U ratios. Analyses ranged from concordant to several percent discordant, with ^{207}Pb/^{206}Pb dates from 2276.9 to 2558.6 Ma (Figure 10).

U-Pb Ion Microprobe Analytical Results

Following U-Pb TIMS analysis, sample 02M133A was selected for ion microprobe study to test whether the cores and rims revealed in cathodoluminescence images correspond to the concordia intercept dates of the well-defined discordia line. Internal structures of zircon grains imaged by cathodoluminescence are similar to those described above. Thirty analyses carried out on twenty-six zircon crystals from the dominant population yielded a range of apparent $^{207}Pb/^{206}Pb$ dates, including thirteen analyses on zircon cores from 2674 ± 15 Ma to 2065 ± 53 Ma, twelve analyses on zircon overgrowths from 2710 ± 27 Ma to 1911 ± 40 Ma, and five analyses on grains without overgrowths from 2600 ± 19 Ma to 2161 ± 45 Ma (Figures 11 and 12). Zircon cores and rims show a similar range of Th/U ratios from 0.15 to 0.42. Eight analyses on four unzoned to weakly zoned zircon grains that are bright in CL yielded consistent dates from 1805 ± 88 Ma to 1949 ± 70 Ma. This subset of ca. 1.9 Ga homogeneous grains display the lowest Th/U ratios (0.08-0.14) and lowest U and Th concentrations of the dataset.

DISCUSSION

Complex U-Pb Accessory Mineral Systematics in Polymetamorphosed Granulites

Evidence for Two Metamorphic Events: U-Pb TIMS Zircon Geochronological Data

U-Pb TIMS zircon data for three mafic granulites and one felsic granulite gneiss define mixing lines with intercepts at ca. 2.55 Ga and ca. 1.8-1.9 Ga. The simplest interpretation of the zircon data and internal zircon zoning characteristics is that the intercept dates represent the timing of two metamorphic events. Zircon U concentrations range from 40 to 720 ppm, with sample zircon systematics partially correlating with U concentrations. Low U (< 300 ppm) zircon crystals from two samples luminesced in CL, allowing detailed assessment of internal zoning patterns, and defined well-behaved mixing arrays. For example, CL images of analyzed 02M133A zircon revealed sector zoning with isometric overgrowths of variable thickness and CL brightness, typical of zircon growth during amphibolite through granulite facies conditions (Figure 6) (e.g. Vavra et al. 1996, 1999; Corfu et al., 2003). Zircon analyses yielded a well-defined mixing line between 2.55 and 1.9 Ga (MSWD = 3.2). A distinct zircon subpopulation characterized by homogeneous bright CL yielded 1.9 Ga dates interpreted to represent new growth at this time. Low U zircon crystals from 03-88A yielded a similar mixing array, although no subpopulation of 1.9 Ga zircon grains was identified (Figure 7). Four unabraded single zircon grains and fragments from these two samples were dissolved by standard procedures in an effort to better define the lower part of the mixing array. Three of these unabraded zircon analyses were among the youngest $^{207}Pb/^{206}Pb$ dates for these samples, consistent with exterior portions of the grains containing generally younger apparent ages than interior portions. In contrast to the lower U zircon grains, higher U (typically >350 ppm) zircon crystals from two (03-175A, 03-159A) samples did not luminesce in CL, yielded scattered arrays with analyses that plot near the upper end of the mixing line, define ca. 2.54 to 2.56 Ga upper intercepts, and provide poorly defined Proterozoic lower intercepts (Figures 8 & 9). The greater scatter in the zircon systematics, despite care taken to select the least altered BE-imaged zircon grains for analysis, is attributed to low temperature Pb loss owing to increased radiation damage in high U zircons, as has been documented in previous studies. In zircon BE images, fractures and darker zircon portions inferred to be metamict domains are consistent with this hypothesis. Complete dissolution of these high U zircon crystals in short, low-temperature leach steps during application of chemical abrasion TIMS techniques, discussed further below, substantiates the highly metamict character of these grains. Seven unabraded zircon grains from these two samples were analyzed by standard procedures in order to better define the lower part of the mixing array by including exterior portions of the crystals assumed to be younger in age than interior portions. Although six analyses yielded younger $^{207}Pb/^{206}Pb$ dates than their abraded counterparts, they scattered below a hypothetical mixing array between 2.55 and 1.9 Ga as defined by the lower U zircon samples. The scatter suggests additional low temperature Pb loss in external portions of grains most accessible to fluids and alteration, consistent with a higher proportion of fractures in the rims of zircon grains imaged by BE.

Evidence for Recrystallization and/or Pb Redistribution in Metamorphic Zircon: U-Pb Ion Microprobe Geochronological Data

Ion microprobe data was acquired to help decipher the significance of the mixing lines defined by TIMS study. Low uranium zircon grains from mafic granulite sample

02M133A were considered the ideal target for this analysis because these crystals yielded the best-defined TIMS mixing array with little scatter, suggesting minimal secondary effects from low temperature Pb loss. In addition, detailed thermobarometric study, petrogenetic modeling and kinematic analysis of this same sample (Mahan et al., 2005), provided a particularly well-documented context for interpretation of the geochronological results.

Ion microprobe analyses revealed more complex U-Pb systematics than could be explained by two-component mixing of cores and overgrowths visible in CL images. Both cores and overgrowths yielded a continuous range of apparent ^{207}Pb/^{206}Pb dates from 2.71 to 1.91 Ga, showed no obvious correlation of dates with zonation, and yielded consistent Th/U ratios that were independent of apparent age (Figure 13A). The data included negatively discordant analyses that suggest the local distribution of unsupported radiogenic Pb, a group of concordant ca. 2.55 Ga zircon analyses, as well as an array of younger dates consistent with local loss of radiogenic Pb. In contrast, the homogeneous bright CL zircon population is characterized by distinctly lower Th/U ratios and consistent ca. 1.9 Ga dates, and is interpreted to represent new growth in the Proterozoic.

Potential mechanisms to explain the complex U-Pb systematics of the dominant zircon population include episodic zircon growth from 2.55 to 1.9 Ga, 1.9 Ga diffusional Pb loss, and 1.9 Ga zircon recrystallization. First, episodic zircon growth does not appear to be a viable interpretation, because a similar range of apparent dates and Th/U ratios are documented for both cores and overgrowths. For example, a zircon overgrowth with an older date than preserved in the core (zircon #15) is inconsistent with an explanation that only invokes episodic growth. In addition, the secondary ca. 1.9 Ga zircon population considered to reflect Proterozoic growth is characterized by distinct CL characteristics and Th/U ratios not observed in the dominant population. Second, simple diffusional Pb loss at 1.9 Ga appears equally improbable, not only because of the extreme sluggishness of Pb diffusion in zircon documented experimentally (Lee et al., 1997; Cherniak et al. 2000), but also because this mechanism cannot easily explain the heterogeneous spatial distribution of variable dates or the local occurrence of unsupported radiogenic Pb. We consider the simplest interpretation to be that all domains of the dominant population, both cores and overgrowths, grew at ca. 2.55 Ga and were heterogeneously reset in the

Proterozoic. Isotopic resetting of zircon during recrystallization, resulting in Pb loss and local Pb gain, is an increasingly well-documented phenomenon typically interpreted to high-temperature metamorphic processes, metasomatic alteration, and/or the instability of impurity rich zircon domains (e.g. Williams et al., 1984; Pidgeon, 1992; Pidgeon et al., 1998; Schaltegger et al., 1999; Hoskin and Black, 2000; Carson et al., 2002). However, in previous studies this process has typically been identified by the textural development of bleached zones and transgressive replacement fronts, changed Th/U ratios, and modified trace-element compositions that affect the zircon CL characteristics. The lack of visual evidence for replacement textures and the consistency of Th/U ratios for zircon crystals in our investigation suggests that if recrystallization was responsible for the perturbed U-Pb systematics, it was a somewhat different process than those proposed in the literature.

Several observations may provide preliminary clues into this problem. Plots of ^{207}Pb/^{206}Pb date versus U concentration reveal that the highest U zircon domains yielded fairly consistent ca. 2.55 Ga dates, while zircon domains characterized by decreasing U concentration display a progressively greater range of apparent zircon dates both older and younger than 2.55 Ga, indicative of local excesses and deficits of radiogenic Pb (Figure 13B). This pattern holds true for all zircon types, although overgrowths show a slightly greater dispersion of dates than other zircon groups. A similar correlation is revealed by inspection of the TIMS data for zircon grains and fragments from four different samples that together are characterized by a greater range of uranium concentrations than that contained within zircon from the single sample analyzed by ion microprobe (Figure 14). The two high U and two low U zircon samples show a similar range of Th/U ratios. The highest U (350-720 ppm) zircon grains from sample 03-159A, excluding fraction z8 tainted by inheritance, record the least 1.9 Ga signature. Analyses of moderate U (275-450 ppm) zircon grains from sample 03-175A display a spread to younger ^{207}Pb/^{206}Pb dates. The lowest U zircon crystals (< 275 ppm) from samples 02M133A and 03-88A yield the youngest ^{207}Pb/^{206}Pb dates of the TIMS dataset, suggesting the greatest 1.9 Ga perturbation of the U-Pb systematics. This trend is opposite of that expected for effects of low temperature Pb loss associated with radiation damage, in which the highest U zircon grains should show the greatest discordance and the youngest $^{207}Pb/^{206}Pb$ dates.

These data suggest that low U zircon domains were preferentially affected by Pb remobilization and/or recrystallization processes. Vavra et al. (1999) reported a similar observation for metamorphic zircon grains in the Ivrea zone, where the lowest U zircon domains were most affected by alteration and resetting of the U-Pb systematics. In this case visual evidence for zircon replacement was observed, and recrystallization was attributed to a subsequent thermal pulse, consistent with petrological evidence for regional metamorphism followed by contact metamorphism at temperatures > 650-750 °C (Barboza et al., 1999, 2000). Observations similar to those in our study were also reported for sector zoned metamorphic zircon in northern Labrador that were affected by contact metamorphism at temperatures >800 °C. Affected zircon displayed an array of normally and reversely discordant analyses, low U domains typically revealed the youngest apparent ages, consistent Th/U ratios were independent of dates, and there was no obvious visual evidence for zircon replacement textures (McFarlane et al., 2004). The study attributed the scattered dates to Pb remobilization during the high temperature event.

Although observations in mafic granulite zircon grains from the East Lake Athabasca region are not entirely identical to those in these two previous studies, the central feature common to all three investigations is that a large range of apparent ages were observed in the lower U domains of sector zoned metamorphic zircon that were subjected to a second high temperature metamorphic event. The U concentrations may correlate with trace element contents or other zircon impurities that exert control on the susceptibility of zircon to this complex isotopic disturbance. Again, we emphasize that metamorphic zircon grains in our study showed no CL evidence for perturbed U-Pb systematics and did not show modified Th/U ratios, suggesting that their behavior during high temperature metamorphic conditions is distinct from the heterochemical transgressive replacement textures typically documented in magmatic zircon grains that have been subjected to high temperatures. Therefore, we suggest that the zircon behavior documented in our study may represent a different response of metamorphic zircon to high temperatures. The lack of other examples may be due to the scarcity of exposed rocks containing the requisite history of two metamorphic events, necessary first to form the primary sector zoned metamorphic zircon population and second to provide the high temperatures necessary to perturb the U-Pb systematics in these crystals. It is possible that this zircon behavior is not uncommon in polymetamorphic terranes, and future investigations may reveal similar examples that will provide further insights into the mechanisms responsible for the complex U-Pb zircon systematics documented in this study.

Complex CA-TIMS Zircon Systematics

Chemical abrasion (CA)-TIMS geochronological techniques developed by Mattinson (2005) are increasingly being utilized for high-resolution U-Pb zircon analysis. This method involves laboratory annealing of radiation damage at high temperatures followed by chemical leaching. Within typical magmatic zircon grains, leach steps are observed to predictably remove the highest U portions of zircon grains that have undergone Pb loss, leaving the lower U portions that have remained a closed system for high-resolution analysis.

Following documentation of complex U-Pb systematics in granulite zircon grains in this study via standard TIMS and ion microprobe methods, select grains were subjected to chemical abrasion in an effort to isolate the lower U portions of zircon crystals inferred to have been most affected by the ca. 1.9 Ga overprinting event, as discussed above. Preliminary data acquired for both low U and high U zircon grains revealed a complex response to the chemical abrasion process. Following a single leach step, two fragments of low U zircon crystals from samples 02M133A and 03-88A yielded CA-TIMS analyses that showed an unexpected enrichment in the older component relative to fragments of the same crystals that previously had been analyzed by standard TIMS methods. These preliminary results suggest that the lower U portions of the grains with disturbed systematics were preferentially removed during the leach step. Additional study is required to more thoroughly explore this problem. In contrast, four of five high U zircon grains from samples 03-175A and 03-159A yielded CA-TIMS results that displayed the anticipated shift toward younger $^{207}Pb/^{206}Pb$ dates, but plotted off a 2.55 to 1.9 Ga mixing array. A relatively gentle hotplate leach step was applied to these higher

U zircon grains, because an initial suite of these crystals completely dissolved during the standard leaching procedure, attesting to their metamict state. Previous studies on radiation-damaged zircon crystals that were not annealed in the lab prior to leaching have shown complex U-Pb, and possibly ^{207}Pb-^{206}Pb fractionation effects during partial dissolution, attributed to preferential leaching of Pb alpha-recoil damaged sites over lattice-bound U, preferential removal of ^{206}Pb in more strongly damaged sites over ^{207}Pb, and/or selective removal of young radiogenic Pb over older radiogenic Pb in previously annealed domains (e.g. Corfu, 2000; Davis and Krogh, 2000; Mattinson, 2005). Laboratory annealing at 800-1000 °C for ~48 hours has been shown to greatly reduce U-Pb and Pb/Pb fractionation effects in zircon characterized by low to moderate radiation damage (Mattinson, 2005). However, more detailed analysis is required to evaluate the effect on more highly radiation damaged crystals such as those in this study.

Evidence for Episodic Monazite Growth: TIMS Monazite Geochronological Data

Imaging techniques, chemical mapping, and IDTIMS monazite geochronological data for the felsic granulite document multiple populations of monazite that preserve both near concordant and discordant ^{207}Pb/^{206}Pb dates between 2.56 and 2.33 Ga. These data do not define a simple mixing line. Images revealed concentrically zoned grains, patchwork textures, and unzoned monazite crystals, with chemical maps indicating a wide variation in Th and Y concentrations. We interpret these data to indicate multiple episodes of growth and/or fluid mediated recrystallization processes. Electron microprobe monazite dating has documented similar complexity of monazite populations in Chipman domain felsic granulites. The observation that garnet exclusively contains ca. 2.55 Ga monazite, with Archean through 1.9 Ga monazite in the matrix assemblage, has been interpreted to indicate growth of garnet in this rock during Archean metamorphism (Mahan et al., 2005). Complex monazite populations with similar characteristics have also been documented in the southern domain (Baldwin et al., in review). We ascribe the occurrence of multiple monazite populations, in contrast to the two discrete episodes of zircon growth in this sample, to the greater propensity of monazite to grow during metamorphic reactions and fluid mediated processes at conditions well below its closure temperature (e.g. Rubatto et al., 2001; Foster et al., 2002).

Implications for Deep Crustal Residence, Continental Stability and Lithospheric Reactivation

Timing of Multiple High-pressure Granulite Facies Metamorphic Events

Deciphering the P-T-t-d histories of multiply deformed polymetamorphic deep crustal terranes is a difficult task, and has presented an ongoing challenge within granulite domains of the East Lake Athabasca region. Our new U-Pb zircon data for mafic and felsic granulite gneisses within the Chipman domain document growth of the dominant population of metamorphic zircon at ca. 2.55 Ga, with subsequent ca. 1.9 Ga perturbation of the isotopic systematics and limited new metamorphic zircon growth at this time. The temporal gap between ca. 2.55 Ga growth of zircon cores and overgrowths in the primary population is unknown, because the U-Pb isotopic systematics have been complicated by the Proterozoic overprinting event. The mafic granulites preserve an M1 garnet-clinopyroxene assemblage (~1.3 GPa, 850 °C) interpreted to have developed from an orthopyroxene-bearing igneous assemblage, a hornblende bearing matrix inferred to represent subsequent retrogression, and a second prograde garnet-orthopyroxene assemblage (~1.0 GPa, >800 °C) (Mahan et al., 2005). We link the dominant population of ca. 2.55 Ga metamorphic zircon to growth during the first HP granulite facies metamorphic event at conditions of ~1.3 GPa, 850 °C. Confident connection of subsequent zircon growth with retrogression and the second episode of granulite facies metamorphism (~1.0 GPa, 800 °C) is more difficult. The second granulite assemblage may have developed 1) as part of the ca. 2.55 Ga metamorphic cycle, or 2) at 1.9 Ga marked by secondary zircon growth and disturbance of the U-Pb systematics of the primary zircon population.

Particularly important for the tectonic implications of this dataset is the documentation of 1896.2 ± 0.2 Ma HP granulite facies metamorphism at conditions of 1.0-1.2 GPa, 750 °C, based on high-precision U-Pb TIMS dates for zircon grains from migmatized Chipman mafic granulite dikes (Williams et al., 1995; Flowers, Chapter 2). The similarity of metamorphic conditions preserved within Chipman mafic granulite dikes intruded across the Chipman domain to those yielded by the second granulite facies assemblage of the mafic gneisses is consistent with the near-synchronous development of the assemblages at ca. 1.9 Ga. In addition, titanite grains from mafic granulite sample 02M133A yield dates of ca. 1885 Ma, consistent with ca. 1.88 - 1.90 Ga titanite dates for five other samples across the Chipman domain, corroborating attainment of temperatures > 650 °C at ca. 1.9 Ga (Flowers, Chapter 3). Thus, the geochronological and petrological datasets provide strong evidence for a ca. 2.55 Ga (~1.3 GPa, 850 °C) HP metamorphic assemblage in the mafic granulite gneisses, and a 1.9 Ga (1.0-1.2 GPa, 750 °C) metamorphic assemblage in the Chipman mafic dikes that may also be preserved in the mafic gneisses, indicating that at least two HP granulite facies metamorphic events impacted the Chipman domain.

Deep Crustal Residence and Lithospheric Stability

We interpret the Chipman domain record of 2.55 Ga (~1.3 GPa, 850 °C) and 1.9 Ga (1.0-1.2 GPa, 750 °C) high-pressure granulite facies metamorphic events to indicate an intervening 650 m.y. period during which the granulites resided in the deep crust. Archean dehydration with minimal subsequent rehydration is consistent with evidence for limited melting and deformation of these rocks when subjected to intense temperatures (> 750 °C) in the Proterozoic. It seems likely that if there had been significant unroofing and subsequent burial during this interval, greater retrogression of Archean assemblages would be observed. Variable monazite dates between 2.55 and 1.9 Ga in Chipman domain felsic granulites, documented both by TIMS data in this study and by additional electron microprobe monazite data (Mahan, 2005), are inferred to record episodic fluid mediated growth during deep crustal residence, rather than discrete episodes of metamorphism characterized by new mineral assemblages. The greater reactivity of monazite at low temperatures explains the lack of coeval zircon growth at these times. Additional information regarding the 2.55 to 1.9 Ga history is required to more fully constrain the P-T path during this period.

We propose that this relatively quiescent interval of deep crustal residence is linked with a prolonged period of lithospheric stability following assembly in the Archean. Lithospheric stabilization was heralded by the 2.55 Ga HP-HT event, followed by isobaric cooling to a cratonic geotherm. Amalgamation of the Laurentian supercontinent between ca. 2.02 and 1.81 Ga played a key role in perturbing the pre-existing lithospheric configuration, and detailed studies of 1.9 Ga tectonometamorphism have begun to yield insight into the nature of this event (Flowers, Chapter 2; Baldwin et al., 2004). Although long-term residence of rocks in the deep crust is a common feature of cratonic regions that have remained relatively unperturbed for billions of years, subsequent exhumation of the lowermost crust in such regions is a rarity, owing to the difficulty of disrupting cratons underlain by thick lithospheric mantle roots. Thus, the 1.9 Ga HP granulite facies metamorphism and subsequent exhumation of lowermost continental crust in the East Lake Athabasca region requires an event of profound significance. The complex record of multiple HP granulite facies metamorphic events in the East Lake Athabasca region is the fingerprint of larger scale changes within the underlying lithospheric mantle due to plate tectonic and asthenospheric mantle activity. Deciphering the complex record preserved in these rocks provides a unique perspective on the evolution of lower continental crust during the stabilization and reactivation of continents.

REFERENCES

Baldwin, J.A., Bowring, S.A., and Williams, M.L., 2003, Petrological and geochronological constraints on high-pressure, high temperature metamorphism in the Snowbird tectonic zone, Canada: Journal of Metamorphic Geology, v. 21,p. 1-19.

Baldwin, J.A., Bowring, S.A., Williams, M.L. and Mahan, K.H., in review, Geochronological constraints on the crustal evolution of felsic high-pressure granulites, Snowbird tectonic zone, Canada: Lithos, ---.

Baldwin, J.A., Bowring, S.A., Williams, M.L., and Williams, I.S., 2004, Eclogites of the Snowbird tectonic zone: petrological and U-Pb geochronological evidence for Paleoproterozoic high-pressure metamorphism in the western Canadian Shield: Contributions to Mineralogy and Petrology, v. 147, p. 528-548.

Barboza, S.A. and Bergantz, G.W., 2000, Metamorphism and anatexis in the Mafic Complex contact aureole, Ivrea Zone, northern Italy: Journal of Petrology, v. 41, p. 1307-1327.

Barboza, S.A., Bergantz, G.W. and Brown, M., 1999, Regional granulite facies metamorphism in Ivrea zone: Is the Mafic Complex the smoking gun or a red herring?: Geology, v. 27, p. 447-450.

Berman, R.G., Davis, W.J., Aspler, L.B. and Chiarenzelli, J.R., 2002, SHRIMP U-Pb ages of multiple metamorphic events in the Angikuni Lake area, western Churchill Province, Nunavut: Geological Survey of Canada Current Research, 2002-F3, 9 pp.

Carson, C.J., Ague, J.J., Grove, M., Coath, C.D. and Harrison, T.M., 2002, U-Pb isotopic behavior of zircon during upper-amphibolite facies fluid infiltration in the Napier Complex, east Antarctica: Earth and Planetary Sciences Letters: v. 199, pl. 287-310.

Cherniak, D.J., Lanford, W.A. and Ryerson, F.J., 1991, Lead diffusion in apatite and zircon using ion implantation and Rutherford Backscattering techniques: Geochimica et Cosmochimica Acta, v. 55, p. 1663-1673.

Cherniak, D.J. and Watson, E.B., 2000, Pb diffusion in zircon: Chemical Geology, v.172, p. 5-24.

Claoue-Long, J. C., Compston, W., Roberts, J. and Fanning, C. M.,1995. Two Carboniferous ages: A comparison of SHRIMP zircon dating with conventional zircon ages and ^{40}Ar/^{39}Ar analysis. In: Geochronology, Time Scales and Global Stratigraphic Correlation (eds Berggren, W.A., Kent, D.V., Aubrey, M.-P. & Hardenbol, J.), pp. 3–21. SEPM (Society for Sedimentary Geology), Tulsa, OK, Special Publication, 54.

Corfu, F., 2000, Extraction of Pb with artificially too-old ages during stepwise dissolution experiments on Archean zircon: Lithos, v. 53, p. 279-291.

Corfu, F., Hanchar, J.M., Hoskin, P.W.O., and Kinny, P., 2003, Atlas of zircon textures, in Zircon, Reviews in Mineralogy and Geochemistry 53, edited by J.M. Hanchar and P.W.O. Hoskin, p. 468-500.

Cumming, G.L. and Richards, J.R., 1975, Ore lead isotope ratios in a continuously changing earth: Earth and Planetary Science Letters, v. 28, p. 155-171.

Davis, D.W. and Krogh, T.E., 2000, Preferential dissolution of 234U and radiogenic Pb from a-recoil-damaged lattice sites in zircon: implications for thermal histories and Pb isotopic fractionation in the near surface environment: Chemical Geology, v. 172, p. 41-58.

Foster, G., Gibson, H.D.,Parrish, R., Horstwood, M., Fraser, J. and Tindle, A., 2002, Textural, chemical and isotopic insights into the nature and behavior of metamorphic monazite: Chemical Geology, v. 191, p. 183-207.

Hanmer, S., 1994, Geology, East Athabasca mylonite triangle, Saskatchewan, In: Geological Society of Canada Map, 1859A.

Hanmer, S., 1997, Geology of the Striding-Athabasca mylonite zone, northern Saskatchewan and southeastern District of Mackenzie, Northwest Territories: Geological Survey of Canada Bulletin, v. 501, pp.1-92.

Hoffman, P.F., 1988, United Plates of America, the birth of a craton: Early Proterozoic assembly and growth of Laurentia: Annual Reviews of Earth and Planetary Science Letters, v. 16, p.545-603.

Hoskin, P.W.O. and Black, L.P., 2000, Metamorphic zircon formation by solid-state recrystallization of protolith igneous zircon: Journal of Metamorphic Geology, v. 18, p. 423-439.

Jaffey, A. H., Flynn, K. F., Glendenin, L. E., Bentley, W. C., and Essling, A. M., 1971,Precision measurements of half-lives and specific activities of 235U and 238U:Physics Review, v. C4, p.1889-1906.

Kopf, C. 1999. Deformation, metamorphism, and magmatism in the East Athabasca mylonite triangle, northern Saskatchewan: Implications for the Archean and Early Proterozoic crustal structure of the Canadian Shield. Ph. D. dissertation thesis, University of Massachusetts-Amherst, p. 139.

Krogh, T.E., 1973, A low contamination method for hydrothermal decomposition of zircon and extraction of U and Pb for isotopic age determinations: Geochimica et Cosmochimica Acta, v. 37, p. 485-494.

Krogh, T.E., 1982, Improved accuracy of U-Pb zircon ages by the creation of more concordant systems using an abrasion technique: Geochimica et Cosmochimica Acta, v. 46, p. 637-649.

Lee, J.K.W., Williams, I.S., and Ellis, D.J., 1997, Pb, U and Th diffusion in natural zircon: Nature, v. 390, p. 159-161.

Lewry, J.F., and Sibbald, T.I.I. 1980. Thermotectonic evolution of the Churchill Province in northern Saskatchewan. Tectonophysics, 68: 5-82.

Ludwig, K. R. (1980) Calculation of uncertainties of U-Pb isotope data: Earth and Planetary Sciences Letters, v. 46, p. 212–220.

Mahan, K.H. and Williams, M.L., 2005, Reconstruction of a large deep-crustal exposure: Implications for the Snowbird tectonic zone and early growth of Laurentia: Geology, v.33, p. 385-388.

Mahan, K.H., 2005, Exhumation of exposed deep continental crust, western CanadianShield: Integrating structural analysis, petrology, and in situ geochronology: PhD *thesis, University of Massachusetts, Amherst, Massachusetts.*

Mahan, K.H., Flowers, R.M., Williams, M.L., Goncalves, P., Bowring, S.A., and Jercinovic, M.J., 2005, A P-T-time-deformation path for exposed deep continental crust in the Snowbird tectonic zone, western Canadian Shield: GSA Cordilleran Session Meeting abstract, San Jose, CA.

Mattinson, J.M., 2005, Zircon U-Pb chemical abrasion ("CA-TIMS") method: Combined annealing and multi-step partial dissolution analysis for improved precision and accuracy of zircon ages: Chemical Geology, v. 220, p. 47-66.

McFarlane, C.R.M., Connelly, J.N. and Carlson, W.D., 2004, Intracrystalline redistribution of Pb in zircon during high-temperature contact metamorphism: Chemical Geology, v. 217, p. 1-28.

Pidgeon, R.T., 1992, Recrystallization of oscillatory zoned zircon: some geochronological and petrological implications: Contributions to Mineralogy and Petrology, v. 110, p. 463-472.

Pidgeon, R.T., Nemchin, A.A., and Hitchen, G.J., 1998, Internal structures of zircons from Archean granites from the Darling Range batholith: Implications for zircon stability and the interpretation of zircon U-Pb ages: Contributions to Mineralogy and Petrology, v.132, p. 288-299.

Ross, G.M., Eaton, D.W., Boerner, D.E. and Miles, W., 2000, Tectonic entrapment and its role in the evolution of continental lithosphere: An example from the Precambrian of western Canada: Tectonics, v. 19, p.116-134.

Ross, G.M., Milkereit, B., Eaton, D., White, D., Kanasewich, E.R., and Burianyk, M.J.A., 1995, Paleoproterozoic collisional orogen beneath the western Canada sedimentary basin imaged by Lithoprobe crustal seismic reflection data: Geology, v. 23, p. 195-199.

Rubatto, D., Williams, I.S., and Buick, I.S., 2001, Zircon and monazite response to prograde metamorphism in the Reynolds Range, central Australia: Contributions to Mineralogy and Petrology, v. 140, p. 458-468.

Schaltegger, U., Fanning, C.M., Gunther, D., Maurin, J.C., Schulmann, K. and Gebauer, D., Growth, annealing and recrystallization of zircon and preservation of monazite in high-grade metamorphism: conventional and in-situ U-Pb isotope, cathodoluminescence and microchemical evidence: Contributions to Mineralogy and Petrology, v. 134, p. 186-201.

Silver, L.T. and Deutsch, S., 1963, Uranium-lead isotopic variations in zircons – a case study: Journal of Geology, v. 71, p. 721-758.

Snoeyenbos, D.R., Williams, M.L. and Hanmer, S., 1995, Archean high-pressure metamorphism in the western Canadian Shield: European Journal of Mineralogy, v. 7, p.1251-1272.

Stacey, J.C. and Kramers, J.D., 1975, Approximation of terrestrial lead isotope evolution by a two-stage model: Earth and Planetary Science Letters, v.26, p.207-221.

Stern, R.A. and Berman, R.G., 2000, Monazite U-Pb and Th-Pb geochronology by ion microprobe, with an application to in situ dating of an Archean metasedimentary rock: Chemical Geology, v. 172, p. 113-130.

Vavra, G., Gebauer, D., Schmid, R., and Compston, W., 1996, Multiple zircon growth and recrystallization during polyphase Late Carboniferous to Triassic metamorphism in granulites of the Ivrea Zone (Southern Alps): an ion microprobe (SHRIMP) study: Contributions to Mineralogy and Petrology, v. 122, p. 337-358.

Vavra, G., Schmid, R., and Gebauer, D., 1999, Internal morphology, habit and U-Th-Pb microanalysis of amphibolite-to-granulite facies zircons: geochronology of the Ivrea Zone (Southen Alps): Contributions to Mineralogy and Petrology, v. 134, p. 380-404.

Williams, I.S., Compston, W., Black, L.P., Ireland, T.R., and Foster, J.J., 1984, Unsupported radiogenic Pb in zircon: a cause of anomalously high Pb-Pb, U-Pb and Th-Pb ages: Contributions to Mineralogy and Petrology, v. 88, p. 322-327.

Williams, M.L., Hanmer, S., Kopf, C. and Darrach,M., 1995, Syntectonic generation and segregation of tonalitic melts from amphibolite dikes in the lower crust, Striding-Athabasca mylonite zone, northern Saskatchewan: Journal of Geophysical Research, v.100(B8), p.15,717-15,734.

Williams, M.L., Mellis, E.A., Kopf,C. and Hanmer,S., 2000, Microstructural Tectonometamorphic processes and the development of gneissic layering: a mechanism for metamorphic segregation: Journal of Metamorphic Geology, v. 18, p.41-57.

FIGURE CAPTIONS

Figure 1. Geological map of the western Canadian Shield showing major tectonic features. AB-Athabasca basin, STZ-Snowbird tectonic zone, TB-Thelon Basin, THO-Trans-Hudson Orogen, TO-Taltson Orogen, TMZ-Thelon Magmatic Zone, UX-Uvauk Complex. The rectangle shows the East Lake Athabasca region enlarged in Figure 2.

Figure 2. Geological map of the East Lake Athabasca region, northern Saskatchewan. The box outline shows the location of the study area enlarged in Figure 3.

Figure 3. Geological map of the Chipman domain with sample locations.

Figure 4. Mg map of thin section from mafic granulite sample 02M133A. Brighter colors represent higher Mg concentrations. Red is primarily garnet and yellow is clinopyroxene or hornblende. Blue dots represent locations of zircon crystals. Thermobarometric estimates for the M1 assemblage in the coarse-grained Grt+Cpx boudin, and in the Grt+Hbl+Cpx+Opx matrix are from Mahan et al. (2005). B) BE images showing petrographic setting of zircon associated with the M1 and matrix assemblages, with enlargements of CL images of zircon.

Figure 5. REE diagrams for Chipman domain A) mafic granulites, and B)felsic granulites. Data for southern domain felsic granulites from Baldwin et al. (in review) are shown in B) for reference. Chrondrite values from Sun and McDonough (1989).

Figure 6. Concordia diagram for zircon analyzed by TIMS from mafic granulite sample 02M133A with CL images of analyzed zircon crystals. Thin lines delineate where the zircon grains were broken prior to analysis. Analyses z7.ip.ca and z17.ip.ca are grains previously analyzed by ion microprobe from the secondary population of ca. 1.9 Ga zircon, and CL images are shown in Figure 13.

Figure 7. Concordia diagram for zircon analyzed by TIMS from mafic granulite sample 03-88A with CL images of all analyzed zircon crystals. Thin lines delineate where the zircon grains were broken prior to analysis.

Figure 8. Concordia diagram for zircon analyzed by TIMS from mafic granulite sample 03-159A with BE images of all analyzed zircon crystals. Thin lines delineate where the zircon grains were broken prior to analysis.

Figure 9. Concordia diagram of zircon analyzed by TIMS from felsic granulite sample 03-175A with BE images of analyzed zircon crystals. Thin lines delineate where the zircon grains were broken prior to analysis.

Figure 10. Concordia diagram of monazite analyzed by TIMS from felsic granulite sample 03-175A. Associated BE images and Th, Ca, Y and U compositional maps are shown for the analyzed monazite.

Figure 11. Concordia diagram of zircon analyzed by ion microprobe from mafic granulite sample 02M133A.

Figure 12. CL images for zircon from mafic granulite 02M133 with locations of ion microprobe spots. $^{207}Pb/^{206}Pb$ and $^{206}Pb/^{238}U$ dates for each spot are indicated.

Figure 13. $^{207}Pb/^{206}Pb$ ion microprobe zircon dates from mafic granulite sample 02M133A plotted against A) Th/U ratio and B) U concentration. The two highest U points are omitted from A) so that the figure could be plotted at the most effective scale.

Figure 14. $^{207}Pb/^{206}Pb$ TIMS zircon dates from all four samples in this study plotted against A) Th/U ratio and B) U concentration. Inherited zircon 03-159A, z8 is excluded from this plot.

Table 1. Major and trace element data for Chipman domain mafic and felsic granulite gneisses

	Mafic granulites (Gt-cpx-hb-opx)					Orthopyroxenites					Felsic Granulites		
Sample.	03-6B	03-88A	03-159A	03-168E	03-228A	03-92B	03-125A	03-158A	03-189A	03-217A	03-20C	03-182A	03-175A
Lake	Merret	Bompas	Lytle	Cora	Wasend	Bompas	Lytle	Lytle	Cora	Wasend	Merret	Cora	Cora
SiO2	47.91	49.56	52.94	50.92	48.37	50.26	53.81	53.77	50.07	49.23	69.75	61.01	62.85
TiO2	0.91	1.01	0.38	0.62	0.48	0.67	0.37	0.39	0.68	0.79	0.81	0.92	0.73
Al2O3	14.87	13.78	16.84	15.80	11.02	4.69	3.73	7.64	7.83	3.91	13.42	17.13	17.05
Fe2O3	15.16	14.23	8.73	14.02	12.81	13.13	10.55	10.46	13.24	13.49	6.02	8.11	8.49
MnO	0.28	0.26	0.15	0.15	0.25	0.23	0.19	0.19	0.23	0.22	0.08	0.09	0.13
MgO	7.50	6.98	6.96	7.16	10.58	18.03	25.99	18.12	13.71	22.41	3.15	5.71	3.79
CaO	10.72	11.48	10.26	7.78	15.51	10.94	3.80	6.96	12.14	7.53	1.42	2.76	2.77
Na2O	2.00	2.39	3.23	2.72	0.74	1.03	0.79	1.39	1.54	1.60	2.18	2.41	2.66
K2O	0.35	0.22	0.67	0.41	0.02	0.35	0.13	0.57	0.38	0.28	3.06	1.97	1.85
P2O5	0.08	0.09	0.04	0.32	0.02	0.08	0.03	0.04	0.06	0.08	0.02	0.05	0.02
Total	99.78	100.00	100.20	99.90	99.80	99.41	99.39	99.53	99.88	99.54	99.91	100.16	100.34
V	241	248	128	195	250	158	97	139	246	110	149	134	134
Cr	170	120	60	240	780	2190	4380	2770	1340	4100	190	640	550
Co	30	47	41	38	46	55	85	60	56	75	23	28	26
Ni	90	110	150	40	140	410	1030	610	250	690	70	170	150
Cu	10	250	90	0	60	90	40	40	120	40	20	20	60
Zn	50	50	60	130	40	0	130	40	0	0	60	30	70
Ga	15	15	15	22	10	7	6	9	11	7	20	18	19
Ge	0	1	1	1	1	0	1	1	1	< 1	1	0	1
As	0	0	0	0	0	0	0	0	0	0	0	0	6
Rb	2	0	17	2	0	2	0	13	3	6	72	91	109
Sr	61	55	221	210	80	79	59	79	79	172	284	208	120
Y	21	22	10	10	12	14	4	10	13	9	35	33	32
Zr	41	65	46	49	15	42	20	36	33	57	178	150	281
Nb	3	3	2	3	0	3	1	3	2	7	9	9	8
Mo	0	0	0	0	0	0	0	0	0	0	0	0	0
Ag	0	0	0	0	0	0	0	0	0	0	0	0	0
In	0	0	0	0	0	0	0	0	0	0	0	0	0
Sn	0	0	0	3	0	0	0	0	0	0	0	0	0
Sb	0	0	0	0	0	0	0	0	0	0	0	0	0
Cs	0	0	0.6	0	0	0	0	0	0	0	0.5	1.2	0.8
Ba	37	11	154	123	0	28	17	87	22	88	510	335	541
La	6	3.7	6.8	8.1	0.4	7.3	2.2	7.8	4.8	9.2	19.4	71.9	21.3
Ce	15.5	9.2	13	18.2	1.7	19.3	4.9	13.5	12.1	20.8	31.3	133	33.5
Pr	2.21	1.36	1.53	2.36	0.33	2.76	0.68	1.52	1.65	2.79	3.14	14.6	3.27
Nd	9.8	6.8	6.3	10	2.2	12.7	3.2	5.8	7.3	12.2	10.8	52.8	10.8
Sm	2.5	2.1	1.4	2	0.8	3	0.8	1.3	1.8	2.6	1.7	8.6	1.9
Eu	0.74	0.89	0.56	0.95	0.38	0.71	0.32	0.44	0.66	0.9	1.51	1.34	1.09
Gd	2.8	3	1.7	2.1	1.3	3.1	1	1.5	2.2	2.5	2.5	6.6	2.6
Tb	0.5	0.6	0.3	0.3	0.3	0.5	0.2	0.3	0.4	0.4	0.6	0.9	0.6
Dy	3.5	3.8	1.8	1.7	1.9	2.8	0.9	1.7	2.4	2	5.1	5.2	4.7
Ho	0.8	0.8	0.4	0.3	0.4	0.5	0.2	0.3	0.5	0.4	1.3	1.1	1.1
Er	2.5	2.6	1.1	1	1.3	1.5	0.5	1	1.4	1	4.1	3.6	3.5
Tm	0.39	0.38	0.17	0.14	0.21	0.21	0.07	0.15	0.19	0.13	0.59	0.54	0.53
Yb	2.5	2.4	1.1	0.9	1.3	1.2	0.4	1	1.2	0.8	3.6	3.3	3.5
Lu	0.4	0.37	0.15	0.14	0.2	0.17	0.06	0.15	0.17	0.1	0.53	0.5	0.51
Hf	1.3	1.8	1.3	1.3	0.5	1.2	0.6	1	1.1	1.5	5.3	4.1	8.3
Ta	0.2	0.2	0.1	0.2	0	0.1	0	0.1	0.1	0.5	0.4	0.5	0.4
W	0	0	0	0	0	0	0	0	0	0	0	0	0
Tl	0	0	0.1	0	0	0	0	0	0	0	0.5	0.3	0.6
Pb	0	0	0	0	0	0	0	0	0	0	9	5	10
Bi	0	0	0	0	0	0	0	0	0	0	0	0	0
Th	0.4	0.5	1.4	0.3	0	0	0.2	1.1	0.1	0.7	2.5	22.4	3.2
U	0.1	0.2	0.4	0.2	0	0	0	0.3	0	0.2	0.5	2.5	0.7
Recalculation of composition of protolith													
Qtz	0.045	0.044	0.044	0.099	0.046	0.083	0.244	0.165	0.049	0.071			
Plag	0.524	0.511	0.602	0.571	0.361	0.177	0.125	0.265	0.293	0.177			
Oliv	0.214	0.172	0.144	0.235	0.178	0.328	0.532	0.362	0.248	0.449			
Cpx	0.179	0.243	0.163	0.054	0.407	0.378	0.085	0.167	0.376	0.272			
Or	0.022	0.014	0.041	0.026	0.001	0.022	0.008	0.035	0.024	0.017			
Sp	0.013	0.014	0.005	0.009	0.007	0.009	0.005	0.005	0.010	0.011			
Ap	0.002	0.002	0.001	0.007	0.000	0.002	0.001	0.001	0.001	0.002			
Ternary Normalization													
Cpx	0.20	0.26	0.18	0.06	0.43	0.43	0.11	0.21	0.41	0.30			
Pl	0.57	0.55	0.66	0.66	0.38	0.20	0.17	0.33	0.32	0.20			
Ol	0.23	0.19	0.16	0.27	0.19	0.37	0.72	0.46	0.27	0.50			

Table 2. U-Pb TIMS isotopic data for zircon

	Composition						Isotopic Ratios								Dates (Ma)					
Fr^a	Wt (μg)^b	U (ppm)	Pb (ppm)	$\frac{Th}{U}^c$	$\frac{Pb^*}{Pbc}^d$	Pbc^d (pg)	$\frac{^{206}Pb}{^{204}Pb}^e$	$\frac{^{208}Pb}{^{206}Pb}^f$	$\frac{^{206}Pb}{^{238}U}^f$	% err^g	$\frac{^{207}Pb}{^{235}U}^f$	% err^g	$\frac{^{207}Pb}{^{206}Pb}^f$	% err^g	$\frac{^{206}Pb}{^{238}U}^h$	$\frac{^{207}Pb}{^{235}U}^h$	$\frac{^{207}Pb}{^{206}Pb}^h$	±	corr. coef.	% disc
02M133A - Mafic granulite																				
z2b	4.7	69.2	35.5	0.270	67.6	2.4	3715.1	0.076	0.475766	(.10)	10.9369	(.11)	0.16672	(.05)	2508.8	2517.8	2525.0	0.8	0.886	0.8
z2c	1.6	56	29	0.280	30.1	1.5	1725.0	0.079	0.472025	(.53)	10.7924	(.56)	0.16583	(.18)	2492.4	2505.4	2515.9	3.0	0.947	1.1
z3a	0.8	281	146	0.302	68.9	1.7	3867.1	0.085	0.478581	(.11)	11.0740	(.12)	0.16782	(.05)	2521.1	2529.4	2536.0	0.8	0.916	0.7
z3b	1.3	175	94	0.309	23.6	5.0	1255.7	0.087	0.482179	(.12)	11.1899	(.13)	0.16831	(.06)	2536.7	2539.1	2540.9	1.0	0.890	0.2
z5b	0.8	194	95	0.255	94.5	0.8	5735.8	0.073	0.463069	(.14)	10.4225	(.16)	0.16324	(.07)	2453.1	2473.1	2489.5	1.1	0.911	1.8
z6a	2.7	107	47	0.266	241.9	0.5	14757.9	0.078	0.415933	(.06)	8.5012	(.07)	0.14824	(.05)	2242.0	2286.1	2325.7	0.8	0.779	4.3
z6b	2.8	154	74	0.287	305.0	0.7	18374.6	0.083	0.448034	(.06)	9.8231	(.08)	0.15901	(.05)	2386.5	2418.3	2445.2	0.8	0.788	2.9
z7a	1.5	165	76	0.272	161.1	0.7	9785.4	0.080	0.431816	(.06)	9.1418	(.08)	0.15354	(.06)	2313.9	2352.3	2385.8	0.9	0.754	3.6
z8a	2.6	141	74	0.311	337.0	0.6	20064.2	0.087	0.483239	(.08)	11.2654	(.09)	0.16908	(.05)	2541.4	2545.3	2548.5	0.9	0.834	0.3
z9a	5.0	55	25	0.214	158.7	0.8	9776.9	0.063	0.434241	(.08)	9.2587	(.09)	0.15464	(.05)	2324.8	2363.9	2397.9	0.8	0.852	3.6
z10a.un	2.7	74	34	0.225	181.2	0.5	11123.9	0.066	0.431690	(.16)	9.1286	(.17)	0.15337	(.07)	2313.3	2351.0	2383.8	1.2	0.912	3.5
z5c.ab.ca	0.9	---	---	---	32.9	1.3	1926.0	0.075	0.475616	(.22)	10.9456	(.26)	0.16691	(.13)	2508.1	2518.5	2526.9	2.2	0.863	0.9
z7.ip.ca	1.5	---	---	---	4.7	1.8	296.9	0.045	0.344838	(.94)	5.5442	(1.07)	0.11661	(.43)	1909.9	1907.5	1904.8	7.7	0.917	-0.3
z17.ip.ca	1.0	---	---	---	8.1	0.6	546.1	0.037	0.345826	(.40)	5.5933	(.46)	0.11730	(.22)	1914.6	1915.1	1915.5	3.9	0.884	0.1
03-88A - Mafic granulite																				
z1	3.0	152	72	0.24	320.5	0.7	19540.1	0.068	0.448281	(.06)	9.8189	(.07)	0.15886	(.04)	2387.6	2417.9	2443.6	0.7	0.803	2.7
z2	1.0	196	84	0.10	108.7	0.8	6899.8	0.031	0.423106	(.08)	8.8137	(.11)	0.15108	(.07)	2274.6	2318.9	2358.2	1.2	0.763	4.2
z3	3.7	35	17	0.24	112.3	0.6	6830.3	0.068	0.463900	(.22)	10.5086	(.24)	0.16429	(.07)	2456.8	2480.7	2500.3	1.2	0.954	2.1
z4	1.7	105	50	0.39	57.9	1.5	3262.9	0.113	0.433846	(.13)	9.2026	(.14)	0.15384	(.07)	2323.0	2358.4	2389.1	1.1	0.892	3.3
z5	2.1	32	15	0.18	76.7	0.4	4752.1	0.051	0.445591	(.14)	9.7934	(.16)	0.15940	(.07)	2375.6	2415.5	2449.3	1.2	0.902	3.6
z6.un	2.0	61	26	0.35	70.1	0.7	4211.8	0.105	0.399378	(.09)	7.9212	(.11)	0.14385	(.06)	2166.2	2222.1	2274.1	1.0	0.849	5.6
z7.un	1.3	235	109	0.14	145.8	1.0	9107.8	0.041	0.447124	(.12)	9.8680	(.14)	0.16007	(.07)	2382.5	2422.5	2456.4	1.2	0.873	3.6
z8a.un	1.8	198	88	0.08	46.4	3.4	2647.4	0.023	0.431747	(.08)	9.1651	(.10)	0.15396	(.05)	2313.6	2354.6	2390.4	0.8	0.872	3.8
z8c.ca	1.1	---	---	---	40.5	3.7	2284.2	0.025	0.450704	(.14)	9.9438	(.15)	0.16001	(.06)	2398.4	2429.6	2455.8	1.0	0.919	2.8
03-159A - Mafic granulite																				
z1a	3.1	662	337	0.25	1473.2	0.7	88957.9	0.071	0.478610	(.07)	11.0621	(.09)	0.16763	(.04)	2521.2	2528.4	2534.1	0.7	0.876	0.6
z1b	1.6	585	303	0.32	354.5	1.4	20191.2	0.089	0.478078	(.07)	11.0516	(.08)	0.16766	(.04)	2518.9	2527.5	2534.4	0.7	0.841	0.7
z2a	2.9	721	362	0.25	1629.9	0.6	98514.2	0.071	0.472077	(.05)	10.7982	(.06)	0.16590	(.04)	2492.7	2505.9	2516.7	0.7	0.771	1.2
z3	0.9	404	201	0.20	438.6	0.4	26799.1	0.058	0.471242	(.06)	10.7828	(.08)	0.16595	(.05)	2489.0	2504.6	2517.2	0.9	0.724	1.4
z4	1.0	446	227	0.28	148.1	1.5	8410.6	0.079	0.473970	(.16)	10.9013	(.17)	0.16681	(.05)	2500.9	2514.7	2525.9	0.9	0.949	1.2
z5.un	0.0	351	173	0.23	275.2	0.6	16708.1	0.067	0.465182	(.06)	10.6276	(.08)	0.16570	(.05)	2462.4	2491.1	2514.6	0.8	0.775	2.5
z6.un	0.7	413	202	0.22	155.0	0.9	9435.6	0.065	0.463449	(.10)	10.6056	(.11)	0.16597	(.05)	2454.8	2489.2	2517.4	0.9	0.867	3.0
z7.un	0.5	395	196	0.22	70.5	1.4	4122.3	0.063	0.467062	(.11)	10.6150	(.15)	0.16483	(.10)	2470.7	2490.0	2505.9	1.7	0.733	1.7
z8.un	1.2	353	184	0.32	350.3	0.6	20668.8	0.092	0.478831	(.08)	11.6078	(.09)	0.17582	(.04)	2522.2	2573.3	2613.8	0.7	0.866	4.2
z10b.ca	0.3	---	---	---	34.2	2.0	1979.9	0.041	0.368947	(.17)	7.9972	(.18)	0.15721	(.05)	2024.4	2230.7	2425.8	0.9	0.956	19.2
z11b.ca	1.4	---	---	---	98.8	2.2	5026.2	0.149	0.403878	(.08)	11.0002	(.09)	0.19754	(.04)	2186.9	2523.2	2806.0	0.7	0.871	25.9

Table 2. (continued)

Table 2. (continued)

	Composition						Isotopic Ratios								Dates (Ma)					
Fr[a]	Wt (µg)[b]	U (ppm)	Pb (ppm)	$\frac{Th}{U}$[c]	$\frac{Pb^*}{Pbc}$[d]	Pbc[d] (pg)	$\frac{^{206}Pb}{^{204}Pb}$[e]	$\frac{^{208}Pb}{^{206}Pb}$[f]	$\frac{^{206}Pb}{^{238}U}$[f]	% err[g]	$\frac{^{207}Pb}{^{235}U}$[f]	% err[g]	$\frac{^{207}Pb}{^{206}Pb}$[f]	% err[g]	$\frac{^{206}Pb}{^{238}U}$[h]	$\frac{^{207}Pb}{^{235}U}$[h]	$\frac{^{207}Pb}{^{206}Pb}$[h]	±	corr. coef.	% disc
03-175A - Felsic granulite																				
z1	1.7	295	141	0.10	324.6	0.7	20376.6	0.029	0.465360	(.06)	10.5381	(.09)	0.16424	(.07)	2463.2	2483.3	2499.8	1.1	0.701	1.8
z2	3.7	457	222	0.14	261.2	3.1	14540.2	0.039	0.467845	(.05)	10.7121	(.07)	0.16606	(.04)	2474.1	2498.5	2518.3	0.7	0.794	2.1
z3a	1.6	385	187	0.13	91.6	3.2	5109.4	0.036	0.465739	(.07)	10.6915	(.08)	0.16649	(.05)	2464.8	2496.7	2522.7	0.8	0.832	2.8
z3b	1.0	347	169	0.14	108.4	1.6	6363.4	0.039	0.467653	(.08)	10.6694	(.10)	0.16547	(.05)	2473.3	2494.8	2512.3	0.8	0.864	1.9
z4	1.4	402	197	0.13	192.5	1.4	11392.3	0.037	0.472672	(.08)	10.8537	(.09)	0.16654	(.05)	2495.3	2510.7	2523.2	0.8	0.851	1.3
z5.un	1.6	401	188	0.10	289.8	1.0	18105.3	0.030	0.456045	(.06)	10.2039	(.07)	0.16228	(.04)	2422.1	2453.4	2479.5	0.7	0.796	2.8
z6.un	1.3	274	129	0.09	119.6	1.4	7184.8	0.026	0.461441	(.22)	10.4195	(.23)	0.16377	(.06)	2445.9	2472.8	2494.9	0.9	0.969	2.4
z7.un	1.4	286	136	0.13	85.3	2.2	4873.9	0.036	0.456323	(.08)	10.3088	(.10)	0.16385	(.07)	2423.3	2462.9	2495.7	1.2	0.737	3.5
z7c.ca	0.5	---	---	---	34.2	1.6	1985.3	0.056	0.413220	(.20)	9.2158	(.21)	0.16175	(.06)	2229.6	2359.7	2474.1	1.1	0.953	11.7
z8.ca	0.7	---	---	---	48.3	4.4	2652.4	0.046	0.392096	(.06)	8.8380	(.08)	0.16348	(.05)	2132.5	2321.4	2492.0	0.8	0.804	16.9
z9.ca	0.5	---	---	---	88.9	1.1	5166.0	0.112	0.470004	(.13)	10.6951	(.14)	0.16504	(.06)	2483.6	2497.0	2507.9	1.0	0.915	1.2
m1b	3.3	125	1149	75.03	967.8	3.9	2865.8	21.088	0.476742	(.13)	10.9549	(.15)	0.16666	(.08)	2513.1	2519.3	2524.3	1.3	0.857	0.5
m2a	1.5	1206	4225	25.54	1794.0	3.5	14259.6	7.129	0.486962	(.05)	11.4200	(.07)	0.17009	(.04)	2557.5	2558.1	2558.5	0.7	0.791	0.0
m2b	3.6	1104	3744	24.59	3121.2	4.3	25415.2	6.862	0.487153	(.12)	11.4255	(.13)	0.17010	(.04)	2558.3	2558.5	2558.6	0.7	0.939	0.0
m3b	0.0	357	169	0.51	64.4	2.3	3474.2	0.144	0.422905	(.13)	8.4017	(.16)	0.14409	(.09)	2273.7	2275.4	2276.9	1.6	0.817	0.2
m4a	0.9	3185	6998	14.56	1322.9	4.8	16542.8	4.084	0.482881	(.08)	11.2629	(.09)	0.16916	(.05)	2539.8	2545.1	2549.4	0.8	0.833	0.5
m5a	2.0	1067	624	1.57	253.7	4.9	10391.1	0.461	0.420338	(.06)	8.6215	(.07)	0.14876	(.04)	2262.0	2298.8	2331.7	0.7	0.805	3.5
m5b	1.1	2744	1583	1.42	440.6	3.9	18735.9	0.411	0.427842	(.13)	8.8702	(.14)	0.15037	(.04)	2296.0	2324.7	2350.1	0.7	0.952	2.7
m6a	1.8	2228	2284	5.21	1633.3	2.5	42030.1	1.474	0.451027	(.05)	9.6772	(.06)	0.15561	(.04)	2399.8	2404.5	2408.5	0.7	0.768	0.4

[a] All fractions are single grains or grain fragments. Fragments are denoted with a letter after the fraction number. All zircon fractions were physically abraded, except for those marked un -- unabraded, or ca -- chemical abrasion. No monazite fractions were physically abraded.

[b] Sample weights were estimated to within 40% using measured grain dimensions and a nominal density of 4.5 g/cm^3 for zircon and 5.0 g/cm^3 for monazite.

[c] Th contents calculated from radiogenic ^{208}Pb and the ^{207}Pb/^{206}Pb date of the sample, assuming concordance between U-Th-Pb systems.

[d] Pb* and Pbc represent radiogenic Pb and common Pb respectively.

[e] Measured ratio corrected for fractionation and spike contribution; Pb fractionation was 0.07 ±0.04%/a.m.u. for Faraday detector or 0.25 ± 0.04%/a.m.u. for Daly detector analysis, based on daily analysis of NBS-981.

[f] Measured ratios corrected for fractionation, spike, blank, and initial common Pb; nominal U blank = 0.1 pg ± 50% (2s); nominal Pb blank = 1.0 pg ± 50% (2s); initial Pb composition estimated using the model for terrestrial Pb evolution of Stacey and Kramers (1975) at the nominal age of the fraction (i.e. 2.55 Ga).

[g] Numbers in parentheses are the % errors reported at the 2 sigma confidence interval, propagated using the algorithms of Ludwig (1980).

[h] Isotopic ages calculated using the decay constants of Jaffey et al. (1971): $\lambda(^{235}U) = 9.8485 \times 10^{-10}$ yr^{-1} and $\lambda(^{238}U) = 1.55125 \times 10^{-10}$ yr^{-1}; uncertainty in ^{207}Pb/^{206}Pb date reported at the 2 sigma confidence interval.

Table 3 SHRIMP U-Th-Pb zircon analyses from mafic granulite sample 02M133A. Errors are given at the 1-sigma level.

		Composition													Apparent ages (Ma)							
Grain[a] Spot	Type[b]	Pb*[c] ppm	U ppm	Th ppm	Th/U	^{204}Pb/^{206}Pb	%±	f206%	^{206}Pb/^{238}U	%±	^{207}Pb/^{235}U	%±	^{207}Pb/^{206}Pb	%±	208/232	±	206/238	±	207/235	±	207/206	±
Zircon Cores																						
28.2	MWzC	26	45	9.3	0.21	2.71E-05	83	0.038	0.5500	2.1	13.83	2.4	0.1823	0.9	3002	127	2825	49	2738	23	2674	15
5.2	DUzC	116	204	60	0.30	4.35E-06	98	0.006	0.5236	1.1	12.91	1.3	0.1789	0.5	2627	43	2714	25	2673	12	2642	8
26.1	DUzC	700	1370	254	0.19	4.31E-06	36	0.006	0.4861	0.4	11.56	0.6	0.1724	0.3	2473	21	2554	9	2569	5	2581	6
21.1	MZC	15	27	5.8	0.21	6.66E-05	58	0.094	0.5174	1.8	12.22	2.3	0.1713	1.2	2539	121	2688	40	2622	22	2571	20
15.2	DUzC	97	188	55	0.30	1.58E-05	58	0.022	0.4806	1.4	11.22	1.6	0.1693	0.7	2446	50	2530	29	2542	15	2551	12
30.1	DUzC	91	174	46	0.26	2.67E-05	39	0.038	0.4919	1.2	11.47	1.6	0.1691	0.9	2576	52	2579	25	2562	15	2549	16
20.1	LWzC	9.0	17	4.9	0.30	4.61E-05	90	0.065	0.4877	2.3	11.32	3.1	0.1684	1.8	2605	139	2561	49	2550	30	2542	31
8.1	DZC	62	118	49	0.42	3.26E-05	63	0.046	0.4739	0.9	10.85	1.2	0.1660	0.7	2449	55	2501	19	2510	11	2517	11
9.1	DUz	81	168	38	0.23	1.21E-05	65	0.017	0.4568	0.8	10.12	1.1	0.1607	0.6	2397	41	2426	17	2446	10	2463	10
6.2	DWzC	40	89	21	0.24	3.00E-06	146	0.004	0.4342	1.2	9.17	1.8	0.1531	1.2	2303	60	2325	24	2355	17	2381	20
12.1	LUzC	12	28	6.3	0.23	3.88E-05	116	0.055	0.4175	3.4	8.28	4.3	0.1439	2.3	2264	178	2249	65	2262	40	2274	39
14.1	MWzC	18	46	10	0.23	1.21E-05	91	0.017	0.3913	1.9	7.62	3.1	0.1412	2.2	2040	88	2129	34	2187	28	2242	39
13.1	LUzC	8.0	21	5.1	0.25	2.35E-04	45	0.360	0.3745	4.1	6.59	5.4	0.1276	3.0	1912	190	2051	73	2058	49	2065	53
Zircon Overgrowths																						
25.1	LWzO	20	33	6.1	0.19	3.16E-05	141	0.045	0.5707	1.8	14.67	2.6	0.1864	1.6	3040	136	2911	42	2794	25	2710	27
15.1	LWzO	16	26	5.6	0.22	1.29E-04	55	0.181	0.5651	2.4	14.39	3.9	0.1847	2.8	2704	201	2888	56	2776	38	2696	47
22.1	LWzO	23	43	11	0.26	2.40E-05	156	0.034	0.5139	2.6	12.13	3.3	0.1711	1.7	2688	146	2673	58	2614	32	2569	29
2.1	MUzO	35	67	14	0.21	5.02E-06	92	0.007	0.5028	1.3	11.79	2.0	0.1701	1.3	2653	67	2626	29	2588	19	2558	22
24.1	LUzO	19	37	9.0	0.24	9.85E-06	132	0.014	0.4861	2.9	11.25	3.5	0.1678	1.7	2504	108	2554	61	2544	33	2536	29
23.1	DUzO	296	554	129	0.23	9.06E-06	73	0.013	0.5038	1.1	11.64	1.3	0.1676	0.6	2624	43	2630	23	2576	12	2534	11
11.1	DWzO	55	105	24	0.22	3.15E-05	49	0.044	0.4942	1.3	11.39	1.7	0.1672	1.0	2407	62	2589	27	2556	16	2530	17
27.1	MWzO	43	87	22	0.25	4.40E-06	189	0.006	0.4704	1.6	10.26	1.9	0.1582	0.9	2448	72	2485	33	2459	18	2436	16
5.1	MWzO	24	49	10	0.21	8.28E-05	46	0.116	0.4641	2.4	9.91	2.8	0.1548	1.2	2320	108	2458	49	2426	26	2400	20
6.1	LWzO	9.0	24	4.8	0.20	6.76E-05	86	0.104	0.3585	2.3	6.33	3.2	0.1281	1.9	2076	118	1975	39	2023	28	2071	34
29.1	LUzO	10	28	6.7	0.24	1.27E-04	89	0.195	0.3663	2.1	6.36	3.6	0.1259	2.7	1894	144	2012	37	2027	33	2042	49
28.1	LZO	13	38	5.8	0.15	2.13E-04	42	0.327	0.3525	2.5	5.69	3.5	0.1170	2.2	1666	168	1946	41	1929	31	1911	40
Zircon Grains Darker in CL																						
1.1	MZ	28	54	9.3	0.17	3.81E-05	68	0.054	0.4988	1.8	11.99	2.2	0.1743	1.1	2658	141	2609	38	2604	21	2600	19
3.1	LZ	14	28	6.3	0.23	1.41E-04	42	0.199	0.4777	2.2	10.62	3.1	0.1612	1.9	2290	124	2517	47	2490	30	2468	33
19.1	LWz	16	35	12	0.36	5.65E-05	77	0.080	0.4176	1.7	8.25	2.5	0.1433	1.6	2223	75	2250	33	2259	22	2267	27
16.1	MWz	29	68	21	0.30	2.00E-05	100	0.028	0.3957	2.2	7.71	2.6	0.1413	1.2	2133	71	2149	41	2198	24	2243	20
10.1	DZ	9.0	23	4.6	0.20	1.48E-04	102	0.227	0.3815	2.0	7.09	3.4	0.1348	2.5	1920	206	2083	35	2123	31	2161	45
Zircon Grains Bright in CL																						
18.1	LWz	3.0	7.6	0.6	0.08	2.35E-04	74	0.361	0.3352	4.7	5.52	6.4	0.1195	3.8	2580	597	1864	77	1904	57	1949	70
18.2	LWz	3.0	8.7	0.7	0.08	1.38E-04	87	0.212	0.3428	4.5	5.33	7.3	0.1128	5.1	1960	441	1900	75	1874	64	1844	96
7.1	LWz	4.0	12	1.5	0.12	1.30E-04	93	0.200	0.3537	4.3	5.52	5.8	0.1132	3.5	1813	292	1952	72	1904	51	1851	64
7.2	LWz	4.0	11	1.3	0.12	2.45E-05	101	0.038	0.3408	5.5	5.23	6.9	0.1113	3.6	2150	257	1890	90	1858	61	1821	67
4.1	LWz	4.0	12	1.1	0.09	6.35E-04	39	0.973	0.3456	3.3	5.26	6.0	0.1103	4.7	909	692	1914	54	1862	53	1805	88
4.2	LWz	3.0	10	1.0	0.09	2.78E-04	56	0.426	0.3371	4.2	5.26	6.8	0.1132	4.9	1872	459	1873	68	1862	60	1851	91
17.1	LUz	4.0	11	1.6	0.14	2.25E-04	72	0.345	0.3422	4.5	5.28	6.1	0.1119	3.5	1851	379	1897	75	1866	53	1831	66
17.2	LUz	4.0	11	1.4	0.12	7.16E-05	100	0.110	0.3345	4.8	5.24	5.8	0.1137	2.8	2098	264	1860	78	1860	51	1859	51

[a] Refers to individual grains shown in Figure X, followed by analysis number

[b] L,M,D -- CL brightness -- Light, Medium, Dark; Uz, Wz, Z -- Zoning -- Unzoned, Weakly zoned, Well zoned; C,O -- Location -- Core, Overgrowth.

[c] Pb* -- radiogenic lead

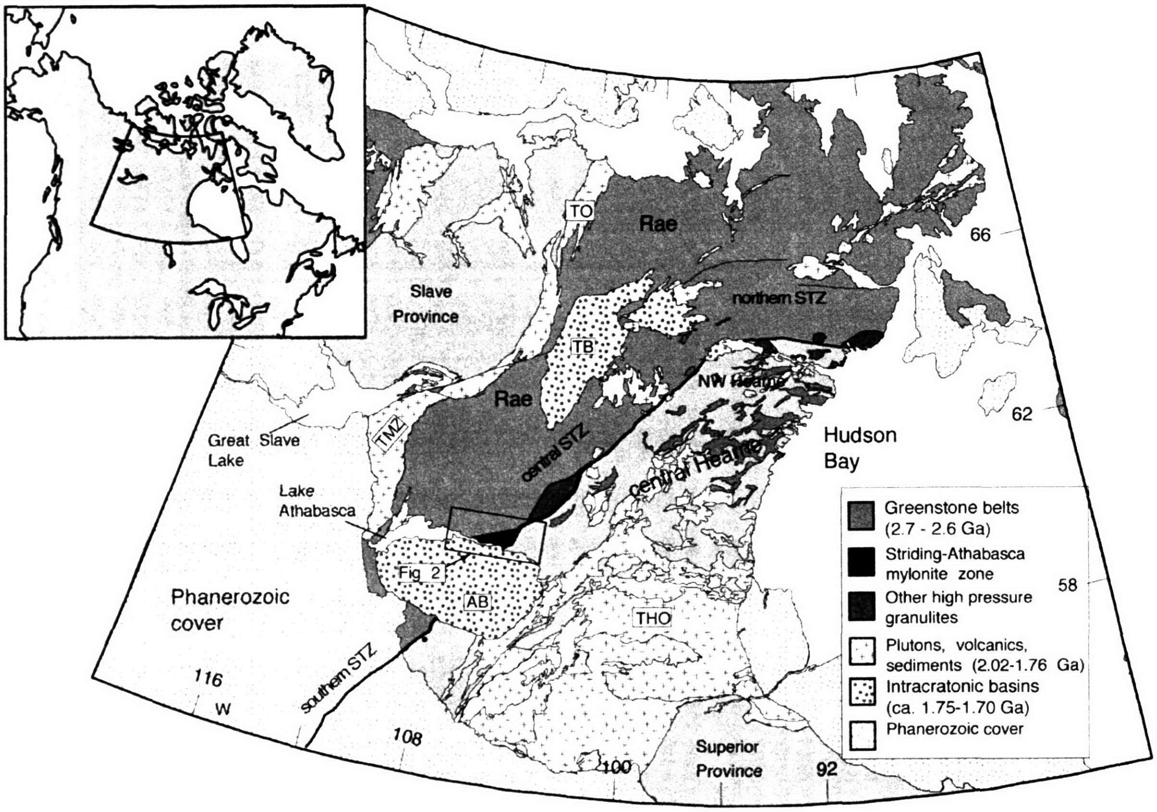
TO
Rae
66
Slave Province
northern STZ
TB
NW Hearne
Rae
62
Great Slave Lake
TMZ
central STZ
central Hearne
Hudson Bay
Lake Athabasca
Fig 2
AB
58
Phanerozoic cover
THO
116 W
southern STZ
108
100
Superior Province
92
Greenstone belts (2.7 - 2.6 Ga)
Striding-Athabasca mylonite zone
Other high pressure granulites
Plutons, volcanics, sediments (2.02-1.76 Ga)
Intracratonic basins (ca. 1.75-1.70 Ga)
Phanerozoic cover

Figure 1

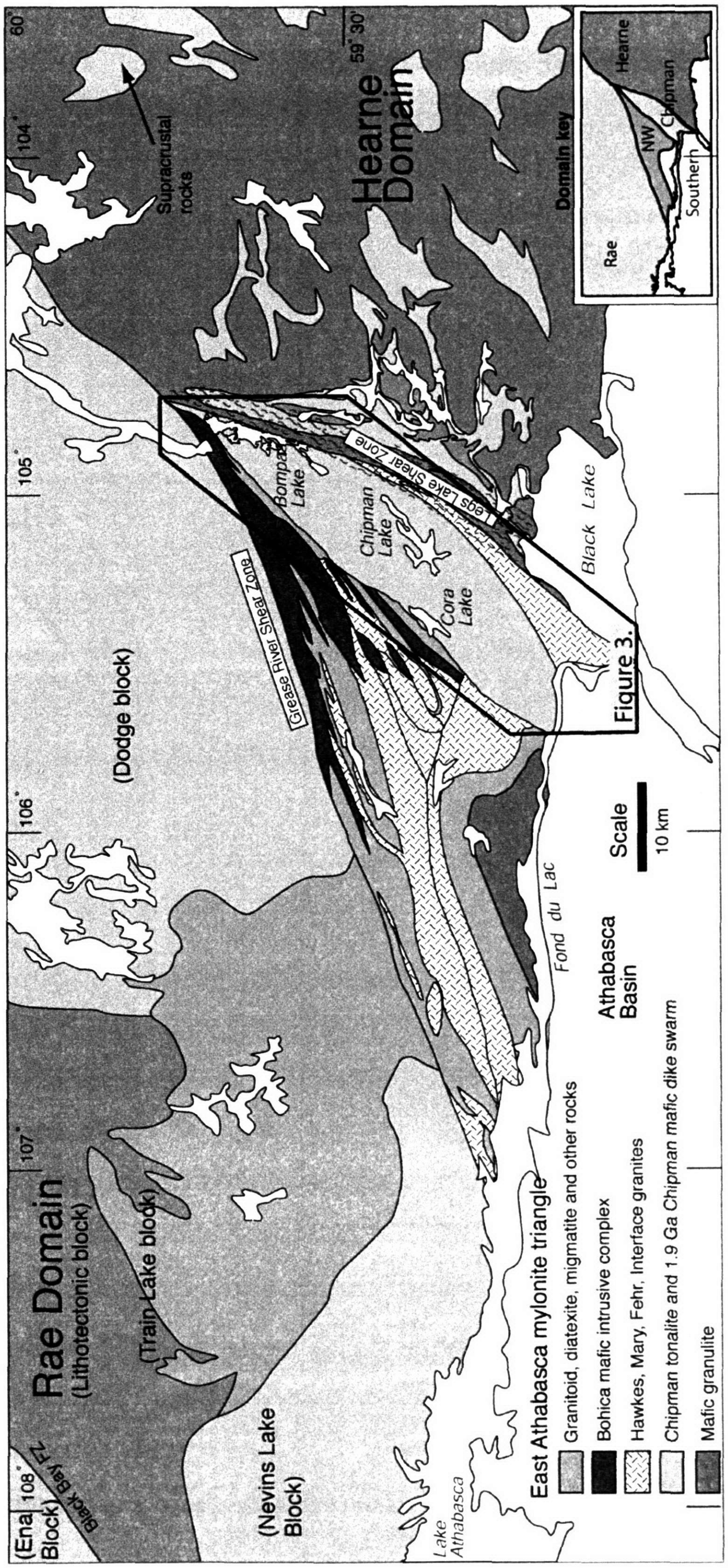
Rae Domain
(Lithotectonic block)
(Train Lake block)
(Ena Block)
Black Bay FZ
(Nevins Lake Block)
(Dodge block)
108°
107°
106°
105°
104°
60°
59° 30'
Grease River Sheat Zone
egs Lake Shear Zone
Bompas Lake
Chipman Lake
Cora Lake
Figure 3.
Black Lake
Fond du Lac
Lake Athabasca
Hearne Domain
Supracrustal rocks
Domain key
Rae
Hearne
NW
Chipman
Southern
Scale
10 km
Athabasca Basin
East Athabasca mylonite triangle
Granitoid, diatexite, migmatite and other rocks
Bohica mafic intrusive complex
Hawkes, Mary, Fehr, Interface granites
Chipman tonalite and 1.9 Ga Chipman mafic dike swarm
Mafic granulite

Figure 2

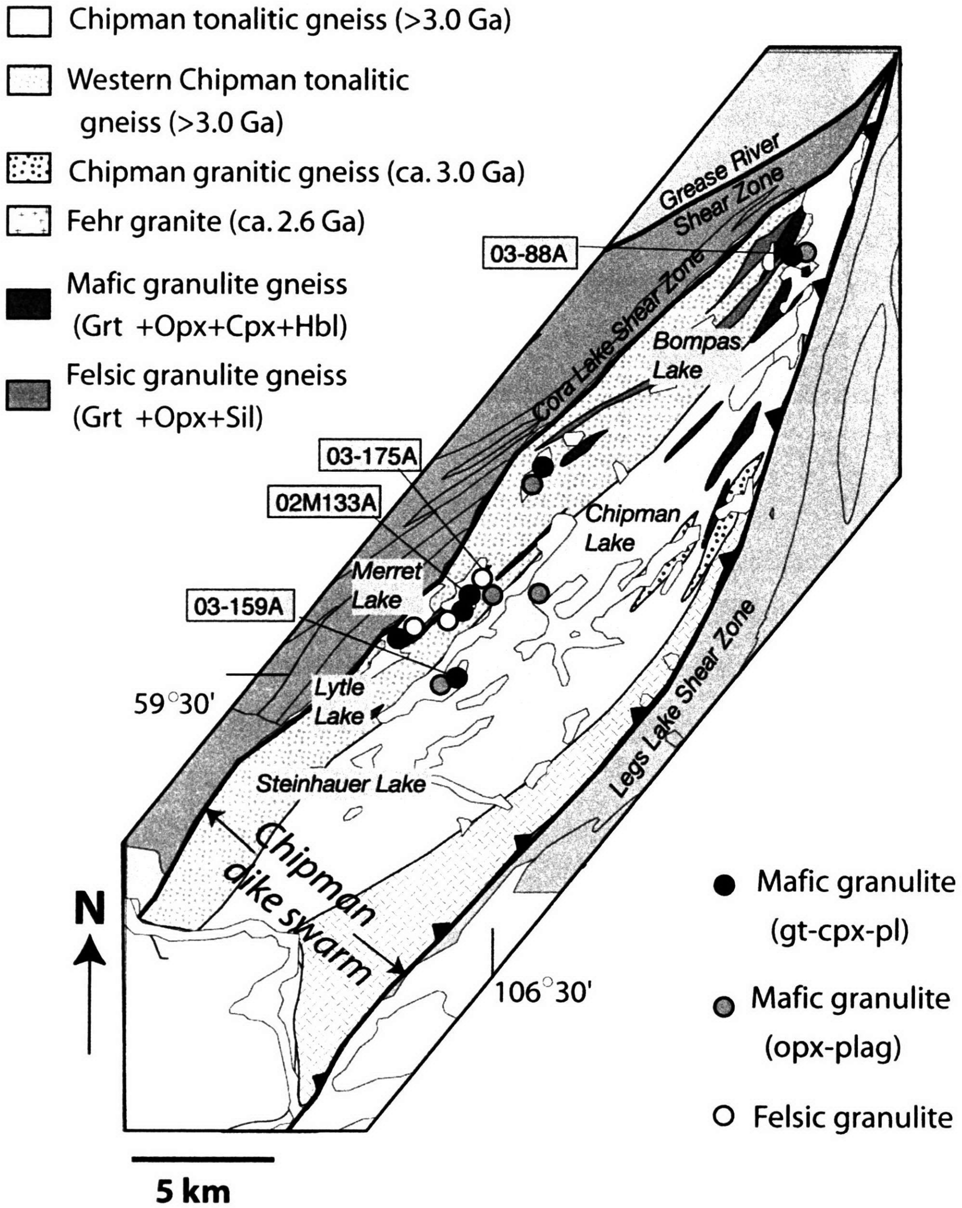
Chipman tonalitic gneiss (>3.0 Ga)
Western Chipman tonalitic gneiss (>3.0 Ga)
Chipman granitic gneiss (ca. 3.0 Ga)
Fehr granite (ca. 2.6 Ga)
Mafic granulite gneiss (Grt +Opx+Cpx+Hbl)
Felsic granulite gneiss (Grt +Opx+Sil)
Grease River Shear Zone
03-88A
Cora Lake Shear Zone
Bompas Lake
03-175A
02M133A
Chipman Lake
Merret Lake
03-159A
Lytle Lake
59°30'
Steinhauer Lake
Legs Lake Shear Zone
Chipman dike swarm
N
106°30'
5 km
Mafic granulite (gt-cpx-pl)
Mafic granulite (opx-plag)
Felsic granulite

Figure 3

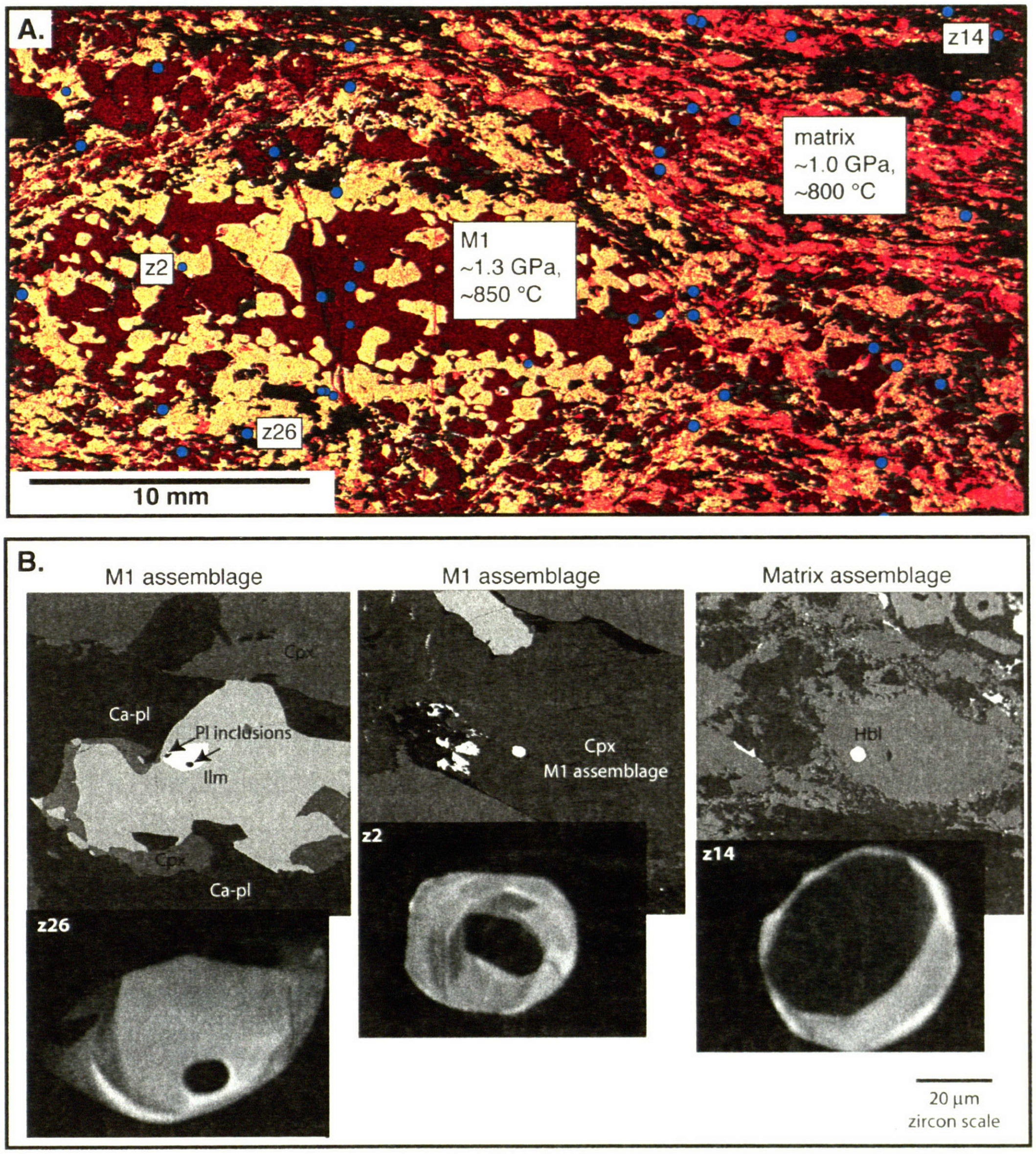
A.
z14
matrix
~1.0 GPa,
~800 °C
M1
~1.3 GPa,
~850 °C
z2
z26
10 mm
B.
M1 assemblage
Cpx
Ca-pl
Pl inclusions
Ilm
Cpx
Ca-pl
z26
M1 assemblage
Cpx
M1 assemblage
z2
Matrix assemblage
Hbl
z14
20 µm
zircon scale

Figure 4

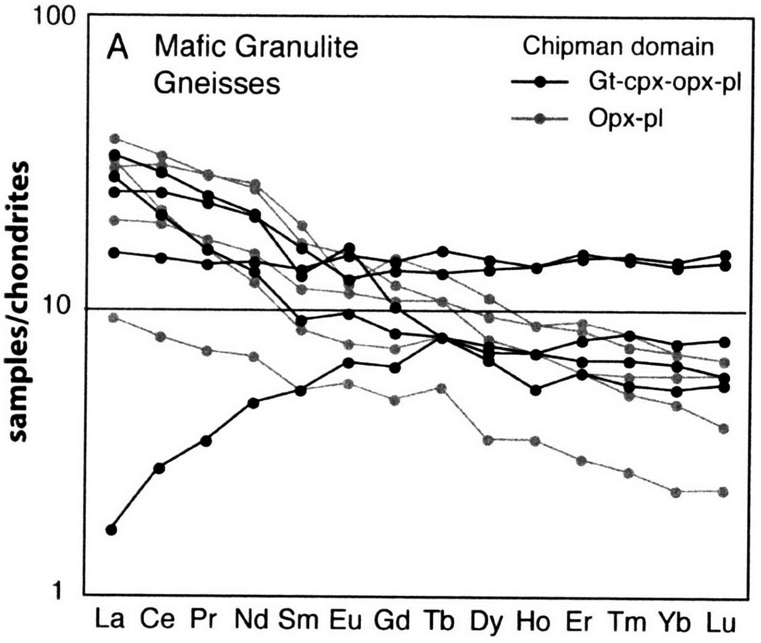
A Mafic Granulite Gneisses
Chipman domain
Gt-cpx-opx-pl
Opx-pl
samples/chondrites
100
10
1
La Ce Pr Nd Sm Eu Gd Tb Dy Ho Er Tm Yb Lu

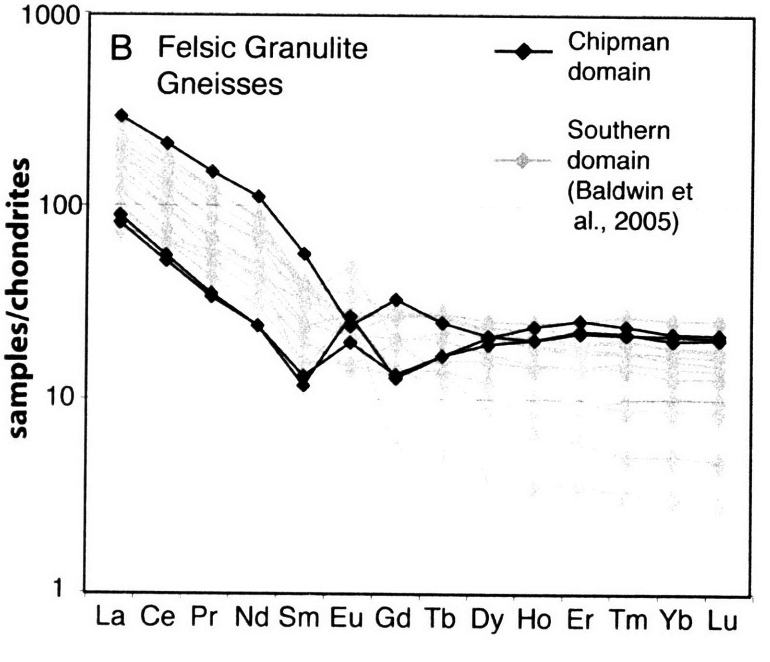
B Felsic Granulite Gneisses
Chipman domain
Southern domain (Baldwin et al., 2005)
samples/chondrites
1000
100
10
1
La Ce Pr Nd Sm Eu Gd Tb Dy Ho Er Tm Yb Lu

Figure 5

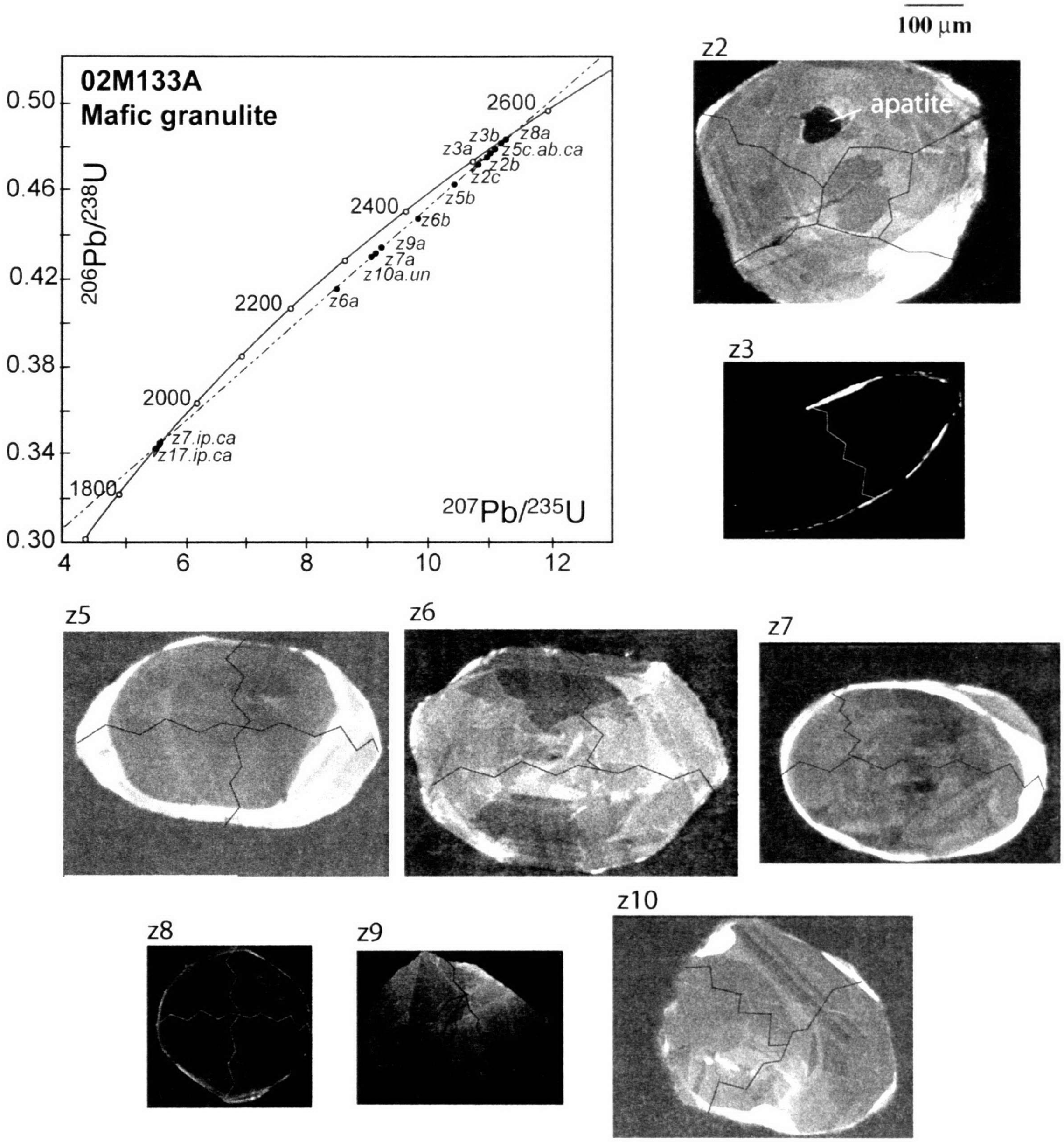
02M133A
Mafic granulite
^{206}Pb/^{238}U
^{207}Pb/^{235}U
0.50
0.46
0.42
0.38
0.34
0.30
4
6
8
10
12
2600
2400
2200
2000
1800
z3b
z8a
z3a
z5c.ab.ca
z2b
z2c
z5b
z6b
z9a
z7a
z10a.un
z6a
z7.ip.ca
z17.ip.ca
100 μm
z2
apatite
z3
z5
z6
z7
z8
z9
z10

Figure 6

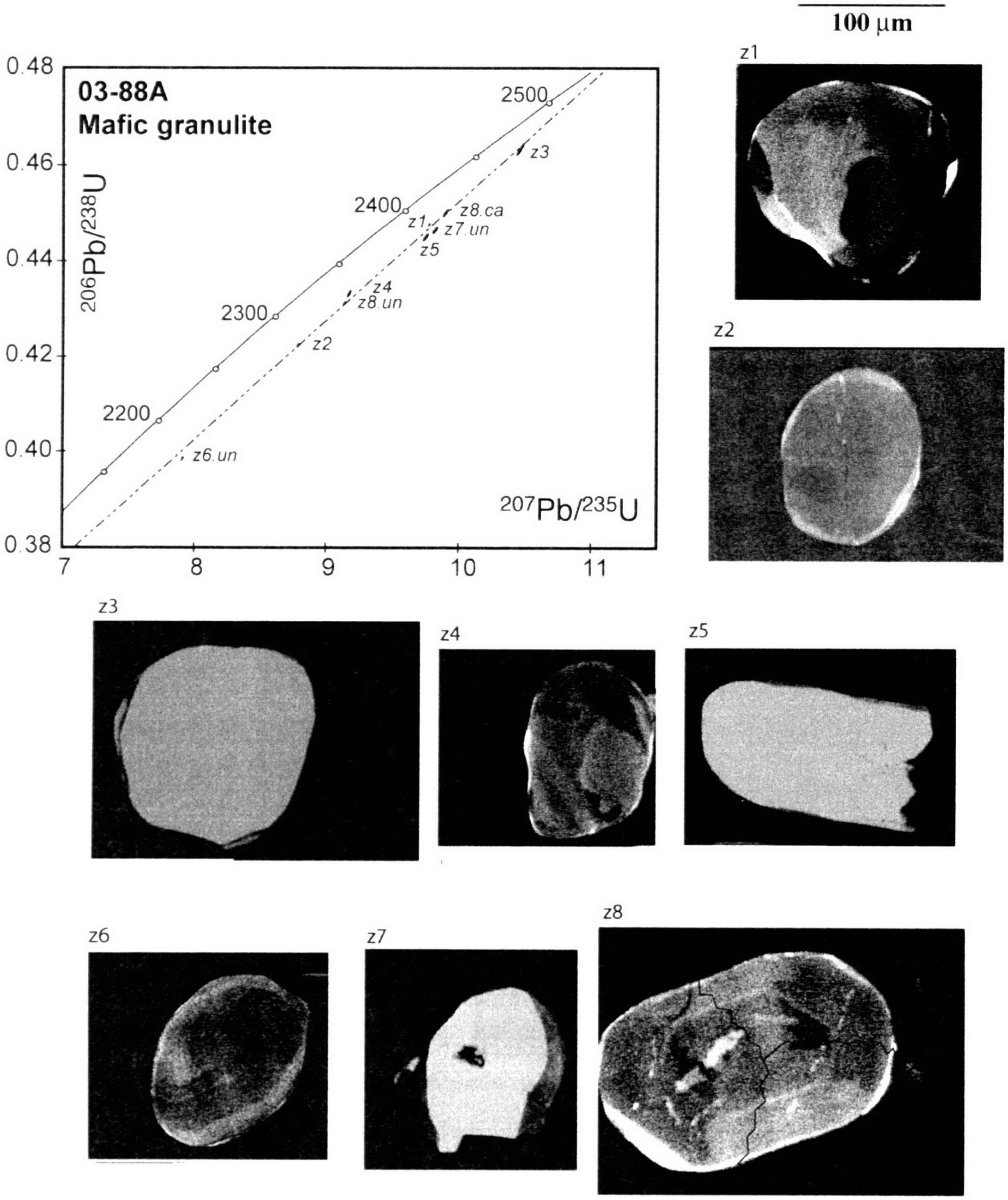
100 μm
03-88A
Mafic granulite
2500
2400
2300
2200
z3
z8.ca
z1
z7.un
z5
z4
z8.un
z2
z6.un
^{206}Pb/^{238}U
^{207}Pb/^{235}U
0.48
0.46
0.44
0.42
0.40
0.38
7
8
9
10
11
z1
z2
z3
z4
z5
z6
z7
z8

Figure 7

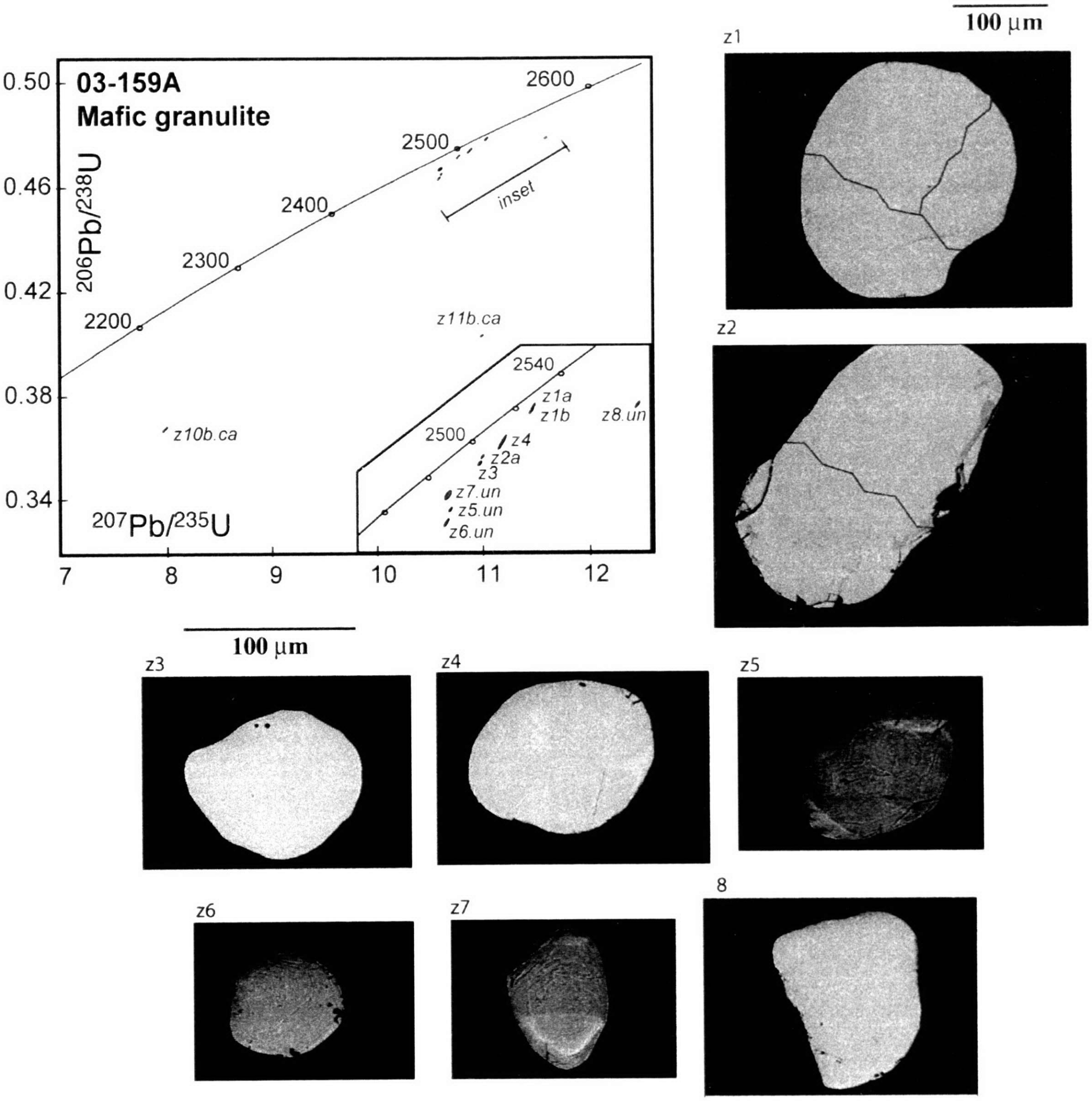
03-159A
Mafic granulite
$^{206}Pb/^{238}U$
$^{207}Pb/^{235}U$
0.50
0.46
0.42
0.38
0.34
7
8
9
10
11
12
2200
2300
2400
2500
2600
inset
z11b.ca
z10b.ca
2540
2500
z1a
z1b
z8.un
z4
z2a
z3
z7.un
z5.un
z6.un
100 μm
z1
z2
z3
z4
z5
z6
z7
8

Figure 8

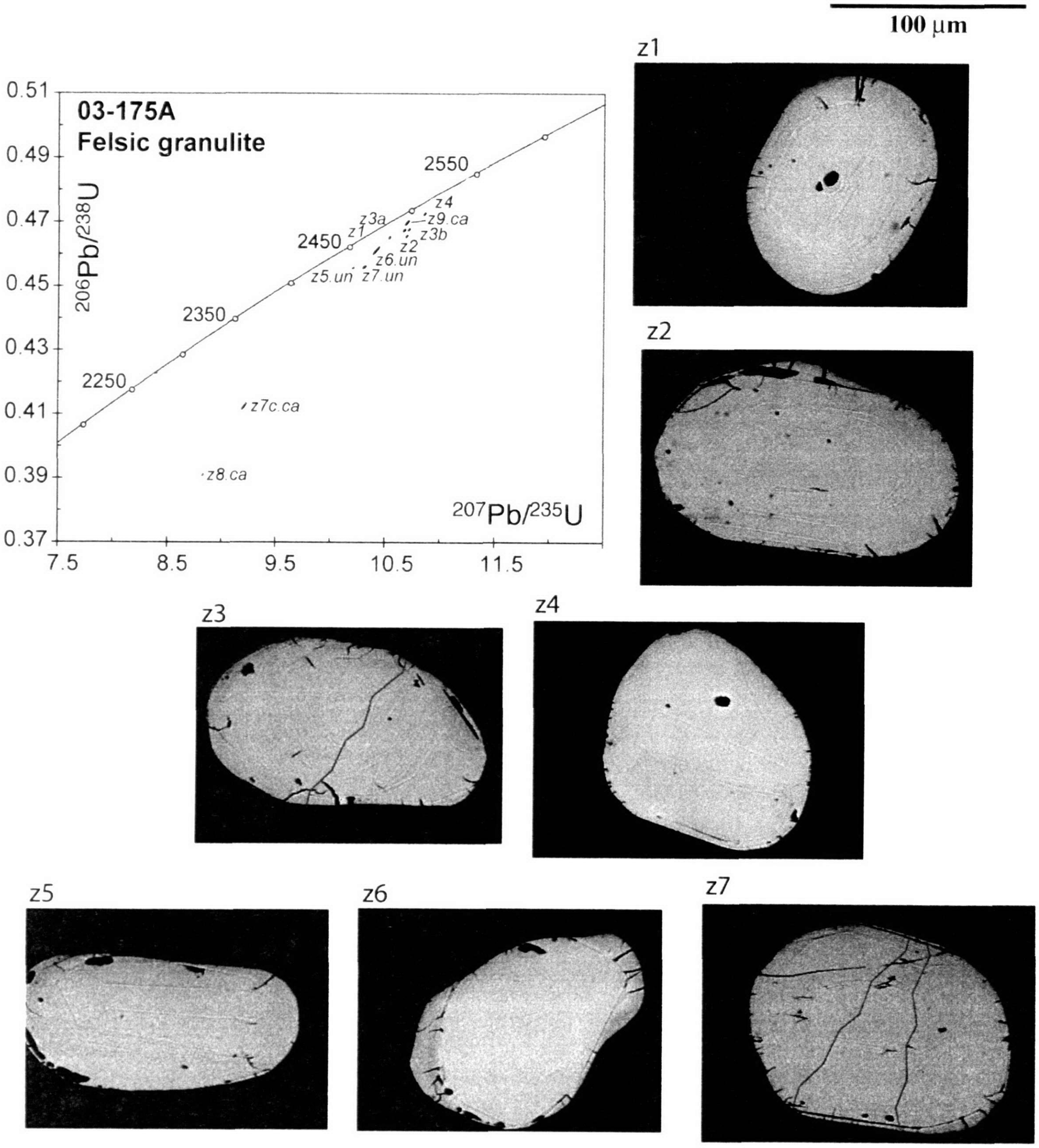
03-175A
Felsic granulite
^{206}Pb/^{238}U
^{207}Pb/^{235}U
0.51
0.49
0.47
0.45
0.43
0.41
0.39
0.37
7.5
8.5
9.5
10.5
11.5
2250
2350
2450
2550
z1
z3a
z4
z9.ca
z3b
z2
z6.un
z5.un
z7.un
z7c.ca
z8.ca
100 μm
z1
z2
z3
z4
z5
z6
z7

Figure 9

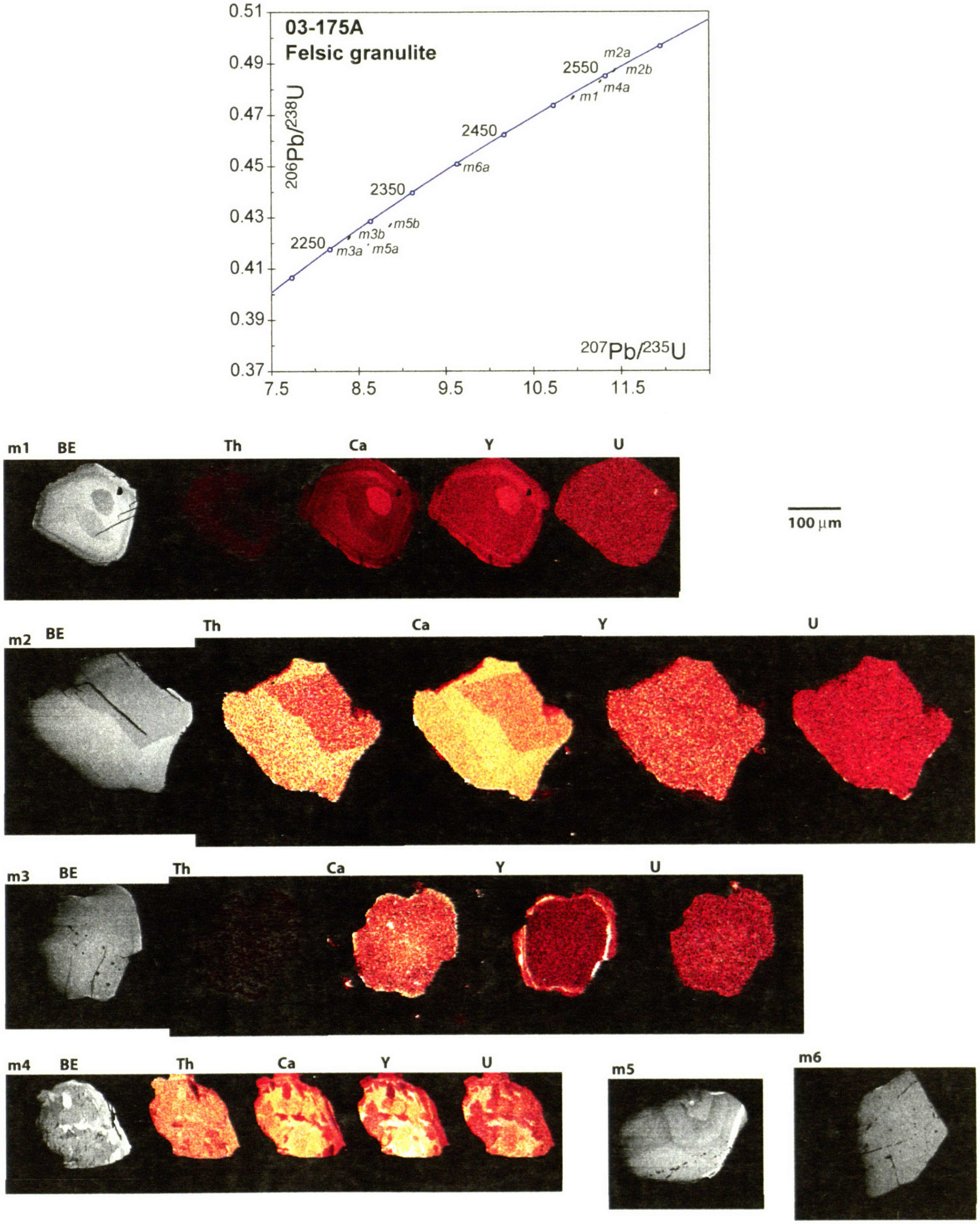
03-175A
Felsic granulite
$^{206}Pb/^{238}U$
$^{207}Pb/^{235}U$
0.51
0.49
0.47
0.45
0.43
0.41
0.39
0.37
7.5
8.5
9.5
10.5
11.5
2250
2350
2450
2550
m1
m2a
m2b
m3a
m3b
m4a
m5a
m5b
m6a
m1
BE
Th
Ca
Y
U
100 µm
m2
BE
Th
Ca
Y
U
m3
BE
Th
Ca
Y
U
m4
BE
Th
Ca
Y
U
m5
m6

Figure 10

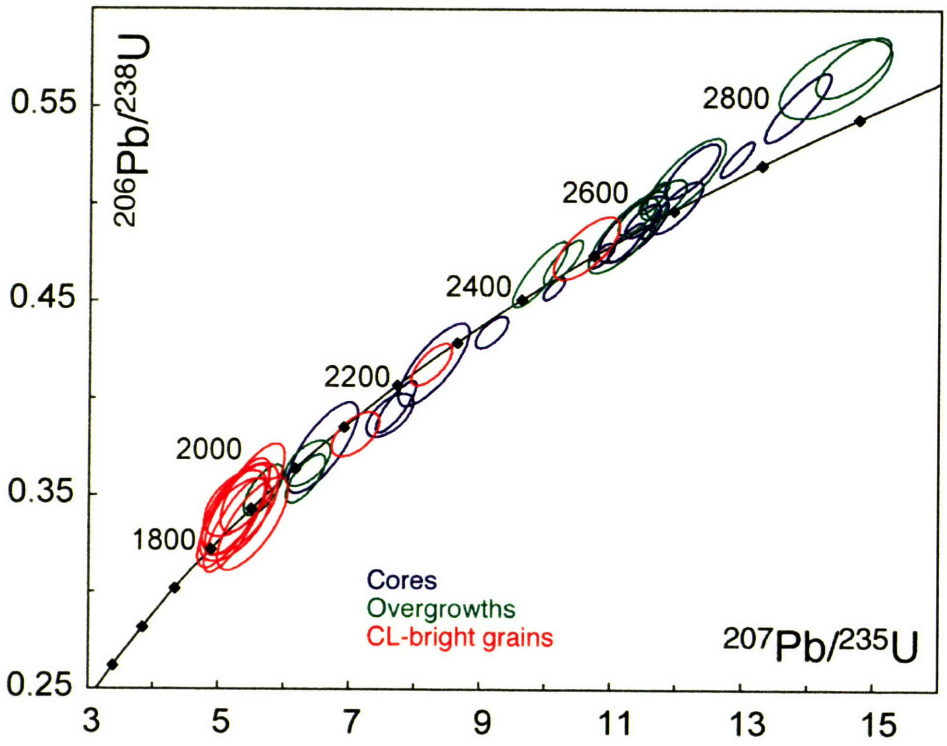
^{206}Pb/^{238}U
0.55
0.45
0.35
0.25
3
5
7
9
11
13
15
^{207}Pb/^{235}U
1800
2000
2200
2400
2600
2800
Cores
Overgrowths
CL-bright grains

Figure 11

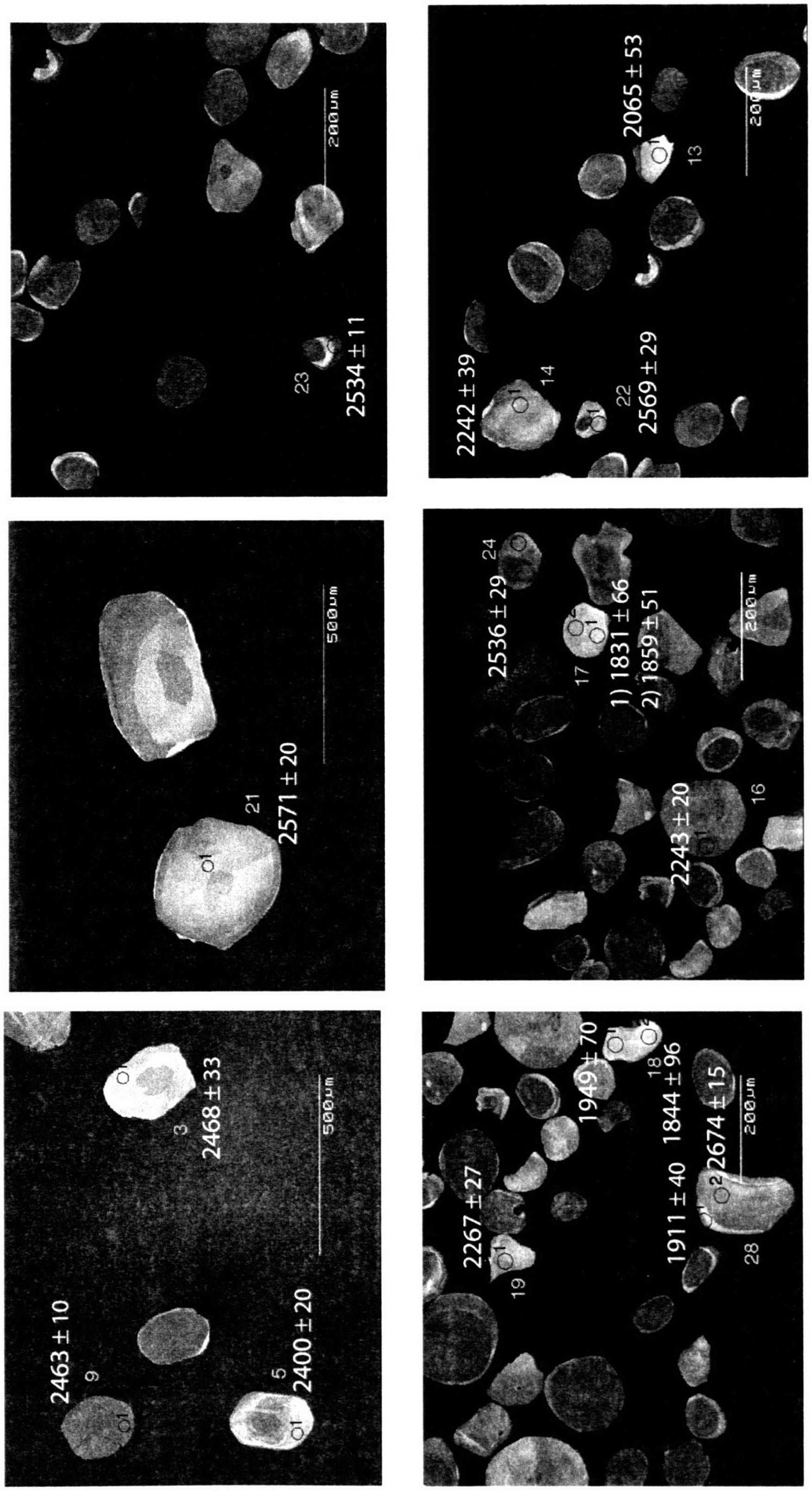
2534 ± 11
23
200μm
2242 ± 39
14
22
2569 ± 29
2065 ± 53
13
200μm
2571 ± 20
21
500μm
2536 ± 29
24
17
1) 1831 ± 66
2) 1859 ± 51
2243 ± 20
16
200μm
2463 ± 10
9
5
2400 ± 20
3
2468 ± 33
500μm
2267 ± 27
19
1949 ± 70
18
1844 ± 96
1911 ± 40
2674 ± 15
28
200μm

Figure 12

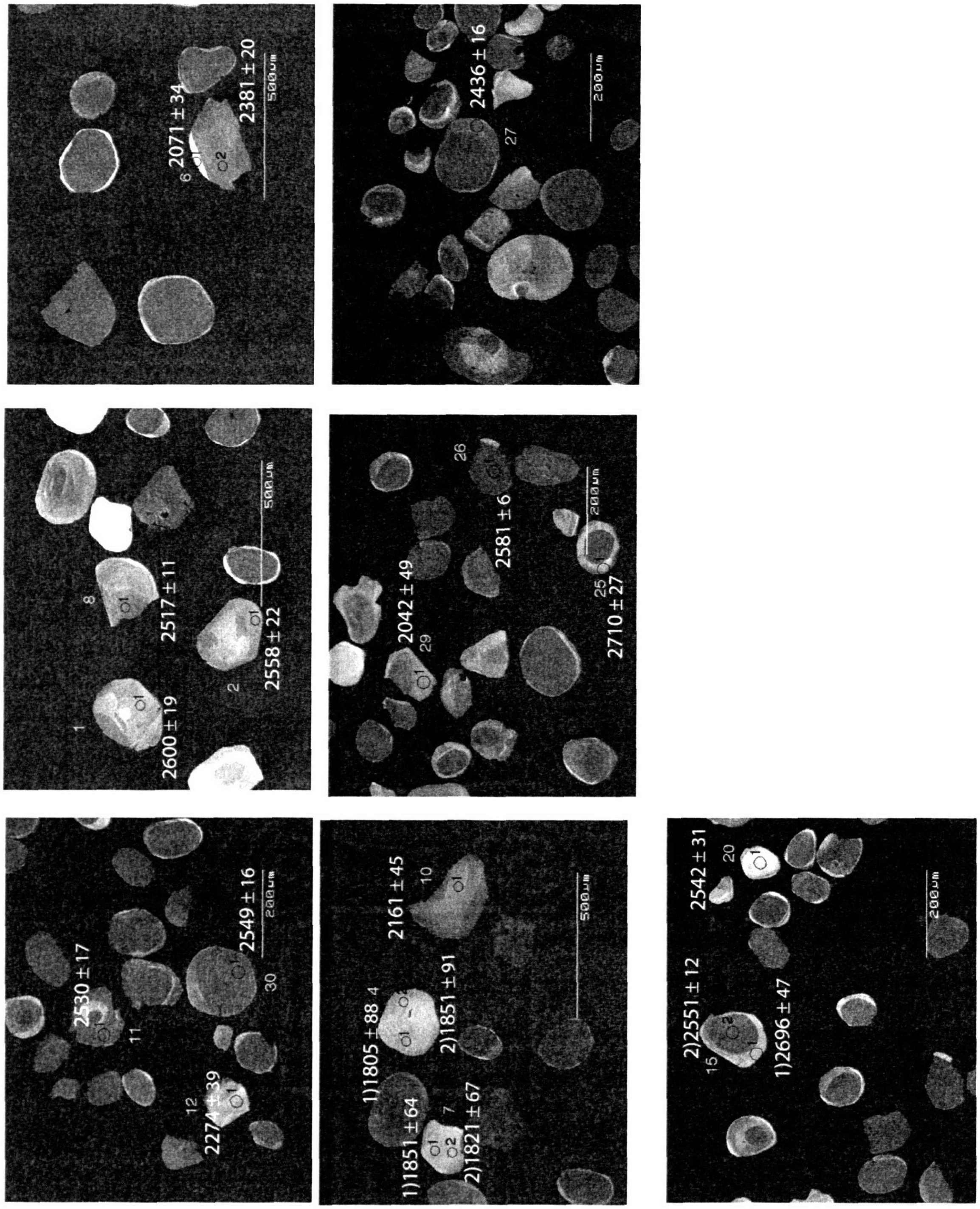

Figure 12 continued

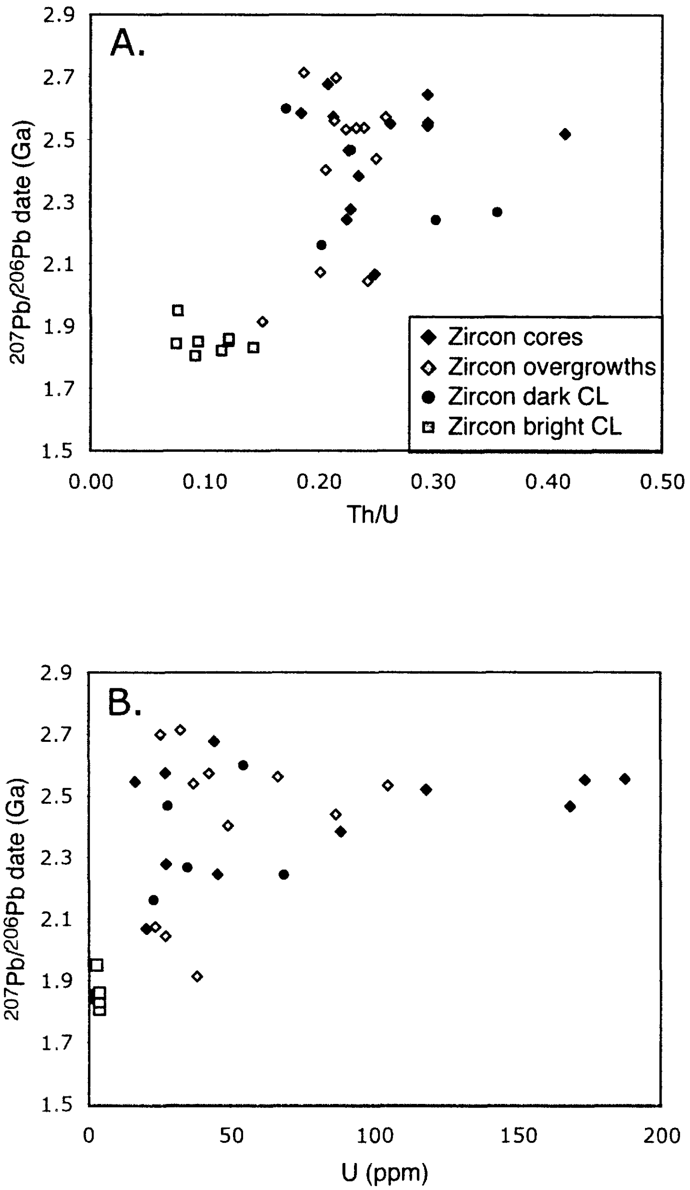
A.
2.9
2.7
2.5
2.3
2.1
1.9
1.7
1.5
207Pb/206Pb date (Ga)
0.00
0.10
0.20
0.30
0.40
0.50
Th/U
◆ Zircon cores
◇ Zircon overgrowths
● Zircon dark CL
▫ Zircon bright CL
B.
2.9
2.7
2.5
2.3
2.1
1.9
1.7
1.5
207Pb/206Pb date (Ga)
0
50
100
150
200
U (ppm)

Figure 13

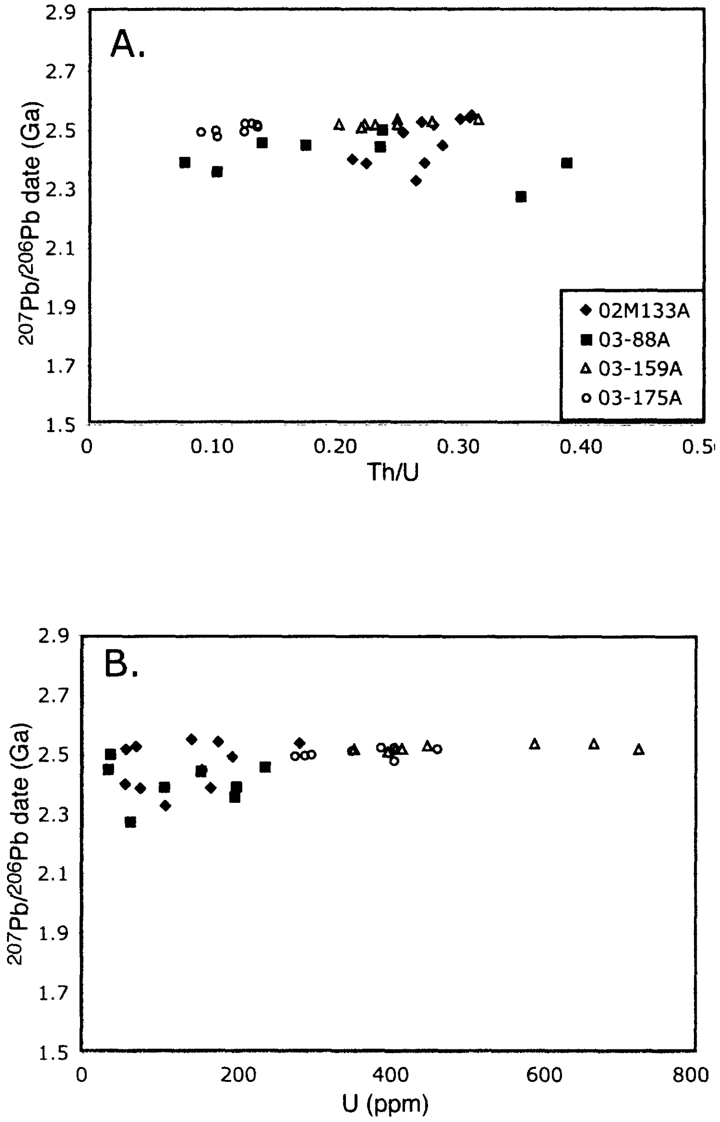
A.
207Pb/206Pb date (Ga)
2.9
2.7
2.5
2.3
2.1
1.9
1.7
1.5
0
0.10
0.20
0.30
0.40
0.5
Th/U
◆ 02M133A
■ 03-88A
△ 03-159A
○ 03-175A
B.
207Pb/206Pb date (Ga)
2.9
2.7
2.5
2.3
2.1
1.9
1.7
1.5
0
200
400
600
800
U (ppm)

Figure 14

Chapter 2

Timescales of high-pressure, high-temperature metamorphism and mafic dike anatexis, Snowbird tectonic zone, Canada

ABSTRACT

New geochronological, isotopic and geochemical data for a spectacular swarm of deep crustal migmatitic mafic dikes along the Snowbird tectonic zone in northern Saskatchewan provide important insight into processes operative during 1.9 Ga high pressure, high temperature metamorphism. High-precision U-Pb ID-TIMS zircon dates reveal mafic dike anatexis at 1896.2 ± 0.3 Ma during syntectonic and synmetamorphic dike intrusion at conditions of 1.0-1.2 GPa, >750 °C. U-Pb zircon dates of 1894-1891 Ma for cross-cutting pegmatites place a lower bound on major metamorphism and deformation at exposed crustal depths. Sm-Nd whole rock isotopic data are consistent with pegmatite derivation from a deeper mafic source, and imply the ongoing maintenance of high temperatures following peak conditions at exposed crustal levels. Limited ca. 1.9 Ga felsic magmatism despite high temperatures is consistent with evidence for previous dehydration of rocks by granulite facies metamorphism in the Archean. Inferred residence of rocks in the deep crust from ca. 2.55 to 1.9 Ga implies a period of lithospheric stability, requiring a significant event at 1.9 Ga to disrupt a stabilized craton. We correlate 1896 Ma Chipman mafic dike emplacement and metamorphism with substantial, almost synchronous, 1.9 Ga mafic magmatism over a minimum along-strike extent of 1200 km of the Snowbird tectonic zone, with additional potential correlation to the south that would coherently link 1.9 Ga observations along the entire 2800 km length of this dramatic geophysical lineament. These data indicate a significant, continent-wide period of asthenospheric upwelling. This unusual deep crustal record of lithospheric disruption, destabilization and exhumation contrasts with the long-term stability of most cratons, and is important for understanding the lithospheric characteristics and tectonic circumstances necessary for the survival of continents.

INTRODUCTION

The rheological, metamorphic, and melting behavior of the lower continental crust exerts important control on crustal differentiation and the growth and maturation of continents. The complex interactions between deep crustal mafic magmatism, silicic melt generation and segregation, metamorphic reactions, and deformation can profoundly impact the behavior of the entire crustal column during vertical transfer of mass, heat and stress through the system. In addition, the deep crust represents the most robust and unfiltered crustal signature of activity in the underlying lithospheric and asthenospheric mantle. Rare exhumed lower crustal terranes offer the best opportunity to directly examine the record of processes preserved in rocks once resident in the deep crustal roots of the continents. Data from these regions regarding changing thermal regimes in the lower crust constrain the nature, intensity and timescales of high-pressure (HP) granulite facies episodes. Such information can yield important insights into the crustal response to these events and the plate tectonic and asthenospheric processes responsible for the disruption..

Along the Snowbird tectonic zone in the western Canadian Shield, vast (>20,000 km^2) well-preserved exposures of lower continental crust (1.0->1.5 GPa) in the East Lake Athabasca region provide an exceptional opportunity to study a record of HP granulite facies metamorphic events. In particular, the Chipman mafic dike swarm, exposed within this tract of rocks, preserves a spectacular snapshot of the dynamic deep crustal environment during a high temperature metamorphic event. During emplacement the mafic dikes were metamorphosed, heterogeneously deformed, and partially melted at 1.0-1.2 GPa, >750 °C to yield segregations of tonalitic and trondhjemitic melt (Williams et al., 1995). We use new high-precision U-Pb ID-TIMS geochronological data, Sm-Nd isotopic systematics, geochemistry data, and field observations to constrain the duration of high pressure-high temperature (HP-HT) metamorphism, anatexis, and deformation in this region, unravel the detailed evolution of the thermal regime during this event, and assess the geodynamic significance of this intense episode of deep crustal magmatism and metamorphism. Our results highlight the exceptional value of the East Lake Athabasca area for understanding the nature, behavior, and response of the lower crust during the evolution, stabilization, and reactivation of continents.

GEOLOGICAL SETTING

The western Churchill Province of the Canadian Shield is an extensive region of Archean crust bounded by the Thelon orogen (2.02-1.90 Ga) to the northwest and the Trans-Hudson orogen (1.85-1.80 Ga) to the southeast (Figure 1). The Snowbird tectonic zone, a 2800 km long NE trending gravity and magnetic anomaly, has been defined as the boundary separating the Rae and Hearne cratons of the western Churchill Province (Goodacre et al., 1987; Hoffman, 1988). This dramatic geophysical feature has alternatively been interpreted as a Paleoproterozoic intercontinental suture (Hoffman, 1988; Ross et al., 1995, 2000), an Archean intracontinental strike-slip shear zone (Hanmer et al., 1994, 1995a,b, 1997), and a Paleoproterozoic intracontinental transform (Lewry and Sibbald, 1980). The central segment of the Snowbird tectonic zone is characterized by an anastomosing internal geometry that recently has been attributed to the interaction of Proterozoic intracontinental thrust and strike-slip shear zones (Mahan and Williams, 2005). In this region, the East Lake Athabasca area in northern Saskatchewan contains an enormous tract of high-grade rocks (1.0 to ≥1.5 GPa, > 750 °C), composed of several disparate domains, spanning the width of this fundamental structure (Figure 2).

The East Lake Athabasca area includes granulite facies rocks of the East Athabasca mylonite triangle along the trace of the Snowbird tectonic zone, deep crustal rocks of the Rae domain to the west, and middle to upper crustal rocks of the Hearne domain to the east. To the south the region is covered by sediments of the Athabasca basin. The East Athabasca mylonite triangle is divided into three distinct lithotectonic domains: 1) the Chipman domain dominated by the heterogeneous > 3.0 Ga Chipman tonalite and the extensive Chipman mafic dike swarm recording metamorphism and melting at 1.0-1.2 GPa and 750-850 °C (Williams et al., 1995), 2) the northwestern domain composed of ca. 2.6 Ga mafic to felsic plutonic rocks, including the Mary granite interpreted to be intruded and metamorphosed at 1.0 GPa (Williams et al., 2000), and 3) the southern domain consisting of felsic and mafic granulites and minor eclogite with peak metamorphic conditions as high as ≥ 1.5 GPa and 900-1000 °C (Snoeyenbos et al., 1995; Baldwin et al., 2003, 2004). A recent study in the southern domain has interpreted high temperature- high pressure metamorphism to have occurred at 1904.0 ± 0.3 Ma (Baldwin et al., 2004). Metamorphic study in the Rae domain at Neil Bay and Wholdaia Lake documents granulite-facies conditions of ~ 0.8 GPa, 900 °C at ca. 1.9 Ga (Kopf, 1999; Krikorian and Williams, 2002). The Legs Lake shear zone along the eastern margin of the Chipman domain juxtaposes granulite facies rocks of the East Athabasca mylonite triangle with lower pressure (~ 0.5 GPa, 600-700 °C) rocks of the Hearne domain, and is associated with regional exhumation of the deep crustal rocks ca. 1850-1800 Ma (Mahan et al., 2003; Mahan and Williams, 2005).

CHIPMAN MAFIC DIKE METAMORPHIC ASSEMBLAGES AND FIELD RELATIONSHIPS

The temporal record of mafic magmatism and granulite facies metamorphism preserved by the Chipman mafic dike swarm is the primary focus of this contribution. Originally named by Macdonald (1980), the dike swarm is exposed across the width of the Chipman domain and is truncated laterally by domain-bounding shear zones (Figure 3). The > 3.0 Ga variably deformed Chipman tonalite gneisses, containing inclusions of anorthosite, peridotite, and mafic and felsic granulites, compose the dominant host unit in the domain. The more homogeneous ca. 2.6 Ga Fehr granite occurs on the eastern margin of the domain. Chipman dikes vary in abundance across the span of the swarm, range in width from less than one to tens of meters, and locally compose 60-100% of the exposure. The northeast striking Chipman dikes are deformed by the more northerly striking Legs Lake shear zone (LLSZ) on the east side of the Chipman domain (Figure 3). Dikes decrease in abundance from the Chipman tonalite into rocks of the Fehr granite, and are increasingly scarce eastward in rocks deformed by the LLSZ. In the western part of the Chipman domain dikes are locally abundant, but do not intrude the adjacent northwestern domain. Near the western boundary of the domain the dikes are locally deformed by mylonites of the Cora Lake shear zone, a structure interpreted to truncate western exposures of the dike swarm (Figure 3). The center of the Chipman domain coincides with an 8 x 20 km positive gravity anomaly that suggests additional dense mafic material at depth (Hanmer et al., 1994).

The Chipman dikes can be texturally and mineralogically subdivided into four major groups: 1) migmatitic granulite dikes, 2) non-migmatitic granulite dikes, 3) non-migmatitic amphibolite dikes, and 4) phenocrystic or phyric dikes. All dikes contain hornblende and plagioclase, with variable titanite, ilmenite, and rutile. Migmatitic dikes are typically characterized by cm-scale garnet and associated quartz and plagioclase leucosomes in a hornblende and plagioclase matrix (Figure 4A). These dikes are zircon-bearing and rarely contain clinopyroxene. Leucosomes occur as tails in strain shadows adjacent to garnet crystals, and, with increasing melt volumes, as discrete leucosomal segregations in pods and veins (Figure 4B). Some migmatitic dikes show an internal textural layering parallel to dike margins. In partly migmatized dikes, the migmatitic components typically occur along dike margins. In non-migmatitic granulite dikes, textures range from fine-grained garnet and clinopyroxene spherical clumps in a hornblende and plagioclase matrix, to a homogeneous fine- to coarse-grained garnet, clinopyroxene, hornblende, and plagioclase matrix (Figure 4C). Non-migmatitic dikes lack zircon. Amphibolite dikes are dominantly hornblende and plagioclase. Rare phenocrystic or phyric plagioclase rich dikes contain variable hornblende, garnet and clinopyroxene. Textures suggest that all dikes crystallized as hornblende-plagioclase rocks and were metamorphosed to produce the granulite facies assemblages. Amphibolite dikes either never reacted to form the high grade assemblage, or are retrogressed varieties of granulite dikes. Additional detailed descriptions of mineralogical assemblages and textures in the Chipman dikes, with particular focus on the migmatitic dikes, were provided in Williams et al. (1995). Thermobarometric estimates for migmatitic and non-migmatitic dikes using garnet hornblende thermometry and garnet-hornblende-plagioclase barometry yielded conditions of 750-850 °C and 1.0-1.2 GPa (Williams et al., 1995).

Migmatitic and non-migmatitic granulites dikes differ in both their distribution and degree of strain. Migmatitic dikes occur in a 10-12 km wide corridor within the broader Chipman dike exposures. They are abundant in the Chipman tonalite in the southeastern part of the domain, are less common in the Fehr granite to the east, and were not observed in the western part of the domain. In contrast, non-migmatitic granulite dikes are distributed across the entire domain. Migmatitic dikes are always deformed by a moderately steep NE-striking fabric, and, in places, show evidence for having been deformed by an earlier, shallower NW-striking fabric. These dikes are commonly boudinaged with leucocratic melt filling boudin necks, or may be folded with leucocratic melt tails either folded or defining the axial surface of the fold (Figure 4D). In contrast, non-migmatitic dikes typically show less strain than migmatitic dikes, are commonly discordant to fabric in the host rocks (Figure 4E), and may preserve original intrusive features such as apophyses into the host tonalite. The differing strain may owe to the inherently greater strength of dikes lacking leucosomes and/or later intrusion of non-migmatitic dikes that missed an earlier phase of deformation.

Documentation of the detailed spatial relationships of dismembered, folded, variably deformed, and cross-cutting dikes suggests their synmetamorphic and syntectonic emplacement at granulite facies conditions (Williams et al., 1995). For example, observations of dikes with straight leucocratic tails cutting dikes with folded leucocratic tails (see Williams et al. 1995, figure 7) are most simply explained by episodic or continuous migmatization of dikes during intrusion rather than a single discrete anatectic event that postdated their emplacement. Importantly, this interpretation implies that determination of the time of dike anatexis also constrains the date of dike intrusion. Although intrusion of multiple dike swarms of widely varying ages with more than one episode of dike migmatization cannot be currently be excluded as a means of explaining the field relationships, this requires a significantly more complex geological history that is not supported by the data in this study.

Pegmatitic dikes and segregations intrude dikes of varying textures and metamorphic assemblages (Figure 4F). Undeformed varieties provide the potential to impose a local lower temporal bound on major magmatism and deformation in the domain. With the exception of the pegmatites and migmatitic dike leucosomes, limited melting during mafic dike intrusion is indicated by field relationships. Centimeter scale felsic bands, segregations, and leucosomal material in the hornblende-bearing Chipman tonalite are inferred to be coeval with Chipman dike intrusion based on structural and lithological relationships. In the biotite-bearing Fehr granite, more abundant felsic segregations up to a half-meter in scale are either directly or indirectly associated with mafic dikes and provide the most convincing evidence for melting of host felsic rocks during dike emplacement (Figure 4G).

WHOLE ROCK GEOCHEMISTRY

Sixteen samples of Chipman dikes, representing the full spectrum of observed textural variation, were analyzed for major and trace elements by XRF and ICPMS, respectively, at Activation Laboratories. Data are reported in Table 1. Data were acquired to 1) evaluate the nature of the dike magma source, and 2) assess the importance of compositional factors for dike anatexis by establishing whether dike geochemistry patterns can be linked with textural and mineralogical observations. These results supplement major element data previously obtained for nine Chipman dike samples (Williams et al., 1995). Migmatitic dikes were characterized by the greatest textural heterogeneity, and particular care was taken to process samples representative of the bulk composition.

The dikes contain SiO_2 ranging from 46.1 to 52.2% and MgO from 3.3 to 7.1%. Samples in this study are relatively high in iron (iron as Fe_2O_3 = 13.5 to 19.5%) and low in Al_2O_3 (11.5 to 15.5%), with the exception of two plagioclase rich phyric to phenocrystic dikes (Figure 5A). Normative calculations and projections into the ol-cpx-qtz and ol-pl-qtz ternary systems result in a distribution of data that plot into the qtz and plag fields, consistent with most dikes representing melt compositions rather than residues of fractional crystallization. Spider diagrams reveal high field strength element (HFSE) enrichments and large ion lithophile element (LILE) depletions (Figure 5B). Rare earth element (REE) patterns are relatively flat, implying an absence of significant garnet in the source. Generally, migmatitic dikes contain higher SiO_2, Fe_2O_3, Ta, Zr and Nb, and lower MgO and Al_2O_3, than non-migmatitic dikes (Figure 5A). Four distinct REE patterns generally correlate with the four major textural and mineralogical groups (Figure 5C): 1) migmatitic granulite dikes contain the highest REE contents, 2) non-migmatitic granulite dikes are characterized by an array of lower REE contents, 3) amphibolite dikes are defined by distinctly flatter REE patterns than those in the granulite facies dikes, and 4) phenocrystic and phyric dikes contain the lowest REE contents and are characterized by Eu anomalies. The occurrence of Eu anomalies in the two plagioclase-rich dike samples is consistent with the involvement of plagioclase fractionation near their source or during emplacement. A distinct coarse-grained sample from the center of a non-migmatitic granulite dike (02-112) is characterized by a shallow positive REE slope, contains the highest analyzed Mg content suggestive of a more primitive composition, and is considered from field observations to be one of the latest intruded dikes.

SM-ND ISOTOPIC SYSTEMATICS

Analytical Methods

Whole rock powders were produced using standard shatterbox procedures. Sample powders (100-200 mg) were spiked with a mixed ^{149}Sm-^{150}Nd tracer, completely dissolved in HF-HNO_3 in Teflon pressure vessels at 220 °C for five days, converted to 6M HCl at 180 °C for 24 hours, then repeatedly fluxed in 6M HCl at 120 °C. The REE were separated from solution using cation exchange chemistry, followed by usage of LN-spec resin to isolate Sm and Nd. All analyses were carried out on the Massachusetts Institute of Technology Isoprobe-T mass spectrometer. Sm was loaded onto single Ta filaments with 1M H_3PO_4 and analyzed as metal ions in multicollector static mode. Nd was loaded on triple Re filaments with 0.1M H_3PO_4 and analyzed as metal ions in dynamic multicollector mode. Sm-Nd results and details regarding isotopic ratio corrections are provided in Table 2.

Analytical Results

Whole rock Sm-Nd isotopic systematics were determined for the same sixteen Chipman dike samples analyzed for major and trace elements. In addition, whole rock Sm-Nd data were acquired for ten mafic granulite gneisses, four Chipman tonalite gneisses, and three pegmatite samples to place constraints on source characteristics. Fifteen of the Chipman dike samples have present day ε_{Nd} values from –16.8 to –3.2 and reflect time-integrated LREE enrichment. One distinct dike (02-112) is characterized by a present day ε_{Nd} value of +10.6 and time-integrated LREE depletion, consistent with its HREE pattern. ε_{Nd} values at the time of 1.9 Ga granulite facies metamorphism range from –9.1 to +2.2, with depleted mantle model dates (T_{DM}) from 4.20 Ga to 2.42 Ga (Figure 6A). A plot of ε_{Nd} values at 1.9 Ga vs. weight percent SiO_2 for the fifteen dikes characterized by time-integrated LREE enrichment reveals that dikes containing higher (> 50.9%) SiO_2 content display an inverse correlation between ε_{Nd} and SiO_2, while dikes with lower (< 50.9%) SiO_2 content lack this correlation (Figure 6B). This observation suggests the influence of crustal assimilation on the subset of dikes, including the migmatitic dikes, containing higher SiO_2.

Five Grt+Cpx+Opx+Pl mafic granulites and five Opx+Pl mafic granulites, collected from lenses in the Chipman tonalite in the western and northern parts of the Chipman domain, were selected for Sm-Nd isotopic analyses. Previous data have established these mafic granulite lenses as Archean in age (Flowers, Chapter 1). Nine of ten mafic granulite samples are characterized by time-integrated LREE enrichment and present day ε_{Nd} values from –24.5 to –0.9. One mafic granulite (03-228A) reflects time-integrated HREE enrichment, and contains a present day e_{Nd} value of 17.5. The ε_{Nd} values at 2.6 Ga range from –7.29 to 2.72, with depleted mantle model dates (T_{DM}) from 3.91 Ga to 2.91 Ga (Figure 6C). Our data show a correlation between ε_{Nd} values at 2.6 Ga and SiO_2 content, consistent with the assimilation of felsic crustal material with more evolved Nd isotopic signatures during the generation and emplacement of the protolith (Figure 6D). The mafic granulite sample with time-integrated HREE enrichment contains one of the lowest SiO_2 contents, suggesting it was least affected by crustal contamination.

The four Chipman tonalitic gneiss samples display evolved Nd isotopic compositions, with time-integrated LREE enrichment, present day ε_{Nd} values from –45.7 to –35.0, ε_{Nd} values at 3.0 Ga from –4.8 to –2.2, and depleted mantle model dates from 3.59 to 3.31 Ga (Figure 6C). These data are consistent with Sm-Nd data acquired for three previous samples of Chipman tonalite characterized by present day ε_{Nd} values from –58.7 to -43.3 (Hanmer, 1994). The signature of crustal contamination preserved in the Chipman mafic dikes and Archean mafic granulite gneisses can be explained by assimilation of the host Chipman tonalite with its highly evolved Nd isotopic composition.

Sm-Nd data were acquired for three pegmatite samples that cross-cut Chipman mafic dikes to evaluate whether they were derived from a mafic source or from the Chipman tonalitic gneisses. The pegmatites reflect time-integrated LREE enrichment, with depleted mantle model dates from 2.67 to 2.33 Ga. Nd signatures for two of three pegmatite samples are characterized by present-day e_{Nd} values from –27.9 to –16.5 and ε_{Nd} values at 1.9 Ga from –7.2 to –3.0. These data are consistent with derivation from the Chipman mafic dikes or mafic gneisses, and are incompatible with generation by melting of the Chipman tonalite (Figure 6C). Data for the third sample containing present-day and 1.9 Ga ε_{Nd} values of –47.1 and –13.4, respectively, are compatible with genesis from the same source as the other pegmatite samples, but the more negative signature suggests a contribution from a more evolved component such as the Chipman tonalite.

U-PB GEOCHRONOLOGY

Analytical Methods

Mineral separation was accomplished using standard crushing, water table, heavy liquid, and magnetic separation techniques. Representative zircon grains from selected samples were mounted in epoxy, polished to expose grain interiors, and characterized with cathodoluminescence (CL) and/or backscattered-electron (BE) imaging to document internal zoning (Figures 7 and 8). Zircon grains for analysis were either selected from this suite of imaged grains, or hand-picked from the general population using the images as a guide. Single grain zircon fractions were photographed, air-abraded with pyrite after the method of Krogh (1982), measured, and rinsed and ultrasonicated in 3 M HNO_3. After initial analyses established greater discordance in higher U zircon, a subset of grains were subjected to a version of the chemical abrasion technique (Mattinson, 2005), in which zircon grains were placed in quartz crucibles in a muffle furnace at ~900 °C for ~60 hours, loaded into Teflon FEP microcapsules and leached in 29 M HF at ~180 °C for 12 hours or into savillex beakers and leached in 29 M HF at ~80 °C for 21 hours, then transferred to savillex beakers and prepared for dissolution according to standard procedures. Zircon fractions dissolved early in the study were loaded with distilled acetone into Teflson FEP microcapsules, ultrasonicated and fluxed at ~80 °C in 3 M HNO_3, and rinsed with several capsule volumes of 3 M HNO_3. Zircon fractions dissolved later in the study were loaded into savillex beakers, ultrasonicated and fluxed at ~80 °C in 3 M HNO_3, rinsed in distilled acetone and high-purity water, and loaded into Teflon FEP microcapsules in high-purity water with no subsequent rinsing in the capsules. Samples were spiked with a mixed ^{205}Pb-^{233}U-^{235}U tracer, dissolved in 29 M HF at 220 °C for 48-96 hours, and converted to 6 M HCl at 180 °C for 12-24 hours. Pb and U were chemically separated using HCl anion exchange chemistry modified after Krogh (1973). Pb and U were loaded on single Re filaments with a silica gel 0.1 M H_3PO_4 emitter solution and analyzed on the MIT VG Sector 54 mass spectrometer. Pb isotopic ratios were measured either by peak jumping using an axial counting Daly detector, or dynamically with Faraday cups and the Daly detector, peak-jumping ^{205}Pb into the axial position to obtain a real-time Faraday-Daly gain calibration. U was measured as an oxide, typically in static mode on three Faraday cups, and less commonly by peak-jumping into the Daly detector for smaller amounts of uranium. U-Pb data and details regarding isotopic ratio corrections are provided in Table 1. Concordia diagrams for all samples are shown in Figures 9 and 10. Data are reported as $^{207}Pb/^{206}Pb$ weighted mean dates, except for samples for somewhat higher discordance for which a york fit upper intercept date is reported. Decay constant and U-Pb tracer calibration uncertainties are systematic errors not included in the cited dates, as these are unnecessary for comparison of data acquired within a single lab. Systematic effects of decay constant inaccuracies are minimized as a function of increasing age, and most $^{207}Pb/^{206}Pb$ dates in this study are within error of concordia when decay constant uncertainties are considered.

Sample Selection

Five representative samples of migmatitic dikes were selected for U-Pb zircon analysis to place precise constraints on the timing of granulite facies metamorphism and anatexis (Figure 3). Due to field observations suggesting episodic dike migmatization during sequential dike intrusion and metamorphism, rather than a single discrete period of anatexis postdating emplacement of the swarm, samples across the corridor of migmatitic dikes were targeted to test for spatial variability in the timing of dike migmatization. Morphological and internal zoning characteristics of zircon extracted from these samples, described further below, are consistent with metamorphic growth or crystallization in leucosomal melts (e.g. Corfu et al., 2003; Vavra et al., 1999). Although non-migmatitic granulite and amphibolite dikes were also processed for accessory minerals, no zircon was recovered. This supports the interpretation of zircon growth owing to reactions associated with mafic dike anatexis, rather than due to igneous crystallization during dike intrusion.

Late, biotite-bearing, cross-cutting and variably deformed pegmatitic segregations and dikes intrude Chipman mafic dikes and other rocks of the Chipman domain. Two pegmatitic veins and two pegmatitic dikes were selected for U-Pb zircon work to place a lower bound on felsic magmatism and local deformational fabrics in the Chipman domain. Three of four samples contained zircon characterized by high U contents (up to 1900 ppm), that decreased the probability of concordant analyses due to long-term accumulation of radiation damage and associated Pb loss at low temperatures.

Analytical Results

Migmatitic Dikes

Sample SZ00-196C, containing cm-scale garnets with cm-scale leucosome tails, was collected from a zone of exceptionally abundant migmatitic dikes at Woolhether Lake. The distribution and petrographic setting of zircon in this sample was characterized by collection of major element and Zr thin section maps with the electron microprobe (Figure 7A). Dozens of ovate to spherical zircon, typically < 15 µm up to 40 mm in diameter, occur as inclusions in amphibole in one of several settings: in amphibole grains in the matrix, in amphibole inclusions in garnet, or associated with other inclusion phases in amphibole such as titanite (Figure 7B,C). CL images commonly show distinct internal and external zircon domains of contrasting luminescence. Rare, irregular < 30 µm zircon agglomerations were identified adjacent to garnet. Crushing procedures extracted clear to light pink zircon that were large (up to 500 µm) prismatic and tabular or small (< 100 µm) spherical to ovate (Figure 7D). Analyzed zircon grains were U-poor, with the lowest mean U concentrations in this study (<35 ppm), and low Th/U ratios (0.01-0.03). Six single grain and one multi-grain zircon fractions yielded a weighted mean ^{207}Pb/^{206}Pb date of 1896.7 ± 0.8 Ma (MSWD = 0.47).

Sample 02-58 is a ~ 3m wide dike from Chipman Lake that is migmatitic throughout its entire width and contains mm-cm scale leucosome stringers with small mm-scale garnets. Zircon grains are clear, spherical to ovate, typically < 100 μm in diameter, with low Th/U ratios (0.05-0.10). Six single grain zircon fractions yielded a weighted mean $^{207}Pb/^{206}Pb$ date of 1896.0 ± 0.7 Ma (MSWD = 1.83), with a seventh older analysis excluded.

Migmatitic dike sample 02-88, collected from Steinhauer Lake, contains coarse cm-scale garnets and asymmetric leucosome tails. Leucosomes in this dike contain both the earlier shallow northwest and the dominant northeast fabrics. Zircon grains are typically 60-120 μm in diameter, are clear and ovate to spherical in morphology, and are characterized by low Th/U ratios (0.01-0.08). Seven single grain zircon fractions yielded a weighted mean $^{207}Pb/^{206}Pb$ date of of 1895.5 ± 0.5 Ma (MSWD = 0.39), with an eighth younger analysis excluded.

Migmatitic dike sample 02-97 intrudes the Fehr granite east of Steinhauer Lake. This sample contained a discrete leucocratic segregation connected to veins emanating from cm-scale garnets and associated leucosome tails in the bulk of the dike (similar relationships shown in Figure 4B). Zircon grains ranged from larger-sized (>150 μm) pink, prismatic, tabular to ovate crystals to smaller-sized (< 150 μm) clearer, facetted, ovate to spherical crystals. Th/U ratios are low (0.01-0.02). Four single grain zircon fractions yielded a weighted mean $^{207}Pb/^{206}Pb$ date of 1896.8 ± 0.5 (MSWD = 0.81).

Sample 03-52 is a somewhat atypical migmatitic dike, with remnant garnet-clinopyroxene textures like that in the non-migmatitic granulite dikes. The dike is deformed, ranges in width from 30 to 150 cm, and intrudes Chipman tonalite on southern Chipman Lake. Zircon grains range from tabular and prismatic to facetted and spherical. Grain size ranges up to 400 μm in length for the tabular population, and is generally < 150 μm for the spherical grains. CL images reveal internal irregular, sector-type zonation, outer shells of concentric zoning, and mineral inclusions such as apatite and quartz (Figure 8A). Fourteen of sixteen zircon fractions were imaged prior to analysis. Zircon grains have U concentrations of 25-85 ppm, with low Th/U ratios from 0.02 to 0.08. Six zircon fractions yielded a weighted mean $^{207}Pb/^{206}Pb$ date of 1896.3 ± 0.5 Ma (MSWD = 0.45), consistent with the data from the other migmatitic dikes. However, ten additional single zircon grains and zircon fragments yielded a range of $^{207}Pb/^{206}Pb$ dates from 1898.9 ± 1.8 Ma to 2015.5± 1.1 Ma. We interpret the scatter of dates along discordant arrays trending toward older ages to indicate the presence of an older inherited zircon component. A general correlation between Th/U ratio and zircon date is consistent with the inherited zircon containing higher Th/U. Analyses of fragments from the same zircon grain yield 1896 Ma and older dates (e.g. z9a and z9b dates of 1920.7 ± 2.5 Ma and 1896.1± 7.0 Ma, respectively, and z11a and z11b dates of 1922.0 ± 1.1 Ma and 1896.4 ± 2.4 Ma, respectively), similarly consistent with the tainting of select fragments by inheritance.

Pegmatitic Dikes and Segregations

Sample 01-SZ26 is an irregular pegmatite vein from Woolhether Lake that intrudes Chipman tonalite adjacent to a migmatitic dike. Zircon grains from this sample are large (up to 300 μm), pinkish brown, and high in U (up to 770 ppm), with Th/U ratios from 0.06 to 0.1. The grains have good crystal faces, are tabular to round, and do not luminesce in CL. BE images are relatively homogeneous, (Figure 8B) but reveal extensive fracturing in most grains, common alteration along fractures, and the presence of occasional xenocrystic cores. Six single grain zircon fractions have $^{207}Pb/^{206}Pb$ dates from 1890.2 ± 0.8 to 1891.7 ± 0.8, with an additional analysis distinguishably younger at 1887.2 ± 1.0 Ma. Up to 0.7% discordance, as well as high common Pb in several analyses, is attributed to the somewhat metamict, fractured nature of the grains due to high U content. Excluding the two youngest analyses, five zircon fractions yielded a York fit upper intercept date of 1890.8 ± 1.4 Ma (MSWD = 0.55).

Sample SZ00-196A is a biotite-bearing pegmatite that cross-cuts an extensive zone of migmatitic dikes at Woolhether Lake. The sample was collected from the same outcrop as migmatitic dike sample SZ00-196C. Internally, the dike lacks a fabric, but is broadly folded at the outcrop scale. Zircon grains are typically hundreds of microns in diameter, pinkish-brown, prismatic, tabular to ovoid, and do not luminesce in CL. BE images generally show little internal structure, except for occasional cores, and some alteration along fractures (Figure 8C). Zircon grains contain the highest mean U contents of the study (500 – 1900 ppm), and Th/U ratios of 0.07 to 0.11. High U concentrations, radiation damage, and associated low temperature Pb loss are likely responsible for the 0.7-2.0 % discordance of six fractions reported in Table 3, and the significantly greater discordance in other fractions analyzed from this sample. ^{207}Pb/^{206}Pb dates range from 1891.8 ± 0.8 Ma to 1895.5 ± 0.8 Ma.

Sample 02-77B is an irregular 10-25 cm wide biotite-bearing pegmatitic vein that intrudes a migmatitic dike at Steinhauer Lake. Zircon grains are typically 150-250 μm in length (up to 400 μm), pinkish-brown, prismatic, and tabular, with common inclusions, and characterized by Th/U ratios of 0.01 to 0.04. High U contents (350-1500 ppm), radiation damage, and inferred low temperature Pb loss in this sample, as in the two previous pegmatite samples, contributed to significant discordance in most analyzed grains, such that only the four most concordant analyses of fifteen analyzed grains are reported in Table 3. Targeting of smaller-sized grains for analysis improved zircon concordance. The upper intercept date of a York fit through these four zircon analyses is 1893.4 ± 0.9 Ma (MSWD = 0.94).

Sample 02-76B is a 40-50 cm wide biotite-bearing pegmatite dike that cross-cuts a deformed granulite facies non-migmatitic dike at Chipman Lake. Zircon grains are up to 500 μm in length, brown, prismatic, and either tabular or ovoid in morphology. U concentrations and Th/U ratios in analyzed zircon grains range from 15 to 85 ppm, and 0.24 to 0.40, respectively. CL images show irregular zoning in both tabular and ovoid zircon crystals (Figure 8D), with occasional xenocrystic cores. Four of six fractions of single zircon fragments yielded a weighted mean ^{207}Pb/^{206}Pb date of 1890.5 ± 0.4 Ma (MSWD = 0.04).

DISCUSSION

Implications for the Evolution of the 1.9 Ga Deep Crustal Thermal Regime

Intensity of HP Granulite Facies Metamorphism

Chipman dike thermobarometric data, metamorphic assemblages in existing mafic lithologies, and the extent of melting in host felsic gneisses allow us to evaluate the intensity of temperatures associated with Chipman dike HP metamorphism. Migmatitic and non-migmatitic dikes record conditions of 750-850 °C, 1.0-1.2 GPa (Williams et al., 1995), and are considered minimum temperature estimates because of evidence for diffusional reequilbration of phases. This is compatible with a variety of experimental studies demonstrating that vapor-absent melting of mafic rocks at 1.0-1.2 GPa can occur at temperatures of 850-1000 °C (e.g. Rapp et al., 1991; Rushmer, 1991; Patino Douce and Beard, 1995; Rapp and Watson, 1995; Springer and Seck, 1997), and possibly as low as 750 °C (Wolf and Wyllie 1993, 1994, 1995). Coeval conditions of >750 °C, 1.0-1.2 GPa preserved in Archean mafic granulite gneisses not immediately adjacent to dikes (Flowers, Chapter 1; Mahan et al., 2005) are consistent with the attainment of high temperatures across the Chipman domain, even outside the corridor where the most abundant Chipman dikes are exposed.

Despite similar P-T constraints for dikes across the swarm, only a subset underwent anatexis. Our field and geochemical data suggest that composition may be an important factor for this process. Internal dike-parallel banding of migmatitic and non-migmatitic textures within a single dike is consistent with successive intrusion of compositionally varying magma batches that may have controlled dike reaction history. Geochemical data suggest that typical migmatitic dikes are characterized by higher SiO_2, HFSEs and REEs, and lower MgO and Al_2O_3 than typical non-migmatitic dikes. These dike compositional variations cannot be simply explained by inappropriate integration of melanosomal and leucosomal fractions during sampling of migmatitic dikes (for example, SiO_2 and Al_2O_3 are not positively correlated). The inverse correlation between e_{Nd} and SiO_2 for migmatitic dikes suggests that assimilation of older crustal material may have increased the SiO_2 content of some dike magma batches, and thus made these dikes more susceptible to subsequent migmatization. Williams et al. (1995) previously suggested that the generally higher SiO_2 contents of migmatitic relative to non-migmatitic Chipman dikes may have played a role in controlling dike reaction history. Similarly, the abundance of quartz has been interpreted as the primary control on reaction progress in migmatitic mafic granulite gneisses of the Kapuskasing Structural Zone, with compositional variation in Fe exerting a secondary influence (Hartel and Pattison, 1996).

Limited anatexis of host felsic gneisses during subjection to this intense metamorphic event suggests that the rocks were vapor absent prior to dike metamorphism. This represents an endmember response of the crust to granulite facies conditions. At pressures of 1.0-1.5 GPa, water-saturated tonalite melting occurs at relatively low temperatures of 625-650 °C (e.g. Lambert and Wyllie, 1974; Schmidt, 1993), but the vapor absent tonalite solidus is defined by biotite and/or hornblende dehydration melting at minimum temperatures of 855-900 °C (Skjerlie and Johnston, 1993, 1996; Patino-Douce, 2005). Compositional effects such as low Ca in the bulk tonalite or high Ti and F in biotite can extend the stability of hornblende and biotite to even higher temperatures (Skjerlie and Johnston, 1993, 1996). At 1.0-1.5 Gpa pressures, biotite dehydration occurs at lower temperatures than amphibole dehydration, consistent with the observation of more abundant melts in the biotite-bearing Fehr granite than in the hornblende-bearing Chipman tonalite. We attribute the absence of free water in the felsic host gneisses to an Archean metamorphic event that left the Chipman domain rocks resistant to melting during subsequent Proterozoic metamorphism (Flowers, Chapter 1; Mahan et al., 2005).

We suggest that the entire Chipman domain was temporarily elevated to temperatures ≥750 °C during Chipman dike intrusion and metamorphism. Spatial heterogeneity in patterns of mafic dike and tonalitic gneiss anatexis can be attributed to lateral peak temperature and geochemical variability. The attainment of the hottest temperatures that exceeded the dry amphibolite and tonalite solidi may in part be locally linked to successive intrusion and crystallization of dike magmas (e.g. Petford and Gallager, 2001). The susceptibility of both mafic dikes and heterogeneous felsic gneisses to anatexis, as discussed above, is also compositionally dependent. Thus, the complex interaction of thermal and compositional factors likely controlled melting of rocks in the Chipman domain during 1.9 Ga HP granulite facies metamorphism.

Constraints on the Timing and Duration of Metamorphism

Metamorphic zircon grains in Chipman migmatitic mafic dikes permit precise dating of anatexis during 1.9 Ga HP granulite facies conditions. Field relationships, discussed previously, are most simply explained by synmetamorphic and syntectonic emplacement of the Chipman dikes, with episodic or continuous migmatization of dikes during intrusion (Williams et al., 1995). This suggests that dates for dike anatexis also constrain the timing of dike intrusion. The possibility that some dikes were emplaced at an earlier time cannot be entirely excluded, although broadly similar dike geochemistry patterns are consistent with mafic magma derivation from a single source region. Four migmatitic dikes distributed across the corridor of dike anatexis yield indistinguishable weighted mean $^{207}Pb/^{206}Pb$ dates from 1896.7 ± 0.8 Ma to 1895.5 ± 0.5 Ma. A fifth migmatitic sample contains a population of 1896.3 ± 0.5 Ma zircon crystals, with additional grains characterized by minor inheritance. These data suggest that the time span for dike migmatization at exposed crustal levels was ≤ 2.5 m.y., established by the errors on the range of sample zircon dates. It is unclear whether the onset of high-grade conditions in the Chipman domain coincided with dike emplacement, or commenced at an earlier time. Regardless, we consider the weighted mean $^{207}Pb/^{206}Pb$ date of 1896.2 ± 0.3 Ma (MSWD = 2.0) for thirty zircon analyses from the five migmatitic Chipman dike samples as the best temporal constraint on emplacement, HP granulite facies metamorphism (>750 °C, 1.0-1.2 GPa), and anatexis of the Chipman dikes.

U-Pb titanite data support the continued elevation of temperatures ≥ 600-650 °C following anatexis of currently exposed Chipman mafic dikes. Titanite grains from six samples distributed across the Chipman domain yielded dates from 1898 to 1882 Ma (Flowers, Chapter 3). This implies either that temperatures ≥ 600-650 °C were heterogeneously maintained for 14 m.y. following of Chipman dike anatexis, or that parts of the domain were reheated following immediate post-1896 Ma cooling. These data suggest the ongoing persistence of a heat source following mafic dike intrusion and anatexis.

U-Pb zircon and Sm-Nd whole rock data for pegmatites similarly imply protracted maintenance of high temperatures at deeper crustal levels following anatexis of currently exposed dikes. Four cross-cutting pegmatitic veins and segregations yielded U-Pb dates from 1893.4 ± 0.9 Ma to 1890.8 ± 1.4 Ma, distinctly postdate the timing of 1896.2 ± 0.3 Ma migmatization of exposed dikes, and impose a lower bound for major magmatism and deformation in Chipman domain exposures. The Nd isotopic signatures of two pegmatite samples are characterized by e_{Nd} values at 1.9 Ga from –7.2 to –3.0. Comparison with the Nd isotopic signatures of the Chipman tonalite, the mafic granulite gneisses, and the Chipman mafic dikes indicates that the pegmatite data are consistent with derivation from either the mafic gneisses or mafic dikes by amphibolite anatexis. Data for a third pegmatite sample suggest a similar genesis, but with a greater contribution from a more evolved component like the Chipman tonalite. Pegmatite generation from mafic lithologies by amphibolite anatexis requires temperature >750 °C, which we interpret to signify the ongoing occurrence of granulite facies conditions at deeper crustal levels. Pegmatite emplacement in cross-cutting geometries from 1894 to 1891 Ma thus reflects intrusion into a cooler thermal regime at the shallower currently exposed levels, postdating earlier 1896 Ma higher temperature anatexis of Chipman mafic dikes at this depth. High temperature cooling from 1896 Ma to 1894-1891 Ma at the current level of exposure may be due to a degree of unroofing associated with extension during mafic dike emplacement, or initial decay of the thermal event. However, as noted above, the titanite data constrain temperatures ≥ 600-650 °C in portions of the domain through 1882 Ma. Together, these constraints on the evolution of the thermal regime suggest a somewhat protracted (~14 m.y.) metamorphic event following attainment of peak conditions.

Implications for Lithospheric Reactivation and Mantle Dynamics

Correlation of Mafic Magmatism

Our finding of the 1896 Ma timing for intrusion and metamorphism of the Chipman mafic dike swarm documents a major episode of Proterozoic mafic magmatism along the central Snowbird tectonic zone. We suggest that the Chipman dikes can be correlated with mafic dikes for a minimum strike-length of 800 km along the Snowbird zone, establishing the Chipman dikes as a substantial mafic dike swarm of regional significance. The Virgin River dikes are along-strike upper amphibolite facies mafic dikes exposed 400 km southwest of the Chipman dikes, are truncated on their eastern side by the Virgin River shear zone, and have previously been correlated with the Chipman dikes and Legs Lake shear zone (Figure 1) (Card, 2002; Mahan et al., 2003). Further northeast in the Selwyn lozenge, 1.1 GPa, 800 °C granulite facies mafic dikes intrude rocks similar to the Chipman tonalite and are similarly truncated on their eastern side with a thrust sense shear zone considered the continuation of the Legs Lake shear zone (Mahan and Williams, 2005). In addition, the NE striking Kazan dikes 400 km northeast of the East Athabasca region contain remnant garnet and clinopyroxene, have yielded bulk K-Ar dates of 1900 Ma, and intrude a 25-30 km wide zone along the Tulemalu fault zone (Fahrig et al., 1984) that has been correlated with the Virgin River and Legs Lake/Black Lake shear zones (Tella and Eade, 1986). The similar relationships, kinematics, location and apparent timing of mafic dikes and shear zone for 800 km along strike provide strong evidence for a genetic link among these exposures.

Intrusion of the extensive Chipman mafic dike swarm was almost precisely coincident with major mafic magmatism along the northern Snowbird tectonic zone, 600-800 km northeast of the East Lake Athabasca area. The 850 km^2 Kramanituar complex is dominated by granulite facies metagabbro, norite and anorthosite that was intruded at 1902 ±1.6 Ma, with subsequent cooling through the 400-450 °C closure temperature of rutile at ca. 1901 Ma (Sanborn-Barrie et al., 2001). Mafic granulite dikes in the Uvauk mafic complex are inferred to have a similar origin and age as mafic granulites in the Kramanituar complex (Mills et al., 2000). The 2500 km^2 Daly Bay complex is an extensive body of mafic to anorthositic rocks, tonalite and paragneiss with preliminary 1.9 Ga zircon dates (Hanmer and Williams, 2001; Williams personal communication or W. Davis, unpublished data?). In addition, the southern subsurface extension of the Snowbird tectonic zone has been inferred to record the opening and closure of a marginal Proterozoic ocean basin (Ross et al., 1995, 2000). Ocean basin development is tectonically compatible with coeval along-strike mafic magmatism. These data indicate widespread distribution of 1.9 Ga mafic magmatism for > 1200 km of the Snowbird tectonic zone, and potential links to the south that would extend the correlation along the entire 2800 km length of the feature.

Geochemical patterns and isotopic signatures of the Chipman dikes are consistent with derivation from a predominantly depleted mantle source with contribution from a component enriched by subduction related processes. HFSE depletions and LILE enrichments are characteristic of arc magmas, and could reflect crustal contamination by extensive 2.6 Ga plutonic rocks across the region or derivation from lithospheric mantle previously affected by the 2.6 Ga granite generation processes. Chipman dike e_{Nd} values at 1.9 Ga range from –9.1 to +2.2, but exclusion of dikes with higher SiO_2 content that may have been influenced by crustal assimilation yields more restricted values from –2.1 to +2.2. For comparison, ca. 1.83 Ga ultrapotassic rocks of the Christopher Island Formation, intruded across a large area in the northern part of the western Churchill

Province, are characterized by arc-like trace element patterns and e_{Nd} values at 1830 Ma from –10.5 to –6, and have been interpreted to represent derivation from an extensive enriched reservoir isolated since an Archean metasomatic subduction-related event (Cousens et al., 2001). The ca. 2.45 Ga Kaminak dikes, ca. 2.19 Ga Tulemalu dikes, and ca. 2.2 Ga basaltic flows of the western Churchill Province have similarly been inferred to contain a contribution from an enriched component (Cousens et al., 2001; Sandeman et al., 2003). Chipman dike patterns are also compatible with a minor enriched component, although the data do not require contribution from an enriched reservoir isolated since 2.6 Ga.

Asthenospheric Upwelling and Lithospheric Reactivation

In the East Lake Athabasca area, evidence for a prolonged period of lithospheric stability preceding 1.9 Ga activity attests to the significance of the Proterozoic event. Archean deep crustal granulite facies metamorphism at ca. 2.55 Ga has been interpreted in the Chipman, northwestern, and southern domains (Flowers, Chapter 1; Mahan et al., 2005; Baldwin et al., 2004; Williams et al., 2000), with subsequent deep crustal 1.9 Ga metamorphism implying an intervening period of deep crustal residence and lithospheric stability. An episode of Archean metamorphism is entirely consistent with the dehydrated nature of Chipman domain lithologies, and their resistance to melting and deformation, when subjected to high temperatures in the Proterozoic. The disruption of a stable Archean craton at 1.9 Ga demands a fundamentally important lithospheric reactivation event.

The widespread, synchronous 1.9 Ga mafic magmatism along a feature spanning thousands of kilometers of the western Canadian Shield provides a robust basis for interpreting a continental-scale 1.9 Ga episode of asthenospheric upwelling that reflects significant mass and thermal input to the crust. The ca. 1.9 Ga activity along the Snowbird tectonic zone is spatially and temporally bounded by the 1.91-2.02 Ga Taltson-Thelon orogen to the northwest and the 1.81-1.91 Ga Trans-Hudson orogen to the southeast during final amalgamation of the western Canadian Shield. These two major, inward-dipping collision zones would have dramatically impacted the intervening Churchill Province lithosphere. Models to accommodate the observed distribution of mafic magmatism include extension induced by a central zone of asthenospheric upwelling and lithospheric thinning as a convective response to the lateral downgoing slabs, or hinterland transtension due to a strike-slip dominated regime initially driven by Slave collision in a manner analogous to Himalayan hinterland activity. Temporal constraints are consistent with the onset of Proterozoic marginal basin opening along the southern Snowbird zone (Ross et al. 1995, 2000) with subsequent northward propagation of magmatism and tectonic activity at 1896-1900 Ma along the central and northern segments. The initiation of major Tran-Hudson orogenic activity to the east is speculated to have driven a transition to hinterland contraction, induced basin closure and associated development of the 1856-1798 Ma Rimbey magmatic arc along the southern segment of the Snowbird tectonic zone (Ross et al. 1995, 2000), and terminated mafic magmatism and the onset of basin development along the central and northern segments. These events ultimately culminated in the exhumation of deep crustal rocks across the East Lake Athabasca region. It is clear that the assembly of Laurentia constituted a major period of 1.9 Ga lithospheric disruption of the western Churchill Province. Our data suggest that a continent-wide episode of asthenospheric upwelling is an integral component of this history, and must be incorporated into comprehensive models for the unusual history of lithospheric reactivation and exhumation preserved in this region.

CONCLUSIONS

The Chipman domain of the East Lake Athabasca area in northern Saskatchewan preserves a spectacular record of 1.9 Ga deep crustal mafic magmatism, silicic melt generation and segregation during mafic dike intrusion, deformation, and HP granulite facies metamorphism. Data indicate dike anatexis at 1896.2 ± 0.3 Ma during conditions of 1.0-1.2 GPa, $\geq$ 750 °C, with subsequent protracted maintenance of high temperatures for several million years. Little melting of felsic host rocks during intense temperatures at 1.9 Ga is consistent with dehydration of deep crustal rocks during Archean metamorphism that left these rocks resistant to subsequent anatexis and deformation. This explains the cryptic expression of the 1.9 Ga event, and reflects an endmember response of the deep crust to mafic magmatism and high temperature metamorphism. The Chipman dikes in the East Lake Athabasca region can be correlated with similar mafic magmatism spanning thousands of kilometers of the western Canadian Shield, indicating regional asthenospheric upwelling along the Snowbird tectonic zone that must be incorporated into models for the evolution of the western Churchill Province. This intense episode of cratonic lithosphere destabilization differs from the stable nature of most preserved cratons following their initial assembly, and provides a unique perspective on crust-mantle coupling and the evolution of continents.

REFERENCES

Baldwin, J.A., Bowring, S.A., and Williams, M.L., 2003, Petrological and geochronological constraints on high pressure, high temperature metamorphism in the Snowbird tectonic zone, Canada: Journal of Metamorphic Geology, v. 21, p. 1-19.

Baldwin, J.A., Bowring, S.A., Williams, M.L., and Williams, I.S., 2004, Eclogites of the Snowbird tectonic zone: petrological and U-Pb geochronological evidence for Paleoproterozoic high-pressure metamorphism in the western Canadian Shield: Contributions to Mineralogy and Petrology, v. 147, p. 528-548.

Card, C.A., 2002, New investigations of basement to the western Athabasca Basin: in Summary of Investigations 2002, v. 2, Saskatchewan Geological Survey, Sask Industry Resources, Misc. Rep. 2002-4.2 CD-ROM, Paper D-12, 17p.

Corfu, F., Hanchar, J.M., Hoskin, P.W.O., and Kinny, P., 2003, Atlas of zircon textures, in Zircon, Reviews in Mineralogy and Geochemistry 53, edited by J.M. Hanchar and P.W.O. Hoskin, p. 468-500.

Cousens, B.L., Aspler, L.B., Chiarenzelli, J.R., Donaldson, J.A., Sandeman, H., Peterson, T.D.and LeCheminant, A.N., 2001, Enriched Archean lithospheric mantle beneath western Churchill Province tapped during Paleoproterozoic orogenesis: Geology, v. 29, p. 827-830.

Fahrig, W.F., Christie, K.W., Eade, K.E., and Tella, S., 1984, Paleomagnetism of the Tulemalu dykes, Northwest Territories, Canada: Canadian Journal of Earth Sciences, v. 21, p. 544-553.

Goodacre, A.K., Grieve, R.A.F., Halpenny, J.F., and Sharpton, V.L. 1987. Horizontal gradient of the Bouguer gravity anomaly map of Canada, Geological Survey of Canada, 1:10000000.

Hanmer, S., 1994, Geology, East Athabasca mylonite triangle, Saskatchewan, In: Geological Society of Canada Map, 1859A.

Hanmer, S., 1997, Geology of the Striding-Athabasca mylonite zone, northern Saskatchewan and southeastern District of Mackenzie, Northwest Territories: Geological Survey of Canada Bulletin, v. 501, pp.1-92.

Hanmer, S., Williams, M. and Kopf, C., 1995a, Modest movements, spectacular fabrics in an intracontinental deep-crustal strike-slip fault: Striding-Athabasca mylonite zone, NW Canadian Shield: Journal of Structural Geology, v. 17, p.493-507.

Hanmer, S., Williams, M. and Kopf, C., 1995b, Striding-Athabasca mylonite zone: implications for the Archean and Early Proterozoic tectonics of the western Canadian Shield: Canadian Journal of Earth Sciences, v.332, p.178-196.

Hanmer, S. and Williams, M., 2001, Targeted fieldwork in the Daly Bay Complex, Hudson Bay, Nunavut: Geological Survey of Canada, Current Research, 2001-C15.

Hartel, T.H.D. and Pattison, D.R.M., 1996, Genesis of the Kapuskasing (Ontario) migmatitic mafic granulites by dehydration of melting of amphibolite: the importance of quartz to reaction progress: Journal of Metamorphic Geology, v. 14, p. 591-611.

Hoffman, P.F., 1988, United Plates of America, the birth of a craton: Early Proterozoic assembly and growth of Laurentia: Annual Reviews of Earth and Planetary Science Letters, v. 16, p.545-603.

Jaffey, A. H., Flynn, K. F., Glendenin, L. E., Bentley, W. C., and Essling, A. M., 1971, Precision measurements of half-lives and specific activities of ^{235}U and ^{238}U: Physics Review, v. C4, p.1889-1906.

Kopf, C. 1999. Deformation, metamorphism, and magmatism in the East Athabasca mylonite triangle, northern Saskatchewan: Implications for the Archean and Early Proterozoic crustal structure of the Canadian Shield. Ph. D. dissertation thesis, University of Massachusetts-Amherst, p. 139.

Krikorian, L. and Williams, M.L. 2002. Paleoproterozoic high grade metamorphism in the Wholdaia Lake segment of the Snowbird Tectonic Zone, Northwest Territories. Geological Association of Canada-Mineralogical Association of Canada, Saskatoon, Saskatchewan, Program with abstracts, 27: 64.

Krogh, T.E., 1973, A low contamination method for hydrothermal decomposition of zircon and extraction of U and Pb for isotopic age determinations: Geochimica et Cosmochimica Acta, v. 37, p. 485-494.

Krogh, T.E., 1982, Improved accuracy of U-Pb zircon ages by the creation of more concordant systems using an abrasion technique: Geochimica et Cosmochimica Acta, v. 46, p. 637-649.

Lambert, I.B. and Wyllie, P.J., 1974, Melting of tonalite and crystallization of andesite liquid with excess water to 30 kilobars: Journal of Geology, v. 82 (1), p. 88-97.

Lewry, J.F., and Sibbald, T.I.I. 1980. Thermotectonic evolution of the Churchill Province in northern Saskatchewan. Tectonophysics, 68: 5-82.

Ludwig, K. R. (1980) Calculation of uncertainties of U-Pb isotope data: Earth and Planetary Sciences Letters, v. 46, p. 212–220.

MacDonald, R., 1980, New edition of the geological map of Saskatchewan, Precambrian shield area, in Summary of Investigations, pp. 19-21, in Sask. Geol. Surv., Regina.

Mahan, K.H., Williams, M.L., and Baldwin, J.A., 2003, Contractional uplift of deep crustal rocks along the Legs Lake shear zone, western Churchill Province, Canadian Shield: Canadian Journal of Earth Sciences, v. 40, p. 1085-1110.

Mahan, K.H. and Williams, M.L., 2005, Reconstruction of a large deep-crustal exposure: Implications for the Snowbird tectonic zone and early growth of Laurentia: Geology, v.33, p. 385-388.

Mahan, K.H., Flowers, R.M., Williams, M.L., Goncalves, P., Bowring, S.A., and Jercinovic, M.J., 2005, A P-T-time-deformation path for exposed deep continental crust in the Snowbird tectonic zone, western Canadian Shield: GSA Cordilleran Session Meeting abstract, San Jose, CA.

Mattinson, J.M., 2005, Zircon U-Pb chemical abrasion ("CA-TIMS") method: Combined annealing and multi-step partial dissolution analysis for improved precision and accuracy of zircon ages: Chemical Geology, v. 220, p. 47-66.

Mills, A., Berman, R.G., Hanmer, S.K., and Davis, W., 2000, New insights into the tectonometamorphic history of the Uvauk complex, Nunavut: GeoCanada 2000 CD-ROM, Geol. Assoc. Canada, May-June, Abstract 733.

Patino Douce, A.E., 2005, Vapor-absent melting of tonalite at 15-32 kbar: Journal of Petrology, v. 46, p. 275-290.

Patino Douce, A.E. and Beard, J.S., 1995, Dehydration-melting of biotite gneiss and quartz amphibolite from 3 to 15 kbar: Journal of Petrology, v. 36, p. 707-738.

Petford, N. and Gallagher, K., 2001, Partial melting of mafic (amphibolitic) lower crust by periodic influx of basaltic magma: Earth and Planetary Science Letters, v. 193, p. 483-499.

Rapp, R.P., Watson, E.B., and C.F. Miller, 1991, Partial melting of amphibolite/eclogite and the origin of Archean trondhjemites and tonalites: Precambrian Research, v. 51, p. 1-25.

Rapp, R.P. and Watson, E.B., 1995, Dehydration melting of metabasalt at 8-32 kbar: Implications for continental growth and crust-mantle recycling: Journal of Petrology, v. 36, p. 891-931.

Ross, G.M., Eaton, D.W., Boerner, D.E. and Miles, W., 2000, Tectonic entrapment and its role in the evolution of continental lithosphere: An example from the Precambrian of western Canada: Tectonics, v. 19, p.116-134.

Ross, G.M., Milkereit, B., Eaton, D., White, D., Kanasewich, E.R., and Burianyk, M.J.A., 1995, Paleoproterozoic collisional orogen beneath the western Canada sedimentary basin imaged by Lithoprobe crustal seismic reflection data: Geology, v. 23, p. 195-199.

Rushmer, T., 1991, Partial melting of two amphibolites: contrasting experimental results under fluid-absent conditions: Contributions to Mineralogy and Petrology, v. 107, p. 41-59.

Sanborn-Barrie, M., Carr, S.D., and Theriault, R., 2001, Geochronological constraints on metamorphism, magmatism and exhumation of deep-crustal rocks of the Kramanituar Complex, with implications for the Paleoproterozoic evolution of the Archean western Churchill Province, Canada: Contributions to Mineralogy and Petrology, v. 141, p. 592-612.

Sandeman, H., Cousens, B., and Hemmingway, D., 2003, Continental tholeiitic mafic rocksof the Paleoproterozoic Hurwitz Geoup, Central Hearne sub-domain Nunavut: insight into the evolution of the Hearne sub-continental lithosphere: Canadian Journal of Earth Sciences, v. 40, p. 1219-1237.

Schmidt, M.W., 1993, Phase-relations and compositions in tonalite as a function of pressure an experimental study at 650 °C: American Journal of Science, v. 293, p. 1011-1060.

Skjerlie, K.P. and Johnston, A.D., 1996, Vapour-absent melting from 10 to 20 kbar of crustal rocks that contrain multiple hydrous phases: Implications for anatexis in the deep to very deep continental crus and active continental margins: Journal of Petrology, v. 37 (3), p. 661-691.

Skjerlie, K.P. and Johnston, A.D., 1993, Fluid absent melting of a layered crustal protolith – Implications for the generation of anatectic granites: Contributions to Mineralogy and Petrology, v. 114 (3), p. 365-378.

Snoeyenbos, D.R., Williams, M.L. and Hanmer, S., 1995, Archean high-pressure metamorphism in the western Canadian Shield: European Journal of Mineralogy, v. 7, p.1251-1272.

Springer, W. and Seck, H.A., 1997, Partial fusion of basic granulites at 5 to 15 kbar: implications for the origin of TTG magmas: Contributions to Mineralogy and Petrology, v. 127, p. 30-45.

Stacey, J.C. and Kramers, J.D., 1975, Approximation of terrestrial lead isotope evolution by a two-stage model: Earth and Planetary Science Letters, v.26, p.207-221.

Sun, S.S. and McDonough, W.F., 1989, Chemical and isotopic systematics of oceanic basalts: implications for mantle composition and processes, In: Saunders, A.D., Norry, M.J.(eds), Magmatism in oceani basins. Geol Soc Spec Publ, p. 313-345.

Tella, S., and Eade, K.E., 1986, Occurrence and possible tectonic significance of high-pressure granulite fragments in the Tulemalu fault zone, District of Keewatin, N.W.T., Canada: Canadian Journal of Earth Sciences, v. 23, p. 1950-1962.

Vavra, G., Schmid, R., and Gebauer, D., 1999, Internal morphology, habit and U-Th-Pb microanalysis of amphibolite-to-granulite facies zircons: geochronology of the Ivrea Zone (Southern Alps): Contributions to Mineralogy and Petrology, v. 134, p. 380-404.

Williams, M.L., Hanmer, S., Kopf, C. and Darrach,M., 1995, Syntectonic generation and segregation of tonalitic melts from amphibolite dikes in the lower crust, Striding-Athabasca mylonite zone, northern Saskatchewan: Journal of Geophysical Research, v.100(B8), p.15,717-15,734.

Williams, M.L., Mellis, E.A., Kopf,C. and Hanmer,S., 2000, Microstructural Tectonometamorphic processes and the development of gneissic layering: a mechanism for metamorphic segregation: Journal of Metamorphic Geology, v. 18, p.41-57.

Wolf, M.B. and Wyllie, P.J., 1993, Garnet growth during amphibolite anatexis: Implications of a garnetiferous restite: The Journal of Geology,, v. 101, p. 357-373.

Wolf, M.B. and Wyllie, P.J., 1994, Dehydration-melting of amphibolite at 10 kbar: the effects of temperature and time: Contributions to Mineralogy and Petrology, v. 115, p. 369-383.

Wolf, M.B. and Wyllie, P.J., 1995, Liquid segregation parameters from amphibolite dehydration melting experiments: Journal of Geophysical Research, v. 100, p. 15,611-15,621.

FIGURE CAPTIONS

Figure 1. Geological map of the western Canadian Shield showing major tectonic features. AB-Athabasca basin, BL-Baker Lake basin, DX- Daly Bay Complex, KX-Kramanituar Complex, STZ-Snowbird tectonic zone, TB-Thelon Basin, TFZ-Tulemalu Fault Zone, THO-Trans-Hudson Orogen, TO-Taltson Orogen, TMZ-Thelon Magmatic Zone, UX-Uvauk Complex, VR-Virgin River shear zone. The rectangle shows the East Lake Athabasca region enlarged in Figure 2.

Figure 2. Geological map of the East Lake Athabasca region, northern Saskatchewan. The box outline shows the location of the study area enlarged in Figure 3.

Figure 3. Geological map of the Chipman domain with sample locations.

Figure 4. Example Chipman mafic dike relationships and textures. A) Large cm-scale garnets with associated leucosome tails. B) Leucocratic segregation, 3-12 cm wide. C) Several cm wide Grt+Cpx clumps in a Hb+Pl matrix. D) Boudins of a migmatitic granulite dike. E) Granulite dike, ~1 m wide, discordantly cutting heterogeneous Chipman gneisses. F) Pegmatite intruding mafic dike. G) Inferred 1.9 Ga melt in Fehr granite.

Figure 5. Major and trace element compositions of Chipman mafic dikes. A) Plots of MgO (weight %) vs. Al_2O_3 (weight %), SiO_2 (weight %), and Ta (ppm). B) Spider diagram for Chipman mafic dike samples. C) REE diagram for Chipman mafic dike samples. Chrondrite values for both spider and REE diagrams from Sun and McDonough (1989).

Figure 6. A) Nd isotope evolution diagram for Chipman mafic dike samples corrected to 1.9 Ga. B) Plot of ε_{Nd} at 1.9 Ga vs. SiO_2 for Chipman mafic dikes. The inverse correlation between ε_{Nd} and SiO_2 for dikes with higher SiO_2 content suggests the influence of crustal assimilation on this subset of dikes. C) Nd isotope evolution diagram for Chipman mafic dikes corrected to 1.9 Ga, for pegmatite dikes corrected to 1.9 Ga, for

mafic granulite gneisses corrected to 2.6 Ga, and for Chipman tonalitic gneisses corrected to 3.0 Ga. D) Plot of ε_{Nd} at 2.6 Ga vs. SiO_2 for mafic granulite gneisses.

Figure 7. A) Mg map of thin section from SZ00-196C. Brighter colors represent higher Mg concentrations. Yellow is primarily hornblende, red is garnet, and black is quartz and feldspar. Blue circles represent locations of zircon grains. B) Backscatter image showing petrographic setting of zircon associated with titanite and hornblende. Insets are CL images of zircon grains with scale bars of 20 microns. C) Backscatter image showing petrographic setting of zircon grains included in hornblende. Insets are CL images of zircon grains with scale bars of 10 microns. D) CL images of larger zircon crystals that were physically separated from this sample.

Figure 8. A) CL images of 03-52 zircon grains that were subsequently analyzed. Lines delineate where the zircon were broken into fragments prior to analysis. B) and C) are BE images of example 01-SZ76 and SZ00-196A zircon, respectively. D) CL images of 02-76B zircon that were subsequently analyzed. Again, lines delineate where the grains were broken into fragments.

Figure 9. Concordia diagrams for migmatitic dikes.

Figure 10. Concordia diagrams for pegmatitic dikes and segregations.

Table 1 Major and trace element data for Chipman mafic dikes

	Granulite dikes with leucosomes			Granulite dikes with no leucosomes					
Sample	02-125	02-58	99B-15	02-112	SZ00-182A	SZ00-182B	SZ00-196D	02-171C	SZ00-201A
Lake	Steinhauer	Chipman	Steinhauer	Steinhauer	Chipman	Chipman	Woolhether	Pellerin	Chipman
SiO2	52.21	51.13	51.71	50.96	51.31	50.52	50.55	53.06	50.93
Al2O3	11.97	11.49	12.65	13.86	13.23	15.54	13.58	13.14	14.71
Fe2O3	17.46	19.46	16.18	13.48	16.15	13.27	15.71	15.54	14.48
MnO	0.21	0.26	0.27	0.22	0.23	0.19	0.23	0.23	0.20
MgO	4.36	3.26	4.89	7.10	5.34	6.04	6.03	5.22	5.59
CaO	9.04	7.77	8.92	11.45	9.57	10.46	10.35	9.27	9.31
Na2O	1.53	2.21	1.88	1.90	2.12	2.07	2.21	2.25	3.00
K2O	1.12	1.13	1.02	0.09	0.73	0.70	0.43	0.54	0.64
TiO2	1.92	2.50	1.78	0.72	1.53	1.22	1.45	1.18	1.17
P2O5	0.18	0.30	0.17	0.05	0.20	0.15	0.14	0.11	0.11
LOI	0.24	0.22	0.62	-0.36	-0.17	-0.14	-0.36	-0.15	-0.15
Total	100.23	99.73	100.06	99.47	100.24	100.03	100.34	100.38	99.99
V	397.89	278.39	321.52	269.74	344.15	278.84	298.92	301.62	250.83
Cr	23.58	-20.00	46.28	119.29	90.02	157.72	112.94	43.46	26.23
Co	51.36	49.46	48.51	51.11	40.73	46.01	52.36	47.11	56.16
Ni	45.56	29.35	50.14	78.64	55.91	88.05	62.02	39.24	63.60
Cu	135.99	74.83	90.39	157.60	94.72	105.39	138.06	55.67	190.97
Zn	136.96	150.42	107.44	85.63	78.71	95.70	109.39	102.64	67.01
Ga	20.66	19.96	18.28	15.32	16.53	16.47	18.80	16.87	20.23
Ge	1.85	1.72	1.72	1.69	1.02	1.47	1.66	1.55	1.06
As	0.00	11.61	0.00	0.00	0.00	0.00	0.00	0.00	0.00
Rb	14.60	31.46	15.91	3.02	16.42	19.53	8.49	14.02	18.00
Sr	89.34	135.57	202.62	70.45	150.35	169.51	179.65	159.63	262.03
Y	34.79	44.91	24.56	19.19	30.29	24.32	22.15	22.77	21.70
Zr	164.88	210.95	115.33	37.83	123.22	101.96	89.54	85.29	74.04
Nb	11.11	13.04	13.77	4.89	6.86	5.98	6.31	5.28	3.82
Cs	0.00	0.00	1.26	0.00	0.00	0.87	0.00	0.00	0.91
Ba	142.44	286.71	168.70	24.64	231.19	224.81	136.46	176.21	219.16
La	15.94	27.00	17.77	2.20	17.38	13.25	9.96	11.02	10.08
Ce	37.46	59.35	37.10	5.02	36.68	27.81	22.42	23.45	20.77
Pr	5.39	7.89	5.07	0.79	4.74	3.79	3.20	3.30	2.77
Nd	24.10	34.37	21.77	4.04	21.25	16.72	14.64	13.95	12.17
Sm	6.21	8.53	5.21	1.53	5.27	4.18	3.95	3.64	3.26
Eu	1.89	2.36	1.66	0.66	1.62	1.32	1.32	1.19	1.22
Gd	6.12	8.24	4.88	2.31	5.87	4.29	4.08	3.75	3.53
Tb	1.13	1.45	0.84	0.50	1.02	0.76	0.73	0.70	0.64
Dy	6.81	8.60	4.88	3.43	5.96	4.71	4.43	4.38	4.11
Ho	1.32	1.71	0.97	0.75	1.21	0.95	0.87	0.92	0.84
Er	3.64	4.79	2.65	2.22	3.39	2.64	2.37	2.56	2.38
Tm	0.54	0.69	0.39	0.34	0.51	0.39	0.35	0.39	0.36
Yb	3.60	4.59	2.66	2.26	3.43	2.61	2.32	2.68	2.37
Lu	0.52	0.68	0.40	0.34	0.51	0.39	0.35	0.40	0.36
Hf	4.91	6.14	3.53	1.24	3.72	2.95	2.67	2.71	2.35
Ta	0.81	1.07	1.08	0.00	0.42	0.32	0.37	0.25	0.20
W	2.44	0.00	0.00	0.00	1.68	0.00	0.00	0.00	0.00
Tl	0.14	0.20	0.15	0.00	0.00	0.11	0.00	0.11	0.00
Pb	0.00	8.22	0.00	0.00	0.00	0.00	0.00	0.00	0.00
Th	4.57	5.27	2.31	0.28	1.64	1.37	1.02	1.52	1.21
U	1.85	2.68	0.55	0.12	0.38	1.40	0.63	0.84	7.12
Recalculation of composition of protolith (Grove et al., 1992)									
Qtz	0.167	0.144	0.142	0.099	0.113	0.085	0.087	0.139	0.055
Plag	0.390	0.416	0.430	0.490	0.465	0.525	0.488	0.469	0.550
Oliv	0.170	0.173	0.172	0.175	0.177	0.169	0.178	0.172	0.171
Cpx	0.171	0.152	0.162	0.219	0.174	0.158	0.197	0.168	0.165
Or	0.071	0.073	0.065	0.006	0.046	0.044	0.027	0.034	0.040
Sp	0.027	0.036	0.025	0.010	0.021	0.017	0.020	0.016	0.016
Ap	0.004	0.006	0.004	0.001	0.004	0.003	0.003	0.002	0.002
Ternary Normalization									
Cpx	0.23	0.21	0.21	0.25	0.21	0.19	0.23	0.21	0.19
Pl	0.53	0.56	0.56	0.55	0.57	0.62	0.57	0.58	0.62
Ol	0.23	0.23	0.23	0.20	0.22	0.20	0.21	0.21	0.19

Table 1 (continued)

	Granulite dikes with possible leucosomes		Hbl-pl dikes			Phyric or phenocrystic plagioclase rich dikes	
Sample:	O2-171B	SZ00-186A	01M123C	O2-120B	O2-123B	SZ00-200A	O2-172
Lake:	Pellerin	Chipman	Balliet	Bompas	Steinhauer	Chipman	Pellerin
SiO2	52.22	49.90	50.55	46.09	48.27	49.60	47.93
Al2O3	13.07	13.32	13.15	13.26	13.12	17.30	21.83
Fe2O3	15.58	16.86	15.48	18.87	16.58	9.95	5.68
MnO	0.23	0.25	0.23	0.27	0.23	0.16	0.11
MgO	5.16	5.72	5.84	5.56	5.38	7.10	5.69
CaO	9.04	9.90	9.71	9.48	9.61	11.76	14.45
Na2O	2.25	2.34	2.30	2.28	2.46	2.11	1.65
K2O	0.71	0.24	0.63	0.93	1.31	0.57	0.67
TiO2	1.12	1.40	1.36	2.36	1.82	0.58	0.29
P2O5	0.11	0.11	0.12	0.20	0.17	0.04	0.03
LOI	0.44	-0.33	0.62	0.51	0.82	1.18	1.67
Total	99.94	99.71	100.00	99.83	99.76	100.35	99.99
V	302.59	314.15	323.54	430.61	346.60	186.94	113.39
Cr	63.67	24.08	64.93	94.82	107.04	213.77	233.19
Co	34.40	50.93	55.97	49.00	45.94	43.01	26.46
Ni	35.46	46.45	49.36	63.95	72.04	89.39	71.83
Cu	63.61	147.20	101.04	70.36	176.06	90.56	23.74
Zn	69.69	96.17	101.83	127.67	111.76	63.35	44.77
Ga	15.60	17.13	17.34	21.15	18.40	13.98	12.53
Ge	0.00	1.62	1.42	1.59	1.25	1.07	1.21
As	0.00	0.00	0.00	0.00	0.00	0.00	0.00
Rb	15.30	2.78	15.64	16.74	29.77	15.87	16.70
Sr	153.44	84.54	184.11	134.71	114.72	181.63	271.98
Y	20.98	31.34	22.22	39.16	33.40	11.29	5.70
Zr	74.82	84.03	88.52	139.73	114.98	34.99	20.47
Nb	4.44	5.71	8.95	8.83	7.54	3.19	2.53
Cs	0.00	0.00	0.00	0.00	0.68	2.32	2.21
Ba	158.18	27.10	118.89	181.40	159.59	86.52	83.72
La	8.36	6.49	11.11	10.51	12.59	3.14	2.13
Ce	19.80	15.32	21.89	26.85	23.38	6.80	4.32
Pr	2.64	2.33	3.00	4.12	3.62	1.00	0.58
Nd	12.14	11.11	13.53	19.22	16.83	4.80	2.59
Sm	3.22	3.56	3.55	5.80	4.89	1.39	0.77
Eu	1.10	1.21	1.17	1.94	1.59	0.58	0.36
Gd	3.86	4.24	3.89	6.36	5.58	1.68	0.85
Tb	0.67	0.86	0.71	1.22	1.03	0.33	0.17
Dy	4.08	5.82	4.01	7.41	6.57	2.08	1.07
Ho	0.85	1.24	0.80	1.50	1.34	0.42	0.22
Er	2.42	3.57	2.22	4.26	3.84	1.20	0.63
Tm	0.37	0.55	0.35	0.65	0.58	0.19	0.10
Yb	2.59	3.66	2.22	4.30	3.87	1.27	0.63
Lu	0.39	0.55	0.32	0.65	0.57	0.19	0.10
Hf	2.40	2.59	2.53	4.30	3.62	1.06	0.66
Ta	0.25	0.32	0.32	0.51	0.42	0.00	0.00
W	0.00	0.00	0.00	0.00	0.00	0.00	0.00
Tl	0.00	0.00	0.00	0.00	0.20	0.00	0.14
Pb	0.00	0.00	0.00	0.00	5.28	0.00	5.47
Th	1.27	0.70	1.29	1.22	0.98	0.40	0.38
U	0.32	0.17	0.30	3.67	0.32	1.13	0.17
Recalculation of composition of protolith (Grove et al., 1992)							
Qtz	0.128	0.086	0.026	0.021	0.026	0.044	0.011
Plag	0.468	0.498	0.473	0.487	0.473	0.580	0.680
Oliv	0.175	0.189	0.173	0.204	0.173	0.157	0.096
Cpx	0.166	0.189	0.212	0.188	0.212	0.174	0.167
Or	0.045	0.015	0.085	0.061	0.085	0.036	0.041
Sp	0.016	0.020	0.026	0.034	0.026	0.008	0.004
Ap	0.002	0.002	0.004	0.004	0.004	0.001	0.001
Ternary Normalization							
Cpx	0.21	0.22	0.23	0.21	0.25	0.19	0.18
Pl	0.58	0.57	0.56	0.55	0.55	0.64	0.72
Ol	0.22	0.22	0.21	0.23	0.20	0.17	0.10

Table 2. Sm-Nd isotopic data for Chipman mafic dikes

Sample	[Sm][1]	[Nd][1]	^{147}Sm/^{144}Nd[2]	^{143}Nd/^{144}Nd[3]	ε_{Nd}	$\varepsilon_{Nd(initial)}$[4]	t_{CHUR}[5]	t_{DM}[6]
Chipman mafic dikes, 1.9 Ga								
Granulite dikes with leucosomes								
02-125	5.65	21.02	0.1624	0.511840 ± 3	-15.56	-7.23	3.56	3.73
02-58	8.19	33.11	0.1495	0.511843 ± 3	-15.51	-4.02	2.58	2.89
99B-15	4.98	20.65	0.1459	0.511812 + 3	-16.11	-3.75	2.49	2.80
Granulite dikes with no leucosomes								
02-112	1.45	3.79	0.2315	0.513183 ± 4	10.64	2.16	2.39	0.27
SZ00-182A	4.91	20.26	0.14644	0.511915 ± 4	-14.11	-1.86	2.20	2.58
SZ00-182B	3.76	15.89	0.1430	0.511863 ± 4	-15.13	-2.04	2.21	2.56
SZ00-196D	3.77	14.59	0.1561	0.512051 ± 3	-11.45	-1.55	2.21	2.65
02-171C	3.41	13.07	0.1580	0.511737 ± 3	-17.57	-8.17	3.56	3.72
SZ00-201A	2.95	10.81	0.1648	0.511776 ± 3	-16.82	-9.08	4.13	4.20
Granulite dikes with possible leucosomes								
02-171B	3.02	11.19	0.1629	0.511881 ± 3	-14.77	-6.55	3.42	3.63
SZ00-186A	3.38	10.83	0.1889	0.512477 ±2	-3.15	-1.24	3.14	3.82
Amphibolite dikes								
01M123C	3.59	14.05	0.1544	0.512032 ± 3	-11.81	-1.50	2.19	2.62
02-120B	5.75	19.51	0.1782	0.512368 ± 3	-5.27	-0.76	2.23	2.98
02-123B	4.49	16.14	0.1681	0.512322 ± 2	-6.16	0.83	1.69	2.42
Phenocrystic or phyric plagioclase rich dikes								
SZ00-200A	1.38	4.72	0.1764	0.512349 ± 7	-5.64	-0.70	2.18	2.91
02-172	0.68	2.50	0.1637	0.512116 ± 5	-10.18	-2.14	2.42	2.87
Pegmatites, 1.9 Ga								
02-76B	2.11	21.8	0.05842	0.510226 ± 3	-47.05	-13.39	2.67	2.78
02-77B	1.03	5.56	0.11185	0.510210 ± 4	-27.85	-7.19	2.57	2.77
03-126	0.09	0.38	0.14129	0.511795 ± 33	-16.45	-2.95	2.33	2.65
Chipman tonalite, 3.0 Ga								
SZ00-186C	4.24	29.31	0.08739	0.510297 ± 3	-45.66	-3.44	3.27	3.36
SZ00-193A	3.95	20.18	0.11833	0.510843 ± 4	-35.02	-4.77	3.50	3.59
SZ00-205A	9.02	54.11	0.10082	0.510622 ± 3	-39.33	-2.29	3.21	3.32
SZ00-208B	7.71	46.73	0.09973	0.510607 ± 8	-39.62	-2.16	3.20	3.31
Mafic (Grt+Cpx+Opx+Pl) granulites, 2.6 Ga								
BF03-6B	2.95	11.89	0.14988	0.511770 ± 3	-16.94	-1.28	2.84	3.10
BF03-88A	2.54	7.94	0.19324	0.512592 ± 3	-0.90	0.69	2.03	3.75
BF03-159A	1.64	6.63	0.14912	0.511451 ± 4	-23.16	-7.29	3.82	3.91
BF03-168E	2.53	11.67	0.13096	0.511410 ± 3	-23.96	-1.98	2.86	3.05
BF03-228A	0.94	2.36	0.24094	0.513535 ± 4	17.5	2.72	3.10	2.70
Mafic (Opx+Pl) granulites, 2.6 Ga								
BF03-92B	3.6	14.78	0.14724	0.511538 ± 3	-21.45	-4.94	3.40	3.55
BF03-125A	0.91	3.68	0.15009	0.511823 ± 4	-15.9	-0.31	2.67	2.97
BF03-158A	1.54	6.57	0.14202	0.511383 ± 5	-24.48	-6.23	3.51	3.63
BF03-189A	2.04	7.97	0.1545	0.511724 ± 3	-17.84	-3.74	3.31	3.51
BF03-217A	3.04	14.06	0.13093	0.511480 ± 4	-22.6	-0.6	2.69	2.91

[1] Concentrations in ppm, as determined by isotope dilution

[2] Sm and Nd were fractionation corrected with an exponental law, normalizing to ^{152}Sm/^{147}Sm = 1.783 and ^{146}Nd/^{144}Nd = 0.7219, respectively. Internal errors in measured ^{147}Sm/^{144}Nd are <0.1% (2s s.d.)

[3] Measured ^{143}Nd/^{144}Nd with internal error (2σ s.e.)

[4] Initial εNd calculated at 1.9 Ga for Chipman dikes and pegmatites, at 3.0 Ga for Chipman tonalite, and at 2.6 Ga for mafic granulite gneisses

[5] t_{CHUR} (Ga) calculated with $(^{147}\text{Sm}/^{144}\text{Nd})_{CHUR} = 0.1967$ and $(^{143}\text{Nd}/^{144}\text{Nd}) = 0.512638$

[6] t_{DM} (Ga) = $(1/\lambda_{147})*\ln[((^{143}\text{Nd}/^{144}\text{Nd})_{sample} - (^{143}\text{Nd}/_{144}\text{Nd})_{DM}/((^{147}\text{Sm}/^{144}\text{Nd})_{sample} - (^{147}\text{Sm}/^{144}\text{Nd})_{DM})) + 1]$;
present day $(^{143}\text{Nd}/^{144}\text{Nd})_{DM} = 0.513151$, $(^{147}\text{Sm}/^{144}\text{Nd})_{DM} = 0.2137$

Table 3. U-Pb TIMS isotopic data for zircon

		Compositions						Isotopic Ratios								Dates (Ma)					
Fr	#[a]	Wt (μg)[b]	U (ppm)	Pb (ppm)	Th[c]/U	Pb*[d]/Pbc	Pbc[d] (pg)	^{206}Pb[e]/^{204}Pb	^{208}Pb[f]/^{206}Pb	^{206}Pb[f]/^{238}U	% err[g]	^{207}Pb[f]/^{235}U	% err[g]	^{207}Pb[f]/^{206}Pb	% err[g]	^{206}Pb[h]/^{238}U	^{207}Pb[h]/^{235}U	^{207}Pb[h]/^{206}Pb	±	corr. coef.	% disc.
SZ00-196C migmatitic dike																					
z1	1	18.7	11.2	3.7	0.02	26.3	2.6	1773.4	0.005	0.341950	(.13)	5.4736	(.15)	0.11609	(.08)	1896.0	1896.5	**1896.9**	1.4	0.867	0.1
z7	1	5.5	25.4	8.4	0.01	11.3	4.1	761.4	0.004	0.340374	(.58)	5.4417	(.59)	0.11595	(.11)	1888.5	1891.4	**1894.7**	2.0	0.981	0.4
z8	1	1.9	10.4	3.6	0.03	8.1	7.9	520.1	0.008	0.335973	(.66)	5.3788	(.67)	0.11611	(.09)	1867.3	1881.5	**1897.2**	1.7	0.990	1.8
z10	1	3.8	9.9	3.4	0.02	3.4	3.7	242.5	0.004	0.345060	(2.05)	5.5226	(2.08)	0.11608	(.25)	1911.0	1904.1	**1896.7**	4.5	0.993	-0.9
z11	2	5.5	19.6	6.8	0.03	6.7	5.3	444.9	0.009	0.342562	(.72)	5.4856	(.78)	0.11614	(.28)	1899.0	1898.3	**1897.6**	5.0	0.934	-0.1
z13	1	8.0	34.8	11.5	0.02	47.0	1.9	3157.5	0.005	0.341519	(.09)	5.4663	(.12)	0.11608	(.07)	1894.0	1895.3	**1896.8**	1.3	0.795	0.2
z14	1	2.0	17.7	5.8	0.02	13.3	0.9	904.3	0.004	0.342571	(.25)	5.4877	(.32)	0.11618	(.20)	1899.0	1898.7	**1898.3**	3.6	0.778	0.0
02-58, migmatitic dike																					
z2	1	0.8	96.1	32.4	0.10	53.8	0.5	3530.3	0.029	0.341698	(.10)	5.4662	(.13)	0.11602	(.08)	1894.8	1895.3	**1895.8**	1.4	0.809	0.1
z3	1	1.0	117.9	39.3	0.07	103.3	0.4	6826.2	0.019	0.341434	(.09)	5.4610	(.12)	0.11600	(.07)	1893.6	1894.5	**1895.5**	1.2	0.820	0.1
z6	1	2.3	208.7	69.7	0.06	73.3	2.1	4576.7	0.016	0.340854	(.09)	5.4518	(.13)	0.11600	(.08)	1890.8	1893.0	**1895.5**	1.5	0.743	0.3
z7	1	1.9	129.6	43.2	0.07	107.5	0.8	7095.0	0.021	0.341274	(.07)	5.4592	(.09)	0.11602	(.05)	1892.8	1894.2	**1895.8**	1.0	0.785	0.2
z8	1	1.1	188.2	62.7	0.06	60.8	1.1	3980.1	0.018	0.341268	(.12)	5.4591	(.13)	0.11602	(.05)	1892.8	1894.2	**1895.7**	0.9	0.918	0.2
z9	1	1.1	123.7	41.6	0.09	43.4	1.1	2843.4	0.027	0.342011	(.19)	5.4713	(.20)	0.11602	(.06)	1896.3	1896.1	**1895.8**	1.1	0.956	0.0
z10	1	1.1	203.3	67.6	0.05	75.3	1.0	4999.3	0.016	0.341736	(.06)	5.4720	(.08)	0.11613	(.05)	1895.0	1896.2	**1897.5**	1.0	0.765	0.2
02-88, migmatitic dike																					
z1	1	6.4	52.5	17.8	0.02	24.4	4.5	1509.1	0.005	0.340300	(.15)	5.4474	(.23)	0.11610	(.17)	1888.1	1892.4	**1897.0**	3.1	0.668	0.5
z4	1	7.0	61.2	20.1	0.02	44.4	3.2	2984.0	0.005	0.340722	(.09)	5.4472	(.11)	0.11595	(.06)	1890.1	1892.3	**1894.7**	1.1	0.814	0.3
z6	1	3.4	57.7	19.6	0.01	11.7	5.5	769.3	0.004	0.341555	(.40)	5.4658	(.41)	0.11606	(.10)	1894.1	1895.2	**1896.4**	1.8	0.971	0.1
z10	1	1.0	190.9	65.4	0.02	10.8	6.1	704.3	0.005	0.341870	(.41)	5.4702	(.43)	0.11605	(.11)	1895.7	1895.9	**1896.2**	1.9	0.969	0.0
z11	1	0.4	320.6	106.1	0.05	22.2	2.0	1489.4	0.013	0.340360	(.21)	5.4467	(.23)	0.11606	(.10)	1888.4	1892.2	**1896.4**	1.8	0.909	0.5
z12	1	3.9	36.8	13.1	0.05	6.7	7.1	438.6	0.014	0.341306	(.56)	5.4603	(.70)	0.11603	(.39)	1893.0	1894.4	**1895.9**	6.9	0.837	0.2
z13	1	3.8	51.3	17.0	0.02	15.0	4.3	1001.0	0.005	0.339851	(.41)	5.4344	(.42)	0.11597	(.07)	1886.0	1890.3	**1895.1**	1.3	0.984	0.6
z15	1	1.3	85.7	28.6	0.08	39.0	1.0	2578.7	0.024	0.340492	(.10)	5.4285	(.12)	0.11563	(.07)	1889.0	1889.4	**1889.7**	1.3	0.810	0.0
02-97, migmatitic dike																					
z1	1	22.0	34.9	11.6	0.01	73.8	3.4	4572.3	0.003	0.341661	(.06)	5.4708	(.08)	0.11613	(.04)	1898.0	1897.3	**1896.6**	0.8	0.804	0.2
z2	1	9.6	13.8	4.5	0.01	61.3	0.7	4116.7	0.004	0.341501	(.09)	5.4645	(.11)	0.11605	(.06)	1896.4	1896.3	**1896.2**	1.1	0.819	0.1
z3	1	6.0	42.1	14.0	0.01	38.4	2.2	2434.3	0.003	0.342030	(.10)	5.4727	(.12)	0.11605	(.06)	1894.7	1896.0	**1897.5**	1.2	0.847	0.0
z4	1	6.0	33.7	11.6	0.02	17.6	3.8	1097.8	0.004	0.342357	(.12)	5.4790	(.14)	0.11607	(.06)	1893.9	1895.0	**1896.3**	1.2	0.889	-0.1

Table 3. (continued)

		Compositions						Isotopic Ratios								Dates (Ma)					
Fr	#[a]	Wt (mg)[b]	U (ppm)	Pb (ppm)	Th/U[c]	Pb*/Pbc[d]	Pbc[d] (pg)	^{206}Pb/^{204}Pb[e]	^{208}Pb/^{206}Pb[f]	^{206}Pb/^{238}U[f]	% err[g]	^{207}Pb/^{235}U[f]	% err[g]	^{207}Pb/^{206}Pb[f]	% err[g]	^{206}Pb/^{238}U[h]	^{207}Pb/^{235}U[h]	^{207}Pb/^{206}Pb[h]	±	corr. coef.	% disc.
03-52, migmatitic dike																					
z3	1	2.9	39.8	13.6	0.02	24.9	5.2	1533.2	0.007	0.342213	(.09)	5.4850	(.11)	0.11625	(.06)	1897.3	1898.2	**1899.3**	2.6	0.856	0.1
z4	1	9.8	42.8	14.9	0.06	20.2	3.5	1248.4	0.016	0.344244	(.18)	5.5571	(.20)	0.11708	(.09)	1907.1	1909.5	**1912.1**	1.0	0.891	0.3
z6a	1	5.0	36.6	12.2	0.05	95.1	1.1	6240.2	0.013	0.342117	(.19)	5.4740	(.20)	0.11605	(.06)	1896.8	1896.5	**1896.2**	1.7	0.956	0.0
z6b	1	8.8	62.8	21.7	0.04	17.9	4.7	1104.1	0.010	0.341996	(.12)	5.4731	(.18)	0.11607	(.14)	1896.3	1896.4	**1896.5**	1.1	0.662	0.0
z8	1	4.0	25.9	8.7	0.06	41.3	1.1	2712.8	0.019	0.342698	(.30)	5.5099	(.31)	0.11661	(.07)	1899.6	1902.1	**1904.9**	2.5	0.978	0.3
z9a	1	5.3	42.8	14.8	0.09	25.5	1.7	1609.5	0.025	0.345985	(.19)	5.6121	(.20)	0.11764	(.07)	1915.4	1918.0	**1920.7**	2.5	0.935	0.3
z9b	1	3.0	45.3	15.1	0.03	34.3	1.3	2242.5	0.007	0.341960	(.18)	5.4713	(.20)	0.11604	(.06)	1896.1	1896.1	**1896.1**	7.0	0.947	0.0
z11a	1	3.0	34.9	11.7	0.03	23.6	0.9	1583.6	0.009	0.345820	(.18)	5.6134	(.21)	0.11773	(.11)	1914.6	1918.2	**1922.0**	1.1	0.861	0.4
z11b	1	1.8	49.5	16.7	0.02	13.7	1.6	892.9	0.005	0.342122	(.39)	5.4747	(.41)	0.11606	(.12)	1896.9	1896.6	**1896.4**	2.4	0.955	0.0
z12a	1	1.3	51.7	17.0	0.02	77.0	0.7	5157.7	0.005	0.341983	(.09)	5.4723	(.11)	0.11606	(.06)	1896.2	1896.3	**1896.3**	2.2	0.847	0.0
z13a	1	3.0	47.3	17.2	0.36	34.7	1.9	2031.1	0.106	0.342147	(.15)	5.4943	(.17)	0.11647	(.07)	1897.0	1899.7	**1902.7**	1.0	0.902	0.3
z13b	1	3.8	49.7	17.1	0.03	13.0	2.0	837.1	0.008	0.342391	(.36)	5.4870	(.38)	0.11623	(.10)	1898.2	1898.6	**1899.0**	1.3	0.961	0.1
z14	1	1.6	84.1	27.7	0.02	89.8	1.0	6006.7	0.007	0.341615	(.17)	5.4671	(.19)	0.11607	(.08)	1894.4	1895.4	**1896.5**	1.8	0.901	0.1
z15a	1	3.1	59.9	20.4	0.05	48.1	0.8	3193.2	0.014	0.348839	(.10)	5.7599	(.12)	0.11975	(.06)	1929.1	1940.4	**1952.5**	1.5	0.850	1.4
z15b	1	2.0	51.0	17.8	0.07	61.8	0.5	4061.4	0.020	0.355573	(.17)	6.0825	(.20)	0.12407	(.10)	1961.2	1987.7	**2015.5**	1.1	0.859	3.1
z16a	1	1.7	26.8	8.8	0.02	63.8	0.4	4272.7	0.006	0.341538	(.23)	5.4730	(.25)	0.11622	(.09)	1894.1	1896.4	**1898.9**	1.8	0.925	0.3
02-76B, pegmatitic dike																					
z1	1	22.0	48.6	17.3	0.34	265.8	1.4	15829.8	0.098	0.340802	(.12)	5.4457	(.14)	0.11589	(.07)	1890.5	1892.1	**1893.8**	1.2	0.873	0.2
z2a	1	1.8	61.9	22.4	0.40	37.1	1.1	2252.9	0.116	0.339989	(.23)	5.4157	(.25)	0.11553	(.10)	1886.6	1887.3	**1888.1**	1.7	0.927	0.1
z3a	1	6.0	249.6	86.6	0.25	512.1	1.0	32246.6	0.071	0.339825	(.06)	5.4197	(.07)	0.11567	(.04)	1885.8	1888.0	**1890.3**	0.8	0.787	0.3
z3b	1	8.3	207.8	72.1	0.24	523.2	1.1	32572.8	0.070	0.340224	(.05)	5.4272	(.07)	0.11569	(.04)	1887.7	1889.2	**1890.7**	0.7	0.794	0.2
z4a	1	4.5	154.2	54.1	0.28	230.1	1.1	14296.9	0.083	0.340207	(.07)	5.4252	(.09)	0.11566	(.05)	1887.7	1888.8	**1890.2**	0.9	0.831	0.2
z5a	1	7.0	60.9	21.7	0.32	86.3	1.8	5094.7	0.094	0.340516	(.07)	5.4331	(.09)	0.11572	(.06)	1889.2	1890.1	**1891.1**	1.0	0.782	0.1
02-77B, pegmatitic vein																					
z1	1	5.7	821.8	270.8	0.03	329.3	4.7	21293.7	0.009	0.340364	(.08)	5.4380	(.09)	0.11588	(.04)	1888.4	1890.9	**1893.6**	0.8	0.884	0.3
z7	1	8.0	1463.7	482.1	0.03	291.5	13.2	17885.1	0.008	0.340102	(.07)	5.4337	(.08)	0.11587	(.04)	1887.2	1890.2	**1893.5**	0.7	0.851	0.4
z12	1	0.7	401.6	132.5	0.04	124.2	0.7	8272.3	0.010	0.340890	(.05)	5.4455	(.08)	0.11586	(.06)	1890.9	1892.0	**1893.3**	1.0	0.700	0.1
z14	1	0.9	348.8	113.7	0.01	81.1	1.2	5447.3	0.003	0.338900	(.07)	5.4144	(.09)	0.11587	(.06)	1881.4	1887.1	**1893.5**	1.0	0.795	0.7

Table 3. (continued)

		Compositions						Isotopic Ratios								Dates (Ma)					
Fr	#[a]	Wt (mg)[b]	U (ppm)	Pb (ppm)	Th[c]/U	Pb*[d]/Pbc	Pbc[d] (pg)	^{206}Pb[e]/^{204}Pb	^{208}Pb[f]/^{206}Pb	^{206}Pb[f]/^{238}U	% err[g]	^{207}Pb[f]/^{235}U	% err[g]	^{207}Pb[f]/^{206}Pb	% err[g]	^{206}Pb[h]/^{238}U	^{207}Pb[h]/^{235}U	^{207}Pb[h]/^{206}Pb	±	corr. coef.	% disc.
01-SZ26, pegmatitic segregation																					
z2	1	12.0	424.8	148.2	0.10	20.5	83.0	1218.7	0.028	0.338943	(.06)	5.4097	(.08)	0.11576	(.05)	1881.6	1886.4	**1891.7**	0.8	0.794	0.6
z3	1	1.3	465.2	154.9	0.08	81.3	2.4	5367.8	0.022	0.340323	(.19)	5.4299	(.20)	0.11572	(.07)	1888.2	1889.6	**1891.1**	1.2	0.941	0.2
z4	1	0.8	98.9	32.8	0.06	23.1	1.1	1546.2	0.018	0.339744	(.20)	5.4229	(.22)	0.11576	(.09)	1885.4	1888.5	**1891.8**	1.6	0.913	0.4
z7	1	3.4	681.4	225.3	0.07	146.5	5.2	9296.1	0.022	0.338478	(.07)	5.3978	(.08)	0.11566	(.04)	1879.3	1884.5	**1890.2**	0.8	0.852	0.7
z8	1	0.8	740.5	257.7	0.09	15.6	12.6	961.9	0.026	0.339045	(.14)	5.3978	(.15)	0.11547	(.05)	1882.1	1884.5	**1887.2**	1.0	0.932	0.3
z9	1	0.9	519.6	172.7	0.09	25.8	5.7	1636.7	0.026	0.339339	(.19)	5.4133	(.21)	0.11570	(.07)	1883.5	1887.0	**1890.8**	1.3	0.940	0.4
z10	1	1.0	767.1	254.9	0.08	114.6	2.2	7554.0	0.022	0.339554	(.14)	5.4175	(.15)	0.11571	(.07)	1884.5	1887.6	**1891.1**	1.2	0.905	0.4
SZ00-196A, pegmatite vein																					
z1	1	9.8	678.5	228.0	0.09	68.5	32.2	4084.1	0.025	0.338172	(.08)	5.3993	(.09)	0.11580	(.04)	1877.9	1884.7	**1892.3**	0.8	0.879	0.9
z2	1	27.3	721.2	241.3	0.09	172.0	24.1	10255.5	0.027	0.338902	(.09)	5.4138	(.10)	0.11586	(.04)	1881.4	1887.0	**1893.3**	0.7	0.913	0.7
z3	1	1.8	506.1	168.3	0.10	90.6	3.3	5944.7	0.028	0.338079	(.14)	5.4008	(.15)	0.11586	(.05)	1877.4	1885.0	**1893.3**	0.9	0.934	1.0
z4	1	1.3	1629.6	549.1	0.11	85.5	8.3	5238.1	0.031	0.339258	(.06)	5.4261	(.08)	0.11600	(.04)	1883.1	1889.0	**1895.5**	0.8	0.826	0.8
z7	1	2.0	606.4	198.4	0.07	139.4	2.8	9186.8	0.022	0.334489	(.09)	5.3409	(.11)	0.11581	(.06)	1860.1	1875.4	**1892.5**	1.1	0.834	2.0
z8	1	6.8	1870.8	632.5	0.08	47.3	88.9	2804.8	0.024	0.338143	(.14)	5.3972	(.15)	0.11576	(.04)	1877.7	1884.4	**1891.8**	0.8	0.955	0.9

[a] Number of grains in fraction

[b] Sample weights were estimated to within 40% using measured grain dimensions and a nominal density of 4.5 g/cm^3 for zircon.

[c] Th contents calculated from radiogenic ^{208}Pb and the ^{207}Pb/^{206}Pb date of the sample, assuming concordance between U-Th-Pb systems.

[d] Pb* and Pbc represent radiogenic Pb and common Pb respectively.

[e] Measured ratio corrected for fractionation and spike contribution; Pb fractionation was 0.12 ±0.04%/a.m.u. for Faraday detector or 0.20 ± 0.04%/a.m.u. for Daly detector analysis, based on daily analysis of NBS-981.

[f] Measured ratios corrected for fractionation, spike, blank, and initial common Pb; nominal U blank = 0.1 pg ± 50% (2s); nominal Pb blank = 3.5 pg ± 50% (2s) for all zircon analyses except samples 02-58, 02-97, 03-52, 02-76B for which a Pb blank of 1.0 ± 50% (2s) is applied; initial Pb composition estimated using the model for terrestrial Pb evolution of Stacey and Kramers (1975) at the nominal age of the fraction (i.e. 1.9 Ga).

[g] Numbers in parentheses are the % errors reported at the 2 sigma confidence interval, propagated using the algorithms of Ludwig (1980).

[h] Isotopic ages calculated using the decay constants of Jaffey et al. (1971): $\lambda(^{235}U) = 9.8485\times10^{-10}$ yr^{-1} and $\lambda(^{238}U) = 1.55125\times10^{-10}$ yr^{-1}; error in ^{207}Pb/^{206}Pb date reported at the 2 sigma confidence interval.

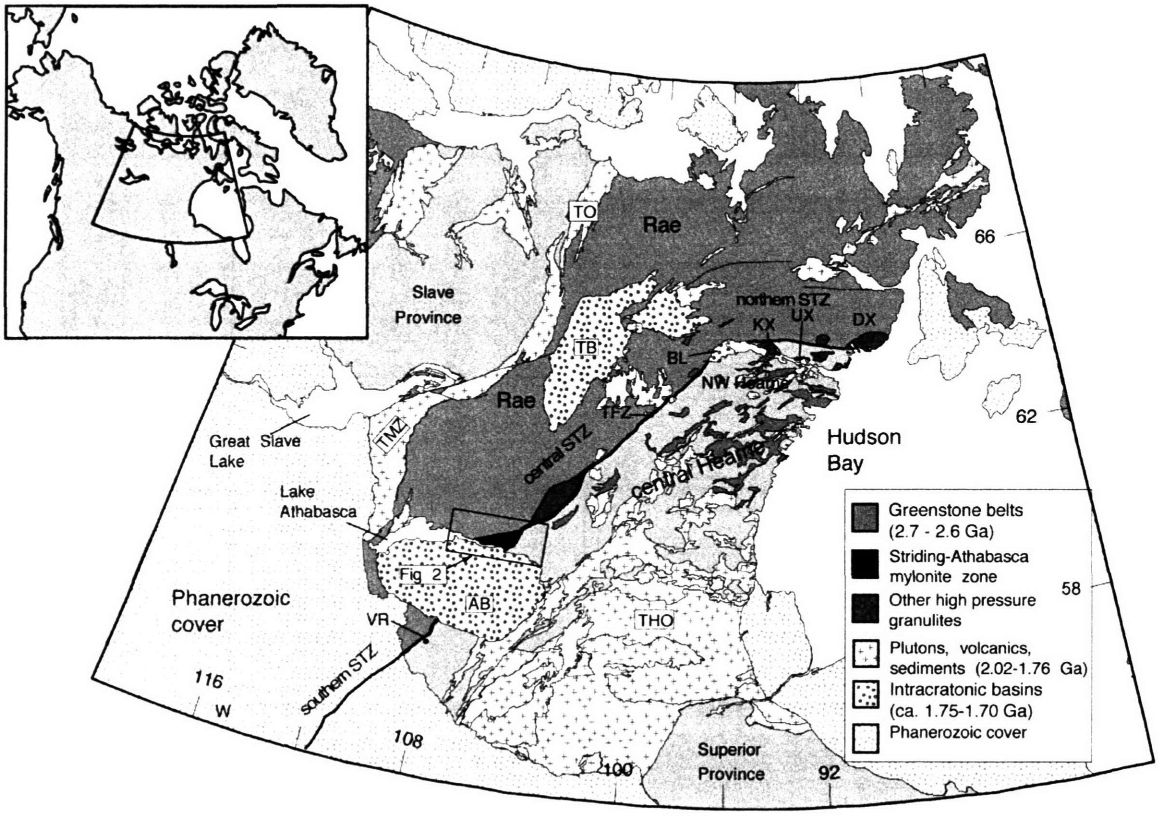
TO
Rae
66
Slave
Province
northern STZ
KX
UX
DX
TB
BL
NW Hearne
Rae
TFZ
62
Great Slave
Lake
TMZ
Hudson
Bay
central STZ
central Hearne
Lake
Athabasca
Fig 2
Phanerozoic
cover
AB
VR
THO
58
116
W
southern STZ
108
100
Superior
Province
92
Greenstone belts
(2.7 - 2.6 Ga)
Striding-Athabasca
mylonite zone
Other high pressure
granulites
Plutons, volcanics,
sediments (2.02-1.76 Ga)
Intracratonic basins
(ca. 1.75-1.70 Ga)
Phanerozoic cover

Figure 1

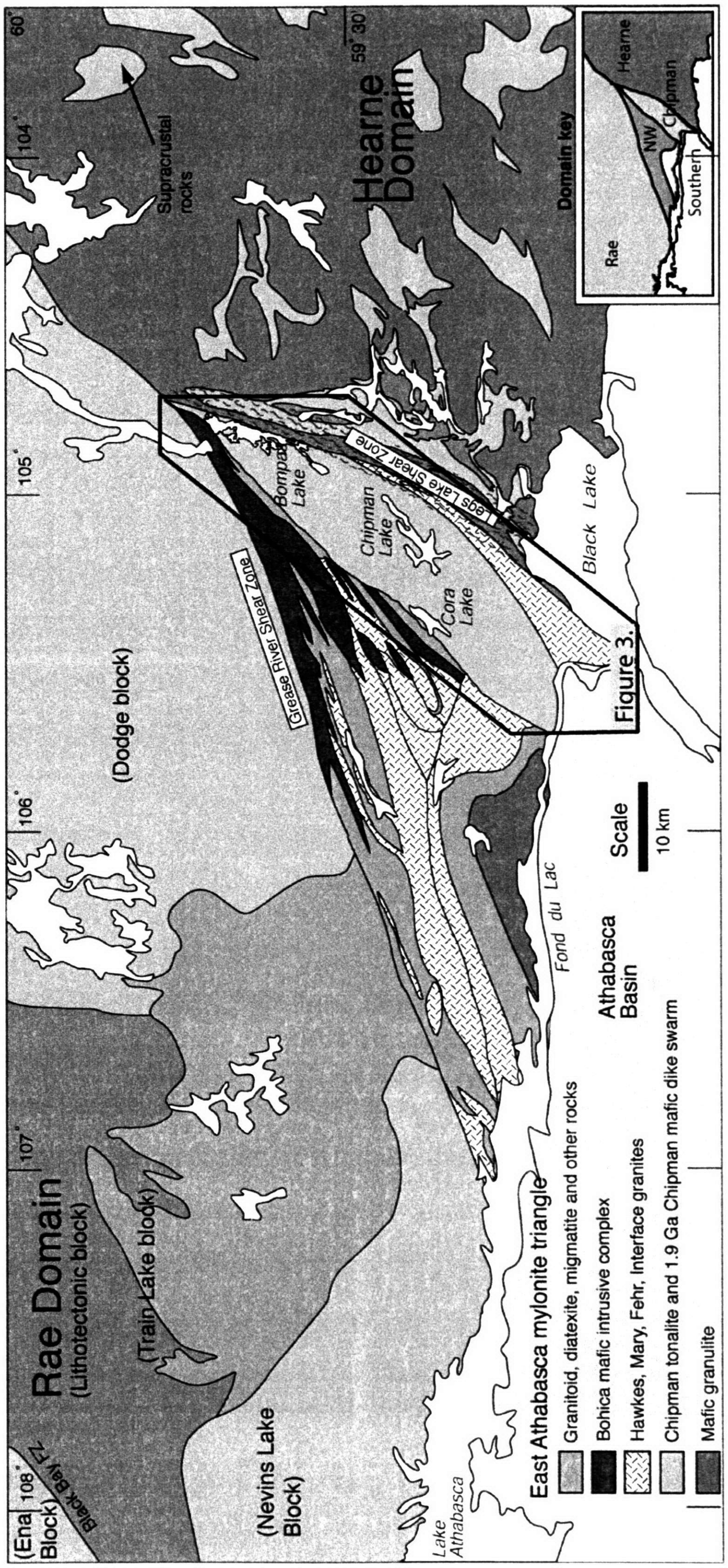
Rae Domain
(Lithotectonic block)
(Train Lake block)
(Dodge block)
(Nevins Lake Block)
(Ena Block)
Black Bay FZ
108°
107°
106°
105°
104°
60°
59° 30'
Hearne Domain
Supracrustal rocks
Grease River Shear Zone
Legs Lake Shear Zone
Bompas Lake
Chipman Lake
Cora Lake
Black Lake
Fond du Lac
Lake Athabasca
Figure 3.
Athabasca Basin
Scale
10 km
Domain key
Rae
Hearne
NW
Chipman
Southern
East Athabasca mylonite triangle
Granitoid, diatexite, migmatite and other rocks
Bohica mafic intrusive complex
Hawkes, Mary, Fehr, Interface granites
Chipman tonalite and 1.9 Ga Chipman mafic dike swarm
Mafic granulite

Figure 2

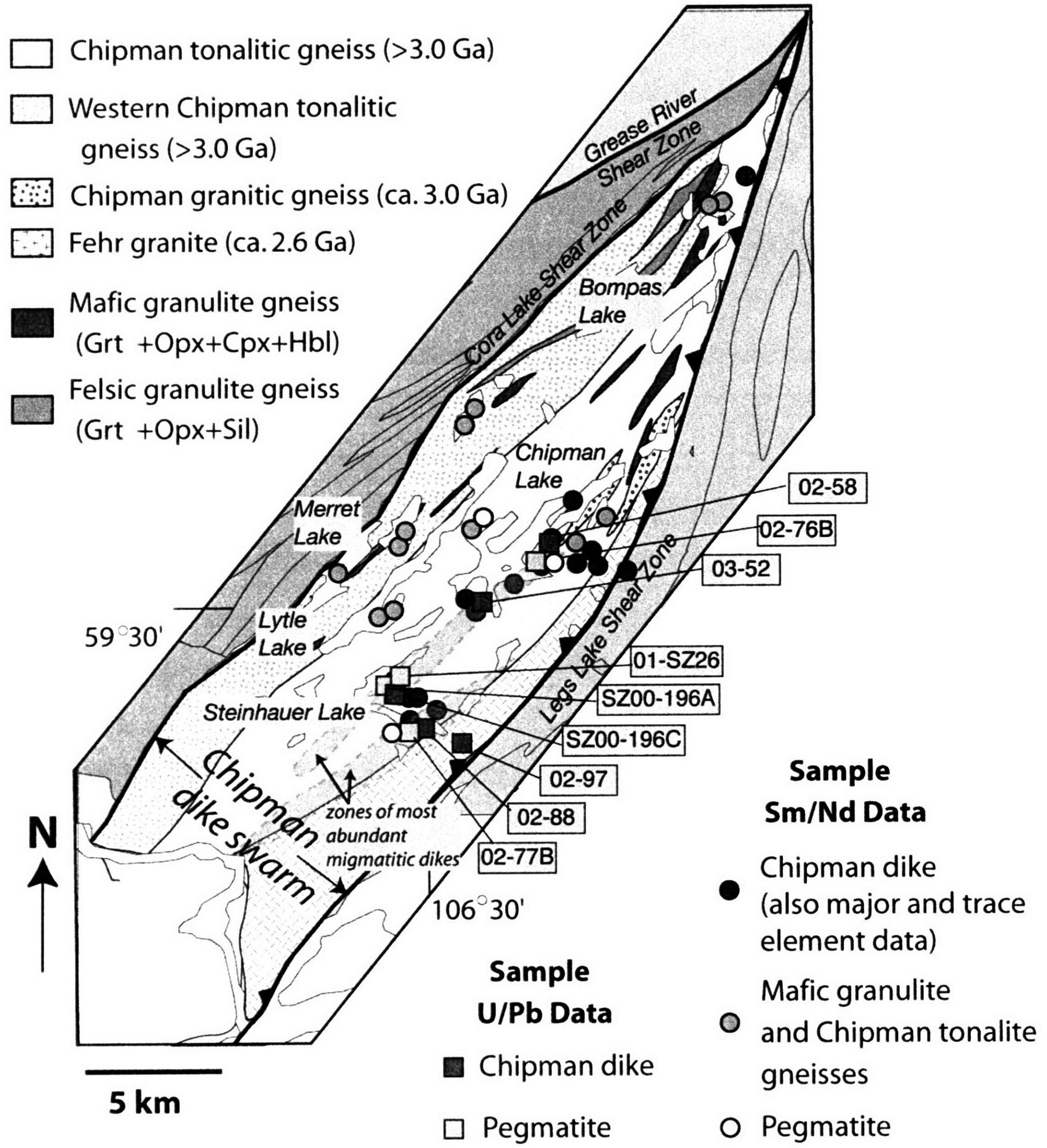
Chipman tonalitic gneiss (>3.0 Ga)
Western Chipman tonalitic gneiss (>3.0 Ga)
Chipman granitic gneiss (ca. 3.0 Ga)
Fehr granite (ca. 2.6 Ga)
Mafic granulite gneiss (Grt +Opx+Cpx+Hbl)
Felsic granulite gneiss (Grt +Opx+Sil)
Grease River Shear Zone
Cora Lake Shear Zone
Bompas Lake
Chipman Lake
Merret Lake
Lytle Lake
Steinhauer Lake
Legs Lake Shear Zone
Chipman dike swarm
zones of most abundant migmatitic dikes
59°30'
106°30'
02-58
02-76B
03-52
01-SZ26
SZ00-196A
SZ00-196C
02-97
02-88
02-77B
N
5 km
Sample U/Pb Data
■ Chipman dike
□ Pegmatite
Sample Sm/Nd Data
● Chipman dike (also major and trace element data)
● Mafic granulite and Chipman tonalite gneisses
○ Pegmatite

Figure 3

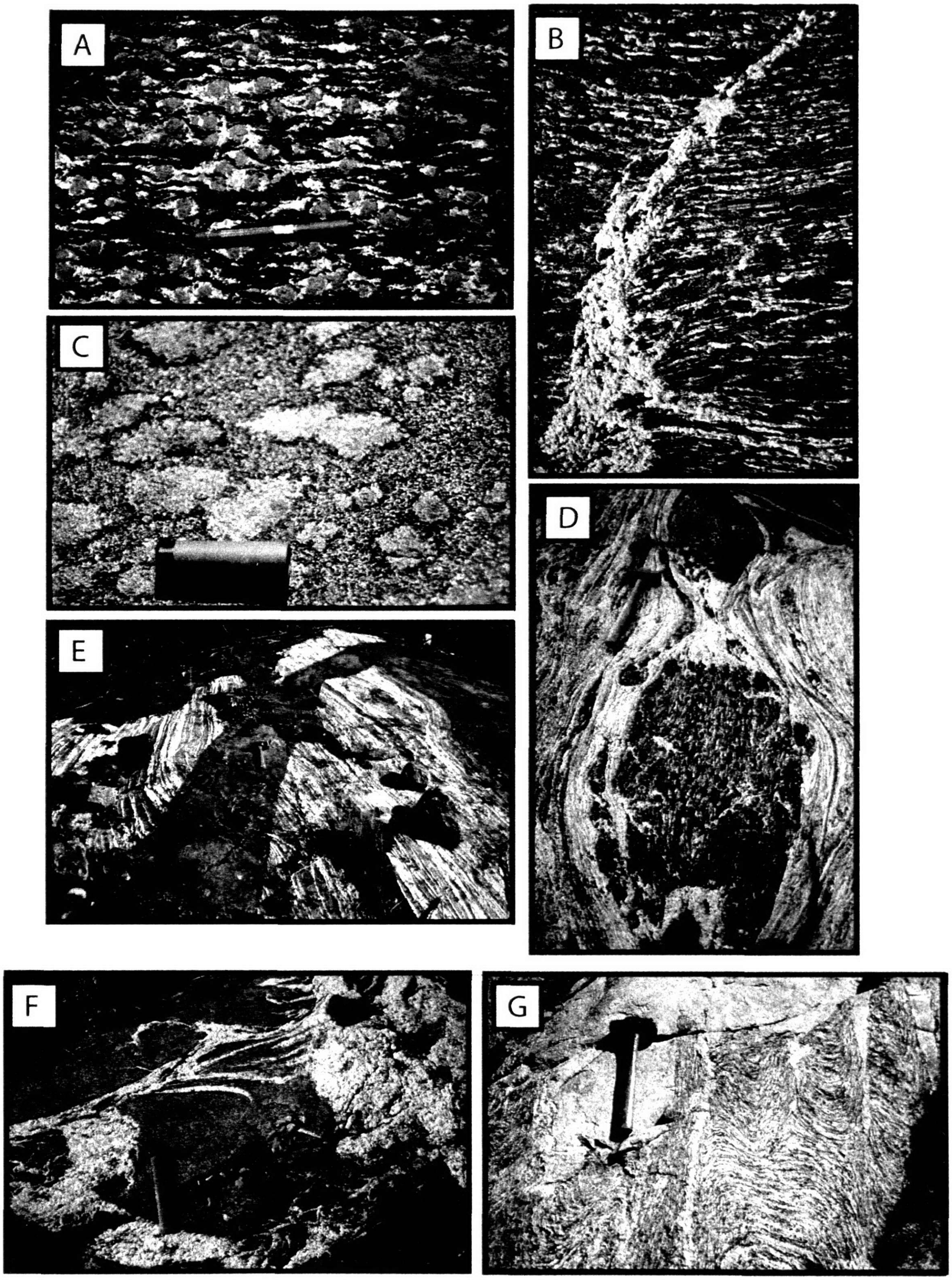

Figure 4

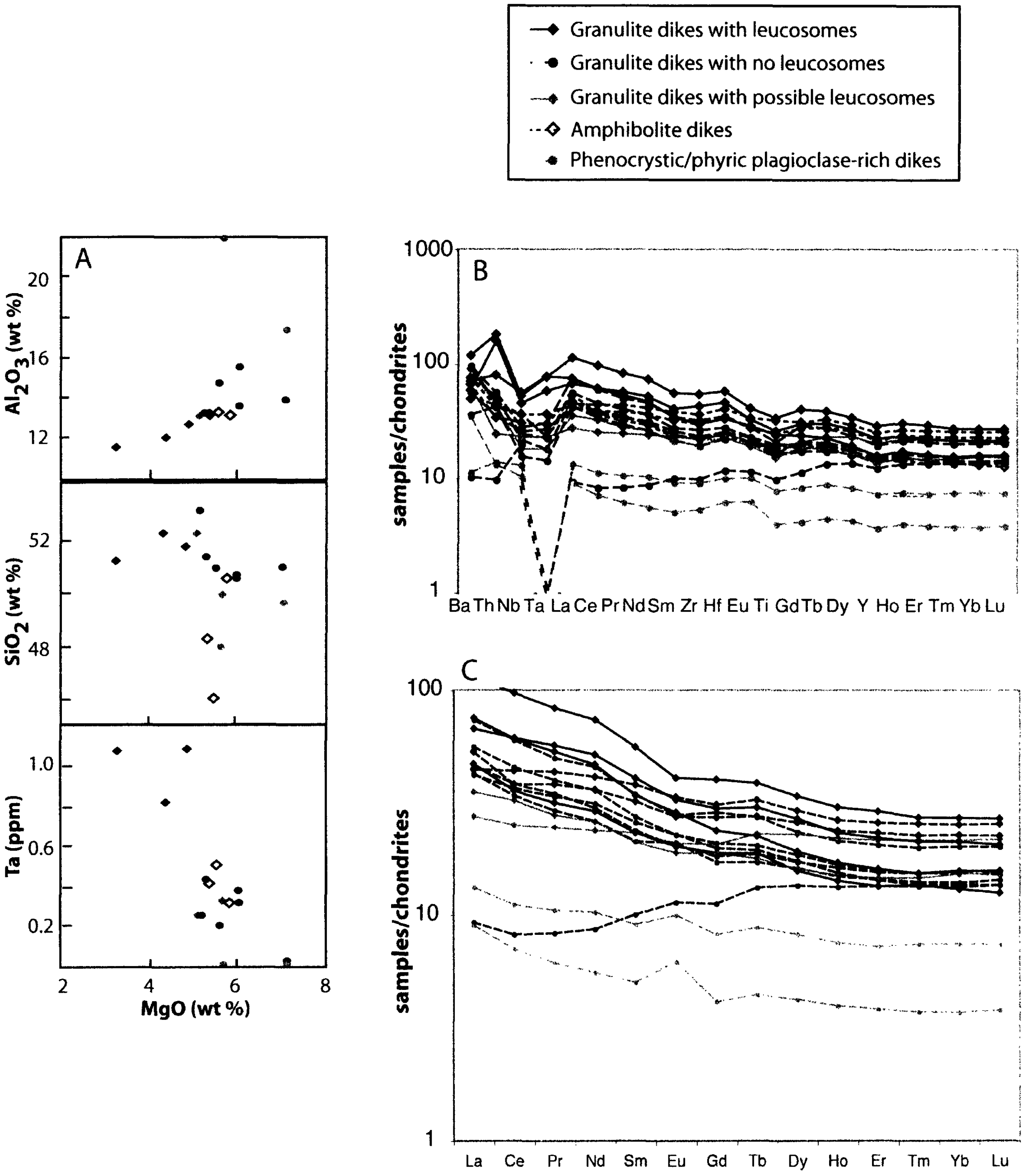
Granulite dikes with leucosomes
Granulite dikes with no leucosomes
Granulite dikes with possible leucosomes
Amphibolite dikes
Phenocrystic/phyric plagioclase-rich dikes
A
Al_2O_3 (wt %)
20
16
12
SiO_2 (wt %)
52
48
Ta (ppm)
1.0
0.6
0.2
2
4
6
8
MgO (wt %)
B
1000
100
10
1
samples/chondrites
Ba Th Nb Ta La Ce Pr Nd Sm Zr Hf Eu Ti Gd Tb Dy Y Ho Er Tm Yb Lu
C
100
10
1
samples/chondrites
La Ce Pr Nd Sm Eu Gd Tb Dy Ho Er Tm Yb Lu

Figure 5

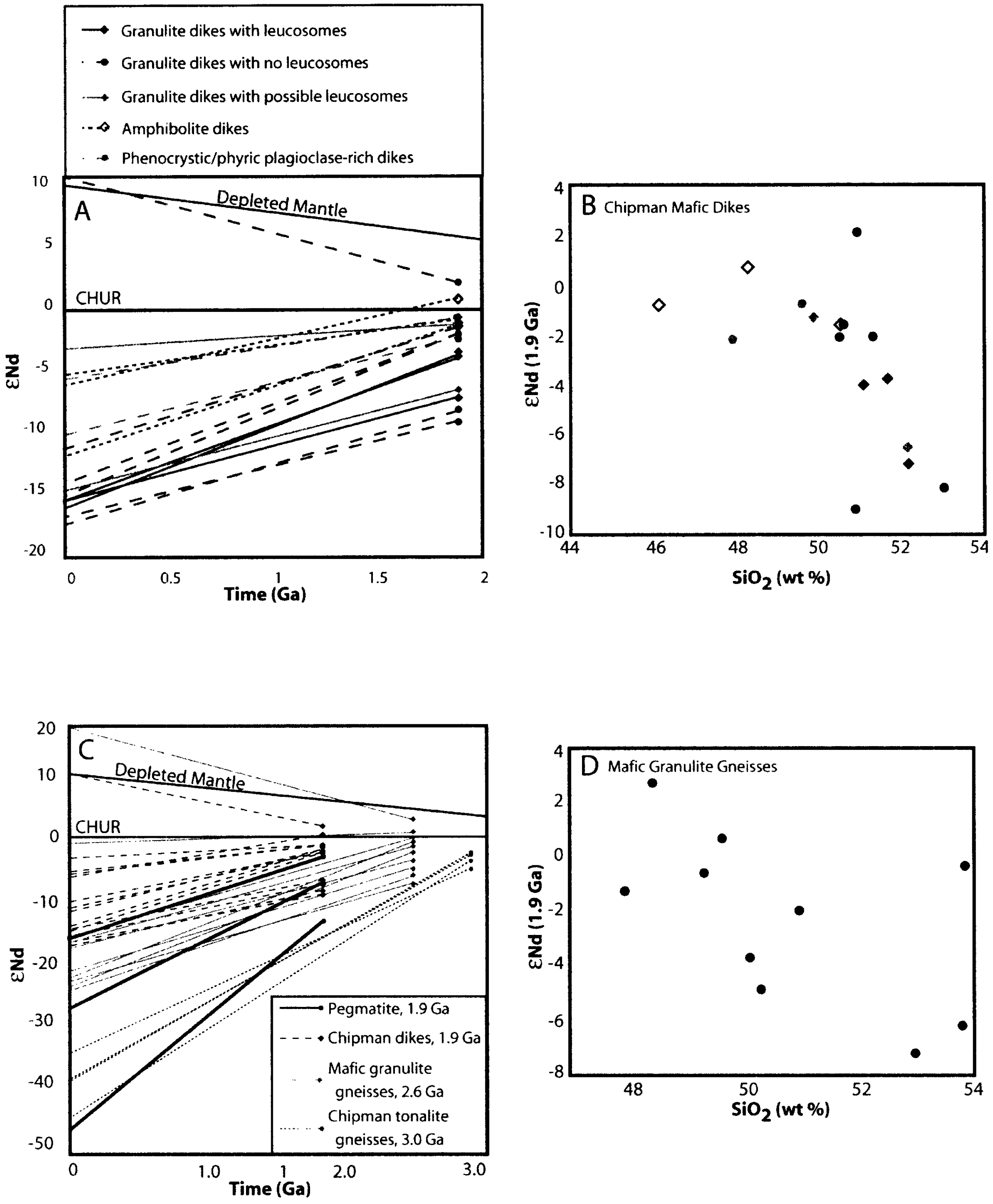
Granulite dikes with leucosomes
Granulite dikes with no leucosomes
Granulite dikes with possible leucosomes
Amphibolite dikes
Phenocrystic/phyric plagioclase-rich dikes
A
Depleted Mantle
CHUR
εNd
10
5
0
-5
-10
-15
-20
0
0.5
1
1.5
2
Time (Ga)
B Chipman Mafic Dikes
εNd (1.9 Ga)
4
2
0
-2
-4
-6
-8
-10
44
46
48
50
52
54
SiO2 (wt %)
C
Depleted Mantle
CHUR
εNd
20
10
0
-10
-20
-30
-40
-50
0
1.0
1
2.0
3.0
Time (Ga)
Pegmatite, 1.9 Ga
Chipman dikes, 1.9 Ga
Mafic granulite gneisses, 2.6 Ga
Chipman tonalite gneisses, 3.0 Ga
D Mafic Granulite Gneisses
εNd (1.9 Ga)
4
2
0
-2
-4
-6
-8
48
50
52
54
SiO2 (wt %)

Figure 6

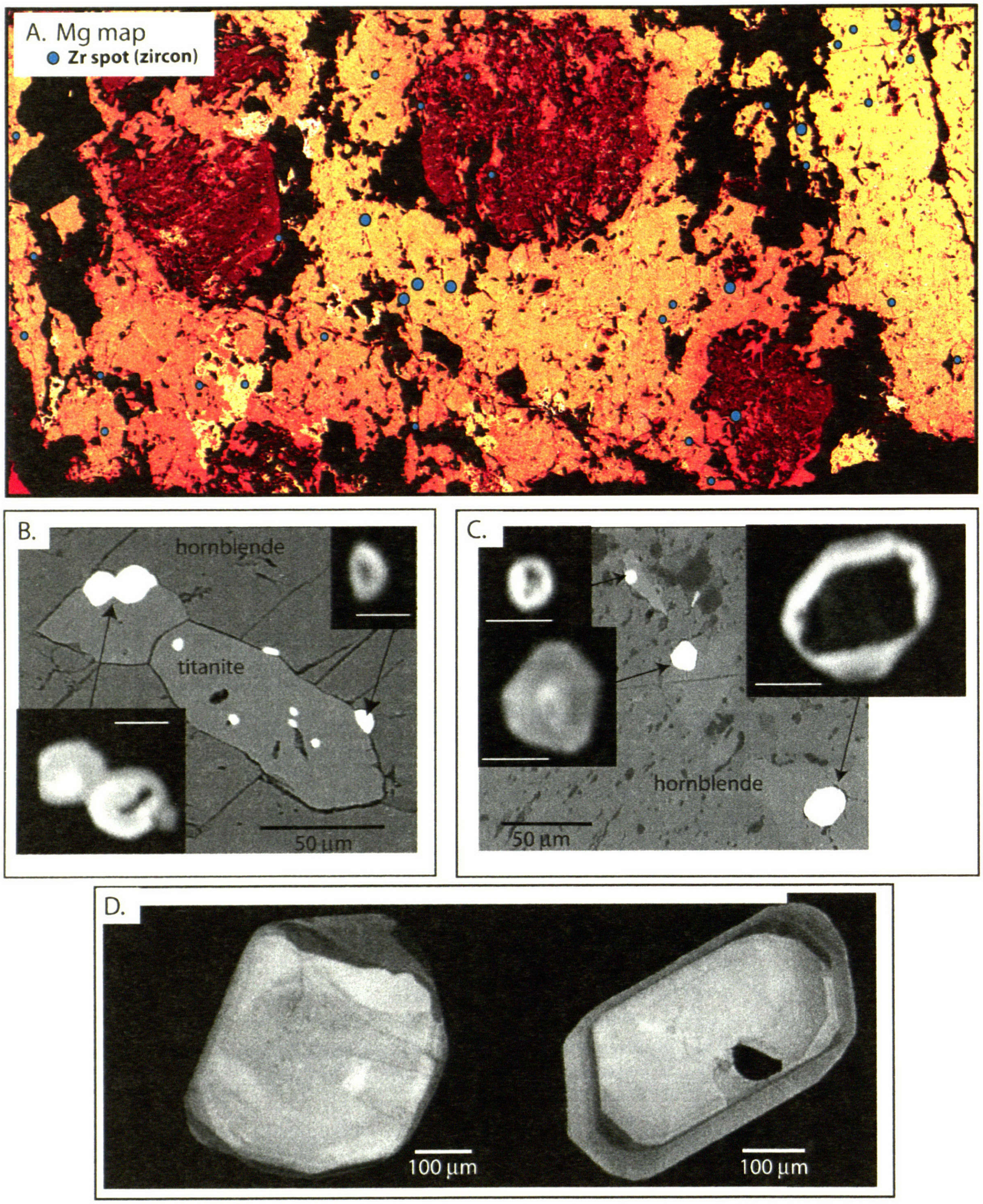
A. Mg map
● Zr spot (zircon)
B.
hornblende
titanite
50 µm
C.
hornblende
50 µm
D.
100 µm
100 µm

Figure 7

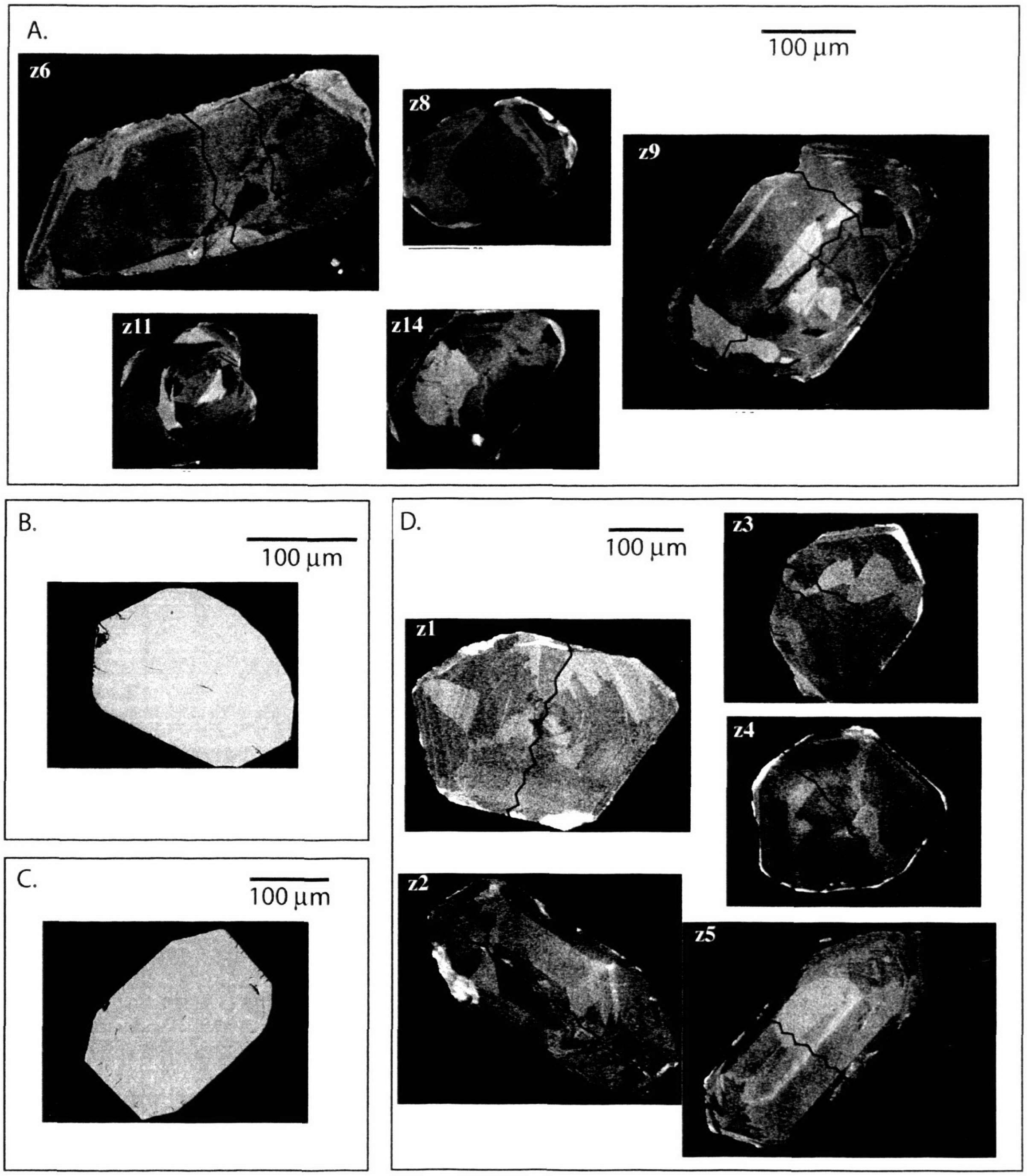

Figure 8

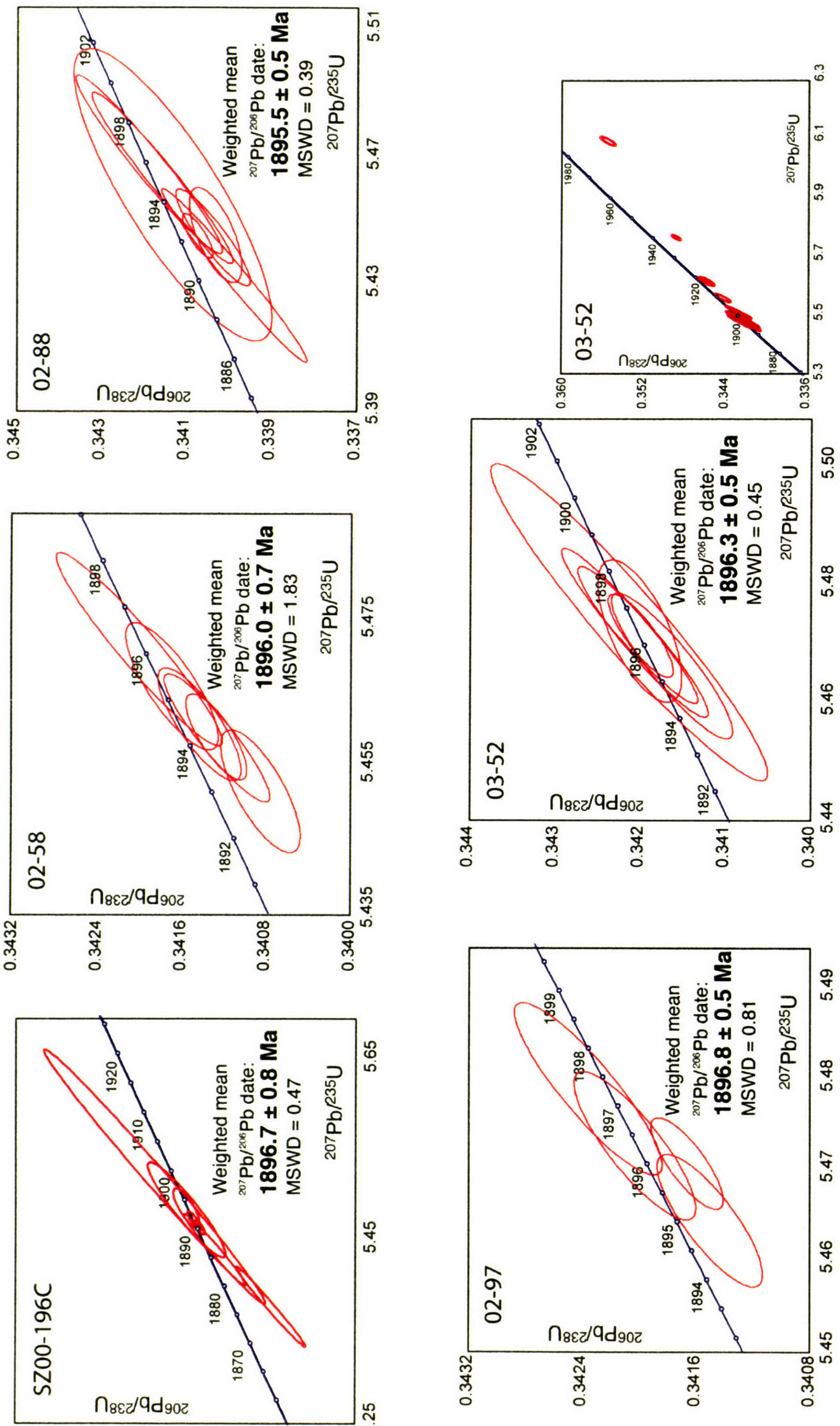
SZ00-196C
Weighted mean
^{207}Pb/^{206}Pb date:
1896.7 ± 0.8 Ma
MSWD = 0.47
02-58
Weighted mean
^{207}Pb/^{206}Pb date:
1896.0 ± 0.7 Ma
MSWD = 1.83
02-88
Weighted mean
^{207}Pb/^{206}Pb date:
1895.5 ± 0.5 Ma
MSWD = 0.39
02-97
Weighted mean
^{207}Pb/^{206}Pb date:
1896.8 ± 0.5 Ma
MSWD = 0.81
03-52
Weighted mean
^{207}Pb/^{206}Pb date:
1896.3 ± 0.5 Ma
MSWD = 0.45
03-52
^{206}Pb/^{238}U
^{207}Pb/^{235}U

Figure 9

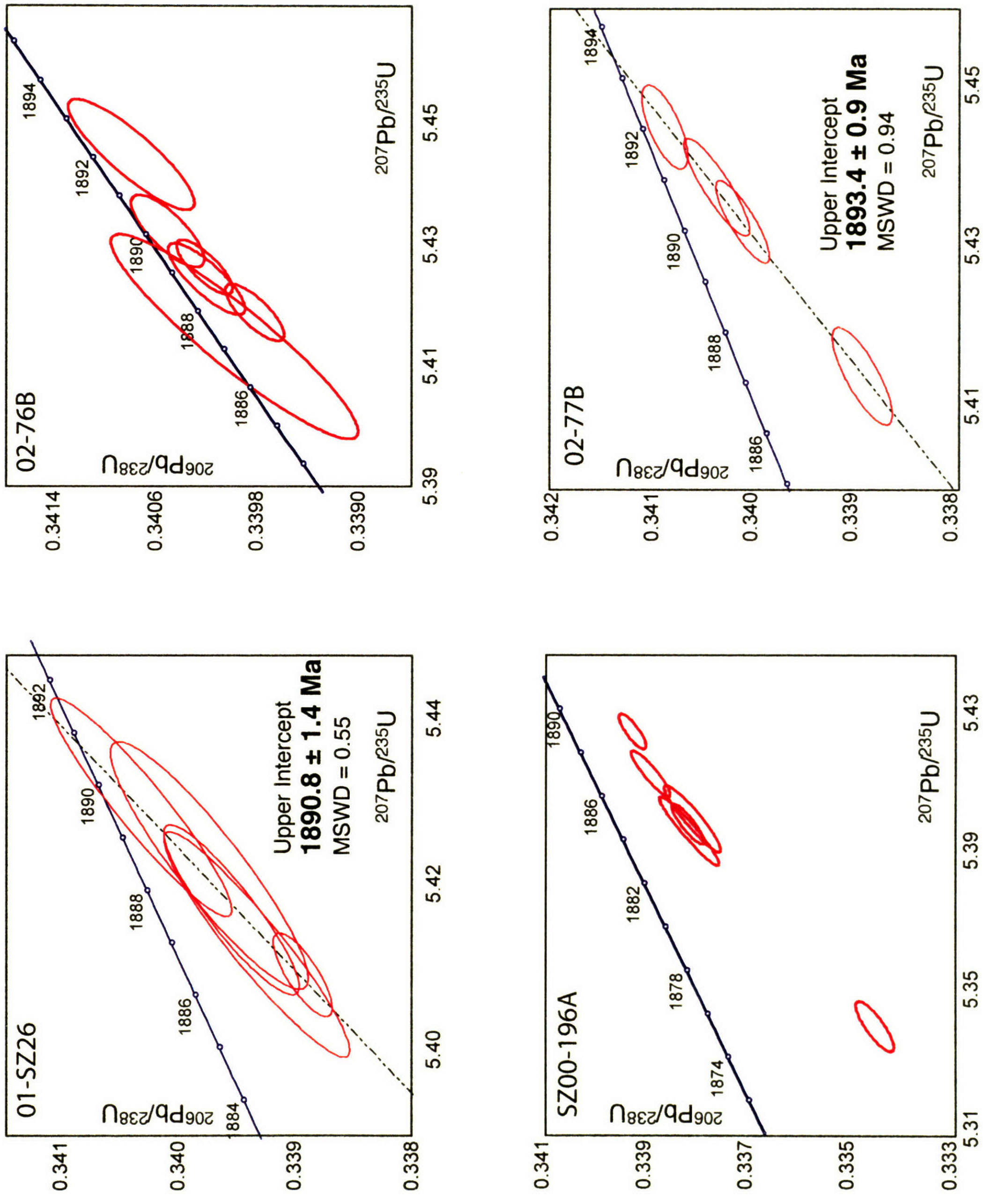
02-76B
206Pb/238U
207Pb/235U
0.3414
0.3406
0.3398
0.3390
5.39
5.41
5.43
5.45
1886
1888
1890
1892
1894
02-77B
Upper Intercept
1893.4 ± 0.9 Ma
MSWD = 0.94
0.342
0.341
0.340
0.339
0.338
01-SZ26
Upper Intercept
1890.8 ± 1.4 Ma
MSWD = 0.55
0.341
0.340
0.339
0.338
5.40
5.42
5.44
1884
SZ00-196A
0.341
0.339
0.337
0.335
0.333
5.31
5.35
5.39
1874
1878
1882
1886

Figure 10

Chapter 3

Temporal constraints on multistage exhumation and juxtaposition of high-pressure granulites in the western Canadian Shield: Linking high-resolution thermochronometry with P-T-D paths

ABSTRACT

New U-Pb (titanite, apatite, rutile) and ^{40}Ar/^{39}Ar (hornblende, muscovite, biotite) data are linked with existing pressure-temperature-deformation paths to impose detailed temporal constraints on the juxtaposition and exhumation of deep crustal domains in the East Lake Athabasca region. In the ~ 200 m.y. between ca. 1.9 Ga high-pressure granulite facies metamorphism of the rocks while in the deep crust, and ca. 1.7 Ga unconformable deposition of Athabasca basin sediments on the exhumed rocks, our analysis reveals at least three distinct phases of unroofing at diverse rates separated by two intervals of crustal residence at different depths. Specifically, we distinguish 1) an early phase of extensional unroofing in the Chipman domain at rates of 1.5-2.0 km/m.y. from 1.0-1.2 GPa to 0.7-0.8 GPa associated with mafic magmatism and metamorphism, 2) an episode of regional contractional uplift along the Legs Lake shear zone at ca. 1850 Ma from 0.7-0.8 GPa to 0.4-0.5 GPa, and 3) a final period of extensional unroofing at rates of 0.2-0.3 km/m.y. from 0.4-0.5 GPa that culminated in transport of current exposures to near-surface conditions. The cooling patterns and retrograde assemblages are consistent with pauses in unroofing during 1) residence of several deep crustal domains at ~ 25 km crustal depth for 20-30 m.y., and 2) storage of domains across the East Lake Athabasca region at ~ 15 km crustal depth for 70-100 m.y. The apparent convergence of disparate higher temperature thermal histories in several deep crustal domains at ca. 1.89-1.88 Ga implies their juxtaposition at 0.7-0.8 GPa conditions. Regional east-directed thrusting of the deep crustal domains as a coherent unit at 1.85 Ga juxtaposed the granulites with middle crustal Hearne domain rocks at 0.4-0.5 GPa conditions. The detailed timing constraints on the exhumational history allow correlation with changing regional tectonic regimes associated with the amalgamation of Laurentia. The temporal and spatial heterogeneity of exhumation patterns in the East Lake Athabasca region may be a common feature of the unroofing histories of lower crustal rocks.

INTRODUCTION

Rare exposures of lower continental crust offer the best opportunity to directly examine the character and in situ relationships of this generally inaccessible level of orogenic systems. As a consequence, these exposures exert a tremendous influence on our understanding of lower crustal processes. Constraining the mechanisms that exhume deep crust is crucial to assess the significance and representativeness of these terranes. For example, a domainal architecture is a central feature of some exhumed portions of lower crust, and it is important to distinguish how much of this segmentation was acquired during exhumation via the juxtaposition of highly disparate crustal blocks, versus the degree to which this heterogeneity represents a primary feature of the lower crust since its earliest stages of evolution. Determining the extent of modification during transport of these rocks from the base of the Earth's crust to the surface necessitates a more complete understanding of the processes responsible for deep crustal exhumation.

The reconstruction of detailed pressure-temperature-deformation (P-T-D) paths, in conjunction with high-resolution timing constraints on unroofing histories, is required to effectively evaluate viable deep crustal exhumation models. Integration of U-Pb, ^{40}Ar/^{39}Ar and (U-Th)/He thermochronometry allows comprehensive reconstruction of deep crustal cooling histories from peak metamorphic conditions through exhumation to the Earth's surface. Linkage of these temperature-time (T-t) paths with P-T-D histories can place robust constraints on the tempo, duration and rates of unroofing. The convergence of disparate thermal histories in different domains also offers information regarding the timing of juxtaposition of exhumed deep crustal blocks.

Vast (>20,000 km^2) tracts of high-pressure (HP) granulites are exposed in the vicinity of the East Lake Athabasca region, along the Snowbird tectonic zone in the western Canadian Shield. This region is characterized by a segmented architecture, with subdivision into distinct lithotectonic domains. Importantly, these HP granulites are interpreted to have resided in the deep crust for a significant portion of their history (Williams et al., 2000; Flowers, Chapter 1), rather than forming in a brief tectonic thickening event as commonly inferred for high- and ultrahigh-pressure granulites characterized by isothermal decompression histories (O'Brien and Rotzler, 2003). Unraveling the exhumational overprint on these rocks is of central importance for deciphering the domainal relationships and the processes operative during their evolution in the deep crust. Existing kinematic data for bounding structures, geochronological information on the timing of shear zone activity, and domainal thermobarometric data constrain a multistage history of unroofing involving regional contractional uplift, temporary residence in the middle crust, and final extensional unroofing (Mahan et al., 2003). This information provides an exceptional opportunity to use thermochronological data to place existing P-T-D paths within a high-resolution temporal framework. Such information can impose important constraints on two outstanding questions in this region regarding 1) the tempo and rates of the punctuated unroofing history, and 2) the timing of domain juxtaposition relative to regional exhumation. We exploit the full temperature range permitted by the U-Pb (zircon, titanite, apatite, rutile) and $^{40}Ar/^{39}Ar$ (hornblende, muscovite, biotite) isotopic systems, combined with (U-Th)/He zircon and apatite data (Flowers, Chapter 4), to constrain the temporal and spatial heterogeneity of exhumation patterns across the East Lake Athabasca region. These results have broader implications for multistage unroofing histories in exhumed deep crustal terranes and for the architecture and heterogeneity of the lower continental crust.

GEOLOGICAL SETTING

The Snowbird tectonic zone coincides with a prominent, 2800 km long, northeast striking magnetic and gravity anomaly in the western Canadian Shield (Figure 1). This feature delineates the boundary between the Rae and Hearne cratons of the western Churchill Province. The western Churchill Province was the upper plate between the bounding Taltson-Thelon and Trans-Hudson orogenic belts, zones of major Proterozoic orogenesis along the Slave-Rae and Superior-Hearne sutures, during the assembly of Laurentia. The history of the Snowbird tectonic zone has long been controversial, owing to a complex history including both Archean and Proterozoic tectonism. This structure has alternatively been interpreted as a Paleoproterozoic intercontinental suture (Hoffman, 1988) and as an Archean intracontinental shear zone that was reactivated in the Paleoproterozoic (Hanmer, 1997).

The East Lake Athabasca region contains extensive tracts (>20,000 km^2) of HP granulites (1.0 to > 1.5 GPa) exposed along the central Snowbird tectonic zone and in the adjacent Rae crustal province. A fundamental characteristic of this region is its segmented architecture, with discrete structurally bounded lithotectonic domains that preserve distinct P-T-D histories (Figure 2). Three HP granulite domains of the East Lake Athabasca mylonite triangle are interpreted to represent part of an isobarically cooled deep crustal terrane that resided in the deep crust for hundreds of millions of years (Williams and Hanmer, 2005). The Chipman domain preserves a spectacular 1.9 Ga mafic dike swarm that intruded heterogeneous Chipman tonalite gneisses at conditions of 1.0-1.2 GPa, 750-850 °C (Williams et al., 1995; Flowers, Chapter 2). The northwestern domain is dominated by mafic and felsic plutonic rocks intruded and metamorphosed at conditions of 1.0 GPa, ~800 °C (Williams et al., 2000). The southern domain contains mafic and felsic granulites with minor eclogite, that record peak metamorphic conditions ≥ 1.5 GPa, 800-1000 °C (Snoeyenbos et al., 1995; Baldwin et al., 2003) interpreted to have occurred at 1.9 Ga (Baldwin et al., 2004). To the west, rocks of the Rae domain preserve granulite facies conditions of 0.8-1.0 GPa, ~900°C at 1.9 Ga (Kopf, 1999; Krikorian, 2002). The Hearne domain to the east records lower pressure, amphibolite facies conditions of 0.4-0.5 GPa, 600-700 °C (Mahan et al., 2003). Sediments of the Athabasca basin unconformably overlie the region to the south.

Exhumation of the East Lake Athabasca region is temporally bracketed by 1.9 Ga metamorphism of the deep crustal domains (Flowers, Chapter 2; Baldwin et al., 2004), and ca. 1.7-1.65 Ga deposition of the overlying Athabasca basin (Rayner et al., 2003; Cummings et al., 1987). This imposes ~200 m.y. interval for unroofing of the HP granulites. Exhumation of deep crustal rocks in the East Lake Athabasca region was a multistage process, in part driven by uplift along the Legs Lake shear zone. This structure, constituting part of a ~500 km long contractional fault system, accommodated > 20 km of vertical displacement and juxtaposed > 1.0 GPa rocks with the shallower Hearne domain (Mahan et al., 2003). Synkinematic monazite growth in the Legs Lake shear zone suggests deformation associated with regional exhumation beginning by ca. 1.85 Ga, and retrograde 0.4-0.5 GPa cordierite assemblages in the Chipman domain have been dated at ca. 1.85 Ga by electron microprobe monazite data (Mahan, 2005). Subsequent ca. 1.8 Ga dextral displacement along the N-NE trending Grease River shear zone disrupted the region (Mahan and Williams, 2005). Greenschist facies extensional reactivation of the Legs Lake shear zone is interpreted to reflect a later part of the exhumation history (Hanmer, 1997; Mahan et al., 2003). Metamorphic constraints on the exhumation path are provided by isothermal decompression textures that record conditions of 0.7-0.9 GPa in the Chipman, southern and Rae domains (Mahan, 2005; Krikorian, 2002; Baldwin et al., 2003; Kopf, 1999).

MINERAL-ISOTOPIC SYSTEM CLOSURE TEMPERATURES

An isotopic closure temperature (Tc) represents the temperature of a mineral-isotopic system at the time of its measured date, and is a function of diffusion parameters, cooling rate, geometry, and effective diffusion dimensions (Dodson, 1973). Closure temperatures can be constrained by experimental and field-based empirical studies. Estimates below are nominal Tc for typical diffusion radii (25-500 μm) and cooling rates (1-100 °C/m.y.). Very low diffusivities of Pb have been experimentally demonstrated in zircon and monazite, indicative of Tc >900-1000°C °C (Cherniak and Watson, 2001; Cherniak et al., 2004), such that these minerals typically crystallize below their Tc, and are widely used to determine the timing of intrusive and metamorphic events. Titanite is increasingly recognized as a useful geochronometer because it is reactive mineral that readily grows during metamorphism (Frost et al., 2000; Aleinikoff et al., 2002). Field and experimental studies suggest titanite closure to Pb diffusion at temperatures of 550-660 °C (Hanson et al., 1971; Cherniak; 1993; Verts et al., 1996). In contrast with these minerals that commonly grow below their Tc, the U-Pb systematics of apatite and rutile are typically dominated by volume diffusion (e.g. Mezger 1989; Chamberlain and Bowring, 2000). Experimental and field studies of apatite provide consistent Tc constraints of 450-550 °C for Pb diffusion (Cherniak et al. 1991; Krogstad and Walker, 1994; Chamberlain and Bowring, 2000). Field estimates for Pb diffusion in rutile are 400-450 °C (Mezger, 1989), with higher estimates from experiments (Cherniak, 2000). In regards to the K-Ar and ^{40}Ar/^{39}Ar isotopic systems, experimental estimates for closure to Ar diffusion yield compositionally dependent ranges from 500-550 °C in hornblende (Harrison, 1981), 350-415 °C for muscovite (Robbins, 1972; Hames and Bowring, 1994) and 300-350 °C for biotite (Grove and Harrison, 1996). It is important to emphasize the dependence of closure temperature on diffusion domain size dimension. Minerals in isobarically cooled terranes may exhibit a range of dates that reflect a continuum of grain-size dependent closure temperatures induced by the effects of protracted cooling. In an analogous manner, age gradients may develop in individual mineral grains during slow cooling, due to closure temperature variations across single crystals (e.g. Hodges et al., 1994).

ANALYTICAL METHODS

U-Pb Analytical Methods

Titanite, apatite and rutile grains were separated using standard crushing, water table, heavy liquid, and magnetic separation techniques. Single and multi-grain fractions of accessory minerals were picked, photographed, measured, ultrasonically washed in high-purity water or ethanol and rinsed in acetone, followed by a second washing in high-purity water and rinsing with double-distilled acetone. Fractions were loaded into Teflon FEP capsules in high-purity water, spiked with a mixed ^{205}Pb-^{233}U-^{235}U tracer, and dissolved in 12 M HCl at 180 °C for 48 hours (apatite) or in 29 M HF at 220 °C for 48-96 hours followed by conversion to 6 M HCl at 180 °C for 12-24 hours (titanite and rutile). Chemical separation of U and Pb was accomplished using HBr-HCl anion exchange chemistry. Pb and U were loaded on separate, previously degassed, single Re filaments with a silica gel 0.1 M H_3PO_4 emitter solution and analyzed on the Massachusetts Institute of Technology VG Sector 54 mass spectrometer. Pb isotopic ratios were measured either by peak jumping all ion beams into an axial ion-counting Daly detector, or dynamically with Faraday cups and the Daly by peak-jumping of ^{205}Pb into the axial position to obtain a real-time Faraday-Daly gain calibration. Uranium was measured as an oxide, typically in static mode on three Faraday cups, but for smaller amounts of uranium by peak-jumping into the Daly detector. U-Pb data and details of fractionation and blank corrections are provided in Table 1. Decay constant and U-Pb tracer calibration uncertainties are systematic errors not included in the cited dates, as these errors are secondary to the uncertainties associated with the common Pb correction, discussed further below. In the text, the ages are reported as a range of ^{207}Pb/^{206}Pb dates for each sample.

Titanite, apatite and rutile have the potential to incorporate common Pb of unknown isotopic composition during crystallization, thus lowering the radiogenic/common Pb ratio (Pb*/Pbc), and introducing uncertainty into the calculated U-Pb date. Thus, analyses with in the lowest Pb*/Pbc are most affected by the choice of initial common Pb isotopic composition. Consideration of this factor is critical for robust interpretation of U-Pb titanite, apatite, and rutile ages. Feldspar replicates from six samples were leached to estimate the initial isotopic composition of common Pb. Feldspar Pb isotopic determination was carried out by handpicking 2-5 mg plagioclase fractions, followed by leach steps at 125 °C with 7 M HNO_3 and 6 M HCl for 15 min each, and with three aliquots of 1 M HF for 20 min, 40 min, and 40 min, respectively, rinsing twice with high-purity water between leaching steps. Pb from the final leach aliquot was separated using standard HBr-HCl anion exchange chemistry, and run on the Massachusetts Institute of Technology Isoprobe-T mass spectrometer in static mode. Isotopic ratios and details regarding corrections are reported in Table 2. All accessory mineral fractions were corrected using the Pb isotopic composition of feldspars either coexisting in the same rock or in a rock of similar composition and age. The isotopic compositions of the feldspars in this study are variable, indicating heterogeneity in the common Pb incorporated into accessory minerals in different rocks. The standard method of correcting for initial common Pb is through application of the Stacey and Kramers (1975) model for terrestrial Pb evolution. The least radiogenic feldspar Pb isotopic compositions induced the greatest deviation of U-Pb dates from those computed using the Stacey and Kramers model. This typically caused an increase in the apparent $^{207}Pb/^{206}Pb$, $^{206}Pb/^{238}U$, and $^{207}Pb/^{235}U$ dates, and shifted negatively discordant U-Pb analyses toward or onto concordia, increasing our confidence in the selection of the feldspar Pb isotopic as a more appropriate isotopic composition than Stacey and Kramers (Figure 3).

$^{40}Ar/^{39}Ar$ Analytical Methods

Fresh, relatively unbroken crystals of muscovite and biotite, as well as fragments of hornblende grains lacking visible inclusions, were handpicked, ultrasonically cleaned in high-purity water and ethanol, packaged in Al foil, and encapsulated in Al disks. Samples were Cd shielded and irradiated at the McMaster University reactor along with flux monitor GA-1550 biotite (98.79 ± 0.96 Ma; Renne et al., 1993) and synthetic salts to permit corrections for interfering nuclear reactions.

Gas was liberated from crystals by three different laser heating procedures: 1) total fusion of hornblende crystal fragments, 2) laser spot ablation mapping of micas, and 3) incremental heating of single mica crystals. Total laser fusion of single hornblende fragments with a range of sizes from each sample was accomplished by loading crystals into copper pan wells with complete degassing via heating for 15 seconds with a Coherent Innova 210 Ar-ion laser beam that encompassed the well diameter and converted the fragments to roughly spherical glass beads. Laser spot ablation mapping of micas was carried out on two to six muscovite and/or biotite crystals from each sample, selected because they contained the most pristine crystal faces of irradiated grains. Crystals were mounted on a Cu surface with Na-silicate. A 90-100 mJ laser beam from a Lambda Physik Compex 102 excimer laser at 20 Hz was focused to produce circular spots 87, 106, 145 or 285 μm in diameter, or a square spot 182 μm in width. Individual spots were ablated in two to five sets of 1000 bursts depending on crystal thickness, or linear scans ≤1700 μm in length were ablated along crystal margins for durations of ≤ 6 minutes. Incremental heating experiments were performed on select single mica crystals placed in Cu wells, with heating by the Coherent Innova 210 Ar-ion laser for 3-minute intervals at successively higher power levels from 0.05 up to 0.95W and a final high power step for fusion of the crystal.

After purification with a series of metal alloy getters, the evolved gas was analyzed on the Massachusetts Institute of Technology MAP 215-50 mass spectrometer with an electron multiplier. Total system blanks were measured at the beginning of each analytical session, between sets of five or ten total fusion hornblende analyses, and between sets of two to six laser spot or incremental heating analyses depending on blank reproducibility. Mass fractionation was monitored by routine analysis of laboratory air over the duration of the analytical campaign. Isotopic measurements were reduced using the ArArCALC routines of Koppers (2002), and corrected for system blanks, mass fractionation, and neutron-induced interferences. Apparent ^{40}Ar/^{39}Ar ages were calculated using decay constants recommended by Steiger and Jaeger (1977) and assuming an initial ^{40}Ar/^{36}Ar ratio of 295.5. Age uncertainties throughout this paper include errors associated with blank and sample isotopic measurements, fractionation, interfering reactions, and J. Laser spot ablation results are cited as weighted mean dates with uncertainties reported at twice the weighted standard error of the mean. Unless noted otherwise, these are the mica dates cited in the text. For samples with weighted mean dates characterized by a MSWD > 1, scatter is assumed to be greater than the contribution from analytical errors, and errors were multiplied by the square root of the MSWD (Koppers, 2002). Inverse isotope correlation diagrams after Roddick et al. (1980) were constructed using a York (1969) regression analysis to compute isochron dates and initial $^{40}Ar/^{36}Ar$ ratios. For incremental heating experiments, plateau dates are calculated using three or more consecutive steps comprising at least 50% of the total $^{39}Ar_K$ released and are considered statistically significant if the MSWD (mean square weighted deviate) of the mean lies within the 2 sigma uncertainty of the expected value of 1.0 (Wendt and Carl, 1991).

THERMOCHRONOLOGICAL RESULTS

Sample Selection

Samples were targeted in an effort to obtain a good spatial distribution of accessory minerals across domains in the region, representing a range of lithologic units and protolith ages. When possible, dates were obtained for coexisting phases in a single sample to allow reconstruction of thermal histories that were independent of lateral spatial variations in thermal regimes. Figures 4 and 5 show the locations and thermochronological results for minerals from samples across the region.

U-Pb Thermochronometry

The U-Pb titanite, apatite, and rutile dates for individual samples commonly show a range of dates, that may in part reflect the variety of factors that control the mineral closure temperature, including grain-size, cooling rate, and potential mineral composition effects. Uncertainty in the isotopic composition of the common Pb initially incorporated in the mineral may also induce an apparent span of ages owing to variable radiogenic/common Pb ratios between samples. The most radiogenic fractions of a given mineral typically yield the tightest distribution of mineral dates in this study, and these fractions are considered the best estimate of cooling through the mineral's closure temperature. Figure 6 shows an example of U-Pb zircon, titanite, apatite and rutile data acquired for a mafic granulite dike sample, demonstrating the potential for constraining cooling histories from granulite facies conditions to temperatures <400 °C through U-Pb analysis of minerals from a single sample. ^{40}Ar/^{39}Ar hornblende and (U-Th)/He zircon data were also obtained for this rock. U-Pb data isotopic are reported in Table 1. Figure 7 depicts concordia diagrams for all titanite, apatite and rutile data from each domain. More detailed descriptions of both samples and the analyzed minerals are provided in Appendix A.

U-Pb titanite dates for the granulite facies Chipman domain are interpreted to record the timing of cooling through ~600 °C following attainment of peak temperatures >750 °C. Sixteen single-grain titanite fractions from six samples yielded ^{207}Pb/^{206}Pb dates from 1898 to 1882 Ma. Titanite from two samples that continue a transect eastward into the amphibolite facies Hearne domain yielded distinctly younger dates than those in the Chipman domain. ^{207}Pb/^{206}Pb dates ranged from 1784 to 1745 Ma for three fractions from one sample, and from 1819 to 1814 Ma for three fractions from the furthest east sample from which titanite data was acquired. These dates are interpreted to reflect resetting and or new growth during the attainment of peak temperatures in this domain. Five titanite analyses for the northern part of the southern domain previously yielded dates from 1900 to 1894 Ma (Baldwin et al. 2003), and although additional samples from the middle and southern parts of this domain were processed to supplement this local data, no additional titanite was identified.

U-Pb apatite analyses constrain the timing of cooling through temperatures of ~500 °C. Apatite is a relatively common mineral in most rocks of the East Lake Athabasca region. However, apatite grains analyzed from some samples were characterized by Pb*/Pbc ratios too low to permit the interpretation of meaningful dates, and only the subset of samples with sufficiently radiogenic apatite data are discussed here. In the Chipman domain, eight fractions from two samples from the central part of the domain yielded a span of ^{207}Pb/^{206}Pb dates from 1853 to 1784 Ma, with three fractions from a third sample from the northeastern margin of the domain that define a systematically younger apatite population from 1752 to 1743 Ma. Three fractions from a northwestern domain sample yielded dates from 1850 to 1768 Ma, coinciding with the span of apatite dates for the central part of the Chipman domain. Seven fractions from two samples in the southern domain yielded $^{207}Pb/^{206}Pb$ dates from 1901 to 1865 Ma that are distinctly older than dates from the other domains. One apatite fraction from the Hearne domain yielded a $^{207}Pb/^{206}Pb$ date of 1746 Ma, consistent with apatite dates from the northeastern margin of the Chipman domain.

U-Pb rutile dates provide information regarding the time of cooling through temperatures of ~450 °C. Six rutile fractions analyzed from the central and west-central part of the Chipman domain yielded dates from 1869 to 1851 Ma, with four distinctly younger analyses from 1808 to 1771 Ma obtained from the northeastern margin of the domain. Six single grain rutile fractions from the northwestern domain yielded dates from 1875 to 1780 Ma. Five single grain fractions of rutile analyzed from the central part of the southern domain were systematically older than rutile grains from the other domains with dates from 1882 to 1874 Ma. Rutile from an eclogite sample in the northern part of the domain previously yielded similar dates from 1851 to 1882 Ma (Baldwin et al. 2004).

$^{40}Ar/^{39}Ar$ Thermochronometry

A variety of techniques were employed to permit the most effective evaluation of diffusional age gradients, excess Ar, and alteration effects on the $^{40}Ar/^{39}Ar$ systematics of hornblende, muscovite and biotite analyzed in this study. Our rationale for laser fusion of hornblende fragments and laser ablation age mapping of mica grains was based on previous studies of slowly cooled Precambrian shield samples that documented large apparent age gradients in single crystals interpreted as diffusive Ar loss during slow cooling (Hodges et al., 1994; Hodges and Bowring, 1995). Incremental heating results from such crystals without knowledge of age gradients may lead to the misinterpretation of thermal histories. Following laser mapping of mica crystals, biotite grains from four samples were targeted for incremental heating experiments to assess the potential for low temperature alteration and excess Ar effects that might not be as apparent in the laser ablation results. Summaries of meaningful $^{40}Ar/^{39}Ar$ laser hornblende fusion data, mica laser ablation data, sample lithologies, and numbers of spots and crystals analyzed are reported in Table 3. Examples of inverse isochron diagrams for $^{40}Ar/^{39}Ar$ laser hornblende fusion data are shown in Figure 8. Examples of laser ablation mapping and incremental heating results are illustrated in Figure 9. Incremental heating results are summarized in Table 4. Refer to Appendix B for single crystal hornblende data, to Appendix C for laser ablation mica spot analysis data and grain spot and transect locations, and to Appendix D for details of incremental heating results and incremental heating spectra.

$^{40}Ar/^{39}Ar$ hornblende dates for nine samples across the East Lake Athabasca region were acquired in an effort to constrain the timing of cooling through temperatures of ~500-550 °C. Total laser fusion was carried out on fifteen to thirty hornblende fragments from each sample to detect potential age dispersion within hornblende populations. One of the nine samples yielded reproducible dates for hornblende fragments. Sample 01M123C, an amphibolite facies Chipman mafic dike within the Legs Lake shear along the Hearne-Chipman domain boundary, provided a statistically significant weighted mean date of 1729 ± 11 Ma (MSWD = 0.7), based on fourteen of eighteen fragments. We consider this date the best estimate of the hornblende age. Data plot near the radiogenic component on an inverse isochron diagram (Figure 8A). Four slightly younger fragment dates induce a scatter in the population greater than the contribution assumed from analytical error. These younger dates are interpreted to be a consequence of secondary alteration, and were excluded from the weighted mean calculation.

In contrast to the relatively well-behaved data from the amphibolite facies sample, the eight granulites contain significant dispersion in hornblende fragment dates that can differ up to 1.5 b.y. in a single sample. These data plot as scatters on inverse isochron diagrams and indicate a mixture of radiogenic, atmospheric and excess ^{40}Ar components (Figure 8B). The evidence for extensive contamination with excess ^{40}Ar makes it challenging to extract reliable ages from this dataset. The youngest date in each sample is generally characterized by the lowest ^{40}Ar excess component, thus providing the tightest constraint on a maximum hornblende age assuming no significant secondary alteration effects. The youngest analyses in seven samples range from 1841 ± 31 Ma to 1901 ± 7 Ma (stated errors do not include uncertainty on J), generally compatible with U-Pb thermochronologic constraints. An eighth sample characterized by the greatest heterogeneity in hornblende dates has a youngest analysis of 2020 ± 6 Ma that is considered an overestimate of the hornblende cooling age based on comparison with U-Pb thermochronologic data for coexisting minerals. The difference in Ar systematics between the amphibolite and granulite facies samples is best illustrated by contrasting the reproducible hornblende data from the amphibolite facies Chipman mafic dike (sample 01M123C), with hornblende data suggesting significant excess ^{40}Ar in a granulite facies Chipman mafic dike (SZ00-196C) (Figure 8). The correlation of an excess ^{40}Ar component with metamorphic grade suggests its incorporation during granulite facies metamorphism. Previous studies in high grade metamorphic terranes have attributed such data dispersion in low K minerals like hornblende to fluid inclusions with variable ^{40}Ar/^{36}Ar ratios (e.g. Cumbest et al. 1994; Reddy et al., 1997; Kelley, 2002).

^{40}Ar/^{39}Ar muscovite data were acquired for six samples by laser ablation mapping to determine the timing of cooling through ~350-415 °C. Muscovite in the highest grade rocks of the Chipman, northwestern, and southern domains is rare, and was analyzed from the one sample in which high-quality grains were identified. In contrast, muscovite-bearing pegmatites, granites, and gneisses are relatively common in the Hearne and Rae domains. No clear age gradients were documented in any analyzed muscovite grains. Weighted mean dates for one sample in the Chipman domain and two samples in the Hearne domain range from 1758 ± 12 Ma to 1739 ± 12 Ma. ^{40}Ar/^{39}Ar muscovite dates for three Rae samples ranged from 1717 ± 11 Ma to 1747 ± 12 Ma.

^{40}Ar/^{39}Ar laser ablation mapping of biotite was conducted on eleven samples distributed across the region to date cooling through 300-350 °C. No age gradients were discerned in the crystals studied. Incremental heating experiments were carried out on two samples that yielded reproducible laser spot data, and on two samples that yielded more complex systematics. Four Chipman domain and two northwestern domain samples yielded dates from 1744 ± 12 Ma to 1780 ± 12 Ma. Incremental heating of one crystal from the oldest sample yielded a statistically significant weighted plateau age of 1776 ± 12 Ma, indistinguishable from the weighted mean laser spot age (Figure 9). Biotite crystals from two Hearne domain samples yielded dates of 1738 ± 13 Ma and 1740 ± 12 Ma, within error of dates for coexisting muscovite mentioned above. The westernmost sample analyzed in this study from the Rae domain yielded the oldest consistent mica dates of 1864 ± 12 Ma, with one incremental heating experiment providing an indistinguishable plateau date of 1875 ± 13 Ma. $^{40}Ar/^{39}Ar$ biotite laser ablation dates acquired for two southern domain pegmatites contain dramatically greater inter- and intra-grain variability in apparent dates than any other samples in this study, yielding individual fusion dates ranging from 1780 to 1874 Ma. No distinct pattern in the spatial distribution of analyses within crystals was detected. For one sample, two single crystal incremental heating experiments yielded statistically significant weighted plateau ages of 1846 ± 12 Ma and 1859 ± 12 Ma, while a third crystal yielded statistically insignificant results. Four single crystal incremental heating experiments for the other sample yielded one statistically significant weighted plateau date of 1827 ± 13 Ma. Data from these two samples do not define a statistically significant linear array on inverse isochron plots, suggesting a heterogeneously distributed excess ^{40}Ar component may be responsible for the complex isotopic systematics.

DISCUSSION

Timing Constraints on P-T-D Paths

Chipman Domain

The Chipman domain is characterized by the most complete thermochronological dataset of this study, based on the range of analyzed phases from a broad spatial distribution of samples. Linkage of the reconstructed T-t history with existing P-T-D constraints in this domain places constraints on the tempo and rates of unroofing during multistage exhumation (Figure 10). Subsequent sections compare and contrast the cooling histories of the other domains with that of the Chipman domain to enable a more succinct discussion of exhumation patterns (Figures 11, 12 and 13).

Quantitative timing constraints on the high-temperature evolution of the thermal regime in the Chipman domain are provided by U-Pb zircon and titanite data. A variety of evidence supports the ongoing maintenance of high temperatures following peak conditions recorded at exposed crustal depths. U-Pb TIMS data for metamorphic zircon grains from five migmatitic Chipman mafic dikes precisely date the timing of dike anatexis at 1896.2 ± 0.3 Ma during syntectonic and synmetamorphic dike emplacement at conditions of 1.0-1.2 GPa, ~800 °C (Flowers, Chapter 2; Williams et al., 1995). Nd whole rock isotopic data for cross-cutting pegmatites dated at 1891-1894 Ma by U-Pb zircon analysis are consistent with derivation from a deeper mafic protolith, requiring temperatures of >750 °C for their generation at this time, while their cross-cutting geometries suggest cooler temperatures at the level of emplacement (Flowers, Chapter 2). Titanite grains from across the domain range down to 1882 Ma. These data imply some lateral variability in subsequent thermal regimes despite synchronous timing of dike migmatization, and suggest the heterogeneous maintenance of temperatures >600-650 °C or episodic thermal perturbations for 14 m.y. following dike anatexis. A record of near isothermal decompression to 0.7-0.8 GPa, 750 °C recorded in metamorphic assemblages of Chipman mafic granulite gneisses (Mahan, 2005), is consistent with cooling of titanite to < 650 °C during unroofing. Together, these data suggest that granulite facies metamorphism and mafic magmatism may have continued at 1.0-1.2 GPa crustal depths, while coeval cooling of exposed crustal levels was driven by exhumation to 0.7-0.8 GPa associated with the extensional regime of mafic dike emplacement. We estimate an early exhumation rate of 1.5-2 km/m.y., using the median pressure estimates of 1.1 GPa and 0.75 GPa for peak and retrograde conditions, the 1896 Ma date for HP conditions, and a median titanite date of 1889 Ma for the timing of decompression. The median rather than the minimum titanite date is considered the best estimate for the calculation, because the near-isothermal decompression textures imply a time lag between unroofing and subsequent cooling.

U-Pb rutile dates impose timing constraints on the next phase of exhumation due to regional contractional uplift along the Legs Lake shear zone. U-Pb rutile dates from 1869-1851 Ma are considered the most robust estimate of cooling < 450-550 °C in the central part of the Chipman domain, because these analyses are significantly more radiogenic than the apatite data from this region. We interpret the record of re-equilibration at 0.7-0.8 GPa to coincide with an apparent slowing of cooling rates implied by the rutile data, and to indicate a 20-30 m.y. interval of residence at ~ 25 km crustal depths following the cessation of mafic magmatism and metamorphism. Cooling below the closure temperature of rutile by 1851 Ma is considered to primarily reflect the subsequent onset of contractional uplift along the Legs Lake shear zone. These data are consistent with local retrograde Grt+Bt+Crd+Sil assemblages within the Legs Lake shear zone that record conditions of 0.4-0.5 GPa, and have been dated at 1850 ± 17 Ma by in situ electron microprobe dates for synkinematic monazite linked with the retrograde reactions (Mahan, 2005). This information suggests exhumation to 0.4-0.5 GPa at ca. 1850 Ma.

The onset of the final phase of extensional exhumation is best constrained by ^{40}Ar/^{39}Ar muscovite and biotite dates from 1780 to 1744 Ma that record cooling < 300 °C. The mica dates imply a 70-100 m.y. period of residence at 0.4-0.5 GPa. These data provide precise timing constraints on the previously proposed hiatus in unroofing between Legs Lake shear zone movement at amphibolite facies conditions and subsequent extensional reactivation at <450 °C (Mahan et al., 2003). (U-Th)/He zircon dates for two samples in the Chipman domain range from ca. 1.65 ± 0.1 Ga to 1.78 ± 0.08 Ga, consistent with cooling <180 °C during this exhumation phase (Flowers, Chapter 4). The ca. 1.66 to 1.7 Ga constraints for Athabasca basin deposition (Rayner et al. 2003; Cumming et al., 1987) impose a lower temporal bound on the unroofing history. Considering the onset of exhumation from 0.45 GPa at 1780-1744 Ma, with unroofing to near surface conditions by ca. 1.7 Ga, yields extensional exhumation rates of 0.2-0.3 km/m.y.

Northwestern Domain

The northwestern domain cooling history from 550 to 300 °C is similar to that in the Chipman domain (Figure 11). Constraining the higher temperature exhumation history has not yet been possible, owing to the absence of titanite in processed samples and complex ^{40}Ar/^{39}Ar hornblende systematics characterized by significant excess ^{40}Ar. Apatite and rutile grains record a comparable range of U-Pb dates as the Chipman domain, with ^{40}Ar/^{39}Ar biotite data falling in the middle of the Chipman domain distribution. These similarities in intermediate temperature histories suggest the two domains were exhuming coherently as a juxtaposed unit during ca. 1850 Ma Legs Lake shear zone contractional uplift and subsequent extension. The timing of juxtaposition is further constrained by the abrupt termination of Chipman mafic dikes at or within the bounding shear zones, indicating decoupled histories during mafic dike intrusion at 1896

Ma. These data imply domain juxtaposition between 1896 and 1850 Ma. This may have occurred at the 0.7-0.8 GPa conditions recorded in the Chipman domain during this time period.

Southern Domain

Post-1.9 Ga cooling of the southern domain occurred distinctly earlier than in the Chipman domain, as recorded by systematically older zircon, titanite, apatite and rutile dates (Figure 12). Peak metamorphic conditions of >1.5 GPa, > 800 °C and 1.2-1.4 GPa, >750 °C, are recorded in the northern and central parts of the southern domain, respectively (Kopf, 1999; Baldwin et al., 2003). Metamorphism at 1904.0 ± 0.3 Ma, with subsequent rapid cooling through the ~650 °C Tc of titanite (Baldwin et al., 2003, 2004), is 8 m.y. older than the metamorphic peak at 1896.2 ± 0.3 Ma in the Chipman domain (Flowers, Chapter 2). Decompression of the southern domain to 0.7-0.9 GPa, >650 °C (Kopf, 1999; Baldwin et al., 2003) is consistent with cooling through the titanite closure temperature during early unroofing.

Apatite and rutile dates from the central part of the southern domain are consistently a minimum of 5-15 m.y. older than dates across the Chipman and northwestern domains. Rutile dates from 1881 to 1851 Ma in the northern part of the domain (Baldwin et al., 2004) overlap with those in the Chipman domain. These dates could reflect isobaric cooling during residence at 0.7-0.9 GPa, or ongoing cooling during decompression to higher levels in the crust. ^{40}Ar/^{39}Ar laser ablation biotite dates for two southern domain samples range from 1780 to 1874 Ma, and are characterized by significantly greater inter- and intra-grain variability than samples from the other domains. Incremental heating results from these samples also show complexity. The oldest laser ablation analyses are consistently older than biotite dates from the Chipman and northwestern domains, such that if the younger dispersion of dates is due to low temperature alteration, the data would indicate earlier cooling to < 300 °C than in the adjacent domains. Earlier cooling would be consistent with the higher temperature segments of the history. Alternatively, if the older dispersion of dates is an artifact of excess ^{40}Ar, the youngest analyses would most closely approximate the cooling age, and would be broadly consistent with the biotite dates in the other domains.

We consider two possibilities for the timing of juxtaposition of the southern domain with the adjacent domains based on the current dataset. Interpretation of the older $^{40}Ar/^{39}Ar$ biotite dates to reflect earlier cooling to < 300 °C, in conjunction with the systematic difference in U-Pb titanite, apatite and rutile dates, may indicate earlier unroofing to shallower (< 0.8 GPa) crustal conditions. This implies juxtaposition during subsequent extensional unroofing. Alternatively, the record of isothermal decompression to ~0.8 GPa in both the southern and Chipman domains raises the possibility that these domains were in proximity to one another at this condition. In this scenario, the disparity in the rutile and apatite data would be due to earlier unroofing and isobaric cooling of the southern domain at ~ 0.8 GPa. Interpretation of the youngest southern domain $^{40}Ar/^{39}Ar$ biotite dates to reflect cooling to < 300 °C at a time consistent with that in the other domains would imply coupled lower temperature histories. Additional thermochronologic and P-T data are required to distinguish these possibilities.

Rae Domain

$^{40}Ar/^{39}Ar$ mica dates in the Rae domain provide insight into its intermediate temperature cooling history. These rocks preserve peak conditions of 0.8-1.0 GPa, ~900 °C at 1.9 Ga (Kopf, 1999; Krikorian, 2002). Muscovite from two samples from the eastern Rae yielded 1732 and 1747 Ma dates in the same range as the Chipman and northwestern domain mica dates. A third samples yielded the youngest date in this study of 1717 Ma, but within error of other samples in the dataset. The fourth and westernmost sample yielded the oldest reproducible laser ablation mica dates of this study with a weighted mean of 1862 Ma, indicative of earlier cooling than the Chipman and northwestern domains.

Hearne Domain

The Hearne domain P-T-D path contrasts with those in the other domains (Figure 13). The metamorphic peak at 0.45-0.5 GPa, 600-700 °C dated at ca. 1.8 Ga by EMP monazite dates in micaceous schists is markedly younger than the timing of peak metamorphism in the granulite domains (Mahan, 2005). The pressure conditions are consistent with regional residence of rocks in the granulite facies domains at 0.4-0.5 GPa following Legs Lake shear zone activity that exhumed the granulites and buried shallower level Hearne domain crust. In this study, two samples yielded U-Pb titanite dates of ca. 1815 and ca. 1750 Ma. The former date is consistent with the timing of peak amphibolite facies conditions documented elsewhere in the Hearne. We suggest that these local peak conditions are in part due to conductive incubation following ca. 1850 Ma burial to mid-crustal depths by the granulites.

The ca. 1750 Ma titanite dates coincide with a period of major intrusive activity in the Hearne domain, and suggest titanite resetting or new titanite growth at or below the closure temperature at this time. ^{40}Ar/^{39}Ar hornblende, muscovite and biotite dates, as well as U-Pb apatite dates, are 1730 to 1750 Ma, indicating rapid cooling in the 550 to 300 °C temperature interval following the reheating event. U-Pb apatite dates in the Chipman domain, near the Chipman-Hearne domain boundary, range from 1752 to 1743 Ma. These dates are distinctly younger than apatite dates in the central and western Chipman domain, and are interpreted to represent resetting due to their proximity to 1750 Ma Hearne domain magmatism. The ca. 1748 to 1738 mica dates are consistent with those across the Chipman, northwestern, and eastern Rae domains. Together, the thermochronological data in the Hearne domain are interpreted to indicate magmatism and reheating immediately prior to, or contemporaneous with, the onset of extensional exhumation at ca. 1750 Ma that unroofed rocks across the region to near-surface conditions.

Tempo of Juxtaposition and Exhumation of High-Pressure Granulite Domains

The linkage of our new thermochronologically constrained T-t histories with existing P-T-D paths constrains the spatial and temporal heterogeneity of exhumation patterns of deep crust in the East Lake Athabasca region. In the ~200 m.y. between ca. 1.9 Ga HP granulite facies metamorphism of the rocks while in the deep crust, and ca. 1.7 Ga unconformable deposition of Athabasca basin sediments on the exhumed rocks, our analysis reveals at least three distinct phases of unroofing at diverse rates separated by two intervals of crustal residence, with domainal juxtaposition during this protracted exhumation history (Figures 10 through 13).

An early phase of extensional unroofing associated with mafic magmatism and HP granulite facies metamorphism at rates of 1.5-2.0 km/m.y. is inferred in the Chipman domain, by correlation of U-Pb zircon and titanite dates with isothermal decompression from 1.0-1.2 GPa to 0.7-0.8 GPa. The apparent convergence of disparate higher temperature thermal histories in several deep crustal domains at ca. 1.89-1.88 Ga implies their juxtaposition at 0.7-0.8 GPa conditions. The second phase of unroofing was driven by regional east-directed thrusting of the deep crustal domains as a coherent unit at ca. 1.85 Ga along the Legs Lake shear zone (Mahan and Williams, 2005). This induced cooling to <500 °C in the Chipman and northwestern domains and juxtaposed the granulites with middle crustal Hearne domain rocks at 0.4-0.5 GPa conditions. The onset of a final period of extensional unroofing at rates of 0.2-0.3 km/yr is dated by ^{40}Ar/^{39}Ar mica dates across the region that generally range from 1.78 to 1.74 Ga, and record final cooling to <300 °C. Extensional reactivation of the amphibolite facies Legs Lake shear zone at greenschist facies conditions is compatible with the low temperatures indicated by the thermochronometry during extensional unroofing. Most (U-Th)/He zircon dates range from ca. 1.78 to 1.63 Ga (Flowers, Chapter 4), consistent with exhumation to near-surface conditions and the onset of deposition of Athabasca basin sediments by ca. 1.70 to 1.65 Ga (Rayner et al., 2003; Cummings et al., 1987).

The cooling patterns and retrograde assemblages imply two pauses in unroofing between exhumational pulses. We infer a 20-30 m.y. interval of residence at ~25 km (0.7-0.8 GPa) crustal depths following early isothermal decompression, prior to the shift to a contractional regime. We similarly interpret a 70-100 m.y. period of storage of domains across the East Lake Athabasca region at crustal depths of ~15 km (0.4-0.5 GPa) preceding final extensional exhumation. This latter interpretation is supported by the ca. 1.85 Ga dates for 0.4-0.5 GPa retrograde assemblages in the deep crustal Chipman domain, and by ca. 1.80 Ga dates for 0.4-0.5 GPa peak assemblages in the Hearne domain (Mahan, 2005). The later attainment of peak temperatures at 1.80 Ga in the Hearne domain is interpreted to reflect the time lag for conductive heating in response to burial to mid-crustal depths by the granulites. Subsequent thermal perturbation at ca. 1.75 Ga in the Hearne domain was associated with local resetting of thermochronometers (titanite, apatite, hornblende) and felsic magmatism before and/or during extensional exhumation. If the Hearne domain temperatures are indicative of a more regional elevation of temperatures that coincided with extensional exhumation at ca. 1.75 Ga, it is possible that the ca. 1.78 to 1.74 Ga ^{40}Ar/^{39}Ar mica dates in the granulite domains reflect combined reheating and unroofing processes. This would imply temperatures of <300 °C in the granulite domains during residence at ~15 km crustal depth, with subsequent resetting and final cooling during the extensional phase of exhumation.

Implications for Multistage Exhumation and the Architecture of Lower Continental Crust

Multistage Exhumation of Lower Continental Crust

Multistage unroofing of the East Lake Athabasca region is linked with changing regional tectonic regimes during a 200 m.y. period of lithospheric instability in the western Churchill Province during and following the assembly of the Laurentian supercontinent. Entrapment of the western Churchill Province as the upper plate between the 2.02-1.91 Ga Taltson-Thelon orogen to the northwest and the 1.91-1.81 Ga Trans-Hudson orogenic belt to the southeast is interpreted to be responsible for its severe reactivation at ca. 1.9 Ga (Figure 1). Intrusion of mafic dikes in the Chipman domain of the East Lake Athabasca region has been linked with a focused episode of ca. 1.9 Ga mafic magmatism along >1200 km of the Snowbird tectonic zone, implying regional asthenospheric upwelling (Flowers, Chapter 2) that induced early extensional unroofing in the Chipman domain. Regional contractional uplift along the Legs Lake shear zone at ca. 1.85 Ga is interpreted to correlate with the onset of arc accretion and major collision of the Superior and Hearne Provinces to the southeast, and thus is considered a hinterland response to Trans-Hudson orogenesis (Mahan et al., 2003). The development of E-NE trending ductile structures across the western Churchill Province, including dextral strike-slip faulting along the ca. 1.8 Ga Grease River shear zone that offsets the Legs Lake shear zone, coincides with the period of 0.4-0.5 GPa residence of rocks in the East Lake Athabasca region. Final extensional unroofing to near-surface conditions is regionally consistent with ca. 1.75 Ga Nueltin suite magmatism, extension, and transtensional basin development across the Rae and Hearne provinces (Peterson et al., 2002; Rainbird et al., 2003). This final phase of extension may be due to lithospheric thinning, lithospheric densification due to mantle metasomatism, and/or some component of lithospheric delamination. The preservation of Proterozoic (U-Th)/He zircon and apatite dates attests to the long-term stability of this region following the 200 m.y. period of tectonism and deep crustal exhumation that culminated in the reattainment of a stable lithospheric configuration at ca. 1.7 Ga (Flowers, Chapter 4).

A number of factors were key in the ultimate exhumation and preservation of deep crust in the East Lake Athabasca region. Unroofing was largely due to the protracted duration of lithospheric instability following lithospheric disruption at 1.9 Ga, as the changing patterns of contraction and exhumation across the Laurentian supercontinent controlled the exhumational pulses. The final geographic position of the exhumed terrane within a stabilized craton, near the middle of the Laurentian supercontinent, protected these rocks from subsequent tectonism. The exceptional preservation of high-pressure assemblages in the granulites we attribute to the repeated episodes of HP granulite facies metamorphism that dehydrated the rocks and limited the availability of fluids for retrogression during unroofing.

Multistage exhumation, characterized by discrete pulses of unroofing separated by intervals of crustal residence, may typify the exhumation of isobarically cooled deep crustal terranes. This highlights the potential for such terranes to permanently become embedded at middle crustal levels following an episode of partial exhumation, if subsequent tectonic events do not induce the resumption of unroofing. Such intervals of middle-crustal residence also increase the probability of fluid introduction, retrogression, and re-equilibration to intermediate crustal conditions, such that peak assemblages may be destroyed prior to exhumation. Thus, the successful transport of well-preserved deep crustal rocks from the base of the Earth's crust to the surface, and their subsequent preservation, may require a fortuitous set of crustal conditions and tectonic circumstances. This explains the paucity of exposures of isobarically cooled deep crustal terranes available for study in the geological record.

The Architecture and Heterogeneity of Lower Continental Crust

The new constraints on unroofing of the East Lake Athabasca region allow us to consider the implications of the block architecture of this exhumed high-pressure granulite terrane for the heterogeneity and structure of the lower continental crust. The apparently decoupled high-temperature thermal history for disparate domains in the East Lake Athabasca region, associated with distinct P-T-D histories, provides compelling evidence for their juxtaposition during unroofing. Thus, the current configuration of these domains does not represent their structural relationship while in the deep crust. However, the prevalent ca. 2.6 Ga protolith ages, the distribution of similar mafic and felsic granulite gneisses in the Chipman, northwestern and southern domains, and the ubiquitous ca. 1.9 Ga metamorphic overprint reflect a common history preserved in these disparate domains during earlier deep crustal residence. The diverse plutonic rocks, tonalitic gneisses, and mafic and felsic granulites that compose the domains reflect a greater degree of lithological heterogeneity than that typically envisioned for the lowermost crust. The extensive tracts of deep crustal rocks exposed in the East Lake Athabasca region may permit easier detection of this heterogeneity than the more common high-pressure granulite exposures of restricted size. This diverse character warrants careful consideration when reconstructing the nature and histories of deep crustal levels based on restricted samples of lower crustal xenoliths. Thus, although the current segmented architecture in the East Lake Athabasca region was primarily acquired during exhumation, this overprinted a primary heterogeneity that was a fundamental characteristic of the rocks during their evolution in the deep crust.

REFERENCES

Aleinikoff, J.N., Wintsch, R.P., Fanning, C.M., and Dorais, M.J., 2002, U-Pb geochronology of zircon and polygenetic titanite from the Glastonbury Complex, Connecticut, USA: an integrated SEM, EMPA, TIMS, and SHRIMP study: Chemical Geology, v. 188, p. 125-147.

Baldwin, J.A., Bowring, S.A., and Williams, M.L., 2003, Petrological and geochronological constraints on high pressure, high temperature metamorphism in the Snowbird tectonic zone, Canada: Journal of Metamorphic Geology, v. 21, p. 1-19.

Baldwin, J.A., Bowring, S.A., Williams, M.L., and Williams, I.S., 2004, Eclogites of the Snowbird tectonic zone: petrological and U-Pb geochronological evidence for Paleoproterozoic high-pressure metamorphism in the western Canadian shield: Contributions to Mineralogy and Petrology, v. 147, p. 528-548.

Chamberlain, K.R., and Bowring, S.A., 2000, Apatite-feldspar U-Pb thermochronometer:A reliable, mid-range (~450°C), diffusion-controlled system: Chemical Geology, v. 172, p. 73-200.

Cherniak, D.J., 1993, Lead diffusion in titanite and preliminary results on the effects of radiation damage on Pb transport: Chemical Geology, v. 110, p. 177-194.

Cherniak, D.J., 2000, Pb diffusion in rutile: Contributions to Mineralogy and Petrology, v. 139, p. 198-207.

Cherniak, D.J., Lanford, W.A., and Ryerson, F.J., 1991, Lead diffusion in apatite and zircon using ion implantation and Rutherford backscattering techniques: Geochimica et Cosmochimica Acta, v. 55, p. 1663-1673.

Cherniak, D.J., and Watson, E.B., 2001, Pb diffusion in zircon: Chemical Geology, v. 172, p. 5-24.

Cherniak, D.J., Watson, E.B., Grove, M., and Harrison, T.M., 2004, Pb diffusion in monazite: A combined RBS/SIMS study: Geochimica et Cosmochimica Acta, v. 68, p. 829-840.

Cumbest, R.J., Johnson, E.L. and Onstott, T.C., Argon composition of metamorphic fluids:Implications for ^{40}Ar/^{39}Ar geochronology: Geological Society of America Bulletin, v. 106, p. 942-951.

Cumming, G.L., Krstic, D., and Wilson, J.A., 1987, Age of the Athabasca Group, northern Alberta: Geological Association of Canada-Mineralogical Society of Canada, Joint Annual Meeting, Program with Abstracts, v. 12, p. 35.

Dodson, M.H., 1973, Closure temperature in cooling geochronological and petrological systems: Contributions to Mineralogy and Petrology, v. 40, p. 259-274.

Frost, B.R., Chamberlain, K.R., and Schumacher, J.C., 2000, Sphene (titanite): phase relations and role as a geochronometer: Chemical Geology, v. 172, p. 131-148.

Grove, M. and Harrison, T.M., 1996, 40Ar* diffusion in Fe-rich biotite: American Mineralogist, v. 81, p. 940-951.

Hames, W.E. and Bowring, S.A., 1994, An empirical evaluation of the argon diffusion geometry in muscovite: Earth and Planetary Science Letters: v. 124, p. 161-167.

Hanmer, S., 1997, Geology of the Striding-Athabasca mylonite zone, northern Saskatchewan and southeastern District of Mackenzie, Northwest Territories: Geological Survey of Canada Bulletin, v. 501, pp.1-92.

Hanson, G.N., Catanzaro, E.J., and Anderson, D.H., 1971, U-Pb ages for sphene in a contact metamorphic zone: Earth and Planetary Science Letters, v. 12, p. 231-237.

Harrison, T.M., 1981, Diffusion of 40Ar in hornblende: Contributions to Mineralogy and Petrology, v. 78, p. 324-331.

Hodges, K.V., Hames, W.E., and Bowring, S.A., 1994, 40Ar/39Ar age gradients in micas from a high-temperature-low-pressure metamorphic terrain: Evidence for very slow cooling and implications for the interpretation of age spectra: Geology, v. 22, p. 55058.

Hodges, K.V. and Bowring, S.A., 1995, 40Ar/39Ar thermochronology of isotopically zoned micas: Insights from the southwestern USA Proterozoic orogen: Geochimica Cosmochimica Acta, v. 59, p. 3205-3220.

Hoffman, P.F., 1988, United Plates of America, the birth of a craton: Early Proterozoic assembly and growth of Laurentia: Annual Reviews of Earth and Planetary Science Letters, v. 16, p.545-603.

Kelley, S., 2002, Excess Ar in K-Ar and Ar-Ar geochronology: Chemical Geology, v. 188, p. 1-22.

Kopf, C. 1999. Deformation, metamorphism, and magmatism in the East Athabasca mylonite triangle, northern Saskatchewan: Implications for the Archean and Early Proterozoic crustal structure of the Canadian Shield. Ph. D. dissertation thesis, University of Massachusetts-Amherst, p. 139.

Koppers, A.A.P., 2002, ArArCALC—software for 40Ar/39Ar age calculations: Computers and Geosciences, v. 28, p. 605-619.

Krikorian, L. and Williams, M.L. 2002. Paleoproterozoic high grade metamorphism in the Wholdaia Lake segment of the Snowbird Tectonic Zone, Northwest Territories. Geological Association of Canada-Mineralogical Association of Canada, Saskatoon, Saskatchewan, Program with abstracts, 27: 64.

Krogstad, E.J. and Walker, R.J., 1994, Higher closure temperatures of the U-Pb system in large apatites from the Tin Mountain pegmatite , Black Hills, South Dakota, USA: Geochimica et Cosmochimica Acta, v. 58, p. 3845-3853.

Ludwig, K. R. (1980) Calculation of uncertainties of U-Pb isotope data: Earth and Planetary Sciences Letters, v. 46, p. 212–220.

Mahan, K.H., Williams, M.L., and Baldwin, J.A., 2003, Contractional uplift of deep crustal rocks along the Legs Lake shear zone, western Churchill Province, Canadian Shield: Canadian Journal of Earth Sciences, v. 40, p. 1085-1110.

Mahan, K.H. and Williams, M.L., 2005, Reconstruction of a large deep-crustal exposure: Implications for the Snowbird tectonic zone and early growth of Laurentia: Geology, v.33, p. 385-388.

Mahan, K.H., 2005, Exhumation of exposed deep continental crust, western Canadian Shield: Integrating structural analysis, petrology, and in situ geochronology: PhD thesis, University of Massachusetts, Amherst, Massachusetts.

Mezger, K., Hanson, G.N., and Bohlen, S.R., 1989, High-precision U-Pb ages of metamorphic rutile: application to the cooling history of high-grade terranes: Earth and Planetary Science Letters, v. 96, p. 106-118.

O'Brien, P.J. and Rotzler, J., 2003, High-pressure granulites: formation, recovery of peak conditions and implications for tectonics: Journal of Metamorphic Geology, v. 21, p. 3-20.

Peterson, T.D., Van Breenan, O., Sandeman, H. and Cousens, B., 2002, Proterozoic (1.85-1.75 Ga) igneous suites of the western Churchill Province: granitoid and ultrapotassic magmatism in a reworked Archean hinterland: Precambrian Research, v. 119, p. 73-100.

Rainbird, R.H., Hadlari, T., Aspler, L.B., Donaldson, J.A., LeCheminant, A.N. and Peterson, T.D., 2003, Sequence stratigraphy and evolution of the Paleoproterozoic intracontinental Baker Lake and Thelon basins, western Churchill Province, Nunavut, Canada: Precambrian Research, v. 1.25, p. 21-53.

Rayner, N.M., Stern, R.A., and Rainbird, R.H., 2003, SHRIMP U-Pb detrital zircon geochronology of Athabasca Group sandstones, northern Saskatchewan and Alberta: GSC Current Research, 2003-F2, 20 pp.

Reddy, S.M., Kelley, S.P. and Magennis, L., 1997, Microstructural and argon laserprobe study of shear zone development at the western margin of the Nanga Parbat-Haramosh Massif, western Himalaya: Contributions to Mineralogy and Petrology, v. 128, p. 16-28.

Renne, P.R., Swisher, C.C., Deino, A.L., Karner, D.B., Owens, T., and DePaolo, D.J., 1998, Intercalibration of standards, absolute ages and uncertainties in 40Ar/39Ar dating: Chemical Geology, v. 145, p. 1119867-152.

Robbins, G.A., 1972, Radiogenic argon diffusion in muscovite under hydrothermal conditions: M.S., Brown University.

Roddick, J.C., Cliff, R.A., and Rex, D.C., 1980, The evolution of excess argon in Alpine biotites—A 40Ar-39Ar analysis: Earth and Planetary Sciences Letters, v. 48, p. 185-208.

Snoeyenbos, D.R., Williams, M.L. and Hanmer, S., 1995, Archean high-pressure metamorphism in the western Canadian Shield: European Journal of Mineralogy, v. 7, p.1251-1272.

Stacey, J.C. and Kramers, J.D., 1975, Approximation of terrestrial lead isotope evolution by a two-stage model: Earth and Planetary Science Letters, v.26, p.207-221.

Steiger, R.H. and Jaeger, E., 1977, Subcommission on geochronology: convention on th use of decay constants in geo- and cosmochronology: Earth and Planetary Science Letters, v. 36, p. 359-362.

Verts, L.A., Chamberlain, K.R., and Frost, C.D., 1996, U-Pb sphene dating of contact metamorphism: the importance of sphene growth in the contact aureole of the Red Mountain pluton, Laramie Mountains, Wyoming: Contributions to Mineralogy and Petrology, v. 125, pl. 186-199.

Wendt, I., and Carl, C., 1991, The statistical distribution of the mean squared weighted deviation: Chemical Geology, v. 86, p. 275-285.

Williams, M.L. and Hanmer, S., 2005, Structural and metamorphic processes in the lower crust: Evidence from an isobarically cooled terrane, the East Athabasca mylonite triangle: ---.

Williams, M.L., Hanmer, S., Kopf, C. and Darrach,M., 1995, Syntectonic generation and segregation of tonalitic melts from amphibolite dikes in the lower crust, Striding-Athabasca mylonite zone, northern Saskatchewan: Journal of Geophysical Research, v.100(B8), p.15,717-15,734.

Williams, M.L., Mellis, E.A., Kopf,C. and Hanmer,S., 2000, Microstructural Tectonometamorphic processes and the development of gneissic layering: a mechanism for metamorphic segregation: Journal of Metamorphic Geology, v. 18, p.41-57.

York, D., 1969, Least squares fitting of a straight line with correlated errors: Earth and Planetary Science Letters, v. 5, p. 320-324.

FIGURE CAPTIONS

Figure 1. Geological map of the western Canadian Shield showing major tectonic features. AB-Athabasca basin, BL-Baker Lake basin, KX-Krumanituar Complex, STZ-Snowbird tectonic zone, TB-Thelon Basin, THO-Trans-Hudson Orogen, TO-Taltson

Orogen, TMZ-Thelon Magmatic Zone, UX-Uvauk Complex, VR-Virgin River dikes and shear zone. The rectangle shows the East Lake Athabasca region enlarged in Figure 2.

Figure 2. Geological map of the East Lake Athabasca region, northern Saskatchewan.

Figure 3. Concordia diagram for apatite from sample 03-52 showing the effect of selection of initial Pb isotopic composition on the computed dates. Gray ellipses are dates calculated using the Stacey and Kramers (1975) model for terrestrial Pb evolution. Green ellipses are dates calculated using the isotopic composition of leached coexisting feldspars from this sample.

Figure 4. Simplified geological maps of the East Lake Athabasca region showing sample locations and ranges of ^{207}Pb/^{206}Pb dates for A) titanite, B) apatite, and C) rutile. Data in italics are from Baldwin et al. (2003, 2004). Chip-Chipman domain, NW-Northwestern domain, Sou-Southern domain.

Figure 5. Simplified geological maps of the East Lake Athabasca region showing sample locations and ^{40}Ar/^{39}Ar dates for A) hornblende, B) muscovite, and C) biotite. The weighted mean of the laser fusion hornblende fragment data is given for the one hornblende sample not characterized by a variable mixtures of excess ^{40}Ar and atmospheric components. Muscovite and biotite dates are weighted means of the laser excimer ablation analyses. Chip-Chipman domain, NW-Northwestern domain, Sou-Southern domain.

Figure 6. U-Pb concordia diagram for Chipman migmatitic dike sample 03-52 including zircon, titanite, apatite and rutile data. Zircon data are discussed in Chapter 2. Photos are examples of minerals analyzed from this sample. ^{40}Ar/^{39}Ar hornblende and (U-Th)/He zircon data were also acquired for this sample.

Figure 7. U-Pb concordia diagrams of titanite, apatite and rutile data for the A) Chipman, B) northwestern, C) southern, and D) Hearne domains.

Figure 8. Inverse isochron diagrams for A) amphibolite facies Chipman mafic dike sample 01M123C and B) granulite facies Chipman mafic dike sample SZ00-196C. Both a York fit through selected data points, and a reference line through an atmospheric component, are depicted. Refer to the text for data interpretations. Green squares are data points included in the data regression. Smaller blue squares are not included.

Figure 9. $^{40}Ar/^{39}Ar$ biotite data for Chipman domain pegmatite sample 02-76B. A) Location of laser spot fusion analyses for one of three crystals analyzed from this sample. Dates given for individual spots do not include the systematic uncertainty in the J-value to facilitate comparison of intra-crystal dates. The error on the weighted mean date includes the J-value uncertainty to permit appropriate comparison with $^{40}Ar/^{39}Ar$ data for other samples and with U-Pb data. B) Incremental heating experiment that yields a weighted mean plateau date indistinguishable from the weighted mean of laser fusion dates for this sample.

Figure 10. Temperature-time diagram for the Chipman domain and associated interpretation of the cooling path.

Figure 11. Temperature-time diagram for the Northwestern domain and associated interpretation of the cooling path. Chipman domain thermal history depicted as the gray dashed line for reference.

Figure 12. Temperature-time diagram for the southern domain and associated interpretation of the cooling path. Chipman domain thermal history depicted as the gray dashed line for reference.

Figure 13. Temperature-time diagram for the Hearne domain and associated interpretation of the thermal history. Chipman domain thermal history depicted as the gray dashed line for reference.

Table 1. U-Pb TIMS isotopic data for titanite, apatite and rutile

		Composition						Isotopic Ratios								Dates (Ma)					
Fr	#[a]	Wt (µg)[b]	U (ppm)	Pb (ppm)	Th[c] U	Pb*[d] Pbc	Pbc[d] (pg)	$^{206}\text{Pb}^{e}/^{204}\text{Pb}$	$^{208}\text{Pb}^{f}/^{206}\text{Pb}$	$^{206}\text{Pb}^{f}/^{238}\text{U}$	% err[g]	$^{207}\text{Pb}^{f}/^{235}\text{U}$	% err[g]	$^{207}\text{Pb}^{f}/^{206}\text{Pb}$	% err[g]	$^{206}\text{Pb}^{h}/^{238}\text{U}$	$^{207}\text{Pb}^{h}/^{235}\text{U}$	$^{207}\text{Pb}^{h}/^{206}\text{Pb}$	±	corr. coef.	% Disc
Chipman domain																					
03-52 - Chipman mafic granulite dike																					
s1	1	12	14.1	9.7	3.61	9.6	10.9	323.1	1.043	0.340130	(.27)	5.3997	(.29)	0.11514	(.10)	1887.3	1884.8	1882.1	1.8	0.942	-0.3
s3	1	5	11.7	9.5	4.25	4.4	8.6	148.1	1.219	0.343388	(.75)	5.4642	(.87)	0.11541	(.38)	1902.9	1895.0	1886.3	6.9	0.897	-1.0
s4	1	5	12.6	8.8	3.78	7.4	4.9	254.2	1.100	0.337786	(.79)	5.3642	(.81)	0.11518	(.15)	1876.0	1879.2	1882.7	2.7	0.983	0.4
a1	1	70	9.6	3.1	0.01	23.1	3.3	1515.1	0.004	0.329877	(.21)	5.1285	(.24)	0.11275	(.11)	1837.8	1840.8	1844.3	2.1	0.887	0.4
a3	3	18	8.9	4.7	1.43	4.0	17.5	194.4	0.415	0.329486	(.28)	5.0863	(.33)	0.11196	(.16)	1835.9	1833.8	1831.4	2.9	0.876	-0.3
a4	6	18	10.9	5.8	1.50	4.3	20.0	208.0	0.429	0.328966	(.23)	5.0039	(.27)	0.11032	(.13)	1833.4	1820.0	1804.7	2.4	0.873	-1.8
a6	1	10	5.7	4.6	2.72	1.6	18.2	75.7	0.780	0.324331	(.70)	4.8797	(.82)	0.10912	(.38)	1810.8	1798.8	1784.8	7.0	0.884	-1.7
a7	1	10	4.1	1.9	1.08	3.4	4.6	189.1	0.312	0.322317	(1.12)	4.8463	(1.15)	0.10905	(.20)	1801.0	1793.0	1783.6	3.7	0.984	-1.1
r1	1	60	9.7	6.5	2.73	4.5	83.3	177.0	0.796	0.335001	(.09)	5.2801	(.15)	0.11431	(.12)	1862.6	1865.7	1869.1	1.3	0.653	0.4
r2	1	25	9.2	3.0	0.01	22.4	7.8	1424.2	0.003	0.332348	(.19)	5.1952	(.20)	0.11337	(.07)	1849.8	1851.8	1854.2	2.0	0.934	0.3
r3	1	15	12.9	4.5	0.04	9.1	6.8	584.2	0.012	0.332240	(.24)	5.1856	(.25)	0.11320	(.07)	1849.2	1850.3	1851.4	1.4	0.955	0.1
r5b	1	12	15.4	5.3	0.01	8.7	6.8	560.9	0.004	0.332984	(.29)	5.2159	(.30)	0.11361	(.08)	1852.8	1855.2	1857.9	1.5	0.963	0.3
03-88A - Mafic granulite gneiss																					
a1	1	28	15.1	5.3	0.31	9.6	14.1	573.1	0.091	0.309856	(.12)	4.5801	(.14)	0.10720	(.07)	1740.0	1745.7	1752.4	1.3	0.876	0.8
a2	2	30	15.3	5.3	0.44	16.8	9.0	967.3	0.129	0.310359	(.24)	4.5735	(.25)	0.10688	(.06)	1742.5	1744.5	1746.8	1.1	0.971	0.3
a3	5	30	10.1	4.1	0.59	4.6	22.2	267.6	0.175	0.308167	(.16)	4.5310	(.20)	0.10664	(.11)	1731.7	1736.7	1742.7	2.0	0.831	0.7
r1	1	2	33.4	9.4	0.02	6.2	2.6	425.8	0.008	0.283999	(.88)	4.2449	(.93)	0.10841	(.29)	1611.5	1682.8	1772.8	5.3	0.951	10.3
r3	1	1	26.7	8.4	0.01	5.4	1.6	378.9	0.003	0.327789	(.63)	4.9952	(.68)	0.11052	(.25)	1827.7	1818.5	1808.1	4.5	0.931	-1.2
r4	1	5	6.9	2.9	0.13	1.6	6.5	112.6	0.039	0.296118	(1.34)	4.4208	(1.39)	0.10828	(.40)	1672.0	1716.3	1770.6	7.3	0.958	6.3
r5	3	2	31.3	10.1	0.02	5.8	3.3	394.7	0.007	0.316166	(.76)	4.7465	(.80)	0.10888	(.24)	1771.0	1775.5	1780.8	4.4	0.952	0.6
SZ00-196C - Chipman mafic granulite dike																					
s4	1	5	54.7	27.9	1.37	6.2	19.6	221.5	0.395	0.342964	(.21)	5.4915	(.26)	0.11613	(.14)	1900.9	1899.3	1897.5	2.1	0.849	-0.2
s6	1	5.6	54.9	23.8	0.99	13.6	9.3	520.7	0.287	0.339424	(.18)	5.4178	(.21)	0.11577	(.10)	1883.9	1887.7	1891.8	1.8	0.878	0.5
s8	1	35	17.0	7.5	1.17	22.1	11.4	1070.7	0.341	0.338936	(.16)	5.4066	(.17)	0.11569	(.06)	1881.5	1885.9	1890.7	1.0	0.944	0.6
s9	1	34	11.6	6.2	1.70	7.3	25.7	326.1	0.492	0.342084	(.15)	5.4748	(.19)	0.11607	(.11)	1896.7	1896.7	1896.6	2.0	0.813	0.0
SZ00-196B Chipman tonalite gneiss																					
s4	1	7.3	72.9	32.9	1.19	15.3	14.8	717.2	0.347	0.339367	(.11)	5.4070	(.14)	0.11555	(.08)	1883.6	1886.0	1888.5	1.4	0.814	0.3
s11	1	3.3	79.0	36.3	1.04	7.8	13.8	385.4	0.302	0.339547	(.19)	5.4016	(.22)	0.11538	(.10)	1884.5	1885.1	1885.8	1.9	0.876	0.1
s12	1	3.1	58.5	24.9	0.93	12.3	6.0	625.1	0.270	0.338625	(.25)	5.3844	(.27)	0.11532	(.08)	1880.1	1882.4	1884.9	1.5	0.951	0.3
a1	1	15.0	5.1	5.2	0.50	0.6	51.2	44.0	0.139	0.347810	(.42)	5.4327	(.70)	0.11328	(.51)	1924.1	1890.0	1852.8	9.2	0.694	-4.5
a2	2	16.0	13.3	10.0	0.47	0.9	86.9	60.8	0.135	0.331148	(.18)	5.0663	(.42)	0.11096	(.35)	1843.9	1830.5	1815.2	6.3	0.582	-1.8
a3	4	18.0	9.6	8.0	0.53	0.8	82.9	54.3	0.150	0.336000	(.21)	5.2017	(.45)	0.11228	(.36)	1867.4	1852.9	1836.6	6.5	0.607	-1.9

Table 1. (Continued)

		Composition						Isotopic Ratios								Dates (Ma)					
Fr	#^{a}	Wt (µg)^b	U (ppm)	Pb (ppm)	$\frac{Th^c}{U}$	$\frac{Pb^{*d}}{Pbc}$	Pbc^d (pg)	$\frac{^{206}Pb^e}{^{204}Pb}$	$\frac{^{208}Pb^f}{^{206}Pb}$	$\frac{^{206}Pb^f}{^{238}U}$	% err^g	$\frac{^{207}Pb^f}{^{235}U}$	% err^g	$\frac{^{207}Pb^f}{^{206}Pb}$	% err^g	$\frac{^{206}Pb^h}{^{238}U}$	$\frac{^{207}Pb^h}{^{235}U}$	$\frac{^{207}Pb^h}{^{206}Pb}$	±	corr. coef.	% Disc
Chipman domain (continued)																					
02M133A - Mafic granulite gneiss																					
s1	1	40.0	12.7	5.9	1.26	11.2	19.6	542.0	0.365	0.339891	(.10)	5.4059	(.12)	0.11535	(.07)	1886.1	1885.8	1885.4	1.2	0.836	0.0
s5	1	5.0	38.6	21.1	1.85	6.4	14.6	283.6	0.539	0.338000	(.30)	5.3784	(.32)	0.11541	(.11)	1877.0	1881.4	1886.3	1.9	0.941	0.6
BF02-5C - Chipman granite gneiss																					
s1	1	20.0	4.9	2.6	0.25	1.7	19.6	108.7	0.073	0.342409	(.45)	5.4786	(.54)	0.11604	(.24)	1898.2	1897.2	1896.1	4.4	0.894	-0.1
s2	1	22.0	11.2	4.9	0.24	3.4	24.9	198.6	0.071	0.335966	(.29)	5.3484	(.33)	0.11546	(.13)	1867.2	1876.6	1887.1	2.4	0.914	1.2
s3	1	15.0	9.9	4.5	0.31	2.9	17.9	170.9	0.089	0.338237	(.30)	5.3742	(.35)	0.11524	(.14)	1878.2	1880.7	1883.6	2.5	0.918	0.3
03-175A - Felsic granulite gneiss																					
r1	1	4.3	8.9	3.3	0.03	5.4	23.0	349.5	0.003	0.333994	(.15)	5.2162	(.19)	0.11327	(.11)	1857.7	1855.3	1852.5	2.0	0.817	-0.3
r4	1	10.0	45.9	17.1	0.01	5.3	27.7	345.2	0.001	0.331529	(.12)	5.1899	(.15)	0.11354	(.09)	1845.8	1851.0	1856.8	1.6	0.825	0.7
02-185 - Fehr granite																					
s1	1	12.0	49.2	24.6	0.23	2.1	95.9	132.1	0.067	0.335630	(.12)	5.3667	(.27)	0.11597	(.22)	1865.6	1879.6	1895.0	4.0	0.596	1.8
Northwestern domain																					
03-196 - Felsic granulite gneiss																					
a1	3	18	19.2	14.2	0.16	0.8	145.2	56.7	0.047	0.328565	(.13)	5.0662	(.42)	0.11183	(.37)	1831.4	1830.5	1829.4	6.7	0.549	-0.1
a2	7	15	18.2	17.9	0.20	0.5	179.4	41.7	0.059	0.333673	(.15)	5.2094	(.55)	0.11323	(.48)	1856.2	1854.2	1851.9	8.8	0.547	-0.3
a3	#	0	11.2	9.6	0.08	0.5	107.6	44.6	0.022	0.314781	(.24)	4.6929	(.73)	0.10813	(.63)	1764.2	1766.0	1768.1	11.5	0.554	0.3
r2	1	6	2.2	0.7	0.00	2.7	1.5	200.9	0.001	0.321204	(1.12)	4.8216	(1.37)	0.10887	(.62)	1795.6	1788.7	1780.6	11.4	0.892	-1.0
r4	1	13	3.9	1.4	0.00	3.1	4.9	207.3	0.000	0.324892	(.94)	5.0106	(1.03)	0.11185	(.26)	1813.6	1821.1	1829.7	4.7	0.969	1.0
r5	1	12	1.4	0.5	0.00	2.0	2.6	150.3	0.000	0.324613	(2.75)	4.9141	(3.01)	0.10979	(.69)	1812.2	1804.7	1796.0	12.5	0.975	-1.0
03M13 - Felsic granulite gneiss																					
r1	1	23	11.2	4.3	0.10	5.2	16.2	307.9	0.029	0.330383	(.53)	5.1458	(.55)	0.11296	(.14)	1840.2	1843.7	1847.6	2.2	0.970	0.5
r2	1	15	4.4	2.4	0.13	1.3	15.8	89.3	0.038	0.335569	(1.17)	5.3068	(1.26)	0.11470	(.38)	1865.3	1870.0	1875.1	6.0	0.953	0.6
r3	1	2	17.3	7.0	0.02	2.0	4.8	137.9	0.005	0.324876	(1.47)	5.0136	(1.62)	0.11193	(.44)	1813.5	1821.6	1830.9	8.0	0.964	1.1
Southern domain																					
01SZ40B - Eclogite																					
a1	1	10.0	3.0	2.2	2.01	1.6	9.3	78.3	0.576	0.340174	(1.31)	5.3478	(1.43)	0.11402	(.35)	1887.5	1876.5	1864.4	6.2	0.972	-1.4
a3	1	41.0	2.0	2.6	1.38	0.5	71.1	36.4	0.394	0.342269	(.43)	5.4105	(1.21)	0.11465	(1.01)	1897.6	1886.5	1874.4	18.3	0.591	-1.4
a4	1	44.0	1.4	1.2	2.70	1.7	19.7	72.2	0.787	0.336743	(.80)	5.3394	(.91)	0.11500	(.35)	1871.0	1875.2	1879.9	6.4	0.922	0.5

Table 1. (Continued)

		Composition						Isotopic Ratios								Dates (Ma)					
Fr	#[a]	Wt (μg)[b]	U (ppm)	Pb (ppm)	Th[c]/U	Pb*[d]/Pbc	Pbc[d] (pg)	^{206}Pb[e]/^{204}Pb	^{208}Pb[f]/^{206}Pb	^{206}Pb[f]/^{238}U	% err[g]	^{207}Pb[f]/^{235}U	% err[g]	^{207}Pb[f]/^{206}Pb	% err[g]	^{206}Pb[h]/^{238}U	^{207}Pb[h]/^{235}U	^{207}Pb[h]/^{206}Pb	±	corr. coef.	% Disc
Southern domain (continued)																					
02-281 - Axis mafic granulite																					
a1	1	100	1.2	1.6	5.79	1.8	56.3	56.5	1.647	0.349421	(.29)	5.6049	(.53)	0.11634	(.41)	1931.8	1916.8	1900.7	7.3	0.652	-1.9
a3	1	9.0	2.9	1.9	0.50	1.1	9.3	70.7	0.142	0.350325	(1.47)	5.6109	(1.64)	0.11616	(.50)	1936.1	1917.8	1897.9	9.0	0.954	-2.3
a4	1	57.0	4.5	3.3	3.26	4.3	35.6	149.3	0.945	0.339377	(.20)	5.3959	(.27)	0.11531	(.17)	1883.7	1884.2	1884.8	3.0	0.785	0.1
a5	1	14.5	5.4	5.2	4.18	2.2	24.4	75.8	1.204	0.343024	(.52)	5.4786	(.64)	0.11584	(.32)	1901.2	1897.2	1892.9	5.8	0.870	-0.5
r1	1	6.4	11.0	77.5	0.04	103.5	4.8	312.2	0.013	0.340965	(.63)	5.4137	(.68)	0.11516	(.17)	1891.3	1887.0	1882.3	3.0	0.970	-0.6
r2	1	2.3	69.1	23.0	0.01	15.5	3.3	988.6	0.004	0.337840	(.29)	5.3564	(.32)	0.11499	(.09)	1876.3	1877.9	1879.7	1.5	0.964	0.2
r4	1	22.8	34.6	11.0	0.01	71.0	3.5	4458.7	0.003	0.329811	(.37)	5.2124	(.38)	0.11462	(.05)	1837.5	1854.6	1874.0	1.0	0.990	2.2
r5	1	8.5	36.4	11.8	0.01	48.5	2.1	3254.4	0.001	0.337209	(.17)	5.3519	(.18)	0.11511	(.06)	1873.2	1877.2	1881.6	1.0	0.949	0.5
r6	1	11.5	9.2	3.0	0.02	16.6	2.1	1123.4	0.006	0.336689	(.45)	5.3293	(.48)	0.11480	(.12)	1870.7	1873.6	1876.7	2.2	0.967	0.4
Hearne Domain																					
01M144 Balliet biotite granite																					
s1	1	7.6	6.0	1.668	1.23	82.1	82.1	65.4	0.483	0.320749	(.19)	4.8248	(.53)	0.10910	(.45)	1793.4	1789.2	1784.4	8.2	0.544	-0.6
s2	1	6.3	2.7	0.289	2.61	16.3	16.3	161.6	0.084	0.311013	(.37)	4.5796	(.43)	0.10679	(.19)	1745.7	1745.6	1745.4	3.4	0.902	0.0
s3	1	16.7	6.6	0.180	3.57	48.4	48.4	218.6	0.052	0.313949	(.15)	4.6603	(.31)	0.10766	(.25)	1760.1	1760.2	1760.2	4.5	0.621	0.0
a4	1	7.1	6.5	2.336	1.04	32.6	32.6	53.1	0.686	0.309637	(.56)	4.5611	(.94)	0.10684	(.70)	1738.9	1742.2	1746.1	12.8	0.677	0.5
02M45 - Charlebois calcsilicate																					
s1	1	140.0	6.3	2.4	0.36	9.1	32.9	522.9	0.106	0.325160	(.08)	4.9764	(.11)	0.11100	(.07)	1814.9	1815.3	1815.8	1.3	0.772	0.1
s2	1	34.0	93.7	35.2	0.31	8.6	125.1	498.0	0.089	0.326314	(.07)	5.0041	(.09)	0.11122	(.06)	1820.5	1820.0	1819.5	1.1	0.749	-0.1
s3	1	10.0	92.6	41.2	0.66	4.4	76.8	243.5	0.191	0.325348	(.11)	4.9736	(.27)	0.11087	(.22)	1815.8	1814.8	1813.7	4.0	0.594	-0.1

[a] Number of grains in fraction

[b] Sample weights were estimated to within 40% using measured grain dimensions and nominal densities of 3.5 g/cm^3 for titanite, 3.2 g/cm^3 for apatite, and 4.2 g/cm^3 for rutile.

[c] Th contents calculated from radiogenic ^{208}Pb and the ^{207}Pb/^{206}Pb date of the sample, assuming concordance between U-Th-Pb systems.

[d] Pb* and Pbc represent radiogenic Pb and common Pb respectively.

[e] Measured ratio corrected for fractionation and spike contribution; Pb fractionation was 0.07 ±0.04%/a.m.u. for Faraday detector or 0.25 ± 0.04%/a.m.u. for Daly detector analysis, based on daily analysis of NBS-981.

[f] Measured ratios corrected for fractionation, spike, blank, and initial common Pb; nominal U blank = 0.1 pg ± 50% (2s); nominal Pb blank = 2.0 pg ± 50% (2s); initial Pb isotopic composition estimated from the isotopic composition of feldspars coexisting in the same rock or in a rock of similar composition and age

[g] Numbers in parentheses are the % errors reported at the 2 sigma confidence interval, propagated using the algorithms of Ludwig (1980).

[h] Isotopic ages calculated using the decay constants of Jaffey et al. (1971): $\lambda(^{235}U) = 9.8485 \times 10^{-10}$ yr^{-1} and $\lambda(^{238}U) = 1.55125 \times 10^{-10}$ yr^{-1}; uncertainty in ^{207}Pb/^{206}Pb date reported at the 2 sigma confidence interval.

Table 2. Pb isotopic composition of leached feldspar separates

sample	wt (mg)	$^{206}\mathrm{Pb}^{a}/^{204}\mathrm{Pb}$	$^{207}\mathrm{Pb}/^{204}\mathrm{Pb}$	$^{208}\mathrm{Pb}/^{204}\mathrm{Pb}$
BF03-52: Chipman mafic dike, Chipman domain				
Fsp 1, lg	5.0	15.510	15.238	36.403
Fsp 2, med	3.4	15.345	15.211	36.296
BF03-88A: Mafic granulite, Chipman domain				
Fsp 2	2.5	16.099	15.502	35.912
BF03-196: Felsic granulite, NW domain				
Fsp 1	5.1	13.807	14.737	33.824
Fsp 2	3.1	13.945	14.768	34.048
01SZ40B: Eclogite, Southern domain				
Fsp 1	7.0	14.006	14.824	34.205
Fsp 2	5.9	14.003	14.819	34.186
BF02-281: Axis mafic granulite, Southern domain				
Fsp1	2.8	14.100	14.814	34.039
01M144: Biotite granite, Hearne domain				
Fsp 1	2.5	14.447	15.035	35.246
Fsp 2	2.9	14.432	15.036	35.215

[a] Standard error on analyses is less than 0.05.

Pb fractionation is 0.12 ±0.04%/a.m.u. for Faraday detector based on daily analysis of NBS-981.

Table 3. ^{40}Ar/^{39}Ar Laser Ablation and Fusion Data[a]

Sample[b]	Min	Lithology	Grain widths analyzed (mm)	# Grains included	# points/ scans	# analyses included	Weighted Mean Age (Ma)	Error	MSWD
Chipman Domain									
02-76B	bt	pegmatite	1.0 - 3.3	4 of 4	11/4	15 of 15	**1780**	12	1.2
03-169E	bt	pegmatite	1.2 - 2.2	4 of 4	9/11	20 of 20	**1765**	12	1.4
02-77B	bt	pegmatite	0.7 -1.8	6 of 6	8/5	13 of 13	**1748**	12	2.6
02-108B	bt	felsic vein	0.75 - 2.0	2 of 2	4/1	5 of 5	**1744**	12	2.7
02-183D	msc	micaceous schist	0.8 - 1.3	4 of 4	9/0	8 of 9	**1758**	12	0.1
01M123C	hb	amphibolite dike	---	14 of 18	---	14 of 18	**1729**	11	0.7
Northwestern Domain									
03-196A	bt	retrogress felsic gran	0.5 - 1.2	5 of 5	12/0	12 of 12	**1760**	12	1.2
03-109A	bt	biotite schist	0.8 - 1.9	3 of 4	13/0	10 of 13	**1756**	12	1.0
Southern Domain									
01SZ122B	bt	pegmatite	0.75 - 1.8	5 of 5	15/0	15 of 15	*1816*	*17*	*21.3*
01SZ78	bt	pegmatite	1.0 - 3.0	4 of 4	11/4	15 of 15	*1831*	*15*	*10.1*
Rae Domain									
99B-87	msc	msc-gt-crd schist	2.0 - 3.3	3 of 3	11/5	16 of 16	*1732*	*12*	*3.3*
03-193B	msc	pegmatite	0.9 - 2.1	3 of 3	6/6	12 of 12	**1717**	11	1.2
03M92	msc	pegmatite	~ 3	3 of 3	11/6	17 of 17	**1747**	12	1.9
96W23E	bt	biotite schist	0.6 - 1.6	4 of 4	11/1	12 of 12	**1862**	12	1.2
Hearne Domain									
01M127B	msc	pegmatite	1.0 - 2.0	4 of 4	8/2	10 of 10	**1748**	11	2.8
01M127B	bt	pegmatite	0.8 - 2.8	4 of 4	12/2	12 of 12	**1739**	12	1.1
02M23B	msc	granite	0.75-1.4	3 of 3	10/0	10 of 10	**1739**	12	0.9
02M23B	bt	granite	0.7-1.2	4 of 4	8/0	8 of 8	**1738**	12	0.2

[a] Bold indicates preferred age. Errors are reported at two times the standard error of the mean and include uncertainty in the J-value. Italics indicate sample with weighted mean for which the error was multiplied by the square root of the MSWD to obtain a more appropriate uncertainty estimate. MSWD, mean square weighted deviate.

[b] Mica dates are excimer laser spot ablation data. A hornblende date, based on laser fusion of fragments, is reported for the one sample not characterized by variable excess ^{40}Ar and atmospheric components such that a reliable date could be determined.

Table 4. $^{40}Ar/^{39}Ar$ Biotite Laser Incremental Heating Data[a]

Sample	Grain widths analyzed (mm)	Total Fusion Age (Ma)	Error	# steps included	Weighted Plateau Age (Ma)	Error	MSWD	% $^{39}Ar_K$ on plateau
Chipman Domain								
02-76B	1	1755.6	11.4	10 of 14	**1776**	12	1.6	63.4
Southern Domain								
01SZ122B-2	1.2	1831.7	11.8	7 of 9	**1846**	12	1.9	95.1
01SZ122B-3	1	1811.9	11.8	7 of 11	**1859**	12	1.3	75.4
01SZ122B-4	0.8	1743.6	11.7	5 of 8	*1828*	23	27.3	66.6
01SZ78-1	1	1806.3	12.2	6 of 8	*1822*	17	4.3	51.0
01SZ78-2	0.8	1826.8	12.9	6 of 8	**1827**	13	1.4	99.8
01SZ78-3	0.8	1833.3	12.0	9 of 13	*1842*	13	4.0	95.1
01SZ78-4	0.6	1761.0	12.0	4 of 7	*1800*	18	15.5	79.4
Rae Domain								
96W23E	0.8	1871.0	12.0	10 of 13	**1874**	13	2.7	94.8

[a] Bold indicates a statistically significant weighted plateau age. Errors are reported at two times the standard error of the mean and include uncertainty in the J-value. Italics indicate sample with error plateau for which the error was multiplied by the square root of the MSWD to obtain a more appropriate uncertainty estimate. MSWD, mean square weighted deviate.

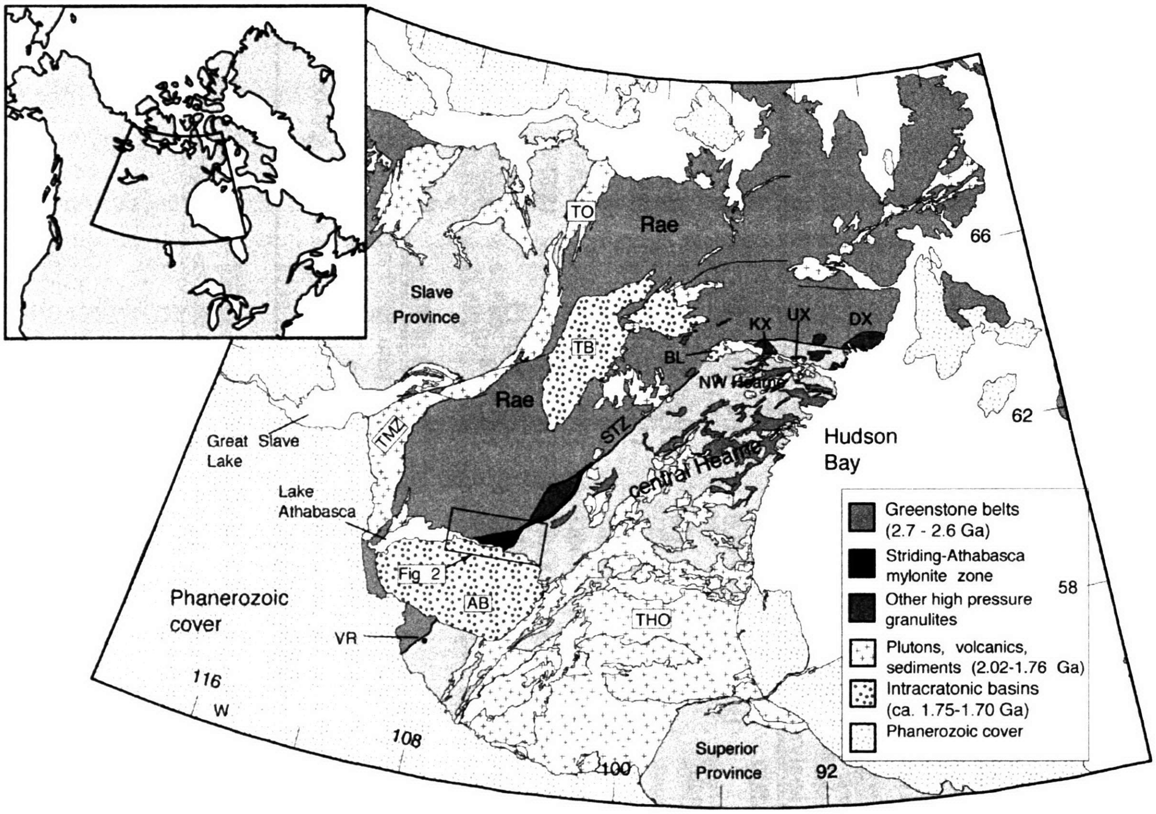
TO
Rae
66
Slave Province
TB
KX
UX
DX
BL
NW Hearne
Rae
62
TMZ
STZ
Hudson Bay
central Hearne
Great Slave Lake
Lake Athabasca
Fig. 2
AB
Phanerozoic cover
VR
THO
58
116
W
108
100
Superior Province
92
Greenstone belts (2.7 - 2.6 Ga)
Striding-Athabasca mylonite zone
Other high pressure granulites
Plutons, volcanics, sediments (2.02-1.76 Ga)
Intracratonic basins (ca. 1.75-1.70 Ga)
Phanerozoic cover

Figure 1

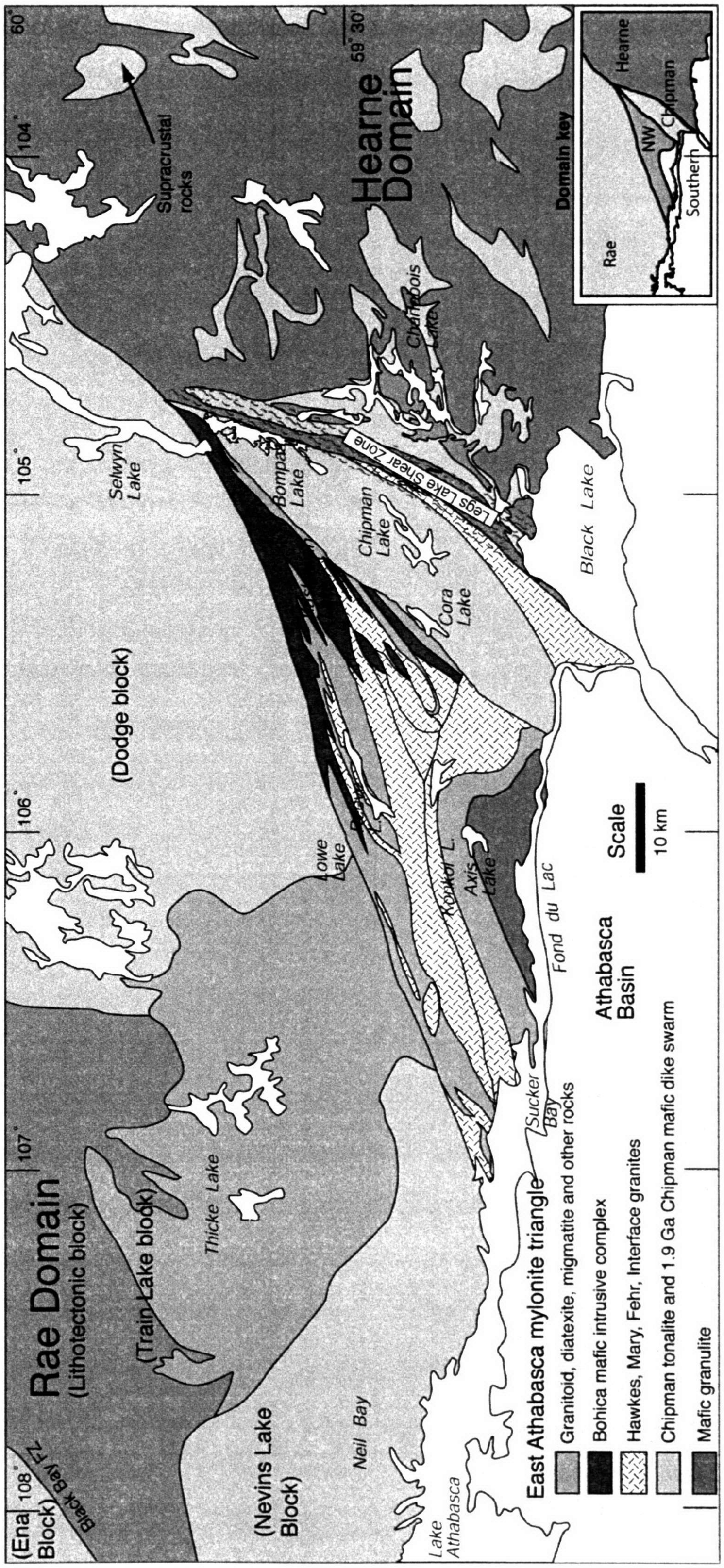
Hearne Domain
Supracrustal rocks
60°
59°30'
104°
105°
106°
107°
108°
Selwyn Lake
Bompas Lake
Legs Lake Shear Zone
Chipman Lake
Cora Lake
Charlebois Lake
Black Lake
(Dodge block)
Lowe Lake
Korkof L.
Axis Lake
Fond du Lac
Scale
10 km
Athabasca Basin
Sucker Bay
Rae Domain
(Lithotectonic block)
(Train Lake block)
Thicke Lake
(Nevins Lake Block)
Neil Bay
Lake Athabasca
(Ena Block)
Black Bay FZ
Domain key
Rae
NW
Southern
Chipman
Hearne
East Athabasca mylonite triangle
Granitoid, diatexite, migmatite and other rocks
Bohica mafic intrusive complex
Hawkes, Mary, Fehr, Interface granites
Chipman tonalite and 1.9 Ga Chipman mafic dike swarm
Mafic granulite

Figure 2

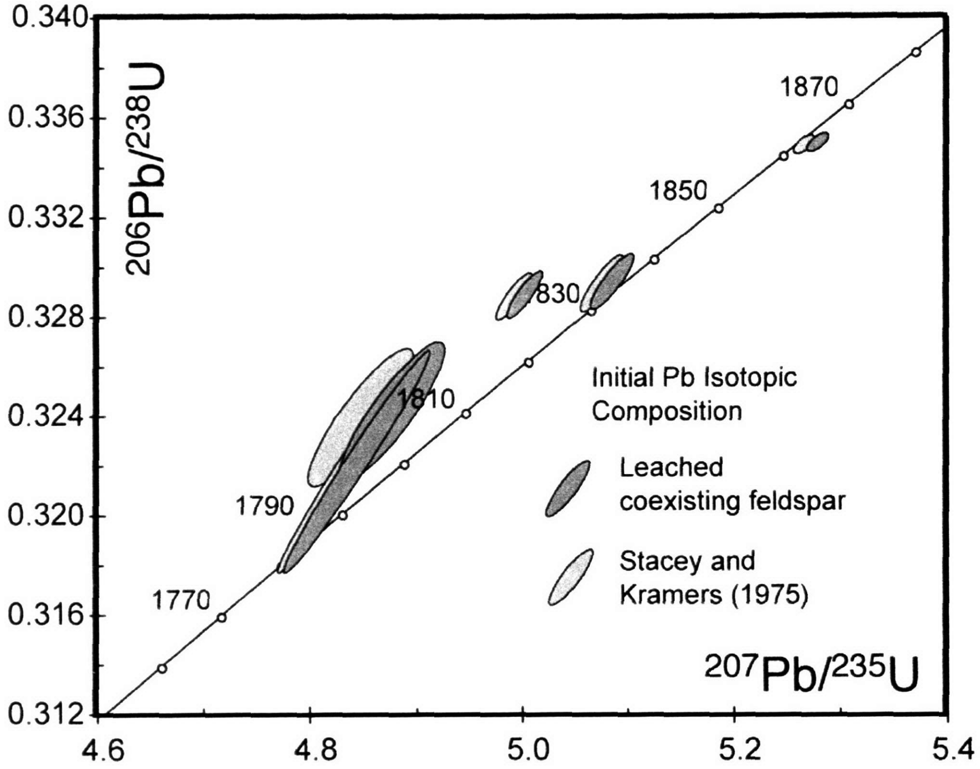
0.340
0.336
0.332
0.328
0.324
0.320
0.316
0.312
^{206}Pb/^{238}U
1870
1850
1830
1810
1790
1770
Initial Pb Isotopic Composition
Leached coexisting feldspar
Stacey and Kramers (1975)
^{207}Pb/^{235}U
4.6
4.8
5.0
5.2
5.4

Figure 3

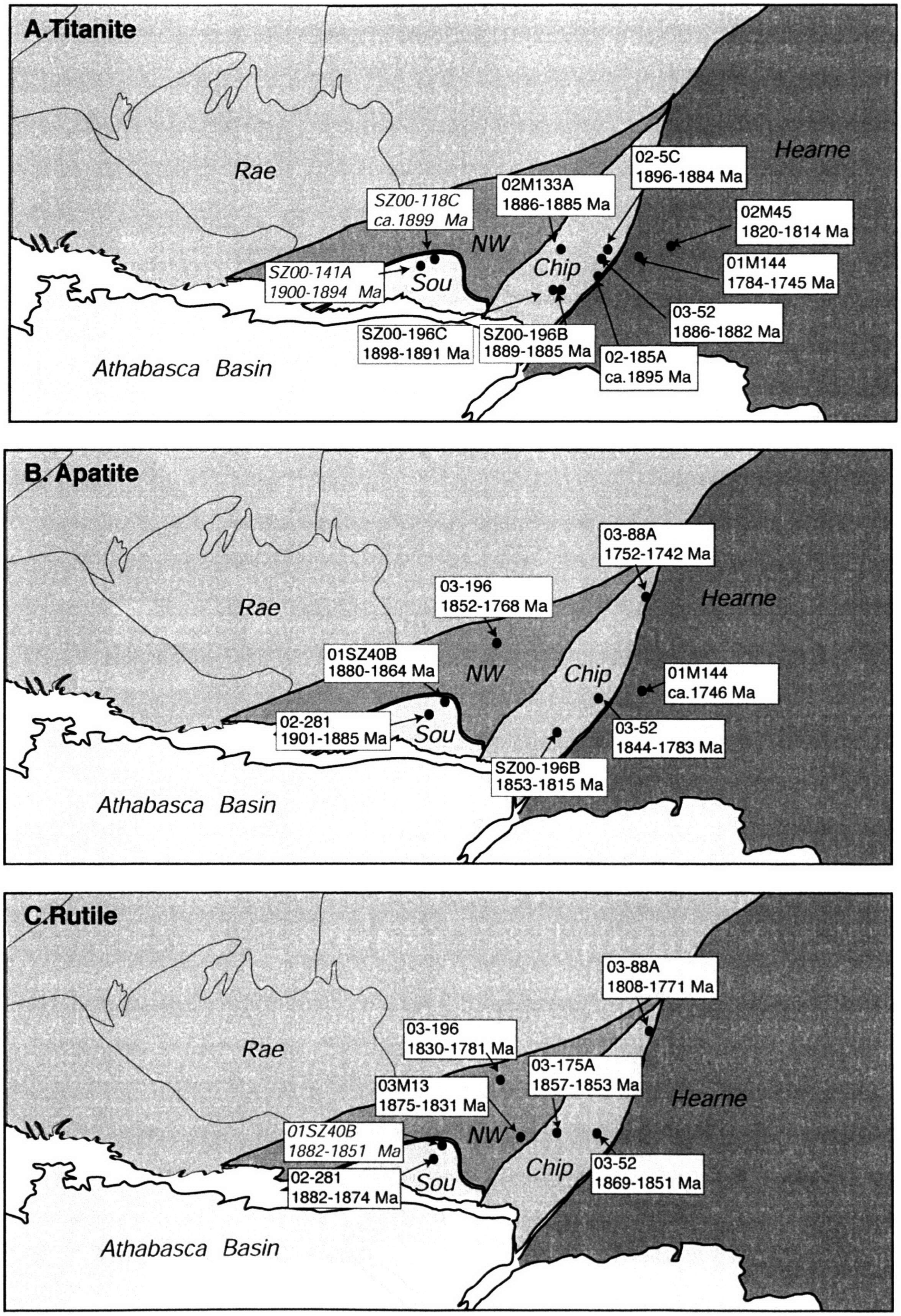
A.Titanite
Rae
Hearne
NW
Chip
Sou
Athabasca Basin
02-5C
1896-1884 Ma
02M133A
1886-1885 Ma
SZ00-118C
ca.1899 Ma
02M45
1820-1814 Ma
01M144
1784-1745 Ma
SZ00-141A
1900-1894 Ma
03-52
1886-1882 Ma
SZ00-196C
1898-1891 Ma
SZ00-196B
1889-1885 Ma
02-185A
ca.1895 Ma
B. Apatite
Rae
Hearne
NW
Chip
Sou
Athabasca Basin
03-88A
1752-1742 Ma
03-196
1852-1768 Ma
01SZ40B
1880-1864 Ma
01M144
ca.1746 Ma
02-281
1901-1885 Ma
03-52
1844-1783 Ma
SZ00-196B
1853-1815 Ma
C.Rutile
Rae
Hearne
NW
Chip
Sou
Athabasca Basin
03-88A
1808-1771 Ma
03-196
1830-1781 Ma
03-175A
1857-1853 Ma
03M13
1875-1831 Ma
01SZ40B
1882-1851 Ma
03-52
1869-1851 Ma
02-281
1882-1874 Ma

Figure 4

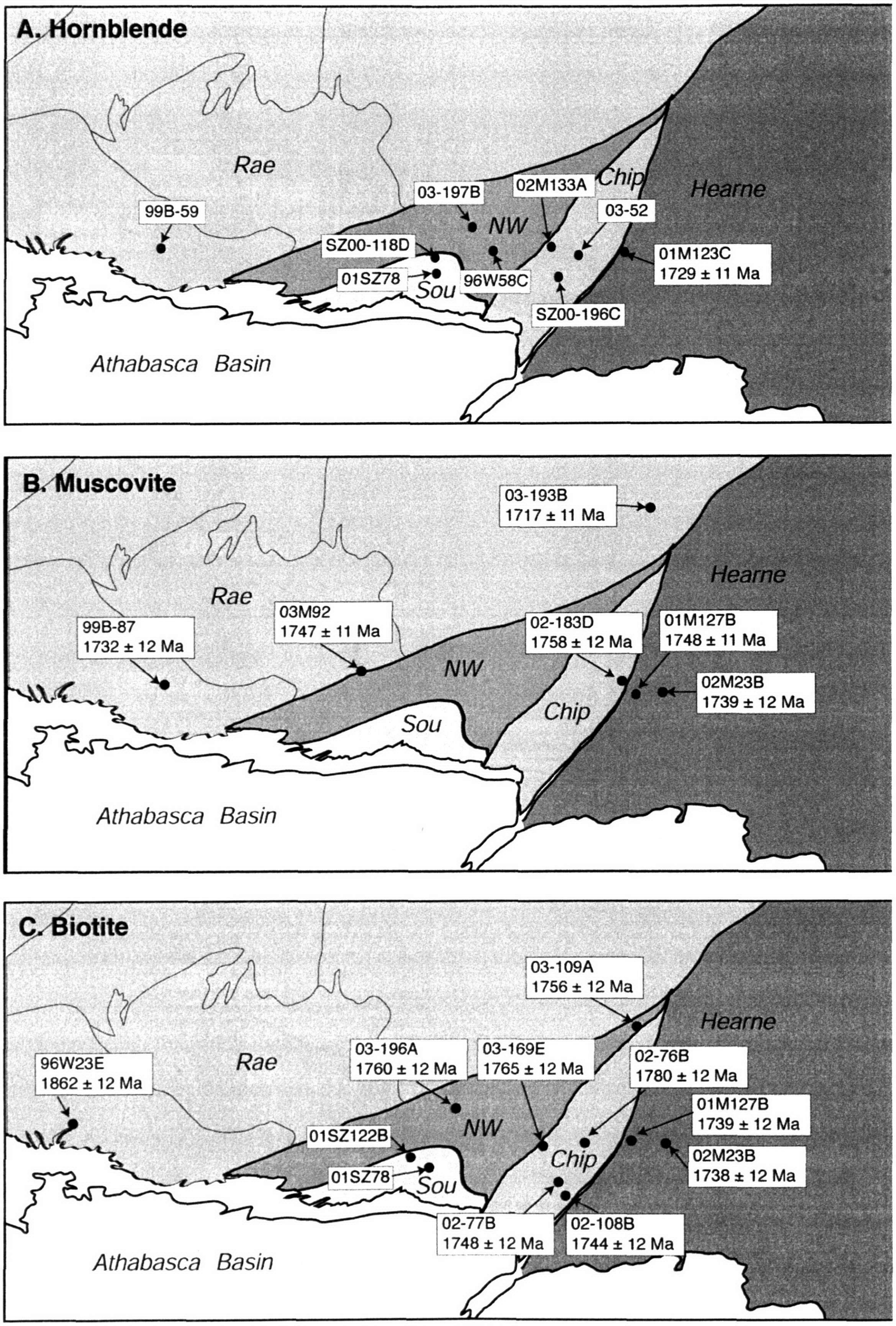
A. Hornblende
Rae
Hearne
Chip
NW
Sou
Athabasca Basin
99B-59
03-197B
02M133A
03-52
SZ00-118D
01SZ78
96W58C
SZ00-196C
01M123C
1729 ± 11 Ma
B. Muscovite
Rae
Hearne
NW
Chip
Sou
Athabasca Basin
03-193B
1717 ± 11 Ma
99B-87
1732 ± 12 Ma
03M92
1747 ± 11 Ma
02-183D
1758 ± 12 Ma
01M127B
1748 ± 11 Ma
02M23B
1739 ± 12 Ma
C. Biotite
Rae
Hearne
NW
Chip
Sou
Athabasca Basin
03-109A
1756 ± 12 Ma
96W23E
1862 ± 12 Ma
03-196A
1760 ± 12 Ma
03-169E
1765 ± 12 Ma
02-76B
1780 ± 12 Ma
01M127B
1739 ± 12 Ma
01SZ122B
01SZ78
02M23B
1738 ± 12 Ma
02-77B
1748 ± 12 Ma
02-108B
1744 ± 12 Ma

Figure 5

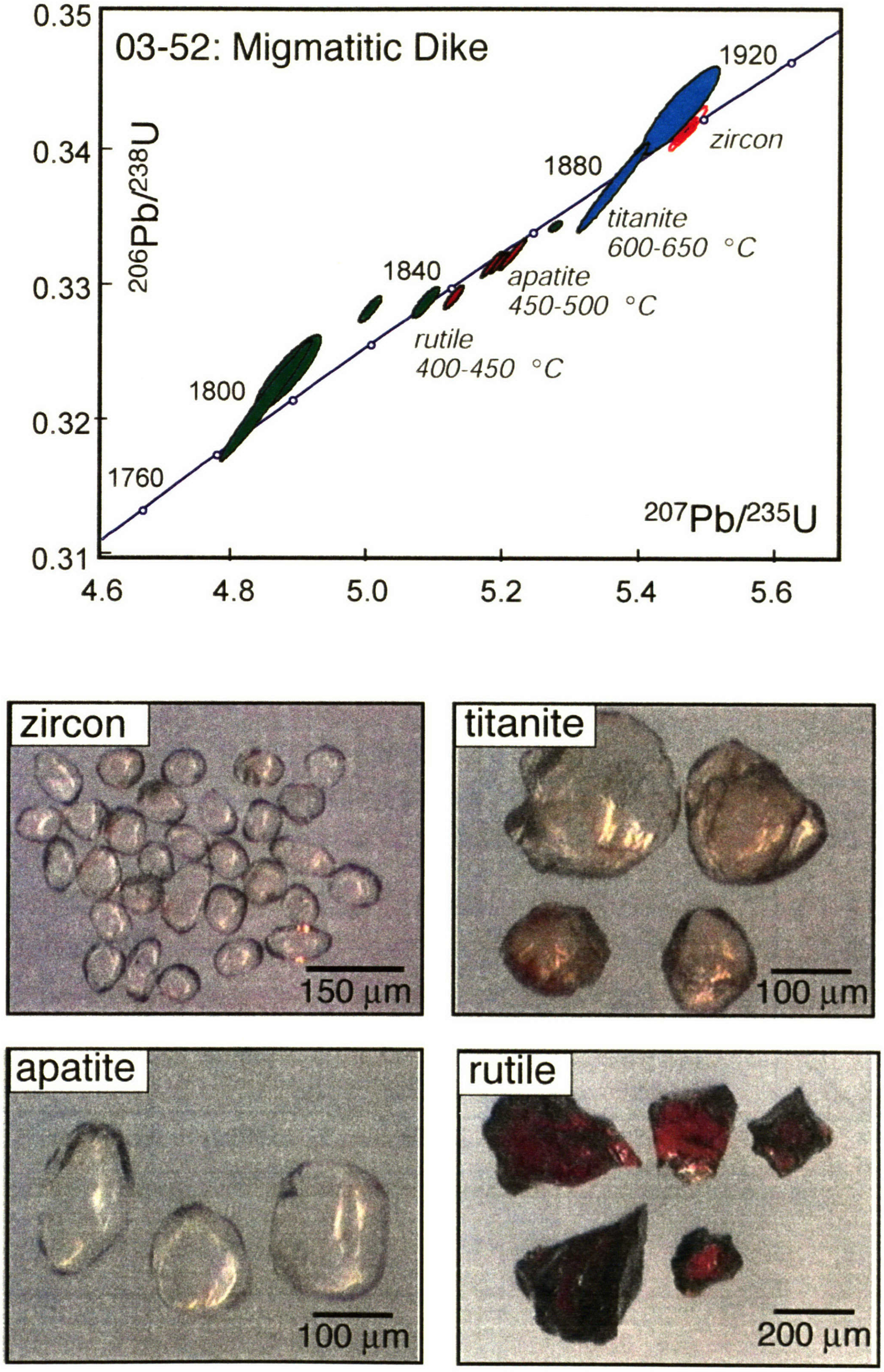
03-52: Migmatitic Dike
0.35
0.34
0.33
0.32
0.31
4.6
4.8
5.0
5.2
5.4
5.6
^{206}Pb/^{238}U
^{207}Pb/^{235}U
1760
1800
1840
1880
1920
zircon
titanite
600-650 °C
apatite
450-500 °C
rutile
400-450 °C
zircon
150 μm
titanite
100 μm
apatite
100 μm
rutile
200 μm

Figure 6

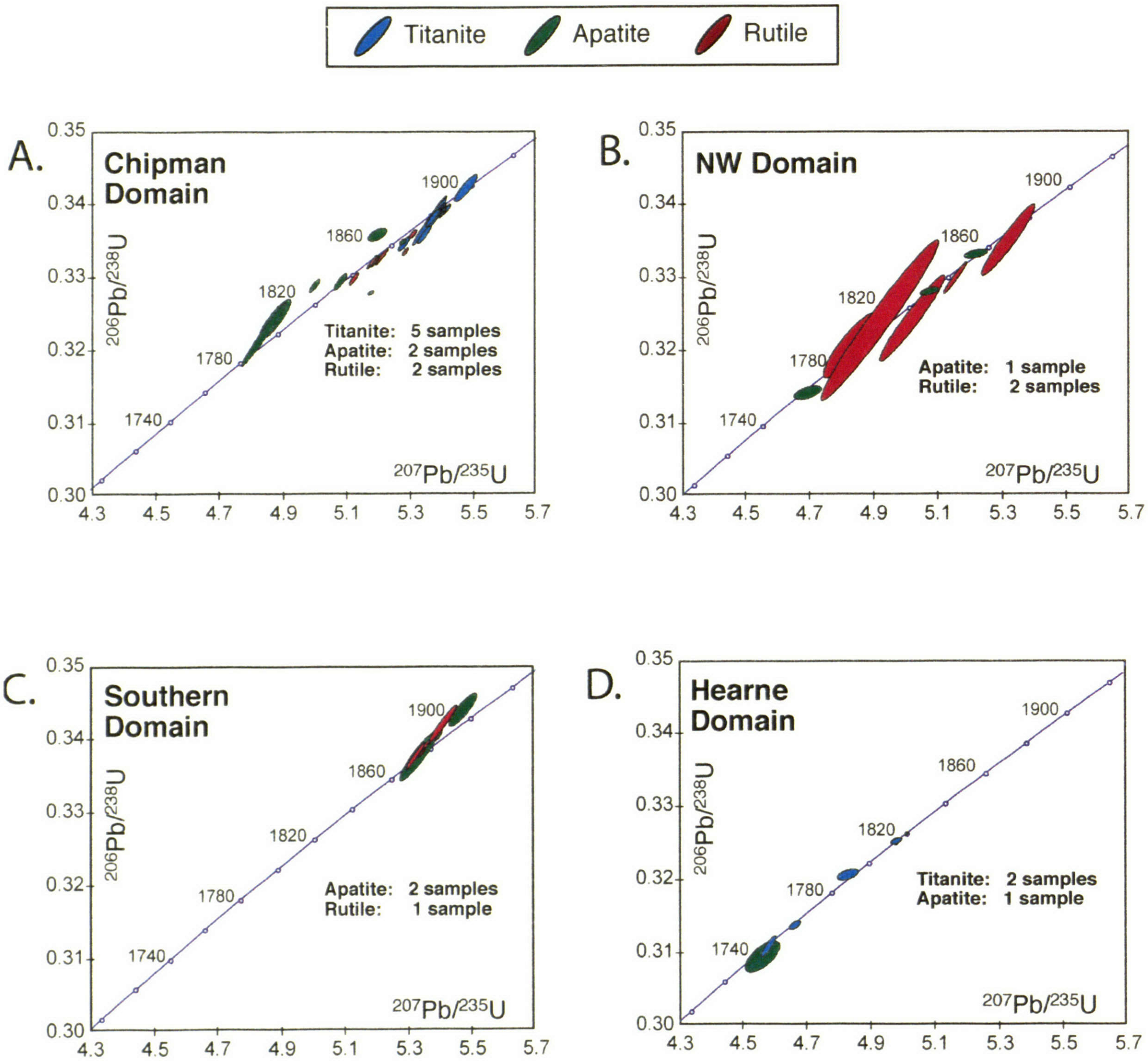
Titanite
Apatite
Rutile
A.
Chipman Domain
Titanite: 5 samples
Apatite: 2 samples
Rutile: 2 samples
B.
NW Domain
Apatite: 1 sample
Rutile: 2 samples
C.
Southern Domain
Apatite: 2 samples
Rutile: 1 sample
D.
Hearne Domain
Titanite: 2 samples
Apatite: 1 sample
1740
1780
1820
1860
1900
$^{206}Pb/^{238}U$
$^{207}Pb/^{235}U$
0.30
0.31
0.32
0.33
0.34
0.35
4.3
4.5
4.7
4.9
5.1
5.3
5.5
5.7

Figure 7

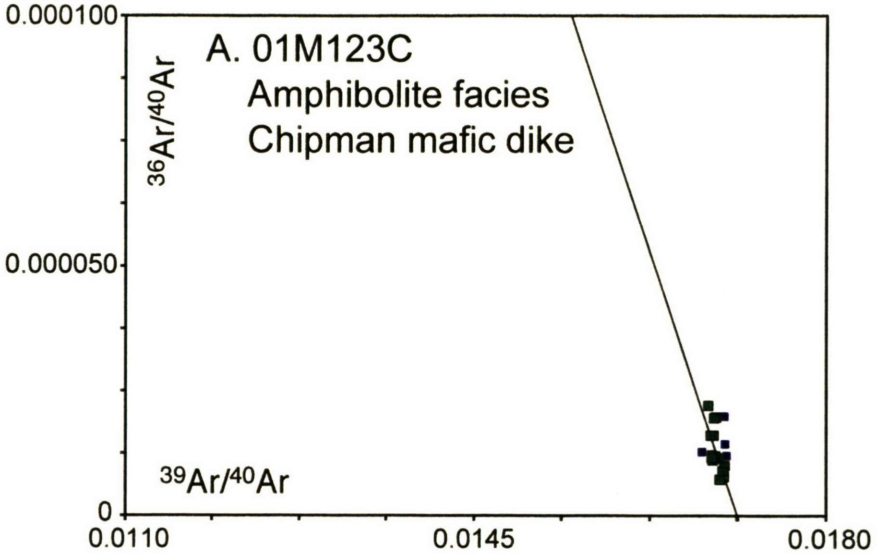
0.000100
0.000050
0
$^{36}Ar/^{40}Ar$
A. 01M123C
Amphibolite facies
Chipman mafic dike
$^{39}Ar/^{40}Ar$
0.0110
0.0145
0.0180

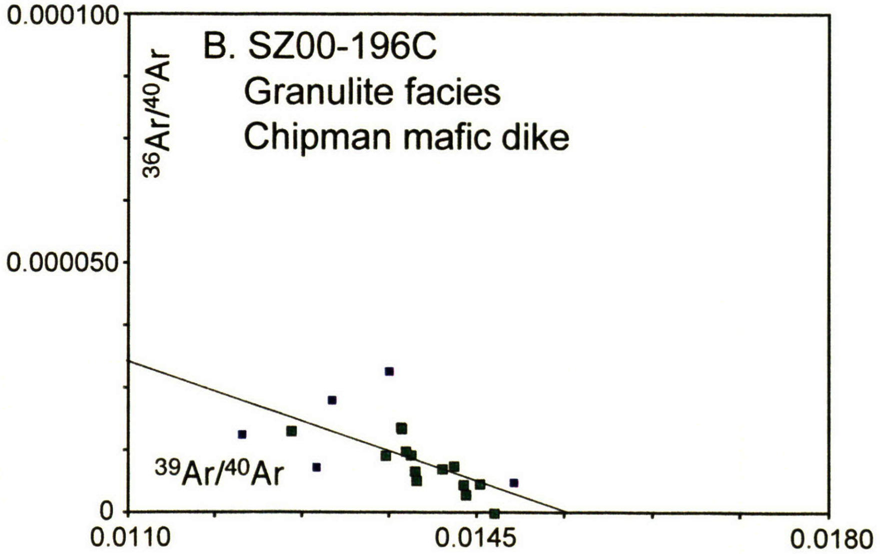
0.000100
0.000050
0
$^{36}Ar/^{40}Ar$
B. SZ00-196C
Granulite facies
Chipman mafic dike
$^{39}Ar/^{40}Ar$
0.0110
0.0145
0.0180

Figure 8

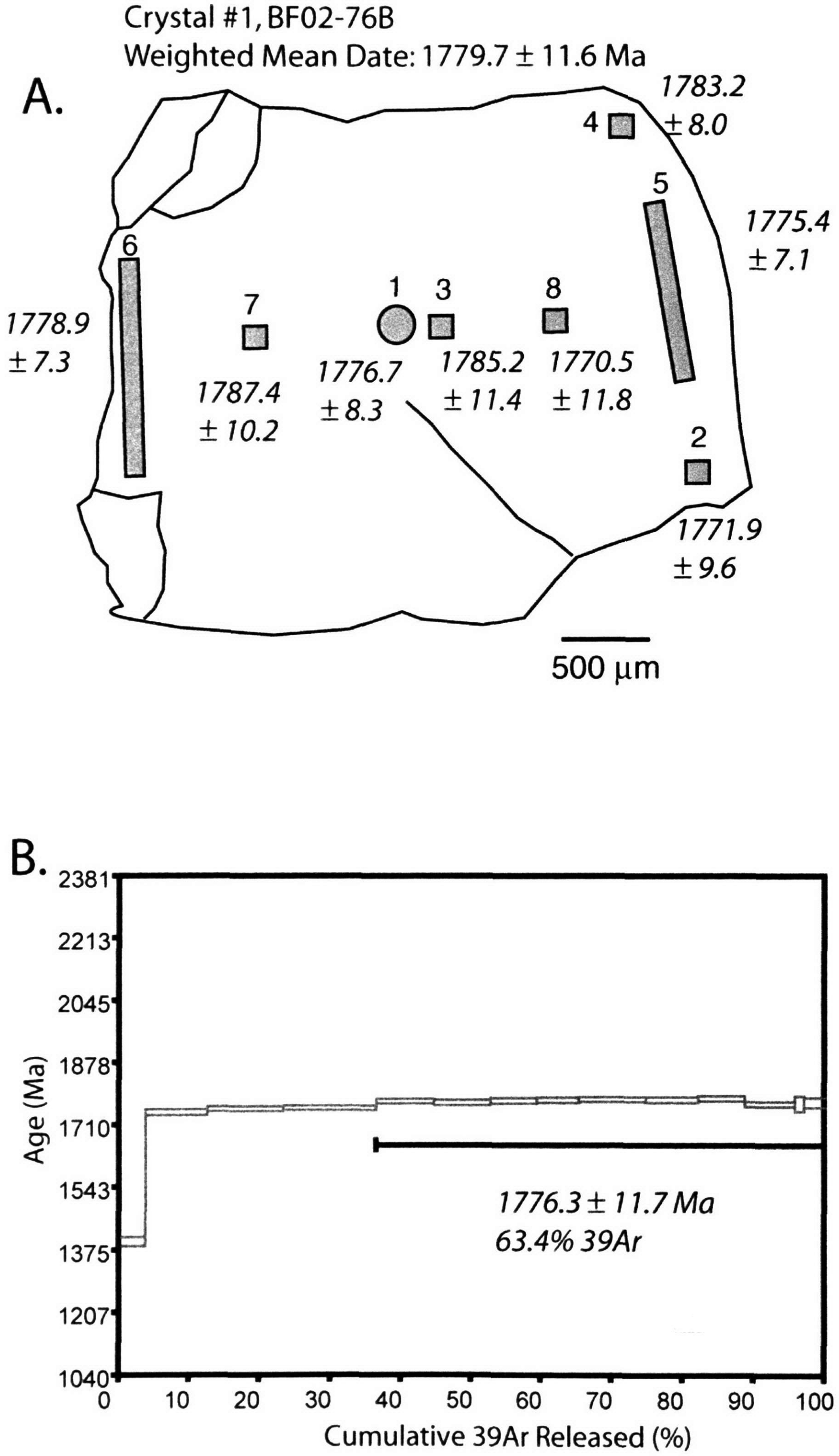
Crystal #1, BF02-76B
Weighted Mean Date: 1779.7 ± 11.6 Ma
A.
4
1783.2 ± 8.0
5
1775.4 ± 7.1
6
1778.9 ± 7.3
7
1787.4 ± 10.2
1
1776.7 ± 8.3
3
1785.2 ± 11.4
8
1770.5 ± 11.8
2
1771.9 ± 9.6
500 μm
B.
2381
2213
2045
1878
1710
1543
1375
1207
1040
Age (Ma)
0
10
20
30
40
50
60
70
80
90
100
Cumulative 39Ar Released (%)
1776.3 ± 11.7 Ma
63.4% 39Ar

Figure 9

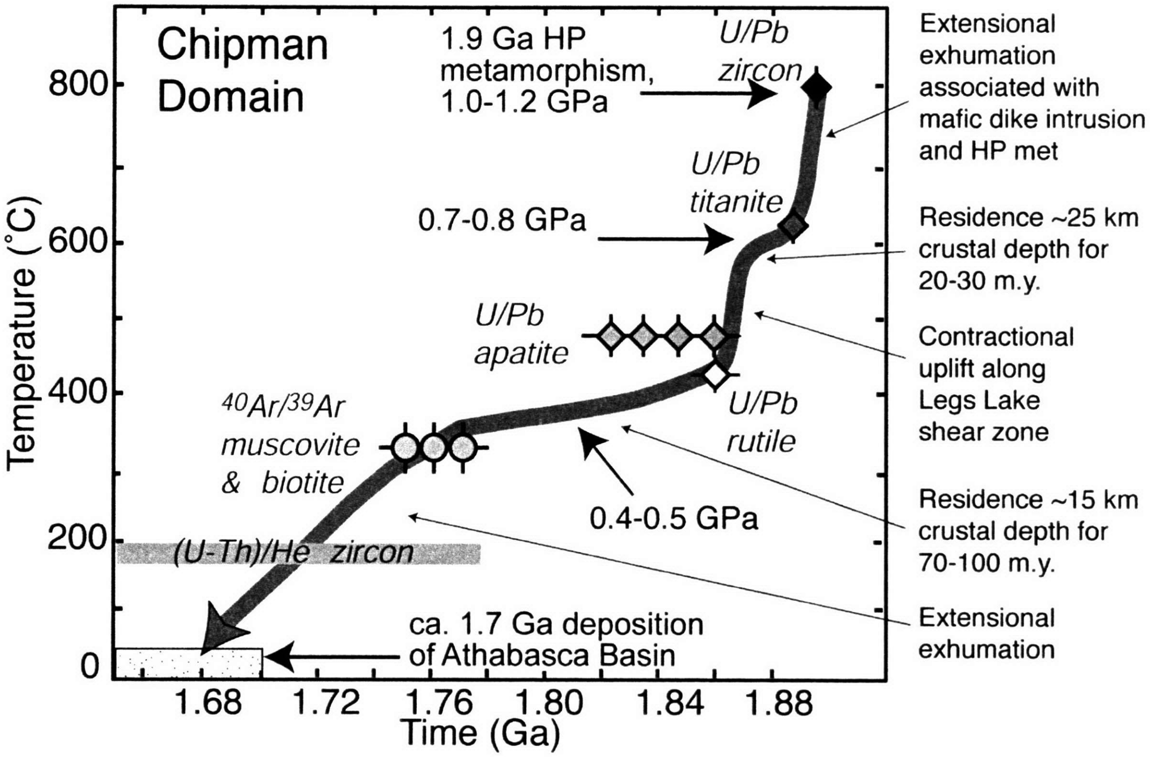
Chipman Domain
1.9 Ga HP metamorphism, 1.0-1.2 GPa
U/Pb zircon
U/Pb titanite
0.7-0.8 GPa
U/Pb apatite
U/Pb rutile
^{40}Ar/^{39}Ar muscovite & biotite
0.4-0.5 GPa
(U-Th)/He zircon
ca. 1.7 Ga deposition of Athabasca Basin
Extensional exhumation associated with mafic dike intrusion and HP met
Residence ~25 km crustal depth for 20-30 m.y.
Contractional uplift along Legs Lake shear zone
Residence ~15 km crustal depth for 70-100 m.y.
Extensional exhumation
Temperature (°C)
0
200
400
600
800
Time (Ga)
1.68
1.72
1.76
1.80
1.84
1.88

Figure 10

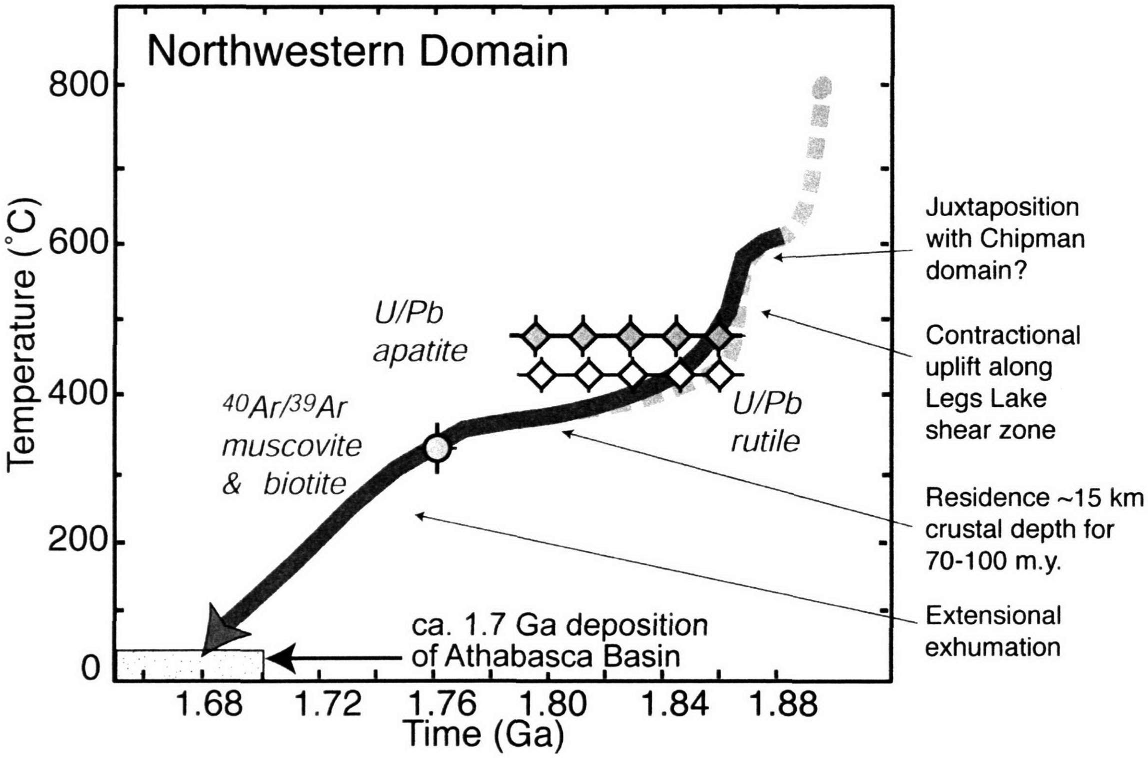
Northwestern Domain
800
600
400
200
0
Temperature (°C)
1.68
1.72
1.76
1.80
1.84
1.88
Time (Ga)
U/Pb apatite
40Ar/39Ar muscovite & biotite
U/Pb rutile
ca. 1.7 Ga deposition of Athabasca Basin
Juxtaposition with Chipman domain?
Contractional uplift along Legs Lake shear zone
Residence ~15 km crustal depth for 70-100 m.y.
Extensional exhumation

Figure 11

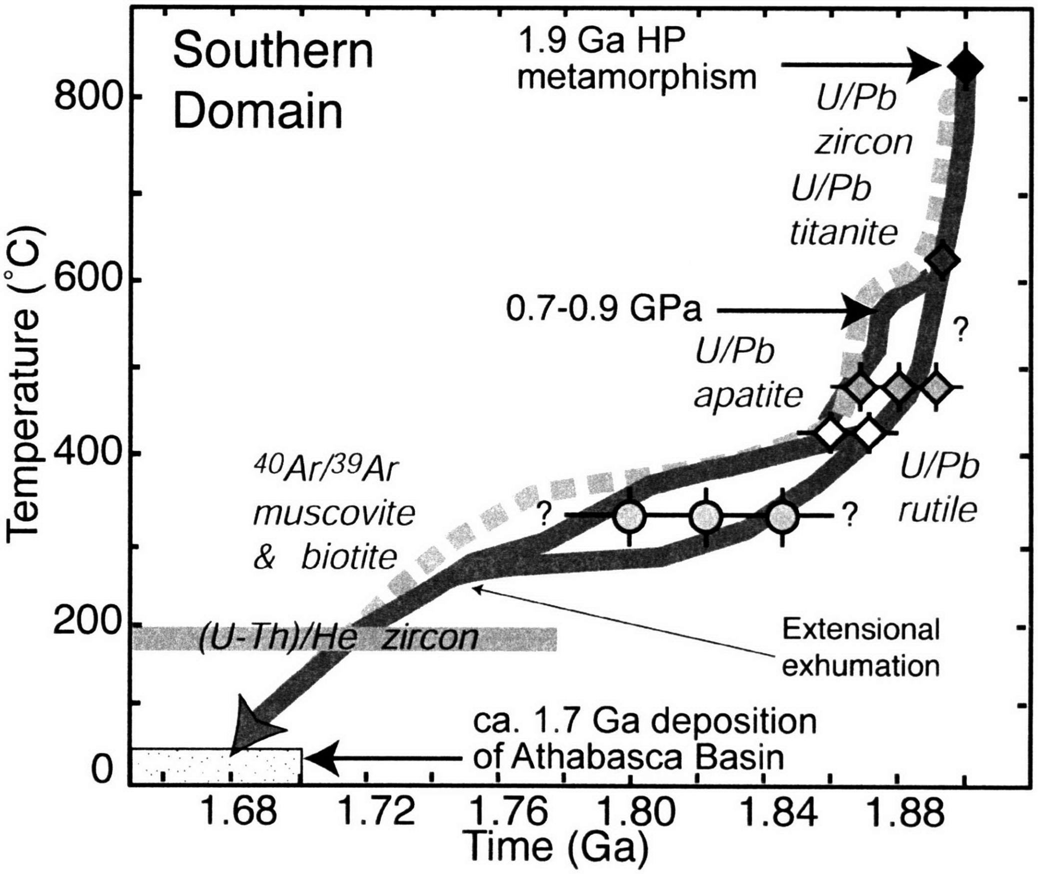
Southern Domain
1.9 Ga HP metamorphism
U/Pb zircon
U/Pb titanite
0.7-0.9 GPa
U/Pb apatite
?
U/Pb rutile
^{40}Ar/^{39}Ar muscovite & biotite
?
?
Extensional exhumation
(U-Th)/He zircon
ca. 1.7 Ga deposition of Athabasca Basin
Temperature (°C)
800
600
400
200
0
1.68
1.72
1.76
1.80
1.84
1.88
Time (Ga)

Figure 12

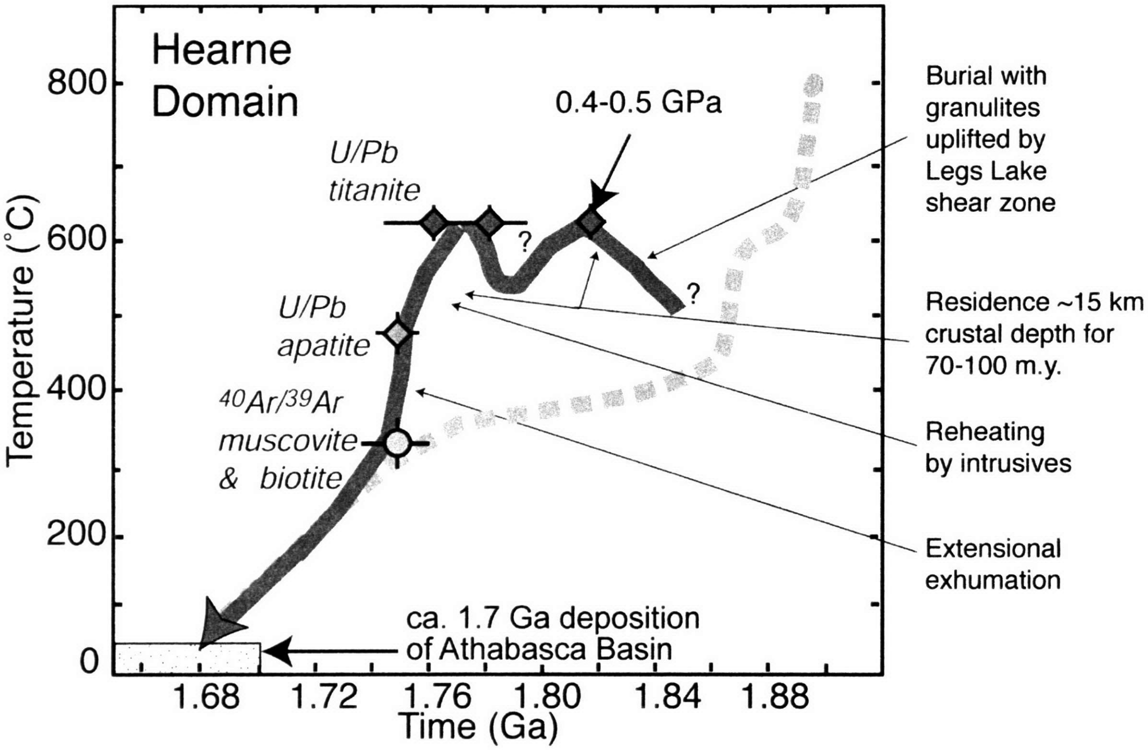
Hearne Domain
U/Pb titanite
U/Pb apatite
40Ar/39Ar muscovite & biotite
0.4-0.5 GPa
?
?
ca. 1.7 Ga deposition of Athabasca Basin
Burial with granulites uplifted by Legs Lake shear zone
Residence ~15 km crustal depth for 70-100 m.y.
Reheating by intrusives
Extensional exhumation
Temperature (°C)
0
200
400
600
800
Time (Ga)
1.68
1.72
1.76
1.80
1.84
1.88

Figure 13

Chapter 4

Ancient (U-Th)/He dates in the western Canadian Shield: Implications for continental stability and mantle dynamics

ABSTRACT

Vertical displacement of the Earth's surface is directly linked to plate tectonics and mantle convection. At active plate margins, high (up to 1 cm/yr) unroofing rates and rapid topographic evolution have been documented. In contrast, billions of years have passed since major tectonic activity perturbed the cratonic cores of some continents. However, new data indicate that even these stable continental interiors undergo episodes of uplift and/or subsidence, linked to tectonic processes and changing patterns of mantle flow. Thus, cratons can preserve a time-integrated record of the potentially subtle effects of asthenospheric convection and dynamic topography that has been overprinted in regions of active tectonism. (U-Th)/He thermochronometry is an underexploited means of constraining low temperature thermal histories in regions of apparent tectonic stability. We present the Earth's oldest reported (U-Th)/He zircon and apatite dates that reveal rocks of the western Canadian Shield have stably resided at temperatures ≤ 30 °C and crustal depths ≤ 2 km for ca 1.0 – 0.7 b.y. Such data allow evaluation of uplift episodes complementary to the depositional records of subsidence commonly incorporated into epeirogenic geodynamic models, and may permit detection of cratonic vertical motions related to coupling between continental lithosphere and the convecting mantle.

INTRODUCTION

The preservation of ancient continental crust through billions of years of Earth's dynamic history is qualitative testimony to the long-term stability of some parts of the continents. These rocks owe their survival to a cratonic architecture characterized by cold, thick (>250 km), chemically depleted lithospheric mantle roots that have shielded the crust from subsequent plate margin processes and underlying asthenospheric mantle activity (e.g. Jordan, 1978). Conventional studies of cratonic denudation based on geomorphic observations and erosion rate calculations have advocated the longevity of cratonic landscapes for hundreds of millions of years, consistent with concepts regarding the tectonic and thermal stability of cratons (Fairbridge and Finkl, 1980; Bishop, 1985; Stewart et al., 1986; Gale, 1992; Nott, 1995). However, the record of regional subsidence and uplift within stable continental areas, such as that preserved by Phanerozoic sedimentary sequences that extend deep into the cratonic interior of North America, has lead to the recognition that these regions may have experienced a more dynamic isostatic history than previously believed (Sloss and Speed, 1974; Bond 1978, 1979). Dynamic topography, the vertical displacement of the Earth's surface in response to mantle flow, has been invoked to explain components of these large-scale epeirogenic continental motions (e.g. Mitrovica et al., 1989; Gurnis, 1993; Lithgow-Bertelloni and Gurnis, 1997; Pysklywec and Mitrovica, 2000).

Analytical techniques that provide quantitative constraints on low temperature thermal histories and place bounds on the magnitude of vertical rock motion since the last significant period of tectonism are required to rigorously evaluate this problem. Models for cratonic vertical motions largely rely on the sedimentary record of submergence and emergence (e.g. Lithgow-Bertelloni and Gurnis, 1997), although this record is complicated by the inherently ephemeral nature of dynamic topography such that these phases are likely to be marked by sequence boundaries (e.g. Burgess et al. 1997). Low temperature thermochronometry can yield insight not only into phases of uplift complementary to the preserved subsidence record, but also can provide a powerful means of evaluating episodes of burial and denudation for which geological evidence has been completely removed. Apatite fission-track (AFT) studies have attempted to constrain low temperature (60-120 °C) thermal histories for this purpose (e.g. Crowley et al., 1986; Gleadow et al., 2004), but the geological significance and reproducibility of these data in slowly cooled regions are a subject of debate (Hendriks and Redfield, in press). In contrast, the application of (U-Th)/He thermochronometry to assess uplift in regions of apparent tectonic stability has been limited. We use this technique to constrain low temperature histories in a geologically well-characterized region of the western Canadian Shield. This area was targeted due to its broad coherency since ca. 1.7 Ga (Hoffman, 1989) and its exceptionally thick lithospheric mantle root (Godey et al. 2004) that together suggest this continental interior may have been more effectively shielded from subsequent perturbation than localities that have been the focus of previous low temperature thermochronological investigation. Our results represent the oldest reported terrestrial (U-Th)/He zircon and apatite dates, confirm the protracted (1.0 – 0.7 b.y.) residence of rocks at shallow (≤ 2 km) crustal depths, and offer insights into the long-term history of vertical motions within this stabilized continent.

LOW TEMPERATURE THERMOCHRONOMETRY IN STABLE CONTINENTAL INTERIORS

Almost all previous investigations aimed at constraining low temperature thermal histories in cratonic regions have employed apatite fission-track thermochronology. This method relies on analysis of preserved spontaneous fission ^{238}U tracks in apatite, which are fully annealed at temperatures ≥110 °C, largely preserved at temperatures ≤ 60 °C, with intervening temperatures known as the partial annealing zone. Early studies yielded dates from 500 to 930 Ma in the mid-continent of the United States and in the southern Canadian Shield (Crowley et al., 1986; Crowley and Kuhlman, 1988). However, recent studies in the southern Canadian Shield, and in the Kaapvaal, Yilgarn, Pilbara, and Brazilian cratons have yielded younger dates from 50 to 400 Ma (Amaral et al., 1997; Gleadow et al., 2002; Kohn et al., 2002; Osadetz et al., 2002; Harman et al., 2003; Saenz et al., 2003; Belton et al., 2004). These data challenge the antiquity of cratonic landscapes and have been interpreted to indicate reheating and/or burial by sedimentary cover with subsequent unroofing in the Phanerozoic. However, new study urges caution in the interpretation of AFT data from slowly cooled terranes, owing to the possibility that overlooked low temperature annealing processes may sometimes lead to an underestimation of AFT dates (Hendriks and Redfield, in press). In Finland, large variations in apparent AFT ages occur over short horizontal distances, with AFT dates anomalously younger than associated (U-Th)/He apatite dates attributed to unaccounted cumulative radiation-enhanced lattice recovery (Hendriks and Redfield, in press).

Low temperature (U-Th)/He thermochronometry has permitted many questions regarding the evolution of the Earth's surfaces in a variety of tectonic settings to become tractable problems. However, despite the potential for this technique to yield insights into regions of apparent tectonic stability, this method has had limited application in slowly cooled terranes. Zircon and apatite are characterized by (U-Th)/He closure temperatures of ~180 °C and 60-70 °C (Farley, 2000; Reiners et al., 2004), corresponding to rock passage through crustal depths of 8-12 km and 3-5 km, respectively, with consideration of a typical ~15-20 °C/km cratonic geothermal gradient. In practice, a measured date reflects the balance between He loss due to diffusion and He ingrowth due to radiogenic decay of U and Th, with a partial helium retention zone for apatite between ~30 and 80 °C depending on grain size and cooling rate. Thus, this method is sensitive to temperatures lower than those accessible by apatite fission track analysis and can effectively monitor temperatures at the shallowest crustal depths that most closely reflect denudational processes. A study in the southern Canadian Shield demonstrated the feasibility of obtaining reproducible (U-Th)/He apatite dates from a cratonic region, and inferred much less sensitivity of the (U-Th)/He system to apatite compositional variation than the AFT system (Lorencak et al., 2004). (U-Th)/He thermochronometry clearly provides an underexploited means of providing additional valuable constraints on low temperature thermal histories within continental interiors.

REGIONAL GEOLOGIC SETTING

The Canadian Shield is an extensive, well-exposed collage of Archean cratons separated by Paleoproterozoic collisional orogens. This region has largely remained intact since that time, with its boundaries modified by the Grenville orogen (1.2-1.0 Ga) along its southern boundary, Neoproterozoic rifting along most of its margin, and Paleozoic arc terrane accretion (Hoffman, 1989). The western portion of the Canadian Shield is currently characterized by a seismic velocity structure consistent with the presence of a cold, >250 km thick lithospheric mantle keel (Godey et al., 2004) (Figure 1).

The East Lake Athabasca region, at the boundary between the Rae and Hearne crustal provinces in the western Canadian Shield, contains extensive (>20,000 km2) tracts of rocks metamorphosed in the deep crust (1.0 to >2.0 GPa), subdivided into disparate lithotectonic domains. This area records a history of Archean lithospheric assembly and stabilization, with dramatic Proterozoic exhumation that ultimately produced the stable lithospheric configuration responsible for the long-term subsequent preservation of these rocks (Hanmer, 1997; Mahan and Williams, 2005; Flowers, Chapters 1 & 3). The unroofing history is temporally bracketed by ca. 1.9 Ga metamorphism of these rocks while in the deep crust and subsequent ca. 1.7 Ga deposition of clastic sedimentary rocks of the Athabasca basin across the exhumed granulites. Detailed structural and metamorphic data used to reconstruct pressure-temperature-deformation paths, in conjunction with high-resolution U-Pb ID-TIMS (zircon, monazite, titanite, apatite, rutile) and ^{40}Ar/^{39}Ar (hornblende, muscovite, biotite) geo- and thermochronological data that constrain high and intermediate temperature cooling histories, reveal an exhumation record interpreted to indicate pulses of unroofing separated by intervals of crustal residence during sequential contractional uplift, strike-slip shearing, and extension (Mahan et al. 2003; Mahan and Williams, 2005; Flowers, Chapter 3) (Figure 2). ^{40}Ar/^{39}Ar muscovite and biotite dates from 1.72 to 1.78 Ga provide a lower bound on final cooling through 350-300 °C, interpreted to reflect the initiation of extensional exhumation followed by transport of the rocks from depths of 0.4-0.5 GPa to near-surface conditions. The tightest minimum timing constraint on subsequent unconformable deposition of Athabasca basin fluvial, lacustrine and marine sediments across the region (Raemakers, 1981) is imposed by the youngest dated detrital zircon grains at 1661 ± 34 Ma in the Wolverine Point formation in the upper part of the basin sequence (Rayner et al., 2003), consistent with less precise ca. 1.65 to 1.70 Ga U-Pb dates for authigenic phosphate sediments (Cumming et al. 1987).

Fluid flow histories, reconstructed due to the economic importance of high-grade uranium deposits, provide some insight into subsequent Athabasca basin evolution. Fluid inclusion and clay mineralogy studies within the basin sediments, U-Pb and Pb-Pb analysis of uranium rich minerals, and $^{40}Ar/^{39}Ar$ and K/Ar investigation of Fe-rich clay paragenesis constrain an early diagenetic event at 1.7-1.6 Ga at temperatures of ~150 °C, burial diagenesis between 1.6 and 1.45 Ga at > 150 °C, fluid remobilization at ~0.9 Ga, and Phanerozoic fluid incursion at < 50 °C (Fayek et al., 2002; Kotzer and Kyser, 1995; Philippe et al., 1993; Percival et al., 1993; Kotzer et al., 1992). The current basin covers an area of ~100,000 km^2 and attains a maximum thickness of ~2300 m near its center, with speculation based on fluid inclusion data of Proterozoic thicknesses up to 5-7 km, although this is poorly constrained (Pagel et al., 1980). The current extent of Paleozoic sedimentary covers lies to the southwest of the Athabasca basin. Some continental reconstructions have speculated that this veneer of sediments may once have covered large portions of the rest of the Canadian Shield, including our area of study (e.g. Ziegler, 1989; Scotese and Golonka, 1992) (Figure 1).

(U-TH)/HE THERMOCHRONOLOGICAL RESULTS

(U-Th)/He zircon and apatite data were acquired to constrain the low temperature history of rocks in the East Lake Athabasca region. Zircon crystals were selected from well-characterized populations previously analyzed by U-Pb ID-TIMS methods, with internal structures imaged by backscatter and cathodoluminescence techniques. Past studies have demonstrated that a high level of accumulated radiation damage in zircon can lead to He loss and anomalously young apparent ages (Reiners et al., in press), and, for this reason, samples containing zircon with low U and Th concentrations (1-65 ppm) were targeted for analysis. Selected zircon crystals included metamorphic grains from three mafic granulite gneisses and igneous grains from one pegmatite sample (Figure 1, inset). Apatite grains were similarly identified in populations previously dated by U-Pb ID-TIMS, and pristine crystals were picked from one sample of Archean tonalitic gneiss. Refer to the data repository for details regarding analytical methods. Table 1 lists analytical results.

Eight of ten zircon grains yielded dates from 1.63 to 1.78 Ga. Two zircon grains from one sample yielded distinctly younger dates of 1.37 and 1.43 Ga. Cathodoluminescence images of zircon crystals in this sample revealed dark or luminescent overgrowths not observed in the other analyzed grains, consistent with higher uranium rims and the potential for underestimation of the alpha-ejection correction, and calculation of dates that are too young. Six apatite crystals yielded dates from 0.70 to 0.98 Ga. The range of apatite Th/U ratios suggests the presence of multiple apatite populations and/or zoning, consistent with the heterogeneous character of the deformed and polymetamorphosed Archean gneiss from which these grains were extracted. The reproducibility of dates from different apatite populations corroborates the significance of the dataset.

IMPLICATIONS FOR THE STABILITY AND VERTICAL MOTIONS OF CONTINENTS

Our (U-Th)/He zircon and apatite dates for the western Canadian Shield are the oldest reported for terrestrial rocks, and confirm the long-term stability of this region since the Proterozoic. (U-Th)/He zircon dates from 1.78 to 1.63 Ga are interpreted as cooling to < 180 °C during exhumation. This is entirely consistent with the well-constrained geological record of unroofing and subsequent basin deposition, bracketed by 1.78 to 1.72 Ga ^{40}Ar/^{39}Ar mica dates attributed to cooling during extensional unroofing, and 1.70 to 1.65 Ga Athabasca basin sediments unconformably deposited across the exhumed rocks (Figure 2). Assuming typical cratonic geothermal gradients of 15-20 °C/km, the preservation of these dates requires residence of the rocks at crustal depths of < 8-12 km for ca. 1.7 b.y.

The detailed constraints on exhumation and basin evolution in the East Lake Athabasca region further allow us to evaluate the implications of the 1.0 to 0.7 Ga (U-Th)/He apatite dates for continental vertical motions during 1.7 b.y. of cratonic stability. In the simplest analysis, these ancient dates are consistent with a history involving cooling below 80 °C and unroofing at 1.0-0.7 Ga, followed by extended exposure at the Earth's surface. In reality, the sensitivity of apatite dates to subtle variations in temperature during long-term residence in the partial retention zone means that a measured date may represent the integrated product of a potentially complex thermal history (Reiners, 2002). Although this behavior precludes direct translation into a cooling age, it offers the potential to use appropriate geological constraints to evaluate viable thermal models that can be linked with uplift and subsidence histories.

Constraints on post-1.7 Ga continental motions that can be used in conjunction with our thermochronometric information are primarily derived from Athabasca basin fluid inclusion studies and basinal records of Canadian Shield unroofing. Fluid inclusion studies have estimated a maximum Proterozoic basin thickness of 5-7 km, such that removing the preserved 2.3 km of sediments in the deepest part of the basin, and making the reasonable assumption of little differential exhumation during basin unroofing, implies a post-1.7 Ga burial of exposed rocks in the East Lake Athabasca region by no more than 2.7 - 4.7 km in the Proterozoic. Following burial diagenesis from ca. 1.6 to 1.45 Ga, fluid mobilization events at ca. 0.9 Ga and in the Phanerozoic have tentatively been linked with uplift during Neoproterozoic rifting along the western margin ca. 750-500 Ma (Kotzer and Kyser, 1995; Fayek et al., 2002). We note that although these same studies interpret temperatures of 150-200 °C in zones of uranium mineralization within the basin, temperatures >180 °C in the East Lake Athabasca region following basin deposition are precluded by the ancient (U-Th)/He zircon data. This is reasonable, given the selectivity of fluid inclusion studies within the most uranium rich and therefore hottest portions of the basin, the potential for localization of brief peak temperatures within the basinal hydrothermal convection system, and the absence of significant basement retrogression that would be suggestive of hot brine circulation in the study area. In addition to these constraints, some continental reconstructions have proposed that most of the western Canadian Shield currently lacking Phanerozoic cover, including the East Lake Athabasca region, was inundated by the Paleozoic seas responsible for sedimentary sequences still preserved over much of the North American cratonic interior (Ziegler, 1989; Scotese and Golonka, 1992). Discovery of Devonian limestone xenoliths in kimberlites of the Slave province provide solid evidence that ≥750 m of now eroded Phanerozoic sediments once blanketed this craton (Cockenboo et al., 1998). Nd isotopic and geochemical data for Arctic basinal sequences have been used to argue that up to 2 km of sedimentary rocks similarly extended over the remainder of the western Canadian Shield from 450 to 80 Ma, followed by progressive removal in the Mesozoic (Patchett et al., 2004).

In light of the above information, and to shed further insight into the speculated phases of continental uplift and subsidence, we consider histories for the East Lake

Athabasca region involving 1) long term (1.6-1.7 b.y.) residence at constant temperature beneath Athabasca basin sediments prior to Phanerozoic unroofing, 2) episodic uplift and removal of Athabasca basin sediments from a maximum thickness in the Proterozoic, and 3) subsequent burial by sediments of some thickness in the Phanerozoic (Figure 3). We use the HeFTy program (Ketcham, in press) to constrain this suite of feasible models by applying a standard He production-diffusion model (Wolf et al., 1998) to our approximate analyzed apatite half-width of ~50 μm. Crustal depths are estimated assuming typical cratonic thermal gradients of 15-20 °C/km. In the simple residence scenario, the data are consistent with burial of the rocks to depths of 1.5-2km beneath Athabasca basin sediments, subsequent residence at temperatures of 25-30 °C for 1.7 to 1.6 b.y., followed by unroofing in the Phanerozoic (Figure 3, T-t path 1). A more complex history involving episodic unroofing synchronous with basinal fluid circulation events can follow a restricted range of temperature-time paths depending on the magnitude of exhumation associated with each uplift pulse, but ultimately requires cooling to temperatures ≤ 30 °C, corresponding to depths of ≤ 2 km, by 0.7-1.0 Ga (Figure 3, T-t path 2). Finally, the data are permissive of burial beneath up to 2 km of Phanerozoic sediments at maximum temperatures of ~30 °C from 450 to 80 Ma (Figure 3, T-t path 3). However, the preservation of ancient (U-Th)/He apatite dates despite this hypothetical period of younger sedimentary accumulation requires an earlier history characterized by much lower temperatures than those modeled in the episode uplift model of scenario two, with residence at crustal depths of < 500 m for prolonged periods in the Proterozoic. This is an important point, because additional information regarding early or recent uplift and subsidence episodes based on geological or other thermochronologic data could dramatically narrow the range of possible temperature-time paths for parts of the history for which no such further data is available. Regardless of the details of each model, the ancient (U-Th)/He apatite dates reveal that rocks in the East Lake Athabasca region resided at temperatures of ≤ 30 °C, at crustal depths of ≤ 2 km, for 1.0 to 0.7 b.y.

IMPLICATIONS FOR MANTLE DYNAMICS

Much attention has focused on the large-scale vertical motions of continental interiors as an avenue for understanding changing patterns of flow within the mantle (e.g.

Gurnis, 1992; Pysklywec and Mitrovica, 1998; Burgess and Moresi, 1999). For example, Late Cretaceous subsidence and Tertiary uplift in the western interior of North America has been attributed to the dynamical effects of changing subduction (Mitrovica et al., 1989). Subduction induced long-wavelength tilting has subsequently been used to explain aspects of subsidence patterns in a number of stable continental regions at different times in the Phanerozoic (Coakley and Gurnis, 1995; Mitrovica et al., 1996; Burgess et al., 1997; Pysklywec and Mitrovica, 2000). Others have attempted to compute the global time-varying dynamic topography for the Cenozoic, predicted differential motions for stable continental regions, and assessed the viability of results based on geological observations (Lithgow-Bertelloni and Gurnis, 1997; Lithgow-Bertelloni and Richards, 1998). These studies have repeatedly called for improved stratigraphic constraints to permit more effective evaluation of geodynamic models. However, because dynamic topography is intrinsically a transient feature driven by changing mantle flow regimes, the resulting sedimentary accumulation has a low preservation potential, and the long-term expected signal in the depositional record is as an unconformity or sequence boundary (e.g. Burgess et al., 1997). This places fundamental limits on a detailed understanding of past episodes of dynamic topography solely based on the stratigraphic record.

Our study demonstrates that low temperature (U-Th)/He thermochronometry within stable cratonic regions provides a powerful tool for deciphering uplift phases complementary to the sedimentary record of subsidence, and can help constrain vertical continental motions for which geological evidence has been completely removed. For example, computation of Cenozoic global dynamic topography predicted 2.5 to 3 km of uplift within portions of the western Canadian Shield, including the area of our study (Lithgow-Bertelloni and Gurnis, 1997). However, the antiquity of our (U-Th)/He apatite dates require residence of exposed rocks at crustal depths $\leq$ 2 km for the last 1.0-0.7 b.y., thus imposing a maximum 2 km of uplift in the Cenozoic. The low amplitude of vertical motions since the Precambrian in the East Lake Athabasca region of the western Canadian Shield indicates this area has exceptional value for deciphering earlier uplift and subsidence phases for which thermal records have been eliminated in regions characterized by greater recent uplift. Uplift since the Precambrian is interpreted for the southern African Plateau and cratonic regions of Australia based on geophysical and AFT data (e.g. Nyblade and Sleep, 2003; Kohn et al., 2002), such that the record preserved within these different continental interiors can provide diverse insight into the driving plate tectonic and mantle flow mechanisms of epeirogenic motion. In the past, (U-Th)/He analysis has received limited application to cratonic regions and therefore has not been exploited in the development and assessment of geodynamic models for vertical motions within continental interiors. In the future, the acquisition of such data, coupled with the sedimentary record, holds the promise of exciting new insights into continental stability and changing mantle dynamics.

REFERENCES

Amaral, G., Born, H., Hadler, J.C., Iunes, P.J., Kawashita, K., Machado Jr., D.L., Oliveira, E.P., Paulo, S.R., and Tello, C.A., 1997, Fission track analysis of apatites from Sao Francisco craton and Mesozoic alkaline-carbonatite complexes from central and southeastern Brazil: Journal of South American Earth Sciences, v. 10, p. 285-294.

Belton, D.X., Brown, R.W., Kohn, B.P., Fink, D., and Farley, K.A., 2004, Quantitative resolution of the debate over antiquity of the central Australian landscape: implications for the tectonic and geomorphic stability of cratonic interiors: Earth and Planetary Science Letters, v. 219, p. 21-34.

Bishop, P., 1985, Southeast Australian late Mesozoic and Cenozoic denudation rates: A test for late Tertiary increases in continental denudation: Geology, v. 13, p. 479-482.

Bond, G.C., 1978, Speculations of real sea-level changes and vertical motions of continents at selected times in the Cretaceous and Tertiary periods: Geology, v. 6, p. 247-250.

Bond, G.C., 1979, Evidence for some uplifts of large magnitude in continental platforms: Tectonophysics, v. 61, p. 285-305.

Burgess, P.M., Gurnis, M., and Moresi, L., 1997, Formation of sequences in the cratonic interior of North America by interaction between mantle, eustatic and stratigraphic processes: Geological Society of America Bulletin, v. 108, p. 1515-1535.

Burgess, P.M. and Moresi, L., 1999, Modelling rates and distribution of subsidence due to dynamic topography over subducting slabs: is it possible to identify dynamic topography from ancient strata: Basin Research, v. 11, p. 305-314.

Coakley, B. and Gurnis, M., 1995, Far-field tilting of Laurentia during the Ordovician and constraints on evolution of a slab under and ancient continent: Journal of Geophysical Research, v. 100, p. 6313-6327.

Cockenboo, H.O., Orchard, M.J. and Daoud, D.K., 1998, Remnants of Paleozoic cover on the Archean Canadian Shield: Limestone xenoliths from kimberlite in the central Slave craton: Geology, v. 26, p. 391-394.

Crowley, K.D., 1991, Thermal history of Michigan basin and southern Canadian Shield from apatite fission track analysis: Journal of Geophysical Research, v. 96, p. 697-711.

Crowley, K.D. and Kuhlman, S.L., 1988, Apatite thermochronometry of western Canadian Shield: Implications for origin of the Williston Basin: Geophysical Research Letters, v.15, p. 221-224.

Crowley, K.D., Naeser, C.W. and Babel, C.A.,, 1986, Tectonic significance of Precambrian apatite fission-track ages from the mid-continent United States: Earth and Planetary Science Letters, v. 79, p. 329-336.

Cumming, G.L., Krstic, D., and Wilson, J.A., 1987, Age of the Athabasca Group, northern Alberta: Geological Association of Canada-Mineralogical Society of Canada, Joint Annual Meeting, Program with Abstracts, v. 12, p. 35.

Fairbridge, R.W. and Finkl Jr., C.W., 1980, Cratonic erosional unconformities and peneplains: Journal of Geology, v. 88, p. 69-86.

Farley, K.A., 2000, Helium diffusion from apatite: general behavior as illustrated by Durango fluorapatite: Journal of Geophysical Research, v. 105, p. 2903-2914.

Fayek, M., Harrison, T.M., Ewing, R.C., Grove, M. and Coath, C.D., 2002, O and Pb isotopic analyses of uranium minerals by ion microprobe and U-Pb ages from the Cigar Lake deposit: Chemical Geology, v. 185, p. 205-225.

Gale, S.J., 1992, Long-term landscape evolution in Australia: Earth surface processes and landforms, v. 17, p. 17323-17343.

Gleadow, A.J.W., Kohn, B.P., Brown, R.W., O'Sullivan, P.B., and Raza, A., 2002, Fission track thermotectonic imaging of the Australian continent: Tectonophysics, v. 349, p. 5-21.

Godey, S., Deschamps, F., Trampert, J. and Snieder, 2004, Thermal and compositional anomalies beneath the North American continent: Journal of Geophysical Research, v. 109, B01308.

Gurnis, M., 1993, Phanerozoic marine inundation of continents driven by dynamic topography above subducting slabs: Nature, v. 364, p. 589-593.

Hanmer, S., 1997, Geology of the Striding-Athabasca mylonite zone, northern Saskatchewan and southeastern District of Mackenzie, Northwest Territories: Geological Survey of Canada Bulletin, v. 501, pp.1-92.

Harman, R., Gallagher, K., Brown, R., Raza, A., and Bizzi, L., 1998, Accelerated denudation and tectonic/geomorphic reactivation of the cratons of northeastern Brazil during the Late Cretaceous: Journal of Geophysical Research: v. 103, p. 27091-27105.

Hendriks, B.W.H. and Redfield, T.F., in press, Apatite fission track and (U-Th)/He data from Fennoscandia: an example of underestimation of fission track annealing in apatite: Earth and Planetary Science Letters, ---.

Hoffman, P.F., 1989, Precambrian geology and tectonic history of North America, in Bally, A.W., and Palmer, A.R., eds, The Geology of North America – An overview: Boulder, Colorado, Geological Society of America, The Geology of North America, v. A.

Jordan, T.H., 1978, Composition and development of the continental tectosphere: Nature, v. 274, p. 544-548.

Ketcham, R., in press, Modeling producation and annealing/diffusion and interpreation of low temperature thermochronometry: in Reiners, P.W. and Ehlers, T.A. (eds.), Thermochronology, Reviews in Mineralogy and Geochemistry, v. xx.

Kohn, B.P., Gleadown, A.J.W., Brown, R.W., Gallagher, K., O'Sullivan, P.B., and Foster, D.A., 2002, Shaping the Australian crust over the last 300 million years: insights from fission track thermotectonic imaging and denudation studies of key terranes: Australian Journal of Earth Sciences: v. 49, p. 697-717.

Kotzer, T.G. and Kyser, T.K., 1995, Petrogenesis of the Proterozoic Athabasca basin, northern Saskatchewan, Canada, and its relation to diagenesis, hydrothermal uranium mineralization and paleohydrogeology: Chemical Geology, v. 120, p. 45-89.

Kotzer, T.G., Kyser, T.K. and Irving, E., 1992, Paleomagnetism and the evolution of fluids in the Proterozoic Athabasca Basin, northern Saskatchewan, Canada: Canadian Journal of Earth Sciences, v. 29, p. 1474-1491.

Lithgow-Bertelloni, C. and Gurnis, M., 1997, Cenozoic subsidence and uplift of continents from time-varying dynamic topography: Geology, v. 25, p. 735-738.

Lithgow-Bertelloni, C. and Richards, M.A., 1998, The dynamics of Cenozoic and Mesozoic plate motions: Reviews of Geophysics, v. 36, p. 27-78.

Lorencak, M., Kohn, B.P., Osadetz, K.G., and Gleadow, A.J.W., 2004, Combined apatite fission track and (U-Th)/He thermochronometry in a slowly cooled terrane: results from a 3440-m-deep drill hole in the southern Canadian Shield: Earth and Planetary Science Letters, v. 227, p. 87-104.

Mahan, K.H., 2005, Exhumation of exposed deep continental crust, western CanadianShield: Integrating structural analysis, petrology, and in situ geochronology: PhD thesis, University of Massachusetts, Amherst, Massachusetts.

Mahan, K.H., Flowers, R.M., Williams, M.L., Goncalves, P., Bowring, S.A., and Jercinovic, M.J., 2005, A P-T-time-deformation path for exposed deep continental crust in the Snowbird tectonic zone, western Canadian Shield: GSA Cordilleran Session Meeting abstract, San Jose, CA.

Mahan, K.H., Williams, M.L., and Baldwin, J.A., 2003, Contractional uplift of deep crustal rocks along the Legs Lake shear zone, western Churchill Province, Canadian Shield: Canadian Journal of Earth Sciences, v. 40, p. 1085-1110.

Mahan, K.H. and Williams, M.L., 2005, Reconstruction of a large deep-crustal exposure: Implications for the Snowbird tectonic zone and early growth of Laurentia: Geology, v.33, p. 385-388.

Mitrovica, J.X., Beaumont, C. and Jarvis, 1989, Tilting of continental interiors by the dynamical effects of subduction: Tectonics, v. 8, p. 1079-1094.

Mitrovica, J.X., Pysklywec, R.N., Beaumont, C. and Rutty, A., 1996, The Devonian to Permian sedimentation of the Russian platform: An example of subduction-controlled long-wavelength tilting of continents: Journal of Geodynamics, v. 22, p. 79-96.

Murrell, G.R., and Andriessen, P.A.M., 2004, Unravelling a long term multi-event thermal record in the cratonic interior of southern Finland through apatite fission track thermochronology: Physics and Chemistry of the Earth, v. 29, p. 695-706.

Nott, J., 1995, The antiquity of landscapes on the north Australian craton and the implications for theories of long-term landscape evolution: The Journal of Geology, v. 103, p. 19-32.

Nyblade, A.A. and Sleep, N.H., 2003, Long lasting epeirogenic uplift from mantle plumes and the origin of the Southern African Plateau: Geochemistry, Geophysics, Geosystems: v. 4, No. 12, 1105, doi: 10.1029/2003GC000573.

Osadetz, K.G., Kohn, B.P., Feinstein, S. and O'Sullivan, P.B., 2002, Thermal history of the Williston basin from apatite fission-track thermochronology -- implications for petroleum systems and geodynamic history: Tectonophysics, v. 349, p. 221-249.

Pagel, M., Poty, B. and Sheppard, S.M.F., 1980, Contributions to some Saskatchewan uranium deposits mainly from fluid inclusion and isotopic data: In, Uranium in the Pine Creek Geosyncline (J. Ferguson and A.B. Goleby, eds.), International Atomic Energy Agency (Vienna), p. 639-654.

Patchett, P.J., Embry, A.F., Ross, G.M., Beauchamp, B., Harrison, J.C., Mayr, U., Isachsen, C.E., Rosenbery, E.J., and Spence, G.O., 2004, Sedimentary cover of the Canadian Shield through Mesozoic time reflected by Nd isotopic and geochemical results for the Sverdrup Basin, Arctic Canada: Journal of Geology, v. 112, p. 39-57.

Percival, J.B., Bell, K., and Torrance, J.K., 1993, Clay mineralogy and isotope geochemistry of the alteration halo at the Cigar Lake uranium deposit: Canadian Journal of Earth Sciences, v. 30, p. 389-704.

Philippe, S., Lancelot, J.R., Clauer, N. and Pacquet, A., 1993, Formation and evolution of the Cigar Lake uranium deposit based on U-Pb and K-Ar isotope systematics: Canadian Journal of Earth Sciences, v. 30, p. 720-730.

Pysklywec, R.N. and Mitrovica, J.X., 2000, Mantle flow mechanisms of epeirogeny and their possible role in the evolution of the Western Canada Sedimentary Basin: Canadian Journal of Earth Sciences, v. 37, p. 1535-1548.

Pysklywec, R.N. and Mitrovica, J.X.,1998, Mantle flow mechanisms for the large-scale subsidence of continental interiors: Geology, v. 26, p. 687-690.

Ramaekers, P., 1981, Hudsonian and Helikian basins of the Athabasca region, northern Saskatchewan: in Proterozoic Basins of Canada, F.H.A. Campbell, ed, Geological Survey of Canada, Paper 81-10, p. 219-233.

Rayner, N.M., Stern, R.A., and Rainbird, R.H., 2003, SHRIMP U-Pb detrital zircon geochronology of Athabasca Group sandstones, northern Saskatchewan and Alberta: GSC Current Research, 2003-F2, 20 pp.

Reiners, P.W., in press, Zircon (U-Th)/He Thermochronometry, in Reiners, P.W. and Ehlers, T.A. (eds.), Thermochronology, Reviews in Mineralogy and Geochemistry, v. xx.

Reiners, P.W., 2002, (U-Th)/He chronometry experiences a renaissance: EOS, Transaction, American Geophysical Union, v. 83, p. 103-105.

Reiners, P.W., Spell, T.L., Nicolescu, S. and Zanetti, K.A., 2004, Zircon (U-Th)/He thermochronometry: He diffusion and comparisons with 40Ar/39Ar dating: Geochimica et Cosmochimica Acta, v. 68, p. 1857-1887.

Saenz, C.A., Hackspacher, P.C., Neto, J.C., Iunes, P.J., Guedes, S., Ribeiro, L.F.B., and Paulo, S.R., 2003, Recognition of Cretaceous, Paleocene, and Neogene tectonic reactivation through apatite fission-track analysis in Precambrian areas of southeast Brazil: association with the opening of the south Atlantic Ocean: Journal of South American Earth Sciences, v. 15, p. 765-774.

Scotese, C.R. and Golonka, J., 1992, PALEOMAP Paleogeographic Atlas: PALEOMAP Progress Report 20, Department of Geology, University of Texas, Arlington.

Sloss, L.L. and Speed, R.C., 1974, Relationships of cratonic and continental-margin tectonic episodes, in Tectonics and Sedimentation, W.R., Dickinson, ed., SEPM Spec. Publ., p. 98-119.

Stewart, A.J., Blake, D.H., and Ollier, C.D., 1986, Cambrian river terraces and ridgetops in central Australia: Oldest persisting landforms?: Science, v. 233, p. 758-761.

Wolf, R.A., Farley, K.A., and Kass, D.M., 1998, Modeling of the temperature sensitivity of the apatite (U-Th)/He thermochronometer: Chemical Geology, v. 148, p. 105-114.

Ziegler, P.A., 1989, Evolution of Laurussia: Kluwer Academic Publications: Dordrecht, The Netherlands.

FIGURE CAPTIONS

Figure 1. Geological map of the western Canadian Shield showing major tectonic features. Box marks location of upper right inset of simplified map of the East Lake Athabasca region with sample locations.

Figure 2. Temperature-time path during exhumation of high-pressure granulites in the Chipman domain, reconstructed from U-Pb, $^{40}Ar/^{39}Ar$ and (U-Th)/He data.

Figure 3. Suite of viable thermal models for an apatite half-width of 50 μm that satisfies the apparent (U-Th)/He apatite dates. Refer to text for more detail regarding the depicted temperature-time paths.

Table 1. (U-Th)/He data for zircon and apatite

Fr	mass (ug)	radius[a] (um)	U ppm	Th ppm	Th/U	4He (nmol/g)	raw age (Ga)	raw est 2σ err (Ga)	Ft[b]	corr age (Ga)	est 2σ err (Ga)
Zircon analyses											
02-76B, Chipman domain pegmatite											
z1	6.7	46.3	66.0	21.2	0.32	603.3	1.38	0.07	0.785	1.76	0.09
z2	103.1	131.3	50.5	14.7	0.30	509.7	1.51	0.09	0.914	1.65	0.10
z3	212.6	195.5	42.1	13.9	0.34	448.7	1.57	0.10	0.934	1.68	0.10
03-52, Chipman mafic granulite dike											
z1	14.2	65.5	33.3	2.9	0.09	299.9	1.42	0.08	0.830	1.71	0.10
z2	6.1	51.3	32.7	3.7	0.12	267.7	1.30	0.08	0.790	1.65	0.10
z3	7.3	46.3	44.5	6.0	0.14	400.6	1.41	0.06	0.788	1.78	0.08
SZ00-141Az1, southern domain mafic granulite											
z1	4.0	45.3	37.0	4.0	0.11	314.7	1.35	0.06	0.757	1.78	0.08
z2	7.3	61.5	15.0	3.6	0.25	126.9	1.31	0.06	0.804	1.63	0.07
SZ00-196C, Chipman domain mafic granulite dike											
z2	5.3	43.5	16.8	2.2	0.14	109.1	1.06	0.05	0.770	1.37	0.07
z3	7.4	49.5	9.5	0.3	0.04	65.4	1.14	0.06	0.796	1.43	0.07
Apatite analyses											
SZ00-196B, Chipman domain tonalitic gneiss											
a1	1.4	36.0	12.2	4.0	0.32	48.1	0.64	0.06	0.651	0.98	0.09
a2	4.7	55.5	5.2	0.5	0.09	17.5	0.57	0.05	0.764	0.74	0.07
a3	4.2	51.0	7.3	2.7	0.38	32.7	0.71	0.05	0.748	0.95	0.07
a4	4.3	57.3	6.1	2.8	0.47	27.2	0.69	0.06	0.763	0.91	0.07
a5	3.3	46.0	12.6	6.3	0.51	50.7	0.63	0.04	0.724	0.86	0.05
a6	2.6	43.5	8.2	7.7	0.97	27.8	0.49	0.04	0.705	0.70	0.06

[a] Radius is defined as average of perpendicular half-widths

[b] Ft is alpha-ejection correction of Farley et al. (2002).

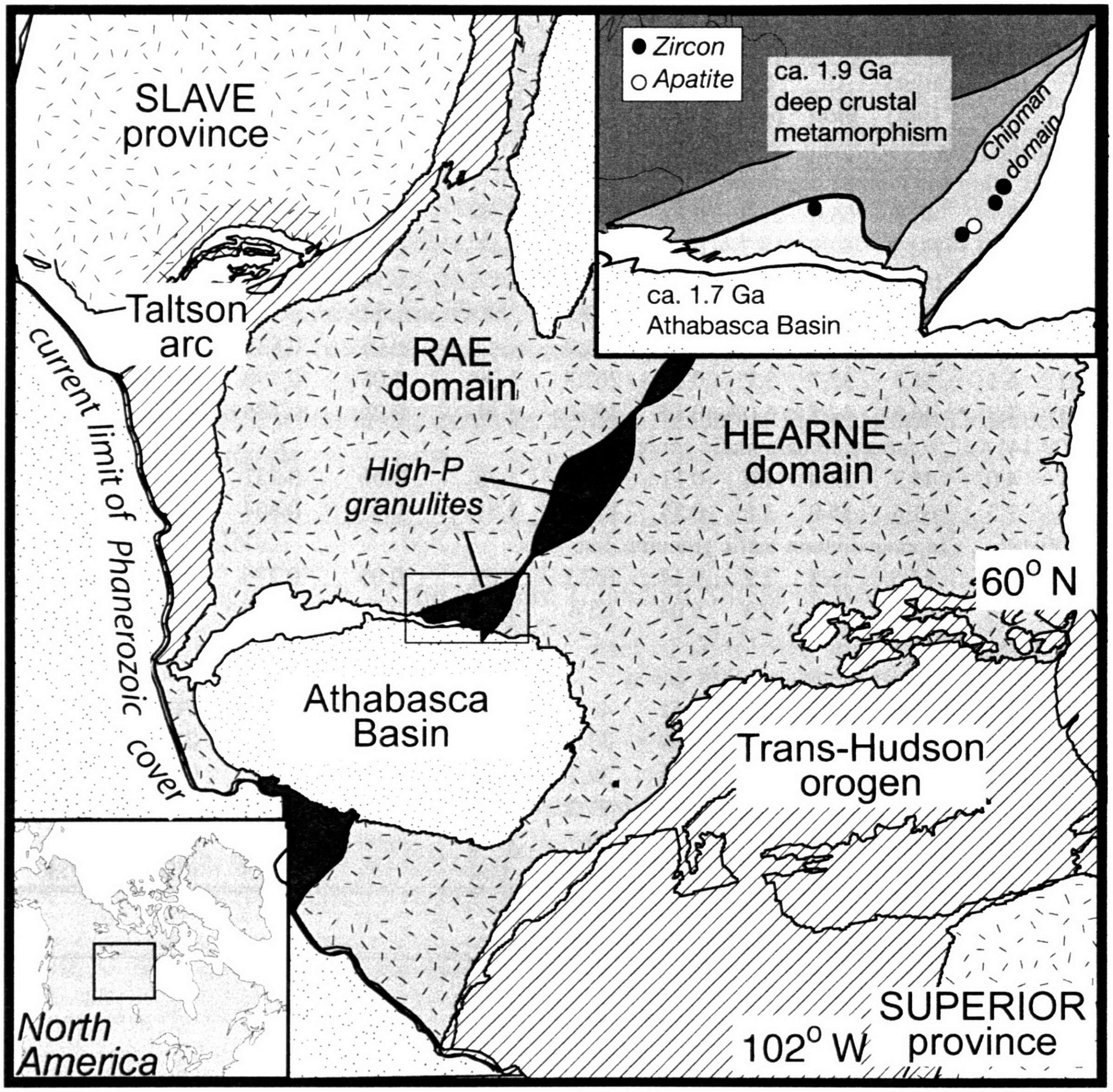
● Zircon
○ Apatite
ca. 1.9 Ga deep crustal metamorphism
Chipman domain
ca. 1.7 Ga Athabasca Basin
SLAVE province
Taltson arc
RAE domain
HEARNE domain
High-P granulites
current limit of Phanerozoic cover
60° N
Athabasca Basin
Trans-Hudson orogen
SUPERIOR province
102° W
North America

Figure 1

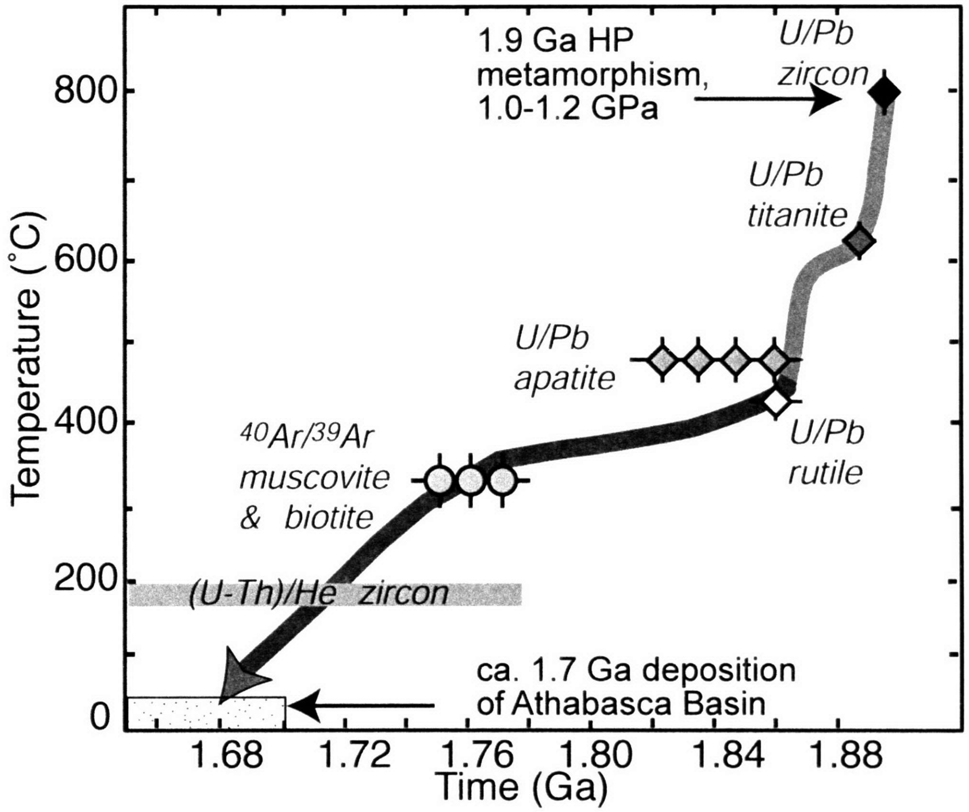
1.9 Ga HP
metamorphism,
1.0-1.2 GPa
U/Pb
zircon
U/Pb
titanite
U/Pb
apatite
U/Pb
rutile
^{40}Ar/^{39}Ar
muscovite
& biotite
(U-Th)/He zircon
ca. 1.7 Ga deposition
of Athabasca Basin
Temperature (˚C)
0
200
400
600
800
1.68
1.72
1.76
1.80
1.84
1.88
Time (Ga)

Figure 2

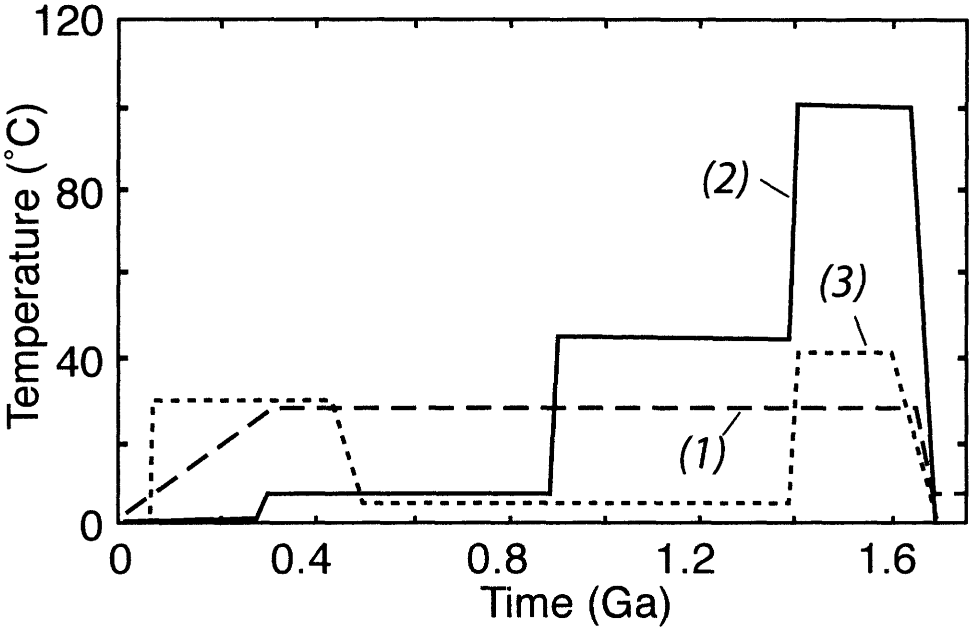

Figure 3

Chapter 5

A lower crustal record of craton reactivation and survival

Chapter 5 - Synthesis

INTRODUCTION

The surviving continents preserve a complex and fragmentary archive of Earth's long dynamic history. Deciphering this record is key to understanding the fundamental processes associated with the growth and stabilization of continental lithosphere. A central component of this problem is determining the magnitude of bias inherent in the preserved record, owing to the selective destruction of less stable continents. Thus, analysis of the lithospheric response to perturbations by asthenospheric and plate margin tectonic processes is essential to constrain both 1) the mechanisms that can disrupt continents, and 2) the lithospheric characteristics that are most conducive to lithospheric survival. This information is essential to gain a more objective perspective on the continental record available for study today.

The oldest continental remnants, the Archean cratons, have survived billions of years of Earth's history and thus are a particularly valuable resource for investigating the potential controls on lithospheric preservation. Cratonic lithosphere is characterized by thick (≥ 200 km) chemically depleted lithospheric mantle roots that have helped insulate the crust from severe overprinting by subsequent tectonism (e.g. Jordan, 1978). However, even these relatively stable portions of the continents have been perturbed following assembly, by episodes ranging from minor lithospheric rejuvenation to major lithospheric disruption. A better understanding of this continuum can yield insights into the factors governing the survival or destruction of continents.

The lower continental crust, as the physical link between the upper crust and mantle, retains a particularly sensitive record of asthenospheric disturbance that may not be as clearly manifested at higher levels of the crustal column. Episodes of lower crustal mafic magmatism, metamorphism and melting thus can have important implications for the larger dynamics of crust-mantle interaction. Much attention has focused on constraining the origins, tectonic settings of formation, P-T paths, and exhumation histories of granulites, because of their importance for broader crustal histories (e.g. Harley , 1989; Bohlen, 1991; O'Brien and Rotzler, 2003). Vast tracts of lower crustal rocks preserved in the East Lake Athabasca region in the western Churchill Province record two different types of high-pressure (HP) granulite facies metamorphic events followed by exhumation. This history can be used to place fundamentally important constraints on the stabilization, reactivation, and preservation of continental lithosphere in the western Canadian Shield.

HIGH-PRESSURE GRANULITE FORMATION IN THE EAST LAKE ATHABASCA REGION

Although granulites have a wide diversity in origin, two endmember tectonic settings have been identified for their formation (e.g. Ellis, 1987; Harley, 1989). These are: 1) granulites that formed at the base of the crust with subsequent isobaric cooling, the potential for long term residence in the deep crust, and exhumation by a mechanism unrelated to their genesis, and 2) granulites that originated in a brief tectonic episode with isothermal decompression and exhumation during the same orogenic cycle. HP granulite xenoliths fall into the former category, as they commonly record isobaric cooling to a steady-state geotherm following metamorphism. Granulite facies exposures of this type include the Ivrea Zone, Kapuskasing uplift, and Napier Complex, with subsequent unroofing in unrelated plate margin and intracratonic settings, respectively (Percival and Card, 1983; Zingg, 1990; Harley and Black, 1997). In contrast, HP granulite exposures generally represent formation by short-lived crustal thickening or subduction events that are also responsible for their exposure (O'Brien and Rotzler, 2003). Examples include the Hengshan Complex of China, the European Variscides, and the Grenville Province (O'Brien and Carswell, 1993; Indares, 1995; Zhao et al., 2001).

Rocks in the East Lake Athabasca region preserve evidence for the subjection of the same rocks to both types of HP granulite facies events. A variety of data provide evidence for a widespread Archean granulite facies event, followed by isobaric cooling and subsequent residence in the deep crust – consistent with the first type of HP granulite formation. New U-Pb zircon results for the Chipman domain document significant metamorphic zircon growth in mafic granulite gneisses at 2.55 Ga (Chapter 1), linked with ~1.3 GPa, 850 °C granulite facies assemblages in these rocks (Mahan et al., 2005). Isobaric cooling paths from peak conditions of ~0.8-1.0 GPa, 900 °C are interpreted to have developed following the Archean emplacement of the Mary granite in the northwestern domain, preceding long-term residence of this domain in the lower crust

(Williams et al., 2000; Williams and Hanmer, 2005). Metamorphic zircon growth at ca. 2.55 Ga has also been reported in the southern domain (Baldwin et al., 2004).

There is compelling evidence for a second HP granulite facies metamorphic event at 1.9 Ga, followed by isothermal decompression – consistent with the second type of HP granulite formation. Mafic dike anatexis at conditions of 1.0-1.2 GPa, ~ 800 °C has been dated at 1896.2 ± 0.3 Ma in the Chipman domain (Williams et al., 1995; Flowers, Chapter 2). This is consistent with 1.9 Ga metamorphic zircon growth at ca. 1.9 Ga in mafic granulite gneisses, linked with a second granulite facies assemblage preserved in this rock (Chapter 1). Metamorphic zircon growth at 1904.0 ± 0.3 Ma has been linked with peak conditions in the southern domain (Baldwin et al., 2004). U-Pb titanite dates from across the region record resetting to temperatures > 600 °C in the Proterozoic (Chapter 3). These and other new thermochronological data in this study, as well as isothermal decompression textures in a number of the domains (Kopf, 1999; Krikorian, 2002; Baldwin et al., 2004; Mahan, 2005), indicate unroofing shortly following HP granulite facies conditions. The thermochronological dataset, in conjunction with constraints on unconformable deposition of Athabasca basin sediments over the exhumed granulites at ca. 1.7 Ga, record the exhumation of the granulites to near-surface conditions within 200 m.y. of deep crustal metamorphism (Chapters 3 and 4).

This is the first reported occurrence of the formation of the two primary types of HP granulites within the same exposure of lower crustal rocks. Additional study is required to verify this inferred history, owing to the inherent complexities associated with deciphering the record preserved in rocks subjected to repeated HP granulite facies events. However, this is considered the most straightforward interpretation of the current dataset. The unique character of this lower crustal record preserved in the East Lake Athabasca region may be directly linked to the unusual nature of the tectonic history required for the genesis, exhumation and preservation of these granulites.

EVOLUTION OF CONTINENTAL LITHOSPHERE IN THE WESTERN CANADIAN SHIELD

Lithospheric Stability

The history inferred for lower crustal exposures in the East Lake Athabasca region has important implications for the evolution of continental lithosphere in the western Canadian Shield. The record of 2.55 Ga HP granulite facies metamorphism, evidence for subsequent isobaric cooling, the still relatively anhydrous nature of lithologies inferred during later metamorphism, and the recurrence of metamorphism at HP conditions at 1.9 Ga implies that these rocks resided in the crust for the intervening 650 m.y. This period of relative quiescence is interpreted to reflect an extended period of lithospheric stability following cooling to a cratonic geotherm. Long-term residence of high-pressure granulites in the deep crust is the history inferred for most lower crustal xenoliths erupted from stable continental interiors, and logically is the history of the lower crust in most Archean cratons. Similarly, lower crustal xenoliths commonly record subsequent thermal perturbations and magmatic episodes in response to plate margin accretionary and asthenospheric upwelling events (e.g. Schmitz and Bowring, 2003; Farmer et al., 2005). The dramatically distinct aspect of the record in the East Lake Athabasca region is that the subsequent episode of lithospheric perturbation was sufficiently severe to destabilize this cratonic region, culminating in the unroofing of the lower continental crust.

An important secondary point is the critical context this exposure provides for the interpretation of the record preserved in lower crustal xenolith samples. A commonly observed disparity in the equilibrium pressure and composition of isobarically cooled granulite xenoliths and terranes suggests that xenolith samples commonly represent samples of the lowermost (1.0 to 1.5 GPa) continental crust, while granulite terranes are exhumed from the upper and middle portions (0.6 to 0.8 GPa) of the lower crust (Bohlen and Mezger, 1989). In contrast, the rocks across the East Lake Athabasca region record conditions from 1.0 to >1.5 GPa during the high-pressure granulite facies episodes. These data suggest that this region represents a true exposure of lowermost continental crust that resided near the Moho for much of its history, comparable in crustal depth to many lower crustal xenolith samples. Thus, this terrane affords an exceptional opportunity to directly examine the rock types and structural relationships in the deepest portions of the crust, and provides a crucial in situ context to enable more robust analysis of the xenolith record.

Lithospheric Reactivation

An event of profound significance is required to disrupt and exhume a stabilized Archean craton. The ca. 1.9 Ga timing of the second episode of HP granulite facies metamorphism broadly coincides with the assembly of the Laurentian supercontinent. The position of the western Churchill Province as the intervening lithosphere spatially and temporally bounded by two inward dipping subduction zones – the 2.02-1.91 Ga Taltson-Thelon orogen to the northwest and the 1.91-1.81 Ga Trans-Hudson orogen to the southeast – must have been a central factor in its destabilization at this time. The Archean versus Proterozoic significance of the Snowbird tectonic zone, a ~2800 km long geophysical anomaly in the western Churchill Province, has long been debated owing to a complex record of both Archean and Proterozoic metamorphic events (Hoffman, 1988; Hanmer, 1997). New data establishes the timing of syntectonic and synmetamorphic intrusion of a major mafic dike swarm in the East Lake Athabasca region at 1.9 Ga (Chapter 2). This mafic magmatism is linked with contemporaneous mafic intrusive activity focused along > 1200 km strike length of the Snowbird tectonic zone. The exploitation of the Snowbird tectonic zone for emplacement of 1.9 Ga mafic magmas is consistent with major Paleoproterozoic reactivation of an earlier Archean structure. These results provide compelling evidence for a continent wide episode of 1.9 Ga asthenospheric upwelling spanning much of the western Canadian Shield, implying the integral role of this upwelling event in the reactivation of the Archean craton.

Lithospheric Exhumation

Multistage exhumation of the extensive regions of lower crust in the East Lake Athabasca region occurred during the ~200 m.y. period of instability following lithospheric disruption. Final unroofing by ca. 1.7 Ga is constrained by thermochronological data (Chapter 3) and the deposition of sediments of the Athabasca basin across the exhumed granulites at this time. The changing tempo of exhumation and associated juxtaposition of HP granulite domains during unroofing was driven by the evolving regional contractional and extensional regimes across the Laurentian supercontinent during and following its final assembly. This suggests the ultimate exposure of deep crust in the western Churchill Province largely owes to the protracted duration of lithospheric instability. Multistage exhumation histories characterized by pulses of exhumation punctuated by intervals of crustal residence may typify the exhumation of lower continental crust. The exceptional preservation of the high-grade assemblages in the rock across the region may be due to their former life as dehydrated granulites in the lowermost crust that limited the availability of fluids for retrogression during unroofing. The exhumation of the unusually extensive and well-preserved exposures of lower crust in the western Churchill Province is directly linked with the record of lithospheric disruption in this region. The unusual nature of this lithospheric history may in part explain the paucity of comparable exposures preserved elsewhere on Earth.

Lithospheric Preservation

The preservation of exhumed lower crust in the East Lake Athabasca region from ca. 1.7 Ga until the present attests to the re-attainment of a stable lithospheric configuration in the western Churchill Province. The spatial location of the East Lake Athabasca region in the middle of the Laurentian supercontinent that originally was a central factor in its lithospheric disruption, is also inferred to have played an important role in this region's subsequent preservation due to lateral shielding within the middle of the Laurentian supercontinent. Low temperature (U-Th)/He zircon and apatite data corroborate the extended residence of these rocks at shallow crustal levels ($\leq$ 2 km) following unroofing (Chapter 4). These data also permit assessment of vertical motions in the western Churchill Province that reflect the ongoing response of the continental interior to plate tectonic and mantle processes during later craton margin accretionary and rifting processes. These subtle episodes of uplift and subsidence represent a continuum with the lithospheric perturbation processes responsible for earlier destabilization of this craton.

CONCLUSIONS

Lower continental crust exposed in the East Lake Athabasca region retains an exceptional record of lithospheric stabilization, reactivation, and exhumation. Early stability is analogous to the history inferred for the rocks resident at the crustal base of most Archean cratons. Similarly, deep crustal perturbation owing to asthenospheric upwelling and plate margin tectonic processes is commonly recorded as episodes of magmatism and metamorphism in the deep crust. However, the history in the East Lake Athabasca of an event severe enough to expose the base of the crust to high temperatures followed by its exhumation dramatically differs from that preserved in most high-pressure granulites. We attribute this unusual record to the location of these rocks at the center of the Laurentian supercontinent during its assembly. The rarity of such records recognized in crustal rocks may be compounded by the common destruction of continental lithosphere that has been destabilized. Following 200 m.y. of lithospheric instability that culminated in the exhumation of the deep crust, this region apparently re-achieved a stable lithospheric configuration. Its subsequent survival was aided by its position within Laurentia, and low temperature thermochronological data help to constrain the uplift and subsidence history of this stabilized continental interior. The changing patterns of mantle dynamics and plate tectonic interactions thus are manifested as a continuum of lithospheric perturbations, from the subtle vertical motions of continents to the destabilization and potential destruction of continental lithosphere. Future studies that document the range of continental behavior in response to a variety of plate tectonic and mantle processes in this and other regions is essential to gain a more complete understanding of continental formation and survival.

REFERENCES

Baldwin, J.A., Bowring, S.A., Williams, M.L., and Williams, I.S., 2004, Eclogites of the Snowbird tectonic zone: petrological and U-Pb geochronological evidence for Paleoproterozoic high-pressure metamorphism in the western Canadian shield: Contributions to Mineralogy and Petrology, v. 147, p. 528-548.

Bohlen, S.R., and Mezger, K., 1989, Origin of granulite terranes and the formation of the lowermost continental crust: Science, v. 244, 326-329.

Bohlen, S.R., 1991, On the formation of granulites: Journal of Metamorphic Geology, v. 9, p. 223-229.

Chopin, C., 2003, Ultrahigh-pressure metamorphism: tracing continental crust into the mantle: Earth and Planetary Science Letters, v. 212, p. 1-14.

Ellis, D.J., 1987, Origin and evolution of granulites in normal thickness crust: Geology, v. 15, p. 167-170.

Farmer, G.L., Bowring, S.A., Williams, M.L., Christensen, N.I., Matzel, J.P. and Stevens, L.P., 2005, Contrasting lower crustal evolution across an Archean-Proterozoic suture: Physical, chemical and geochronologic studies of lower crustal xenoliths in southern Wyoming and northern Colorado, in, The Rocky Mountain region: an evolving lithosphere, eds. K.E. Karlstrom, G.R. Keller, eds.: Geophysical Monograph Series, v. 154, p. 139-162.

Hanmer, S., 1997, Geology of the Striding-Athabasca mylonite zone, northern Saskatchewan and southeastern District of Mackenzie, Northwest Territories: Geological Survey of Canada Bulletin, v. 501, pp.1-92.

Harley, S.L., 1989, The origins of granulites: a metamorphic perspective: Geological Magazine, v. 126, p. 215-247.

Harley, S.L. and Black, L.P., 1997, A revised Archean chronology for the Napier Complex, Enderby Land, from SHRIMP ion-microprobe studies: Antarctic Science, v. 9, p. 74-91.

Hoffman, P.F., 1988, United Plates of America, the birth of a craton: Early Proterozoic assembly and growth of Laurentia: Annual Reviews of Earth and Planetary Science Letters, v. 16, p.545-603.

Indares, A., 1995, Metamorphic interpretation of high-pressure-temperature pelites with preserved growth zoning in garnet, Eastern Grenville Province, Canadian Shield: Journal of Metamorphic Geology, v. 13, p. 475-486.

Jordan, T.H., 1978, Composition and development of the continental tectosphere: Nature, v. 274, p. 544-548.

Kopf, C. 1999. Deformation, metamorphism, and magmatism in the East Athabasca mylonite triangle, northern Saskatchewan: Implications for the Archean and Early Proterozoic crustal structure of the Canadian Shield. Ph. D. dissertation thesis, University of Massachusetts-Amherst, p. 139.

Krikorian, L. and Williams, M.L. 2002. Paleoproterozoic high grade metamorphism in the Wholdaia Lake segment of the Snowbird Tectonic Zone, Northwest Territories. Geological Association of Canada-Mineralogical Association of Canada, Saskatoon, Saskatchewan, Program with abstracts, 27: 64.

Mahan, K.H., 2005, Exhumation of exposed deep continental crust, western Canadian Shield: Integrating structural analysis, petrology, and in situ geochronology: PhD thesis, University of Massachusetts, Amherst, Massachusetts.

Mahan, K.H., Flowers, R.M., Williams, M.L., Goncalves, P., Bowring, S.A., and Jercinovic, M.J., 2005, A P-T-time-deformation path for exposed deep continental crust in the Snowbird tectonic zone, western Canadian shield: GSA Cordilleran Session Meeting abstract, San Jose, CA.

O'Brien, P. J. & Carswell, D. A., 1993. Tectonometamorphic evolution of the Bohemian Massif: evidence from high-pressure metamorphic rocks. Geologische Rundschau, v. 82, p. 531–555.

O'Brien, P.J. and Rotzler, J., 2003, High-pressure granulites: formation, recovery of peak conditions and implications for tectonics: Journal of Metamorphic Geology, v. 21, p. 3-20.

Percival, J. A. & Card, K. D., 1983. Archean crust as revealed in the Kapuskasing Uplift, Superior Province, Canada. Geology, v. 11, p. 323–326.

Schmitz, M.D. and Bowring, S.A., 2003, Ultrahigh-temperature metamorphism in the lower crust during Neoarchean Ventersdorp rifting and magmatism, Kaapvaal Craton, southern Africa: GSA Bulletin, v. 115, p. 533-548.

Williams, M.L., Hanmer, S., Kopf, C. and Darrach,M., 1995, Syntectonic generation and segregation of tonalitic melts from amphibolite dikes in the lower crust, Striding-Athabasca mylonite zone, northern Saskatchewan: Journal of Geophysical Research, v.100(B8), p.15,717-15,734.

Williams, M.L., Mellis, E.A., Kopf,C. and Hanmer,S., 2000, Microstructural Tectonometamorphic processes and the development of gneissic layering: a mechanism for metamorphic segregation: Journal of Metamorphic Geology, v. 18, p.41-57.

Williams, M.L. and Hanmer, S., 2005, Structural and metamorphic processes in the lower crust: Evidence from an isobarically cooled terrane, the East Athabasca mylonite triangle, In: Evolution and Differentiation of the Continental Crust, ed. M. Brown and R. Rushmer: Cambridge University Press, ---.

Zhao, G., Cawood, P.A., Wilde, S.A. and Lu, L., 2001, High-pressure granulites (retrograded eclogites) from the Hengshan complex, North China craton: Petrology and tectonic implications: Journal of Petrology, v. 42, p. 1141-1170.

Zingg, A., 1990. The Ivrea crustal cross-section (northern Italy and southern Switzerland). Exposed cross-sections of the continental crust; proceedings. NATO Advanced Study Institute on Exposed Cross-Sections of the Continental Crust, 317, 1–19.

APPENDIX A: DESCRIPTION OF MINERALS ANALYZED BY U-Pb

Titanite

Sixteen single-grain titanite fractions from six samples across the Chipman domain yielded $^{206}Pb/^{207}Pb$ dates that range from 1882.1 to 1897.5 Ma. Mafic granulite sample 02M133A from Cora Lake on the western side of the domain contains scarce, yellowish-brown titanite fragments that yielded two indistinguishable dates of 1885 and 1886 Ma. Chipman mafic granulite dike sample 03-52 and Chipman tonalite sample 03-5C were both collected from the central part of the Chipman domain at Chipman Lake. Three titanite fractions from 03-52 comprising light brown grains yielded dates from 1882 to 1886 Ma. Abundant titanite grains from 03-5C are honey-colored and anhedral, with three fractions that yielded dates from 1883 to 1896 Ma. Sample SZ00-196C is a Chipman mafic dike, and sample SZ00-196B is a heterogeneous Chipman tonalite, both from Woolhether Lake in the southern central part of the domain. Titanite grains in both samples are abundant, medium to dark brown, flattish grains with common core and rim morphologies that yielded seven fraction dates ranging from 1885 to 1898 Ma. One titanite fraction from Fehr granite sample 02-185, collected from the easternmost Chipman domain and containing abundant tan, ovate to rounded titanite, yielded a date of 1895 Ma.

Titanite grains from two samples in the Hearne domain are distinctly younger than those in the Chipman domain. Three titanite fractions from biotite granite sample 01M144 of Balliet Lake, comprising anhedral light brown titanite, yielded dates from 1745 to 1784 Ma. Calcsilicate sample 02M45, collected at Charlebois Lake, is the furthest east sample for which titanite data was acquired, and contains abundant, brown to dark brown irregular grain. Three fractions range from 1814 to 1819 Ma.

Apatite

Apatite fractions from three Chipman domain samples, one northwestern domain sample, two southern domain samples, and one Hearne domain sample yielded successful, radiogenic analyses. Eight apatite fractions from two samples in the Chipman domain yielded a span of $^{206}Pb/^{207}Pb$ dates from 1784 to 1853, with three fractions from a third sample that define a systematically younger apatite population. Chipman mafic dike sample 03-52 from the central Chipman domain contains clear, ovate flat apatite grains. Three single and two multigrain fractions characterized by a range of grains sizes yielded dates from 1784 to 1844 Ma. One single and two multigrain fractions of clear, ovate apatite grains with a range of grain sizes from Chipman tonalite sample SZ00-196B yielded dates from 1815 to 1853 Ma. Chipman mafic granulite sample 03-88A is from the northeastern margin of the Chipman domain at Bompas Lake. Clear, irregularly shaped blocky apatite grains in this sample were characterized by the highest Pb*/Pbc ratios of analyzed apatite grains, and yielded distinctly younger dates single and multigrain fraction dates from 1743 to 1752 Ma.

Northwestern domain felsic granulite sample 03-196 contains ovate to round, clear apatite. Three multigrain fractions yielded dates from 1768 to 1850 Ma, coinciding with the span of apatite dates for the central part of the Chipman domain.

Seven apatite fractions from two samples in the southern domain yielded dates from 1865 to 1901 Ma, distinctly older than dates obtained from the other domains. Axis mafic granulite sample 02-281 from the central part of the southern domain contains round to ovate apatite grains that yielded four single grain fraction dates from 1885 to 1901 Ma. Three apatite single grain fractions from eclogite sample 01SZ40B from the northern part of the southern domain, comprising irregular hazy grains, yielded dates from 1865 to 1880 Ma.

One single grain fraction of ovate, somewhat irregular apatite from biotite granite sample 01M144 from the Hearne domain yielded a $^{206}Pb/^{207}Pb$ date of 1746 Ma, consistent with apatite dates from sample 03-88A on the eastern margin of the Chipman domain. Five other apatite fractions from this sample contained Pb*/Pbc ratios two low to yield meaningful dates.

Rutile

Rutile grains in three samples from the western, central and northern Chipman domain were analyzed. Rutile fractions were analyzed from two samples in the northwestern domain, and one sample from the central part of the southern domain. No rutile was identified in lower grade, amphibolite facies rocks processed from the Hearne domain.

Six single grain rutile fractions analyzed from the central and west-central part of the Chipman domain yielded dates from 1851 to 1869 Ma, with four distinctly younger analyses obtained from the northeastern margin of the domain. Rutile grains from Chipman dike sample 03-52 are scarce, translucent, irregular red shards that are highly radiogenic and yielded four precise single fragment dates from 1851 to 1869 Ma. Felsic granulite sample 03-175A from the western part of the domain contains abundant, large (hundreds of microns), opaque, dark red fragments with external Fe-Ti oxide staining that yielded two dates of 1853 and 1857 Ma. A limited population of small, elongate, translucent, light red tabular rutile fragments were extracted from mafic granulite sample 03-88A near the northeastern edge of the domain. Three single and one multigrain fractions yielded dates from 1771 to 1808 Ma, systematically younger than rutile analyses from the central and western parts of the domain.

Six single grain rutile fractions from the northwestern domain yielded dates from 1780 to 1875 Ma. Three fractions from felsic granulite sample 03-196A, comprising mostly opaque, dark red fragments with Fe-Ti oxide staining, yielded dates from 1796 to 1830 Ma. Felsic granulite sample 03M13 from the eastern side of the domain contains abundant, large, dark red, opaque rutile grains, and yielded three fractions from 1831 to 1875 Ma.

Five single grain fractions of rutile analyzed from the central part of the southern domain were systematically older than rutile grains from the other domains. Axis mafic granulite sample 02-281 contains abundant, irregular, translucent to opaque rutile grains that yielded dates from 1874 to 1882 Ma.

Appendix A

APPENDIX B. ^{40}AR/^{39}AR LASER FUSION HORNBLENDE FRAGMENT DATA

Table B1. Chipman domain ^{40}Ar/^{39}Ar laser fusion hornblende fragment data[a]

	36Ar(a)	39Ar(k)	40Ar(r)	40Ar(r)	Age	± 2s
				(%)	(Ma)	
02M133A						
4A025@29	0.00010	0.13702	9.22261	99.69	1875.95	± 5.94
4A025@24	0.00004	0.12105	8.16848	99.85	1878.88	± 6.20
4A025@27	0.00008	0.12646	8.71564	99.73	1903.65	± 6.18
4A025@36	0.00000	0.08745	6.08527	100.00	1915.00	± 7.17
4A025@38	0.00003	0.10464	7.45452	99.87	1942.77	± 6.62
4A025@26	0.00004	0.11899	8.68821	99.85	1972.27	± 6.89
4A025@23	0.00002	0.09094	6.66424	99.92	1976.65	± 7.06
4A025@21	0.00003	0.10853	7.96838	99.90	1978.88	± 6.65
4A025@22	0.00002	0.08811	6.66045	99.93	2014.12	± 7.20
4A025@25	0.00005	0.12944	9.78811	99.83	2014.49	± 6.29
4A025@37	0.00000	0.10994	8.33088	100.00	2017.05	± 7.33
4A025@28	0.00006	0.07985	6.14462	99.73	2035.79	± 10.08
4A025@40	0.00002	0.06661	5.31785	99.91	2080.85	± 8.93
4A025@34	0.00008	0.09500	8.07868	99.71	2159.67	± 6.93
4A025@35	0.00004	0.05923	5.09197	99.78	2173.40	± 10.05
4A025@31	0.00005	0.08887	7.67034	99.81	2178.33	± 7.89
4A025@32	0.00005	0.07925	7.14264	99.80	2233.41	± 7.62
4A025@33	0.00007	0.07134	6.87450	99.72	2320.04	± 8.29
4A025@39	0.00004	0.07103	7.73459	99.84	2482.27	± 8.77
4A025@30	0.00009	0.08636	9.56393	99.72	2504.96	± 8.44
SZ00-196C						
4A028@89	0.00005	0.12296	8.25724	99.82	1873.23	± 6.32
4A028@100	0.00000	0.09336	6.36313	100.00	1890.56	± 6.50
4A028@88	0.00005	0.12313	8.46193	99.83	1900.34	± 6.21
4A028@84	0.00003	0.08078	5.61715	99.83	1914.12	± 8.63
4A028@85	0.00003	0.10625	7.37993	99.89	1912.79	± 6.37
4A028@91	0.00006	0.09526	6.66187	99.72	1920.90	± 7.15
4A028@87	0.00007	0.10655	7.51321	99.74	1930.68	± 6.91
4A028@99	0.00005	0.08707	6.26103	99.75	1953.91	± 7.42
4A028@82	0.00005	0.10946	7.86677	99.81	1953.32	± 6.68
4A028@90	0.00008	0.10118	7.29013	99.66	1956.33	± 6.80
4A028@92	0.00013	0.10206	7.39395	99.49	1962.90	± 6.93
4A028@83	0.00010	0.10945	7.91268	99.63	1960.40	± 6.28
4A028@96	0.00015	0.12608	9.13124	99.50	1962.45	± 6.27
4A028@97	0.00024	0.11335	8.25613	99.16	1969.35	± 6.17
4A028@81	0.00009	0.10966	8.04709	99.66	1978.20	± 6.60
4A028@98	0.00019	0.10967	8.35140	99.33	2023.00	± 6.39
4A028@86	0.00005	0.06606	5.11196	99.73	2042.63	± 8.86
4A028@95	0.00014	0.10823	8.52350	99.51	2064.12	± 6.43
4A028@94	0.00014	0.10987	9.00964	99.53	2114.13	± 6.90

Table B1. (Continued)

	36Ar(a)	39Ar(k)	40Ar(r)	40Ar(r) (%)	Age (Ma)	± 2s
03-52						
4A023@85	0.00016	0.16380	12.36031	99.61	2020.06	± 6.46
4A023@92	0.00005	0.07469	5.64884	99.72	2022.74	± 8.08
4A023@79	0.00015	0.15160	11.97808	99.64	2076.36	± 5.90
4A023@99	0.00011	0.08503	6.78723	99.52	2088.94	± 7.55
4A023@100	0.00008	0.06339	5.50936	99.56	2195.74	± 9.89
4A023@80	0.00019	0.11457	9.99917	99.43	2200.99	± 6.29
4A023@78	0.00007	0.07592	6.83827	99.69	2241.23	± 8.46
4A023@93	0.00004	0.05214	4.86466	99.75	2286.61	± 9.40
4A023@97	0.00013	0.07388	6.92192	99.44	2292.13	± 8.01
4A023@73	0.00013	0.09150	8.66841	99.55	2306.45	± 9.19
4A023@96	0.00018	0.07148	6.87650	99.25	2326.50	± 7.77
4A023@86	0.00021	0.12980	12.58105	99.52	2336.34	± 6.50
4A023@83	0.00017	0.13587	13.58436	99.63	2377.11	± 7.35
4A023@91	0.00002	0.01384	1.49880	99.62	2483.64	± 23.61
4A023@89	0.00019	0.11731	12.75806	99.57	2489.56	± 6.65
4A023@82	0.00008	0.05649	6.22666	99.60	2507.81	± 9.48
4A023@87	0.00019	0.07410	8.80797	99.38	2610.96	± 9.45
4A023@77	0.00010	0.05477	6.69494	99.56	2649.56	± 9.44
4A023@71	0.00005	0.05391	6.90515	99.79	2714.76	± 11.10
4A023@81	0.00011	0.05624	7.16381	99.54	2706.97	± 12.76
4A023@95	0.00011	0.03942	5.11971	99.36	2734.50	± 12.41
4A023@76	0.00009	0.05978	8.09056	99.66	2792.59	± 10.72
4A023@84	0.00012	0.06498	8.79731	99.60	2793.07	± 9.60
4A023@72	0.00007	0.05305	7.31417	99.71	2818.97	± 10.38
4A023@94	0.00013	0.08930	13.77583	99.72	2981.01	± 12.20
4A023@74	0.00007	0.04554	7.17753	99.70	3012.37	± 11.02
4A023@75	0.00005	0.03957	6.46288	99.77	3064.74	± 15.04
4A023@98	0.00004	0.03031	6.79371	99.81	3543.93	± 14.00
4A023@90	0.00007	0.03038	6.89486	99.70	3563.24	± 18.43

[a] Percentage of radiogenic 40Ar is reported for each analysis. Uncertainties are quoted at 2 sigma and do not include the propagated errors in irradiation parameter J.

Table B2. Northwestern domain $^{40}Ar/^{39}Ar$ laser fusion hornblende fragment data[a]

	36Ar(a)	39Ar(k)	40Ar(r)	40Ar(r) (%)	Age (Ma)	± 2s
96W23C						
4A025@43	0.00009	0.11560	7.95172	99.67	1901.42	± 7.02
4A025@46	0.00012	0.12597	8.82465	99.59	1922.95	± 6.41
4A025@56	0.00002	0.09775	6.91439	99.90	1934.37	± 6.79
4A025@42	0.00017	0.11087	7.84543	99.37	1934.88	± 6.13
4A025@58	0.00015	0.07458	5.43675	99.18	1970.24	± 9.34
4A025@49	0.00009	0.08246	6.03222	99.56	1974.46	± 6.80
4A025@45	0.00012	0.07464	5.46798	99.36	1976.15	± 8.19
4A025@53	0.00006	0.09450	6.96169	99.74	1982.97	± 7.14
4A025@44	0.00013	0.10305	7.62904	99.49	1988.84	± 6.49
4A025@48	0.00015	0.07993	6.04327	99.27	2014.36	± 11.15
4A025@47	0.00018	0.09419	7.20082	99.29	2027.74	± 6.98
4A025@51	0.00006	0.08028	6.12753	99.71	2025.88	± 7.50
4A025@55	0.00005	0.08135	6.25128	99.74	2034.05	± 8.30
4A025@41	0.00009	0.12324	9.42375	99.73	2028.08	± 6.34
4A025@59	0.00026	0.10027	7.99447	99.03	2079.27	± 7.39
4A025@52	0.00008	0.09311	7.52804	99.70	2096.55	± 7.69
4A025@60	0.00010	0.10775	8.72379	99.66	2098.25	± 6.48
4A025@54	0.00007	0.10292	8.76975	99.76	2162.20	± 6.99
4A025@50	0.00011	0.07998	7.24702	99.55	2240.30	± 7.50
03-197B						
4A023@50	0.00008	0.13020	8.67227	99.72	1868.25	± 6.44
4A023@39	0.00005	0.11057	7.48617	99.79	1887.33	± 6.40
4A023@37	0.00009	0.12305	8.34531	99.70	1889.38	± 6.85
4A023@49	0.00005	0.12099	8.20878	99.81	1889.79	± 6.08
4A023@46	0.00003	0.11973	8.12492	99.87	1890.00	± 6.46
4A023@44	0.00008	0.10980	7.56880	99.68	1908.49	± 6.58
4A023@33	0.00008	0.08874	6.12821	99.60	1910.61	± 8.87
4A023@41	0.00006	0.12157	8.39925	99.78	1911.17	± 6.16
4A023@32	0.00005	0.08923	6.17342	99.74	1912.83	± 8.97
4A023@38	0.00004	0.10143	7.14185	99.85	1933.58	± 7.60
4A023@34	0.00009	0.09261	6.52963	99.60	1935.14	± 8.81
4A023@35	0.00008	0.10425	7.38663	99.67	1940.98	± 7.03
4A023@42	0.00008	0.13456	9.64287	99.76	1954.50	± 6.30
4A023@40	0.00007	0.12449	8.94889	99.76	1958.21	± 6.25
4A023@47	0.00003	0.12022	8.68623	99.91	1964.28	± 7.01
4A023@45	0.00006	0.11558	8.40325	99.78	1971.81	± 6.46
4A023@36	0.00008	0.12170	9.00887	99.72	1993.46	± 7.91
4A023@43	0.00008	0.12098	9.00429	99.74	1999.96	± 7.13
4A023@48	0.00007	0.10512	7.88091	99.76	2008.82	± 7.87
4A023@31	0.00006	0.08427	6.93209	99.75	2122.96	± 8.89

[a] See notes in Table B1.

Table B3. Southern domain ^{40}Ar/^{39}Ar laser fusion hornblende fragment data[a]

	36Ar(a)	39Ar(k)	40Ar(r)	40Ar(r) (%)	Age (Ma)	± 2s
SZ00-118D						
4A028@63	0.00000	0.07665	5.22105	100.00	1889.95	± 6.33
4A028@69	0.00001	0.10562	7.28722	99.96	1904.97	± 5.93
4A028@80	0.00000	0.09334	6.44366	100.00	1905.61	± 5.92
4A028@70	0.00000	0.10057	7.03490	100.00	1921.15	± 5.60
4A028@68	0.00005	0.11462	8.03303	99.81	1923.45	± 5.94
4A028@64	0.00006	0.10081	7.18827	99.74	1943.86	± 6.12
4A028@76	0.00001	0.11953	8.56951	99.96	1950.39	± 5.74
4A028@71	0.00010	0.10794	7.80424	99.63	1960.51	± 5.69
4A028@77	0.00003	0.12029	8.87153	99.89	1984.30	± 5.71
4A028@61	0.00011	0.13488	9.96689	99.67	1986.59	± 6.04
4A028@65	0.00004	0.09772	7.26210	99.84	1993.46	± 6.22
4A028@78	0.00003	0.08517	6.41527	99.86	2009.81	± 6.40
4A028@74	0.00005	0.09658	7.40432	99.78	2031.20	± 6.44
4A028@66	0.00005	0.07985	6.23949	99.76	2054.47	± 6.80
4A028@67	0.00002	0.10522	8.36370	99.92	2075.58	± 6.51
4A028@62	0.00008	0.08561	6.81870	99.64	2078.10	± 6.56
4A028@75	0.00002	0.09906	8.18063	99.92	2122.86	± 7.40
4A028@79	0.00008	0.11215	9.53658	99.76	2159.61	± 5.88
4A028@72	0.00010	0.10345	8.92769	99.67	2178.19	± 6.53
4A028@73	0.00005	0.08961	8.70449	99.82	2330.39	± 7.64
01SZ78						
4A023@52	0.00008	0.11731	7.97917	99.72	1896.01	± 7.54
4A023@59	0.00002	0.09171	6.27920	99.89	1903.77	± 9.06
4A023@61	0.00008	0.13765	9.41634	99.75	1902.78	± 5.91
4A023@56	0.00004	0.12266	8.48736	99.84	1916.18	± 6.89
4A023@66	0.00009	0.12959	8.98837	99.69	1919.03	± 7.99
4A023@55	0.00006	0.12033	8.40686	99.80	1927.61	± 7.26
4A023@54	0.00011	0.12659	8.86604	99.64	1930.52	± 6.07
4A023@70	0.00005	0.09773	6.85990	99.77	1933.15	± 10.31
4A023@69	0.00014	0.13699	9.66109	99.57	1938.77	± 6.47
4A023@63	0.00006	0.11460	8.11762	99.77	1944.00	± 8.37
4A023@68	0.00008	0.10662	7.59218	99.70	1950.25	± 6.97
4A023@62	0.00013	0.10010	7.05038	99.45	1937.24	± 8.16
4A023@58	0.00004	0.11724	8.42876	99.86	1961.65	± 6.28
4A023@53	0.00010	0.13228	9.63530	99.68	1977.36	± 6.04
4A023@57	0.00002	0.09930	7.28860	99.94	1986.58	± 8.92
4A023@51	0.00004	0.10233	7.58602	99.85	1998.51	± 7.46
4A023@64	0.00009	0.11286	8.36106	99.67	1997.69	± 8.02
4A023@60	0.00006	0.12480	9.28673	99.82	2003.10	± 6.99
4A023@65	0.00003	0.07750	6.08850	99.86	2069.24	± 10.54
4A023@67	0.00003	0.09815	8.02603	99.88	2118.99	± 7.61

[a] See notes in Table B1.

Table B4. Rae domain ^{40}Ar/^{39}Ar laser fusion hornblende fragment data[a]

	36Ar(a)	39Ar(k)	40Ar(r)	40Ar(r) (%)	Age (Ma)	± 2s
99B-59						
4A025@74	0.00000	0.00853	0.55692	100.00	1841.15	± 31.38
4A025@75	0.00003	0.01532	1.05604	99.28	1903.54	± 29.32
4A025@71	0.00000	0.01147	0.83619	100.00	1970.04	± 24.77
4A025@70	0.00005	0.01809	1.35228	98.96	2000.22	± 23.43
4A025@66	0.00026	0.02122	1.63644	95.49	2038.12	± 20.51
4A025@79	0.00000	0.00632	0.52196	100.00	2122.46	± 50.38
4A025@65	0.00001	0.01498	1.39071	99.69	2271.31	± 27.30
4A025@76	0.00007	0.02793	2.86481	99.25	2402.02	± 15.10
4A025@68	0.00016	0.01631	1.75216	97.38	2463.92	± 24.63
4A025@69	0.00070	0.02423	2.91126	93.38	2616.26	± 17.74
4A025@78	0.00013	0.01070	1.51534	97.62	2848.00	± 35.80
4A025@67	0.00098	0.01603	2.82545	90.74	3167.45	± 27.26
4A025@73	0.00082	0.01507	2.98559	92.49	3344.05	± 28.33
4A025@72	0.00119	0.01552	3.20736	90.11	3408.32	± 27.28
4A025@80	0.00029	0.01179	2.57177	96.81	3491.50	± 36.57
4A025@77	0.00043	0.00820	2.26852	94.71	3865.23	± 45.01

[a] See notes in Table B1.

Table B5. Hearne domain ^{40}Ar/^{39}Ar laser fusion hornblende fragment data[a]

	36Ar(a)	39Ar(k)	40Ar(r)	40Ar(r) (%)	Age (Ma)	± 2s
01M123C						
4A025@05	0.00018	0.14828	8.67564	99.40	1721.84	± 5.99
4A025@13	0.00013	0.18262	10.69851	99.64	1723.24	± 5.71
4A025@10	0.00009	0.10140	5.94054	99.57	1723.26	± 7.79
4A025@18	0.00010	0.16529	9.69880	99.69	1724.98	± 5.82
4A025@11	0.00009	0.18130	10.64914	99.76	1726.14	± 5.87
4A025@17	0.00008	0.15691	9.22139	99.73	1726.73	± 6.08
4A025@07	0.00012	0.09947	5.84959	99.41	1727.45	± 7.93
4A025@06	0.00013	0.18852	11.09501	99.65	1728.34	± 5.64
4A025@19	0.00013	0.10750	6.32995	99.41	1728.91	± 7.03
4A025@03	0.00006	0.14108	8.30866	99.78	1729.12	± 6.95
4A025@14	0.00012	0.12070	7.11495	99.52	1730.09	± 6.84
4A025@04	0.00008	0.10860	6.40285	99.64	1730.33	± 7.54
4A025@08	0.00012	0.08752	5.16681	99.34	1731.82	± 8.11
4A025@16	0.00011	0.11540	6.81593	99.52	1732.33	± 6.92
4A025@12	0.00008	0.12175	7.19179	99.66	1732.42	± 6.58
4A025@15	0.00014	0.18942	11.19234	99.63	1732.78	± 5.65
4A025@09	0.00007	0.09446	5.58297	99.65	1733.01	± 7.78
4A025@20	0.00007	0.09426	5.60152	99.61	1739.09	± 7.64

[a] See notes in Table B1.

APPENDIX C. ^{40}AR/^{39}AR LASER ABLATION MICA DATA

Table C1. Chipman domain ^{40}Ar/^{39}Ar Mica Laser Ablation Spot Data^{a}

	36Ar(a)	39Ar(k)	40Ar(r)	40Ar(r) (%)	Age (Ma)	± 2s
03-169E, biotite						
4X022D1	0.01110	0.05125	3.12566	48.8	1749.58	± 22.87
4X022D2	0.00132	0.03974	2.47095	86.3	1771.12	± 14.13
4X022D3	0.00266	0.04263	2.64287	77.0	1767.91	± 13.39
4X022D4	0.00031	0.03381	2.05490	95.7	1745.79	± 17.88
4X022D5	0.00140	0.06437	4.00253	90.7	1771.18	± 8.72
4X022D6	0.00501	0.07411	4.54283	75.4	1755.20	± 10.78
4X022E1	0.00176	0.02510	1.54529	74.8	1760.17	± 18.36
4X022E2	0.00116	0.02725	1.67499	83.1	1758.49	± 17.50
4X022E3	0.00207	0.02798	1.73936	74.0	1770.92	± 18.24
4X022E4	0.00237	0.03225	1.97208	73.8	1752.55	± 17.20
4X022F1	0.00154	0.06603	4.09754	90.0	1768.94	± 8.40
4X022F2	0.00025	0.04182	2.60223	97.3	1771.94	± 11.34
4X022F3	0.00078	0.02572	1.60141	87.4	1772.68	± 17.18
4X022F4	0.00028	0.01977	1.23788	93.8	1779.21	± 21.17
4X022G1	0.00040	0.07734	4.77973	97.6	1764.31	± 8.17
4X022G2	0.00102	0.06005	3.68786	92.5	1757.37	± 9.33
4X022G3	0.00009	0.04346	2.69488	99.0	1768.21	± 10.45
4X022G4	0.00030	0.08042	4.95097	98.3	1760.10	± 8.11
4X022G5	0.00044	0.06673	4.11957	96.9	1763.12	± 9.61
4X022G6	0.00039	0.06902	4.27745	97.4	1767.56	± 7.57
02-183C, muscovite						
4X024JC1	0.00002	0.04387	2.69010	99.8	1759.45	± 12.01
4X024JC2	0.00035	0.04984	3.05483	96.7	1758.99	± 10.83
4X024JC3	0.00005	0.01632	0.98729	98.5	1744.37	± 15.91
4X024JC4	0.00002	0.04668	2.85784	99.8	1757.72	± 10.33
4X024JC5	0.00001	0.04514	2.76917	99.9	1759.99	± 11.49
4X024JD1	0.00035	0.06741	4.12093	97.5	1756.02	± 10.49
4X024JD2	0.00011	0.06568	4.02430	99.2	1758.57	± 7.72
4X024JD3	0.00002	0.06705	4.10747	99.9	1758.36	± 8.28
4X024JD4	0.00004	0.06530	3.99771	99.7	1757.69	± 11.38
02-108B, biotite						
4X032CA1	0.00280	0.07489	4.51516	84.5	1740.50	± 7.74
4X032CA2	0.00167	0.07472	4.49199	90.1	1737.30	± 8.64
4X032CA3	0.00085	0.07185	4.33778	94.6	1742.15	± 7.93
4X032CA4	0.00090	0.10498	6.35894	96.0	1745.81	± 6.14
4X032CB1	0.00370	0.06981	4.26507	79.6	1755.33	± 8.65

Table C1. (Continued)

	36Ar(a)	39Ar(k)	40Ar(r)	40Ar(r) (%)	Age (Ma)	± 2s
02-77B, biotite						
4X022H4	0.00135	0.05723	3.48105	89.7	1746.54	± 12.08
4X022I2	0.00302	0.05489	3.33405	78.9	1744.85	± 14.14
4X022J2	0.00107	0.07098	4.31475	93.2	1745.80	± 14.81
4X032EA1	0.01237	0.05470	3.37533	48.0	1762.64	± 26.32
4X032EA2	0.00318	0.06083	3.74197	79.9	1759.23	± 18.47
4X032EC1	0.00243	0.06803	4.19824	85.4	1762.80	± 18.18
4X032EF1	0.00465	0.05972	3.68658	72.9	1763.07	± 19.72
4X032EF2	0.00181	0.04539	2.79299	83.9	1759.41	± 19.14
KX022I3	0.00058	0.05840	3.59877	95.5	1761.03	± 11.41
KX022K1	0.00137	0.05644	3.38782	89.3	1731.82	± 10.85
KX022K2	0.00105	0.07373	4.44951	93.5	1737.69	± 9.65
KX022L1	0.00299	0.05556	3.36500	79.2	1741.72	± 11.88
KX022L2	0.00084	0.03548	2.17712	89.7	1756.43	± 14.42
02-76B, biotite						
4X032HA1	0.00491	0.09156	5.72176	79.8	1776.71	± 8.34
4X032HA2	0.00160	0.04728	2.94221	86.1	1771.90	± 9.64
4X032HA3	0.00267	0.05201	3.27459	80.6	1785.23	± 11.35
4X032HA4	0.00121	0.06088	3.82658	91.4	1783.18	± 8.01
4X032HA5	0.00121	0.07799	4.86821	93.2	1775.41	± 7.08
4X032HA6	0.00173	0.08132	5.09198	90.9	1778.85	± 7.26
4X032HA7	0.00184	0.04894	3.08736	85.1	1787.35	± 10.21
4X032HA8	0.00489	0.04815	2.99276	67.4	1770.47	± 11.82
4X032HB1	0.00205	0.04458	2.81271	82.3	1787.52	± 15.27
4X032HB2	0.00198	0.05976	3.74528	86.5	1780.01	± 8.90
4X032HB3	0.00211	0.03351	2.11825	77.3	1789.77	± 13.05
4X032HB4	0.00106	0.05404	3.39735	91.6	1783.35	± 10.37
4X032HC1	0.00142	0.05673	3.56304	89.5	1782.42	± 11.84
4X032HC2	0.00166	0.05486	3.43919	87.5	1780.17	± 9.55
4X032HD2	0.00162	0.02570	1.59793	77.0	1770.97	± 18.53

aPercentage of radiogenic 40Ar is reported for each analysis. Uncertainties are quoted at 2 sigma and do not include the propagated errors in irradiation parameter J.

Table C2. Northwestern domain ^{40}Ar/^{39}Ar Mica Laser Ablation Spot Data[a]

	36Ar(a)	39Ar(k)	40Ar(r)	40Ar(r) (%)	Age ± 2s (Ma)	
03-196A						
4X024JA1	0.00050	0.07360	4.49599	96.82	1755.28	± 7.70
4X024JA2	0.00061	0.06432	3.96855	95.63	1766.51	± 8.01
4X024JA3	0.00062	0.05438	3.32053	94.79	1754.70	± 9.92
4X024JA4	0.00014	0.05206	3.19701	98.70	1761.09	± 9.83
4X024JA5	0.00069	0.05941	3.65474	94.73	1763.07	± 9.62
4X024JB1	0.00048	0.04423	2.72551	95.07	1765.07	± 11.56
4X024JB2	0.00047	0.04116	2.52434	94.82	1759.75	± 11.09
4X024JB3	0.00108	0.03662	2.26943	87.70	1771.48	± 12.77
4X032DD1	0.00004	0.12496	7.66744	99.86	1760.22	± 7.58
4X032DD2	0.00010	0.13255	8.09807	99.64	1755.34	± 7.08
4X032DF1	0.00040	0.06364	3.88957	97.06	1755.79	± 8.96
4X032DF2	0.00007	0.06061	3.73024	99.47	1763.70	± 10.11
BF02-109A						
4X024FC1	0.00043	0.05996	3.66480	96.62	1751.73	± 10.09
4X024FC2	0.00047	0.05139	3.14126	95.76	1751.82	± 8.72
4X024FC3	0.00004	0.05695	3.51904	99.66	1763.94	± 8.14
4X024FC4	0.00042	0.04723	2.91477	95.93	1762.56	± 9.28
4X024FC5	0.00058	0.04371	2.67446	93.99	1752.79	± 9.01
4X024FC6	0.00019	0.04063	2.49305	97.83	1756.07	± 11.77
4X024FC7	0.00004	0.01140	0.69671	98.13	1751.43	± 33.89
4X024FD1	0.00128	0.08384	4.57374	92.39	1626.99	± 8.14
4X024FD2	0.00047	0.04184	2.24473	94.20	1609.27	± 11.14
4X024FD3	0.00045	0.04546	2.65703	95.24	1701.99	± 11.95
4X024FE1	0.00575	0.06708	4.10731	70.75	1753.67	± 12.06
4X024FE2	0.00043	0.06559	4.00634	96.91	1751.04	± 9.56
4X024FE3	0.00186	0.06208	3.81311	87.41	1757.21	± 9.45

[a] See notes in Table C1.

Table C3. Southern domain ^{40}Ar/^{39}Ar Mica Laser Ablation Spot Data[a]

	36Ar(a)	39Ar(k)	40Ar(r)	40Ar(r) (%)	Age ± 2s (Ma)	
01SZ78, Biotite						
4X024GA1	0.00290	0.06015	3.91178	82.03	1822.03	± 8.93
4X024GA2	0.02197	0.06411	4.14818	38.99	1816.25	± 31.19
4X024GA3	0.00148	0.03443	2.23774	83.64	1821.39	± 12.57
4X024GA4	0.00088	0.04709	3.04332	92.13	1814.91	± 7.37
4X024GA5	0.00190	0.03415	2.24723	80.01	1835.75	± 11.27
4X024GA6	0.00068	0.05255	3.47143	94.51	1840.06	± 9.67
4X024GB1	0.00225	0.04013	2.67700	80.11	1851.35	± 14.30
4X024GB2	0.00023	0.04127	2.68465	97.56	1822.47	± 14.69
4X024GB3	0.00663	0.04954	3.29775	62.75	1848.79	± 17.03
4X024GB4	0.00132	0.03586	2.38558	85.93	1848.21	± 15.73
4X024HE1	0.00053	0.03627	2.44837	94.03	1864.96	± 14.05
4X024HE2	0.00179	0.07937	5.32187	90.95	1857.33	± 8.33
4X024HE3	0.00029	0.07281	4.75856	98.21	1827.72	± 10.73
4X024HE4	0.00383	0.05145	3.28672	74.39	1801.67	± 12.57
4X024HE5	0.00271	0.04139	2.66898	76.95	1812.22	± 13.63
01SZ122B, Biotite						
4X024IA1	0.00068	0.07738	5.01957	96.13	1819.20	± 8.19
4X024IA2	0.00049	0.06114	3.91567	96.43	1804.44	± 7.97
4X024IA3	0.00027	0.04694	3.06768	97.44	1827.58	± 16.00
4X024IA4	0.00026	0.04134	2.68261	97.20	1819.61	± 24.67
4X024IB1	0.00223	0.05514	3.68577	84.81	1853.66	± 9.20
4X024IB2	0.00015	0.02899	1.95728	97.76	1865.35	± 12.18
4X024IB3	0.00004	0.02838	1.93059	99.38	1874.09	± 23.53
4X024IC1	0.00266	0.05347	3.52259	81.75	1836.93	± 9.10
4X024IC2	0.00347	0.04895	3.19014	75.66	1824.40	± 13.33
4X024JE1	0.00613	0.11023	7.11303	79.71	1813.15	± 8.40
4X024JE2	0.00212	0.09665	6.16838	90.78	1800.54	± 6.88
4X024JE3	0.00499	0.06728	4.25164	74.24	1789.31	± 9.67
4X024JE4	0.00444	0.06257	3.92143	74.94	1779.93	± 10.27
4X024JE5	0.00163	0.06147	4.02330	89.29	1829.39	± 11.53
4X024JE6	0.00152	0.05942	3.80762	89.46	1805.21	± 12.08

[a] See notes in Table C1.

Table C4. Rae domain ^{40}Ar/^{39}Ar Mica Laser Ablation Spot Data[a]

Grain/Analysis	36Ar(a)	39Ar(k)	40Ar(r)	40Ar(r) (%)	Age (Ma)	± 2s
99B-87, muscovite						
4X022B1	0.00040	0.00637	0.38820	76.61	1762.00	± 50.92
4X022B2	0.00788	0.01937	1.12537	32.58	1709.16	± 44.69
4X022B3	0.00116	0.02196	1.30803	79.18	1736.70	± 16.61
4X022B4	0.00567	0.04007	2.35298	58.41	1720.97	± 20.16
4X022B5	0.00032	0.02175	1.27464	93.00	1718.90	± 21.37
4X022B6	0.00589	0.04423	2.66555	60.50	1749.97	± 17.59
4X022B7	0.00105	0.03174	1.85883	85.75	1718.20	± 11.58
4X022B8	0.00006	0.05215	3.11548	99.47	1740.29	± 7.81
4X022M1	0.00386	0.08480	5.02146	81.50	1730.36	± 8.53
4X022M2	0.00006	0.04298	2.58240	99.30	1746.59	± 10.39
4X022M3	0.00006	0.05299	3.12698	99.47	1726.49	± 8.70
4X022M4	0.00248	0.05963	3.53975	82.84	1733.06	± 11.18
4X022N1	0.00359	0.06812	4.02965	79.18	1729.26	± 10.92
4X022N2	0.00047	0.05967	3.54679	96.23	1734.67	± 7.71
4X022N3	0.00334	0.06897	4.12987	80.71	1742.88	± 10.05
4X022N4	0.00113	0.06409	3.74181	91.78	1714.61	± 8.99
03-193B, muscovite						
4X024FA1	0.00053	0.04834	2.85189	94.78	1716.50	± 10.35
4X024FA2	0.00011	0.05795	3.41885	99.02	1716.34	± 7.37
4X024FA3	0.00025	0.04417	2.59064	97.27	1709.97	± 8.25
4X024FA4	0.00006	0.04138	2.43845	99.31	1715.13	± 9.19
4X024FB1	0.00088	0.03383	2.01154	88.56	1725.20	± 12.18
4X024FB2	0.00117	0.02820	1.67197	82.84	1722.04	± 12.65
4X024FB3	0.00147	0.03173	1.86664	81.08	1713.21	± 15.06
4X024FB4	0.00125	0.03567	2.11071	85.06	1719.76	± 13.45
4X024GE1	0.00002	0.05361	3.17524	99.86	1720.73	± 7.83
4X024GE2	0.00006	0.04883	2.86000	99.35	1708.42	± 8.63
4X024GE3	0.00027	0.05375	3.17233	97.58	1716.83	± 7.67
4X024GE4	0.00007	0.04077	2.42432	99.20	1725.15	± 9.65
03M92, muscovite						
4X024GC1	0.00999	0.03492	2.06334	41.13	1727.68	± 31.83
4X024GC2	0.00011	0.03181	1.84543	98.27	1707.25	± 17.00
4X024GC3	0.00221	0.03314	1.98405	75.24	1742.24	± 18.40
4X024GC4	0.02155	0.04432	2.54864	28.58	1697.45	± 47.65
4X024GC5	0.00070	0.03068	1.84838	89.91	1749.09	± 19.43
4X024GC6	0.00000	0.04080	2.42132	100.00	1732.33	± 8.30
4X024GC7	0.00009	0.03904	2.35508	98.85	1750.63	± 14.97
4X024GD1	0.02881	0.01072	0.57381	6.32	1619.88	± 259.94
4X024GD2	0.00610	0.03188	1.94757	51.92	1764.83	± 25.60
4X024GD3	0.00668	0.04405	2.65760	57.40	1750.75	± 17.96
4X024GD4	0.00023	0.02492	1.48742	95.62	1738.89	± 16.45
4X024GD5	0.00026	0.03812	2.31020	96.81	1755.92	± 17.17
4X024GD6	0.00765	0.04105	2.50498	52.56	1763.50	± 22.01
4X032FC1	0.00298	0.07342	4.43144	83.41	1751.29	± 9.28
4X032FC2	0.00104	0.04740	2.85209	90.31	1747.77	± 8.39
4X032FC3	0.00001	0.07516	4.54728	99.96	1753.92	± 7.66
4X032FC4	0.00068	0.07962	4.78302	95.96	1745.97	± 8.45
96W23E, biotite						
4X032GA1	0.00418	0.11554	7.81563	86.37	1871.88	± 7.00
4X032GA2	0.00178	0.09419	6.38529	92.40	1874.38	± 8.40
4X032GA3	0.00027	0.02993	2.03128	96.22	1875.86	± 11.77
4X032GB1	0.00097	0.08271	5.53853	95.08	1860.02	± 6.74
4X032GD1	0.00017	0.10578	7.08304	99.30	1860.03	± 7.29
4X032GD2	0.00035	0.08724	5.85836	98.26	1863.36	± 6.91
4X032GD3	0.00014	0.08112	5.47286	99.24	1868.75	± 6.79
4X032GE1	0.00022	0.07139	4.76377	98.65	1855.96	± 7.38
4X032GE2	0.00325	0.08023	5.36080	84.81	1857.54	± 7.42
4X032GE3	0.00007	0.06850	4.59750	99.53	1862.81	± 7.09
4X032GE4	0.00070	0.05091	3.41039	94.28	1860.42	± 7.11
4X032GE5	0.00048	0.05113	3.43573	96.06	1864.10	± 7.68

[a] See notes in Table C1.

Table C5. Hearne domain ^{40}Ar/^{39}Ar Mica Laser Ablation Spot Data[a]

	36Ar(a)	39Ar(k)	40Ar(r)	40Ar(r) (%)	Age (Ma)	± 2s
02M23B, muscovite						
4X024HA1	0.00020	0.02051	1.22340	95.50	1728.40	± 17.70
4X024HA2	0.00000	0.01884	1.13887	100.00	1743.63	± 11.27
4X024HA3	0.00004	0.03368	2.03676	99.44	1743.97	± 11.22
4X024HA4	0.00001	0.03335	2.00225	99.86	1735.78	± 9.35
4X024HA5	0.00054	0.03567	2.15189	93.11	1741.22	± 11.07
4X024HA6	0.00036	0.03182	1.91780	94.70	1740.01	± 12.02
4X024HA7	0.00001	0.02158	1.28868	99.79	1729.87	± 20.83
4X024HB1	0.00000	0.01966	1.19332	100.00	1747.97	± 11.93
4X024HB2	0.00000	0.02378	1.42599	100.00	1734.75	± 12.65
4X024HB3	0.00000	0.02310	1.38418	100.00	1733.59	± 10.87
02M23B, biotite						
4X024HC1	0.00104	0.02282	1.36867	81.61	1734.86	± 16.44
4X024HC2	0.00087	0.02334	1.40494	84.53	1738.70	± 14.22
4X024HC3	0.00059	0.01884	1.12747	86.59	1732.10	± 19.36
4X024HC4	0.00033	0.01915	1.15524	92.28	1741.48	± 18.25
4X024HD1	0.00264	0.03345	2.02611	72.19	1745.77	± 17.10
4X024HD2	0.00157	0.03050	1.83202	79.75	1736.27	± 15.06
4X024HD3	0.00062	0.03200	1.92493	91.37	1738.17	± 11.65
4X024HD4	0.00052	0.02305	1.38483	89.95	1736.72	± 18.33
01M127B, muscovite						
4X032AA1	0.00072	0.14553	8.86115	97.66	1751.63	± 6.19
4X032AA2	0.00038	0.15330	9.21674	98.80	1737.45	± 5.80
4X032AB3	0.00018	0.06195	3.78769	98.61	1756.22	± 8.41
4X032AB4	0.00027	0.06391	3.88608	98.01	1750.12	± 8.30
4X032AC1	0.00012	0.13199	8.05809	99.58	1754.61	± 7.29
4X032AC2	0.00029	0.06416	3.88596	97.83	1745.62	± 6.92
4X032AC3	0.00001	0.13347	8.08666	99.98	1746.04	± 5.97
4X032AC4	0.00146	0.07460	4.55013	91.34	1753.60	± 7.97
4X032AD1	0.00003	0.10084	6.12525	99.87	1748.86	± 7.15
4X032AD2	0.00009	0.11052	6.68678	99.61	1744.49	± 8.78
01M127B, biotite						
4X032BA1	0.00622	0.05865	3.53455	65.78	1740.04	± 15.20
4X032BA2	0.00095	0.09865	5.91369	95.45	1734.12	± 6.21
4X032BA3	0.00229	0.10252	6.18261	90.13	1740.84	± 6.86
4X032BB1	0.00111	0.02919	1.78268	84.45	1754.82	± 17.55
4X032BB2	0.00226	0.02480	1.48333	68.92	1731.54	± 16.23
4X032BB3	0.00595	0.01300	0.78953	30.99	1748.66	± 48.40
4X032BB4	0.00209	0.01248	0.74736	54.77	1733.05	± 33.07
4X032BC1	0.00045	0.04461	2.70582	95.36	1747.21	± 9.48
4X032BC2	0.00073	0.03754	2.25910	91.27	1738.56	± 14.87
4X032BC3	0.00021	0.03421	2.06500	97.03	1741.79	± 13.67
4X032BC4	0.00017	0.03348	2.02417	97.62	1743.71	± 14.91
4X032BD1	0.00281	0.05190	3.14293	79.07	1745.49	± 8.63
4X032BD2	0.00119	0.05139	3.09487	89.83	1739.39	± 8.78
4X032BD3	0.00033	0.04985	2.98650	96.86	1733.46	± 7.80

[a] See notes in Table C1.

BF03-169E, Biotite, Filename 4X022G
Cora Lake pegmatite

500 µm

All analyses (N = 20): 1764.6 ± 11.5 (± .65%), MSWD = 1.38

K24-a, BF03-169E bt, 4X022G

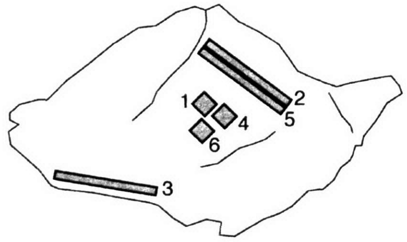

1) 1764.3 ± 8.2
2) 1757.4 ± 9.3
3) 1768.2 ± 10.5
4) 1760.1 ± 8.1
5) 1763.1 ± 9.6
6) 1767.6 ± 7.6

all
1763.5 ± 11.8
(± .67%)
MSWD = 0.89

Analyses 1-5, 10/1/04; Analysis 6, 10/6/04; M/F gain of 100
Pt #1: 182 µm, 90 sec, 20 Hz, 1800 bursts
Scan #2: 770 µm, 3 passes, 10 µm/sec, 20 Hz, 87 µm spot, 4:40 min
Scan #3: 770 µm, 3 passes, 10 µm/sec, 20 Hz, 87 µm spot, 4:40 min
Pt #4: 182 µm, 90 sec, 20 Hz, 1800 bursts
Scan #5: 770 µm, 3 passes, 10 µm/sec, 20 Hz, 87 µm spot, 5:28 min
Pt #6: 182 µm, 90 sec, 20 Hz, 1800 bursts

K24-b, BF03-169E bt, 4X022D

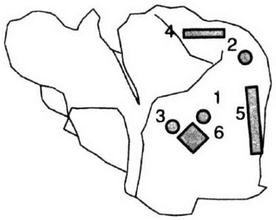

1) 1749.6 ± 22.9
2) 1771.1 ± 14.1
3) 1767.9 ± 13.4
4) 1745.8 ± 17.9
5) 1771.2 ± 8.7
6) 1755.2 ± 10.8

all:
1763.7 ± 12.4
(± .70%)
MSWD = 2.5

Analyses 1-5, 9/30/04; Analysis 6, 10/1/04; M/F gain of 100
Pt #1: 145 µm, 90 sec, 20 Hz, 1800 bursts
Pt #2: 145 µm, 90 sec, 20 Hz, 1800 bursts
Pt #3: 145 µm, 90 sec, 20 Hz, 1800 bursts
Scan #4: 350 µm, 3 passes, 10 µm/sec, 20 Hz, 106 µm spot, ~2 min
Scan #5: 470 µm, 4 passes, 10 µm/sec, 20 Hz, 106 µm spot, 3:44min
Pt #6: 182 µm, 90 sec, 20 Hz, 1800 bursts

K24-c, BF03-169E bt, 4X022E

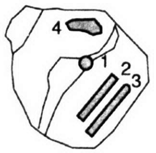

1) 1760.2 ± 18.4
2) 1758.5 ± 17.5
3) 1770.9 ± 18.2
4) 1752.6 ± 17.2

1760.2 ± 14.3
(± .81%)
MSWD = 0.74

All analyses 10/1/04; M/F gain of 100
Pt #1: 145 µm, 90 sec, 20 Hz, 1800 bursts
Scan #2: 380 µm, 5 passes, 10 µm/sec, 20 Hz, 87 µm spot, 3:50 min
Scan #3: 420 µm, 5 passes, 10 µm/sec, 20 Hz, 87 µm spot, 4:15 min
Scan #4: 260 µm, 5 passes, 10 µm/sec, 20 Hz, 106 µm spot, 2:40 min

K24-d, BF03-169E bt, 4X022F

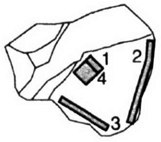

1) 1768.9 ± 8.4
2) 1771.9 ± 11.3
3) 1772.7 ± 17.2
4) 1779.2 ± 21.2

all
1771.1 ± 12.8
(± .72%)
MSWD = 0.3

All analyses 10/1/04; M/F gain of 100
Pt #1: 182 µm, 90 sec, 20 Hz, 1800 bursts
Scan #2: 670 µm, 3 passes, 10 µm/sec, 20 Hz, 87 µm spot, 4:50 min
Scan #3: 418 µm, 5 passes, 10 µm/sec, 20 Hz, 87 µm spot, 4:11 min
Pt #4: 182 µm, 90 sec, 20 Hz, 1800 bursts

Final reduction, 12/19/04: Final blanks, irradiation parameters, fractionation, J-values, error on J 0.5%

Figure C1

BF02-183C, Muscovite, Filename BF4X024H (75% of 1.5x scale)
Pellerin Lake msc rich schistose gneiss

500 µm

All analyses excluding JC#3 (N = 8): 1758.3 ± 11.8 (± .67%), MSWD = 0.05

J94-a, BF02-183C msc (pos JC)

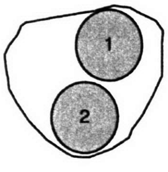

1) 1759.5 ± 12.0
2) 1759.0 ± 10.8

1759.2 ± 13.8
(± .79%)
MSWD = 0.00

Analyses 1-2, 12/11/04 (M/F gain of 60);
Pt #1: 256 µm, 20 Hz, 3000 bursts
clean with 5 bursts
Pt #2: 256 µm, 20 Hz, 4000 bursts
clean with 10 bursts

J94-b, BF02-183C msc (pos JC)

3) 1744.4 ± 15.9
4) 1757.7 ± 10.3
5) 1760.0 ± 11.5

1756.0 ± 13.2
(± .75%)
MSWD = 1.37

exclude #3:
1758.7 ± 13.6
(± .77%)
MSWD = 0.09

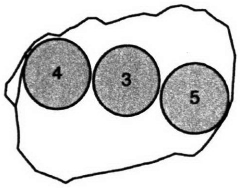

Analyses 3-5, 12/11/04 (M/F gain of 60);
Pt #3: 256 µm, 20 Hz, 1000 bursts (wanted more)
clean with 10 bursts
Pt #4: 256 µm, 20 Hz, 4000 bursts
clean with 10 bursts
Pt #5: 256 µm, 20 Hz, 4000 bursts
clean with 12 bursts

J94-c, BF02-183C msc (pos JD)

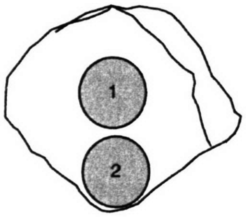

1) 1756.0 ± 10.5
2) 1758.6 ± 7.7

1757.7 ± 12.8
(± .73%)
MSWD = 0.15

Analyses1-2, 12/11/04 (M/F gain of 60);
Pt #1: 256 µm, 20 Hz, 4000 bursts
clean with 5 bursts
Pt #2: 256 µm, 20 Hz, 4000 bursts
clean with 10 bursts

J94-d, BF02-183C msc (pos JD)

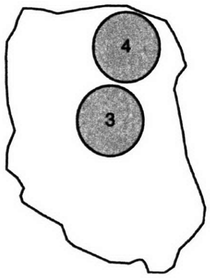

3) 1758.4 ± 8.3
4) 1757.7 ± 11.4

1758.1 ± 13.1
(± .74%)
MSWD = .01

Analyses 3-4, 12/11/04 (M/F gain of 60);
Pt #3: 256 µm, 20 Hz, 4000 bursts
clean with 5 bursts
Pt #4: 256 µm, 20 Hz, 4000 bursts
clean with 10 bursts

Final reduction 12/16/04: Final blanks, irradiation parameters, fractionation, J-values, error on J 0.5%

Figure C2

BF02-108B, Biotite, Filename BF4X032C (75% of 1.5x scale)
Steinhauer Lake, melt in Fehr granite

500 µm

All analyses (N = 5): 1744.2 ± 11.7 (± .67%), MSWD = 2.65

J4-a, BF02-108BB bt, 4X032Ca (pos 5)

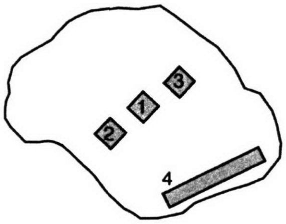

1) 1740.5 ± 7.7
2) 1737.3 ± 8.6
3) 1742.2 ± 7.9
4) 1744.8 ± 6.1

mean:
1742.2 ± 11.8
(± .68%)
MSWD = 0.95

Analyses 1-4, 12/17/04 (M/F gain of 60);
Pt #1: 182 µm, 20 Hz, 3000 bursts (clean 5) (hole through)
Pt #2: 182 µm, 20 Hz, 3000 bursts (clean 5) (hole through)
Pt #3: 182 µm, 20 Hz, 3000 bursts (clean 5) (hole through)
Scan #4: 145 µm, 20 Hz, 6 min manual

J4-a, BF02-108BB bt, 4X032Cb (pos 5)

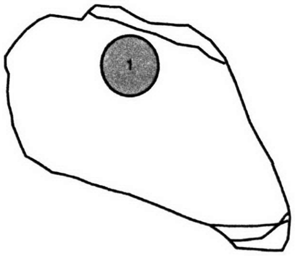

1) 1755.3 ± 8.7

Analysis 1, 12/17/04 (M/F gain of 60);
Pt #1: 285 µm, 20 Hz, 2000 bursts (clean 5)
79.8% rad 40Ar, 0.070V 39Ar, 4.3V rad 40Ar
Pt#2: Jumped out of pan at start of 2nd shot.

Final reduction 12/21/04: Final blanks, irradiation parameters, fractionation, J-values, error on J 0.5%

Figure C3.

BF02-77B, Biotite, File names 4X022J-I;BF4X032E
Steinhauer Lake pegmatitic segregation

All analyses (N = 13): 1747.6 ± 11.8 (± .68%), MSWD = 2.55
All analyses except K25-b, (N = 11):
1752.7 ± 12.1 (± .69%), MSWD = 1.29

500 µm

K25-a, BF02-77B bt (4X022J; pos BF4X032Ea)

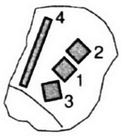

1) 2010.2 ± 15.4
2) 1745.8 ± 14.8
3) 1762.6 ± 26.3
4) 1759.2 ± 18.5

mean:
1752.8 ± 15.4
(± .88%)
MSWD = 0.97

Analysis 1, 10/2/04; Analysis 2, 10/6/04
Pt #1: 182 µm, 90 sec, 20 Hz, 1800 bursts (hole through)
Pt #2: 182 µm, 90 sec, 20 Hz, 1800 bursts

Analysis 3-4, 12/18/04; M/F gain of 60
Pt #3: 182 µm, 20 Hz, 2500 bursts
Scan #4: 186 µm, 20 Hz, ~ 6 min manual

KX022K, K25-b, BF02-77B

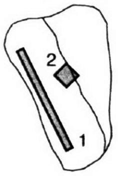

1) 1731.8 ± 10.9
2) 1737.7 ± 9.7

mean:
1735.1 ± 13.3
(± .77%)
MSWD = 0.65

Analyses 1-2, 10/6/04
Scan #1: 1075 µm, 2 passes, 10 µm/sec, 20 Hz,
87 µm spot, 4:19 min
Point #2: 182 µm, 90 sec, 20 Hz, 1800 bursts

K25-c, BF02-77B bt (4X022L; pos BF4X032Ec)

1) 1741.7 ± 11.9
2) 1756.4 ± 14.4
3) 1762.8 ± 18.2

mean:
1750.7 ± 13.9
(± .79%)
MSWD = 2.34

Analyses 1-2, 10/6/04
Pt #1: 182 µm, 90 sec, 20 Hz, 1800 bursts (hole through)
79.5% rad 40Ar, 0.055V 39Ar, 3.36V rad 40Ar
Scan#2: 400 µm, 5 passes,10 µm/sec, 20 Hz,
87 µm spot, 4:45 min
90.2% rad 40Ar, 0.035V 39Ar, 2.16 V rad 40Ar

Analysis 3, 12/18/04; M/F gain of 60
Pt #3: 285 µm, 20 Hz, 2000 bursts (clean 5) (hole through)
86.7% rad 40Ar, 0.047V 39Ar, 3.0 V rad 40Ar

4X022H, K25-d, BF02-77B bt

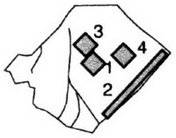

1) 2394.4 ± 25.2
2) 2401.6 ± 12.4
3) 2402.9 ± 18.3
4) 1746.5 ± 12.1

Analyses 1-2, 10/2/04; Analysis 3-4, 10/7/04
Pt #1: 182 µm, 90 sec, 20 Hz, 1800 bursts
Scan#2: 840 µm (25%), 3 passes, 10 µm/sec, 20 Hz, 87 µm spot, 5:03 min
Pt #3: 182 µm, 90 sec, 20 Hz, 1800 bursts
Pt #4: 182 µm, 90 sec, 20 Hz, 1800 bursts

4X022I, K25-e, BF02-77B bt

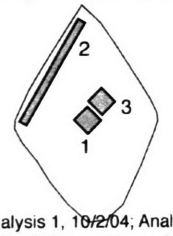

1) 2365.0 ± 11.4
2) 1744.9 ± 14.1
3) 1761.0 ± 11.4

mean:
1754.6 ± 14.3
(± .82%)
MSWD = 3.18

Analysis 1, 10/2/04; Analysis 2-3, 10/6/04
Pt #1: 182 µm, 90 sec, 20 Hz, 1800 bursts
Scan #2: 1050 µm (25%), 2 passes, 10 µm/sec, 20 Hz,
87 µm spot, 4:13 min
very irregular scan, stage kept hanging up.
Pt #3: 182 µm, 90 sec, 20 Hz, 1800 bursts

Grain loose when loaded in 4X032, unsuccessful

K25-f, BF02-77B bt (pos BF4X032Ef)

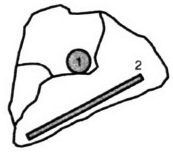

1) 1763.1 ± 19.7
2) 1759.4 ± 19.1

mean:
1761.2 ± 17.8
(± 1.01%)
MSWD = 0.07

Analyses 1-2, 12/18/04; M/F gain of 60
Pt #1: 285 µm, 20 Hz, 3000 bursts
Scan #2: 106 µm, 20 Hz, ~ 6 min manual

Final reduction 12/21/04: Final blanks, irradiation parameters, fractionation, J-values, error on J 0.5%

Figure C4

BF02-76B, Biotite, Filename BF4X032H (75% of 1.0x scale)
Chipman Lake pegmatite

500 µm

All analyses (N = 15): 1779.7 ± 11.6 (± .65%), MSWD = 1.15

K15-a, BF02-76B bt, 4X032Ha (pos 4)

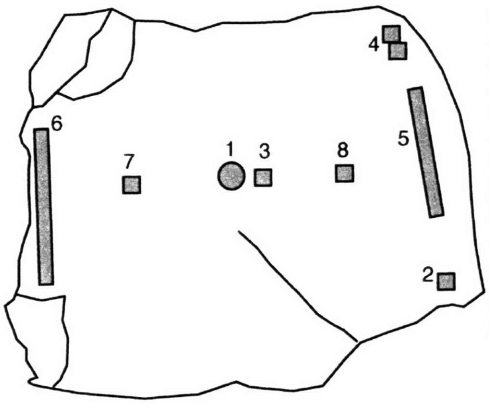

1) 1776.7 ± 8.3
2) 1771.9 ± 9.6
3) 1785.2 ± 11.4
4) 1783.2 ± 8.0
5) 1775.4 ± 7.1
6) 1778.9 ± 7.3
7) 1787.4 ± 10.2
8) 1770.5 ± 11.8

mean:
1778.5 ± 11.7
(± .66%)
MSWD = 1.49

Analyses 1-8, 12/18/04, (M/F gain of 60);
Pt #1: 145 µm, 20 Hz, 6000 bursts (clean 10)
Pt #2: 185 µm, 20 Hz, 5000 bursts (clean 10)
Pt #3: 185 µm, 20 Hz, 6000 bursts (clean 10)
Pt #4: 185 µm, 20 Hz, 5000 bursts (clean 10)
two spots b/c went thru
Scan #5: 145 µm, 20 Hz, 10 µm/sec, 4 passes (clean 1 Hz)
Scan #6: 145 µm, 20 Hz, 10 µm/sec, 6 min manual (clean 2 Hz)
Pt #7: 185 µm, 20 Hz, 6000 bursts (clean 8)
Pt #8: 185 µm, 20 Hz, 6000 bursts (clean 5)

K15-b, BF02-76B bt, 4X032Hb (pos 4)

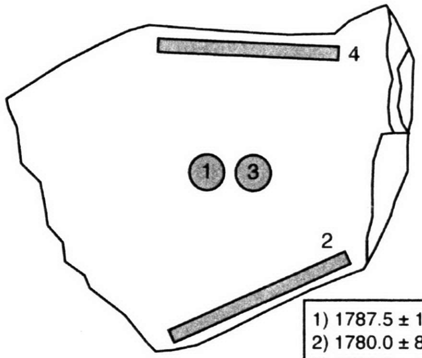

1) 1787.5 ± 15.3
2) 1780.0 ± 8.9
3) 1789.8 ± 13.1
4) 1783.4 ± 10.4

mean:
1783.8 ± 12.6
(± .71%)
MSWD = 0.60

Analyses 1-4, 12/19/04, (M/F gain of 60);
Pt #1: 285 µm, 20 Hz, 5000 bursts (clean 5)
Scan #2: 145 µm, 20 Hz, 10 µm/sec, 6 min manual (clean 2 Hz)
Pt #3: 285 µm, 20 Hz, 6000 bursts (clean 5)
Scan #4: 145 µm, 20 Hz, 10 µm/sec, 6 min manual (clean 2 Hz)

K15-d, BF02-76B bt, 4X032Hd (pos 4)

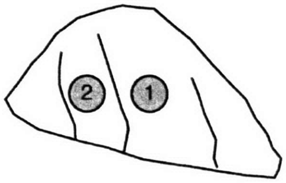

1) discard
2) 1780.0 ± 8.9

K15-c, BF02-76B bt, 4X032Hc (pos 4)

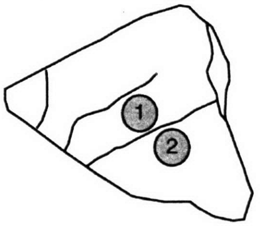

1) 1782.4 ± 11.8
2) 1780.2 ± 9.6

mean:
1781.1 ± 13.5
(± .76%)
MSWD = 0.09

Analyses 1-2, 12/19/04, (M/F gain of 60);
Pt #1: 285 µm, 20 Hz, 6000 bursts (clean 5)
only 7 cycles taken b/c rebooted
Pt #2: 285 µm, 20 Hz, 6000 bursts (clean 5)

Analyses 1-2, 12/19/04, (M/F gain of 60);
Pt #1: 285 µm, 20 Hz, 6000 bursts (clean 5)
Pt #2: 285 µm, 20 Hz, 6000 bursts (clean 5)

Final reduction 12/21/04: Final blanks, irradiation parameters, fractionation, J-values, error on J 0.5%

Figure C5

BF03-196A, Biotite, Filename BF4X024E (75% of 1.5x scale)
Reeve Lake retrogressed diatexite

500 µm

All analyses (N = 12): 1760.1 ± 11.5 (± .66%), MSWD = 1.17

J6-a, BF03-196A bt (pos JA)

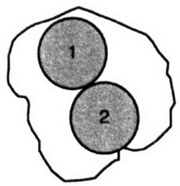

1) 1755.3 ± 7.7
2) 1766.5 ± 8.0

mean:
1760.7 ± 12.5
(± .71%)
MSWD = 4.09

Analyses 1-2, 12/10/04 (M/F gain of 60);
Pt #1: 256 µm, 20 Hz, 1500 bursts
clean with 5 bursts
Pt #2: 256 µm, 20 Hz, 1500 bursts
clean with 5 bursts

J6-b, BF03-196A bt (pos JA)

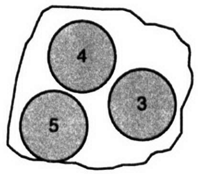

3) 1754.7 ± 9.9
4) 1761.1 ± 9.8
5) 1763.1 ± 9.6

mean:
1759.7 ± 12.6
(± .71%)
MSWD = 0.80

Analyses 3-4, 12/10/04; Analysis 5, 12/12/04 (M/F gain of 60);
Pt #3: 256 µm, 20 Hz, 1500 bursts
clean with 5 bursts
Pt #4: 256 µm, 20 Hz, 1500 bursts
clean with 5 bursts
Pt #5: 256 µm, 20 Hz, 1500 bursts
clean with 5 bursts

J6-c, BF03-196A bt (pos JB)

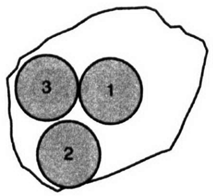

1) 1765.1 ± 11.6
2) 1759.8 ± 11.1
3) 1771.5 ± 12.8

mean:
1764.9 ± 13.1
(± .74%)
MSWD = 0.96

Analyses 1-2, 12/10/04;
Analysis 3, 12/12/04 (M/F gain of 60);
Pt #1: 256 µm, 20 Hz, 1500 bursts
clean with 10 bursts
Pt #2: 256 µm, 20 Hz, 1500 bursts
clean with 10 bursts
Pt #3: 256 µm, 20 Hz, 1500 bursts
clean with 6 bursts

J6-d, BF03-196A bt (pos BF4X032Dd)

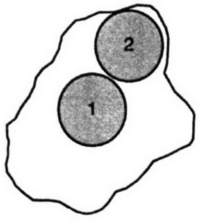

1) 1760.2 ± 7.6
2) 1755.3 ± 7.1

mean:
1757.6 ± 12.4
(± .70%)
MSWD = 0.89

Analyses 1-2, 12/18/04 (M/F gain of 60);
Pt #1: 256 µm, 20 Hz, 2500 bursts (clean 5)
Pt #2: 256 µm, 20 Hz, 2500 bursts (clean 5)

J6-f, BF03-196A bt (pos BF4X032Df)

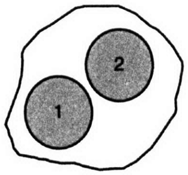

1) 1755.8 ± 9.0
2) 1763.7 ± 10.1

mean:
1759.3 ± 13.1
(± .74%)
MSWD = 1.37

Analyses 1-2, 12/18/04 (M/F gain of 60);
Pt #1: 256 µm, 20 Hz, 2000 bursts (clean 5)
Pt #2: 256 µm, 20 Hz, 2000 bursts (clean 5)

Final reduction J6a-c, 12/18/04: Final blanks, irradiation parameters, fractionation, J-values, error on J 0.5%
Final reduction J6d-e, 12/21/04: Final blanks, irradiation parameters, fractionation, J-values, error on J 0.5%

Figure C6

500 μm

BF02-109A, Biotite, Filename BF4X024I (75% of 1.5x scale)
Bompas Lake bt rich crenulated schist

All analyses excluding grain K14-c (N = 10): 1756.0 ± 11.7 (± .66%), MSWD = 1.03

K14-a, BF03-183C bt (pos FC)

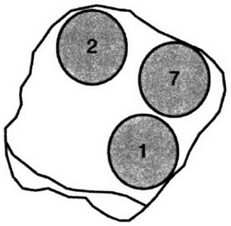

1) 1751.7 ± 10.1
2) 1751.8 ± 8.7
7) 1751.4 ± 33.9

1751.8 ± 13.0
(± .74%)
MSWD = 0.00

Analyses 1-2, 12/11/04; Analysis 7, 12/12/04; (M/F gain of 60);
Pt #1: 256 μm, 20 Hz, 3000 bursts
clean with 5 bursts
Pt #2: 256 μm, 20 Hz, 3000 bursts
clean with 5 bursts
Pt #7: 256 μm, 20 Hz, 2500 bursts
clean with 5 bursts

K14-b, BF03-183C bt (pos FC)

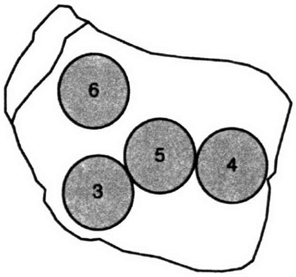

3) 1763.9 ± 8.1
4) 1762.6 ± 9.3
5) 1752.8 ± 9.0
6) 1756.1 ± 11.8

1759.4 ± 12.2
(± .69%)
MSWD = 1.39

Analyses 3-6, 12/11/04 (M/F gain of 60);
Pt #3: 256 μm, 20 Hz, 3000 bursts
clean with 5 bursts
Pt #4: 256 μm, 20 Hz, 3000 bursts
clean with 5 bursts
Pt #5: 256 μm, 20 Hz, 3000 bursts
clean with 5 bursts
Pt #6: 256 μm, 20 Hz, 3000 bursts
clean with 5 bursts

K14-c, BF03-183C bt (pos FD)

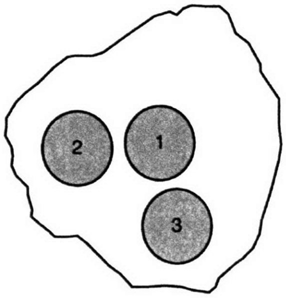

1) 1627.0 ± 8.1
2) 1609.3 ± 11.1
3) 1702.0 ± 12.0

1638.7 ± 12.2
(± .75%)
MSWD = 72.5

Analyses 1-3, 12/12/04; (M/F gain of 60);
Pt #1: 256 μm, 20 Hz, 3000 bursts
clean with 5 bursts
Pt #2: 256 μm, 20 Hz, 2000 bursts
clean with 5 bursts
Pt #3: 256 μm, 20 Hz, 2500 bursts
clean with 5 bursts

K14-d, BF03-183C bt (pos FE)

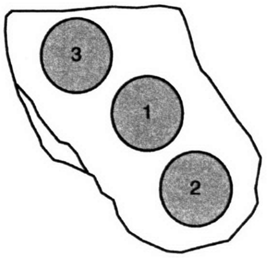

1) 1753.7 ± 12.1
2) 1751.0 ± 9.6
3) 1757.2 ± 9.5

1754.0 ± 12.7
(± .72%)
MSWD = 0.42

Analyses 1-3, 12/12/04; (M/F gain of 60);
Pt #1: 256 μm, 20 Hz, 2000 bursts
clean with 5 bursts
Pt #2: 256 μm, 20 Hz, 2000 bursts
clean with 5 bursts
Pt #3: 256 μm, 20 Hz, 2000 bursts
clean with 5 bursts

Final reduction 12/16/04: Final blanks, irradiation parameters, fractionation, J-values, error on J 0.5%

Figure C7

01SZ78, Biotite, Filename BF4X024B (1.0x scale)
Konkol Lake pegmatite

500 μm

K16-a, 01SZ78 bt (pos HE)

1) 1865.0 ± 14.1
2) 1857.3 ± 8.3
3) 1827.7 ± 10.7

all:
1849.4 ± 13.0
(± .70%)
MSWD = 12.51

All analyses 12/9/04 (M/F gain of 60)
(after Malcolm tried turning gain back up to 100)
Pt #1: 182 μm, 20 Hz, 1600 bursts (but may have drilled through after 800)
clean surface with 40 bursts
Pt #2: 285 μm, 920 Hz, 1500 bursts
clean surface with 6 bursts
Pt #3: 285 μm, 920 Hz, 1500 bursts
clean surface with 5 bursts

K16-b, 01SZ78 bt (pos HE)

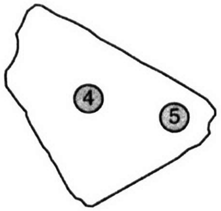

All analyses 12/9/04 (M/F gain of 60)
(after Malcolm tried turning gain back up to 100)
Pt #4: 285 μm, 20 Hz, 1500 bursts
clean surface with 40 bursts
Pt #5: 285 μm, 20 Hz, 1500 bursts
clean surface with 6 bursts

4) 1801.7 ± 12.6
5) 1812.2 ± 13.6

1806.5 ± 14.7
(± .81%)
MSWD = 1.29

K16-c, 01SZ78 bt (pos GA)

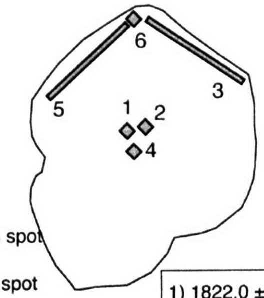

Analyses 1-5 12/2/04 (M/F gain of 57);
Analysis 6, 12/9/04 (M/F gain of 60)
Pt #1: 182 μm, 90 sec, 20 Hz, 1800 bursts
Pt #2: 182 μm, 90 sec, 20 Hz, 1800 bursts
Scan #3: ~900 μm, 2 passes, 10 μm/sec, 20 Hz, 87 μm spot
Pt #4: 182 μm, 90 sec, 20 Hz, 1800 bursts
Scan#5: ~900 μm, 2 passes, 10 μm/sec, 20 Hz, 87 μm spot
Pt #6: 182 μm, 2x1000 bursts, 20 Hz, 1800 bursts
clean with 285 micron 5 bursts

1) 1822.0 ± 8.9
2) 1816.3 ± 31.2
3) 1821.4 ± 12.6
4) 1814.9 ± 7.4
5) 1835.8 ± 11.3
6) 1840.1 ± 9.7

all:
1824.75 ± 12.2
(± .67%)
MSWD = 4.37

K16-d, 01SZ78 bt (pos GB)

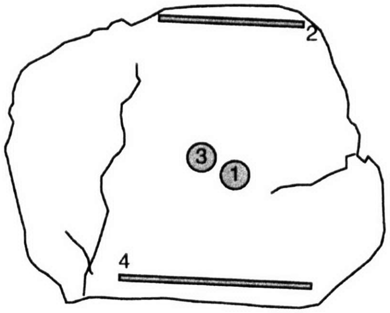

1) 1851.4 ± 14.3
2) 1822.5 ± 14.7
3) 1848.8 ± 17.0
4) 1848.2 ± 15.7

all:
1842.1 ± 13.9
(± .75%)
MSWD = 3.37

exclude #2:
1849.6 ± 14.7
(± .79%)
MSWD = 0.05

All analyses 12/10/04 (M/F gain of 60)
(after Malcolm tried turning gain back up to 100)
Pt #1: 285 μm, 20 Hz, 1500 bursts
cleaned surface previously, (prob 10s bursts)
Scan #2: 106 μm, 20 Hz, 3 scans, ~6:30
did not clean surface
Pt #3: 285 μm, 20 Hz, 2000 bursts
cleaned surface with 10 bursts
Scan #4: 106 μm, 20 Hz, 2 auto passes & 1 manual, ~6 min
did not clean surface

Final reduction 12/16/04: Final blanks, irradiation parameters, J-values, fractionation, error on J 0.5%

Figure C8

01SZ122B, Biotite, Filename BF4X024D (75% of 1.5x scale)
Currie Lake pegmatite

500 μm

K17-a, 01SZ122B bt (pos JE)

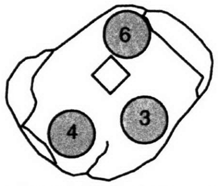

3) 1789.3 ± 9.7
4) 1779.9 ± 10.3
6) 1805.2 ± 12.1

mean:
1789.97 ± 12.9
(± .72%)
MSWD = 5.09

Analyses 3-4, 12/10/04; Analysis 6, 12/12/04; (M/F gain of 60);
Pt #1: 256 μm, 20 Hz, 1500 bursts
clean with 10 bursts
Pt #2: 256 μm, 20 Hz, 1500 bursts
clean with 10 bursts
Pt #6: 256 μm, 20 Hz, 2000 bursts
clean with 5 bursts
Note that 182 μm analysis was in October, only ~30% rad Ar

K17-b, 01SZ122B bt (pos JE)

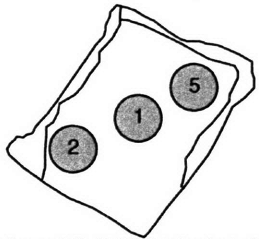

1) 1813.2 ± 8.4
2) 1800.5 ± 6.9
5) 1829.4 ± 11.5

mean:
1809.7 ± 12.4
(± .69%)
MSWD = 9.67

Analyses 1-2, 12/10/04; Analysis 5, 12/12/04; (M/F gain of 60);
Pt #1: 256 μm, 20 Hz, 2000 bursts
clean with 10 bursts
Pt #2: 256 μm, 20 Hz, 2000 bursts
clean with 10 bursts
Pt #5: 256 μm, 20 Hz, 2000 bursts
clean with 5 bursts

K17-c, 01SZ122B bt (pos IA)

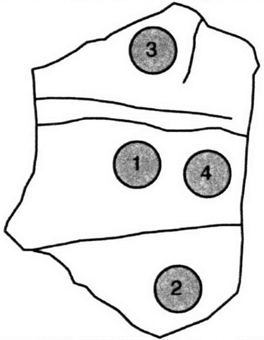

1) 1819.2 ± 8.2
2) 1804.4 ± 8.0
3) 1827.6 ± 16.0
4) 1819.6 ± 24.7

mean:
1813.6 ± 12.6
(± .69%)
MSWD = 3.48

Analyses 1-2, 12/10/04; Analyses 3-4, 12/12/04; (M/F gain of 60);
Pt #1: 256 μm, 20 Hz, 2000 bursts
clean with 5 bursts
Pt #2: 256 μm, 20 Hz, 2000 bursts
clean with 5 bursts
Pt #3: 256 μm, 20 Hz, 3000 bursts
clean with 5 bursts
Pt #4: 256 μm, 20 Hz, 3000 bursts
clean with 5 bursts

K17-d, 01SZ122B bt (pos IB)

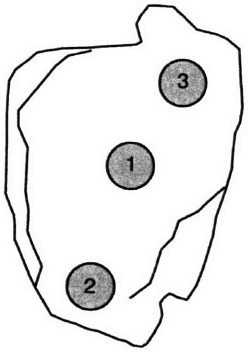

1) 1853.7 ± 9.2
2) 1865.4 ± 12.2
3) 1874.1 ± 23.5

mean:
1859.3 ± 13.6
(± .73%)
MSWD = 2.03

Analyses 1-3 12/10/04; Analysis 3, 12/12/04 (M/F gain of 60);
Pt #1: 256 μm, 20 Hz, 2000 bursts
clean with 10 bursts
Pt #2: 256 μm, 20 Hz, 1000 bursts
clean with 10 bursts
Pt #3: 256 μm, 20 Hz, 2500 bursts
clean with 5 bursts

K17-e, 01SZ122B bt (pos IC)

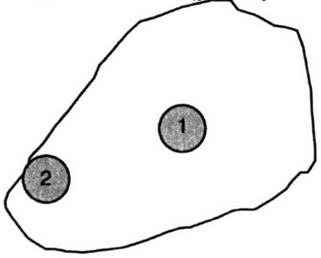

1) 1836.9 ± 9.1
2) 1824.4 ± 13.3

mean:
1832.9 ± 13.8
(± .75%)
MSWD = 2.42

Analyses 1-2 12/10/04 (M/F gain of 60);
Pt #1: 256 μm, 20 Hz, 2000 bursts
clean with 10 bursts
Pt #2: 256 μm, 20 Hz, 2000 bursts
clean with 10 bursts

Final reduction 12/16/04: Final blanks, irradiation parameters, J-values, fractionation, error on J 0.5%

Figure C9

99B-87, Muscovite (Filename BF4X022B)
Lowe Lake msc-pl rich rock with cd&gt

500 µm

All analyses (N = 16): 1732.0 ± 11.5 (± .66%), MSWD = 3.33

4X022B, I87-b, 99B-87 msc

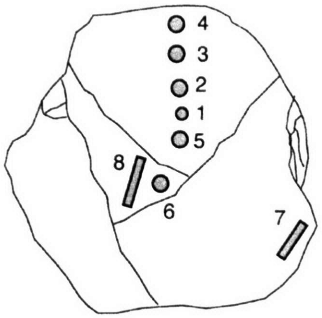

1) 1762.0 ± 50.9
2) 1709.2 ± 44.7
3) 1736.7 ± 16.6
4) 1721.0 ± 20.2
5) 1718.9 ± 21.4
6) 1750.0 ± 17.6
7) 1718.2 ± 11.6
8) 1740.3 ± 7.8

1733.3 ± 12.3
(± .71%)
MSWD = 2.79

Analyses 1-6, 9/29/04; Analyses 7-8, 9/30/04; M/F gain of 100
Pt #1: 106 µm, 20 Hz, 1000 bursts @ 100mJ
Pt #2: 145 µm, 20 Hz, 1000 bursts @ 100mJ
Pt #3: 145 µm, 20 Hz, 2000 bursts @ 90mJ
Pt #4: 145 µm, 20 Hz, 2000 bursts @ 90mJ
Pt #5: 145 µm, 20 Hz, 2000 bursts @ 90mJ
Pt #6: 145 µm, 20 Hz, 2000 bursts @ 90mJ
Scan #7: 350 µm, 3 passes, 10 µm/sec, 20 Hz, 106 µm spot, ~2 min
Scan #8: 500 µm, 3 passes, 10 µm/sec, 20 Hz, 106 µm spot, ~3 min

4X022N, I87-a, 99B-87 msc

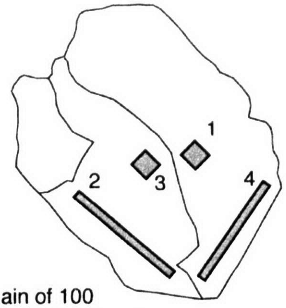

1) 1729.3 ± 10.9
2) 1734.7 ± 7.7
3) 1742.9 ± 10.1
4) 1714.6 ± 9.0

1730.1 ± 12.0
(± .70%)
MSWD = 6.60

All analyses 10/7/04; M/F gain of 100
Pt #1: 182 µm, 120 sec, 20 Hz, 2400 bursts
Scan#2: 900 µm (25%), 3 passes, 10 µm/sec, 20 Hz, 108 µm spot, 4:47 min
Pt #3: 182 µm, 120 sec, 20 Hz, 2400 bursts
Scan#4: 775 µm (25%), 3 passes, 10 µm/sec, 20 Hz, 87 µm spot, 4:37 min

4X022M, I87-c, 99B-87 msc

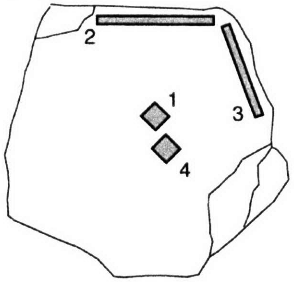

1) 1730.4 ± 8.5
2) 1746.6 ± 10.4
3) 1726.5 ± 8.7
4) 1733.1 ± 11.2

1733.1 ± 12.1
(± .70%)
MSWD = 3.14

All analyses 10/7/04; M/F gain of 100
Pt #1: 182 µm, 120 sec, 20 Hz, 2400 bursts
Scan#2: 900 µm (25%), 3 passes, 10 µm/sec, 20 Hz, 87 µm spot, 5:24 min
Scan#3: 930 µm (25%), 3 passes, 10 µm/sec, 20 Hz, 87 µm spot, 5:35 min
irregular path y-axis stage jerkiness, scan #2 was fine
Pt #4: 182 µm, 120 sec, 20 Hz, 2400 bursts

Final reduction 12/19/04: Final blanks, irradiation parameters, fractionation, J-values, error on J 0.5%

Figure C10

BF03-193B, Muscovite, Filename BF4X024A (1.0x scale)
Selwyn Lake msc-gt pegmatite

500 µm

All analyses (N = 12):	**1716.8 ± 11.4 (± .66%), MSWD = 1.24**
All cores (N = 6):	1718.1 ± 11.7 (± .68%), MSWD = 0.53
All rims (N = 6):	1715.3 ± 11.8 (± .69%), MSWD = 1.99

4X024FA, J96-a, BF03-193B msc (pos FA)

1) 1716.5 ± 10.4
2) 1716.3 ± 7.4
3) 1710.0 ± 8.3
4) 1715.1 ± 9.2

1714.4 ± 11.9
(± .69%)
MSWD = 0.54

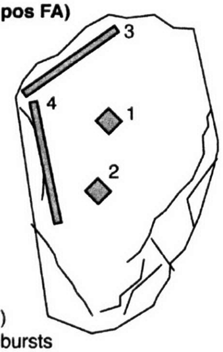

All analyses 12/2/04 (M/F gain of 57)
Pt #1: 182 µm, 90 sec, 20 Hz, 1800 bursts
Pt #2: 182 µm, 90 sec, 20 Hz, 1800 bursts
Scan #3: 500 µm, 5 manual passes, 10 µm/sec, 20 Hz, 87 µm spot
Scan#4: 675 µm, 5 manual passes, 10 µm/sec, 20 Hz, 87 µm spot

4X024GE, J96-b, BF03-193B msc (pos GE)

1) 1720.7 ± 7.8
2) 1708.4 ± 8.6
3) 1716.8 ± 7.7
4) 1725.2 ± 9.7

1717.5 ± 11.8
(± .69%)
MSWD = 2.56

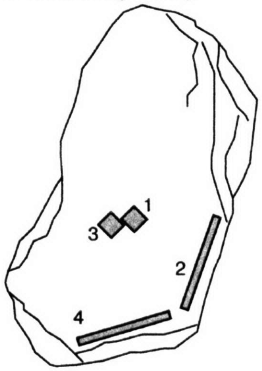

All analyses 12/3/04 (M/F gain of 57)
Pt #1: 182 µm, 2x1000 bursts, 20 Hz, 200 bursts
Scan #2: ~600 µm, 5 min manual, 10 µm/sec, 20 Hz, 87 µm spot
Pt #3: 182 µm, 2x1000 bursts, 20 Hz, 200 bursts
Scan #4: ~600 µm, 6 passes, 10 µm/sec, 20 Hz, 87 µm spot

4X024FB, J96-c, BF03-193B msc (pos FB)

All analyses 12/3/04 (M/F gain of 57)
Pt #1: 182 µm, 90 sec, 20 Hz, 1800 bursts
Scan #2: ~850 µm, 3 manual passes, 10 µm/sec, 20 Hz, 87 µm spot
Pt #3: 182 µm, 90 sec, 20 Hz, 1800 bursts
Scan #4: 1700 µm, manual for ~5:30, 10 µm/sec, 20 Hz, 87 µm spot

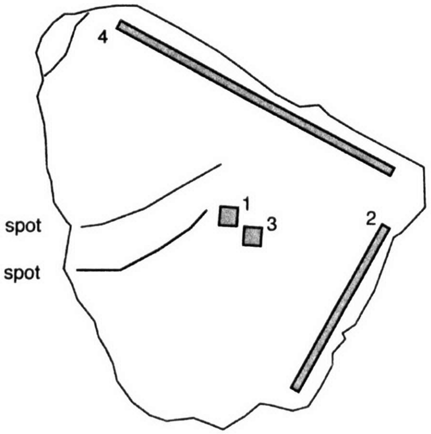

1) 1725.2 ± 12.2
2) 1722.0 ± 12.7
3) 1713.2 ± 15.1
4) 1719.8 ± 13.5

1720.7 ± 12.9
(± .75%)
MSWD = 0.53

Final reduction 12/16/04: Final blanks, irradiation parameters, fractionation, J-values, error on J 0.5%

Figure C11

03M92, Muscovite, Filename BF4X024C (75% of 1.0x scale)
Straight River msc pegmatite

500 µm

All analyses (N = 14): 1747.1 ± 11.7 (± .67%), MSWD = 1.94

4X024GC, H77-a, 03M92 msc (pos GC)

All analyses 12/3/04 (M/F gain of 57)
Pt #1: 182 µm, 2x1000 bursts, 20 Hz, 2000 bursts
Scan #2: ~1000 µm, 5 min manual, 10 µm/sec, 20 Hz, 87 µm spot
Pt #3: 182 µm, 2x1000 bursts, 20 Hz, 2000 bursts
Pt #4: 182 µm, 3x1000 bursts, 20 Hz, 3000 bursts
Scan #5: ~900 µm, 5 passes, 10 µm/sec, 20 Hz, 87 µm spot
Pt #6: 182 µm, 3x1000 bursts, 20 Hz, 3000 bursts
100 bursts to clean surface
Pt #7: 182 µm, 3x1000 bursts, 20 Hz, 3000 bursts
100 bursts to clean surface

1) 1727.7 ± 31.8
2) 1707.3 ± 17.0
3) 1742.2 ± 18.4
4) 1697.5 ± 47.7
5) 1749.1 ± 19.4
6) 1732.3 ± 8.3
7) 1750.6 ± 15.0

exclude 2&4:
1738.2 ± 12.8
(± .74%)
MSWD = 1.66

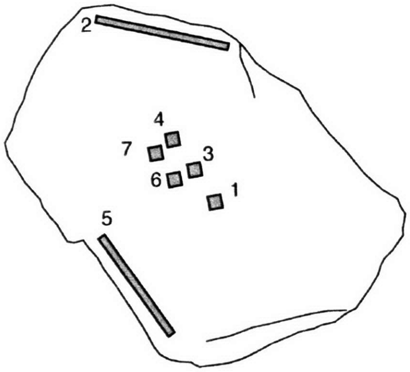

4X024GD, H77-b, 03M92 msc (pos GD)

All analyses 12/9/04 (M/F gain of 60)
(after Malcolm tried turning gain back up to 100)
Pt #1: 182 µm, 2x1000 bursts, 20 Hz, 2000 bursts
clean surface with 80 bursts
Pt #2: 182 µm, 2x1000 bursts, 20 Hz, 2000 bursts
clean surface with 100 bursts
Pt #3: 182 µm, 3x1000 bursts, 20 Hz, 2000 bursts
clean surface with 100 bursts
Scan #4: ~ µm, 6 min manual, 10 µm/sec, 20 Hz, 87 µm spot
clean scan with 145 micron at 1 Hz automatic
Scan #5: ~µm, 6 min manual, 10 µm/sec, 20 Hz, 87 µm spot
clean scan with 145 micron at 2 Hz manual
Pt #6: 182 µm, 3x1000 bursts, 20 Hz, 3000 bursts
clean surface with 100 bursts

1) discard
2) 1764.8 ± 25.6
3) 1750.8 ± 18.0
4) 1738.9 ± 16.5
5) 1755.9 ± 17.2
6) 1763.5 ± 22.0

1752.2 ± 14.1
(± .80%)
MSWD = 1.22

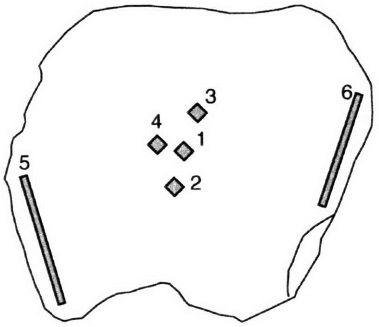

1) 1751.3 ± 9.3
2) 1747.8 ± 8.4
3) 1753.9 ± 7.7
4) 1746.0 ± 8.5

1749.9 ± 12.0
(± .68%)
MSWD = 0.77

4X032F, H77-c, 03M92 msc (pos 1)

All analyses 12/18/04 (M/F gain of 60)
Pt #1: 285 µm, 20 Hz, 4000 bursts (clean 5)
Scan #2: 106 µm, 10 µm/sec, 20 Hz, 6 min manual
Pt #3: 285 µm, 20 Hz, 4000 bursts (clean 5)
Scan#4: 145 µm, 10 µm/sec, 20 Hz, 6 min manual

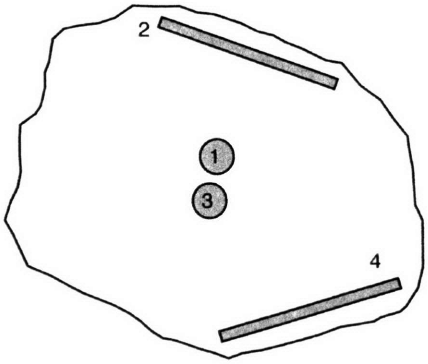

Final reduction H77a-b, 12/18/04: Final blanks, irradiation parameters, fractionation, J-values, error on J 0.5%

Final reduction H77c, 12/18/04: Final blanks, irradiation parameters, fractionation, J-values, error on J 0.5%

Figure C12

96W23E, Biotite, Filename BF4X032G (75% of 1.5x scale)
Neil Bay, C.Kopf P-T work

500 µm

All analyses (N = 12): 1863.8 ± 11.8 (± .63%), MSWD = 2.60
All analyses except J5-a, (N = 19): 1861.6 ± 11.9 (± .64%), MSWD = 1.16

J5-a, 96W23E bt, 4X032Ga (pos 3)

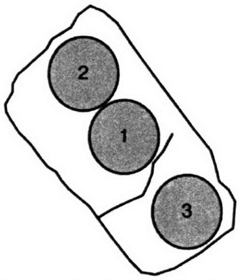

1) 1871.9 ± 7.0
2) 1874.4 ± 8.4
3) 1875.9 ± 11.8

mean:
1873.4 ± 12.6
(± .67%)
MSWD = 0.21

Analyses 1-2, 12/18/04; Analysis 3, 12/19/04 (M/F gain of 60);
Pt #1: 285 µm, 20 Hz, 3000 bursts (clean 5)
Pt #2: 285 µm, 20 Hz, 3000 bursts (clean 5)
Pt #3: 285 µm, 20 Hz, 3000 bursts (clean 5)

J5-b, 96W23E bt, 4X032Gb (pos 3)

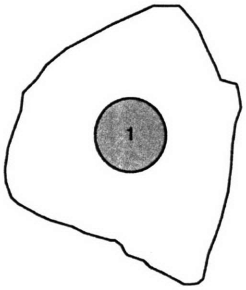

1) 1860.0 ± 6.7

Analysis 1, 12/18/04 (M/F gain of 60);
Pt #1: 285 µm, 20 Hz, 3000 bursts (clean 5)
Grain was loose after 1st analysis

J5-c, 96W23E bt, 4X032Gc (pos 3)
Grain loose on first burst

J5-d, 96W23E bt, 4X032Gd (pos 3)

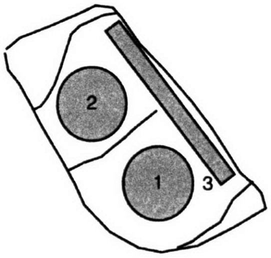

1) 1860.0 ± 7.3
2) 1863.4 ± 6.9
3) 1868.8 ± 6.8

mean:
1864.2 ± 12.3
(± .66%)
MSWD = 1.58

Analyses 1-2, 12/18/04; Analysis 3, 12/19/04 (M/F gain of 60);
Pt #1: 285 µm, 20 Hz, 3000 bursts (clean 5)
Pt #2: 285 µm, 20 Hz, 3000 bursts (clean 3)
Scan #3: 145 µm, 20 Hz, 10µm,/sec, 6 min manual

J5-e, 96W23E bt, 4X032Ge (pos 3)

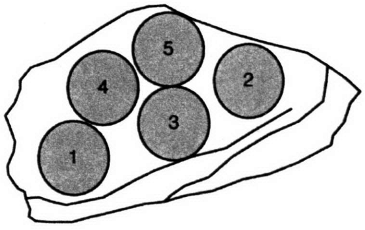

1) 1856.0 ± 7.4
2) 1857.5 ± 7.4
3) 1862.8 ± 7.1
4) 1860.4 ± 7.1
5) 1864.1 ± 7.7

mean:
1860.2 ± 12.1
(± .65%)
MSWD = 0.85

Analyses 1-5, 12/18/04, (M/F gain of 60);
Pt #1: 285 µm, 20 Hz, 3000 bursts (clean 5)
Pt #2: 285 µm, 20 Hz, 4000 bursts (clean 5)
Pt #3: 285 µm, 20 Hz, 4000 bursts (clean 10)
Pt #4: 285 µm, 20 Hz, 4000 bursts (clean 10)
Pt #5: 285 µm, 20 Hz, 4000 bursts (clean 10)

Final reduction 12/21/04: Final blanks, irradiation parameters, fractionation, J-values, error on J 0.5%

Figure C13

02M23B, Muscovite, Filename BF4X024F (75% of 1.5x scale)
Charlebois Lake two-mica granite

500 µm

All analyses (N = 10): 1739.0 ± 11.8 (± .68%), MSWD = 0.89

J97-a, 02M23B msc (pos HA)

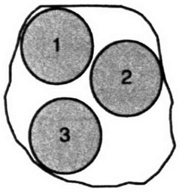

1) 1728.4 ± 17.7
2) 1743.6 ± 11.3
3) 1744.0 ± 11.2

mean:
1741.2 ± 13.3
(± .76%)
MSWD = 1.27

Analyses 1-3, 12/10/04 (M/F gain of 60);
note that image might be flipped
Pt #1: 285 µm, 20 Hz, 1500 bursts
clean with 10 bursts
Pt #2: 285 µm, 20 Hz, 1500 bursts
clean with 10 bursts
Pt #3: 285 µm, 20 Hz, 300 bursts
clean with 10 bursts

J97-b, 02M23B msc (pos HA)

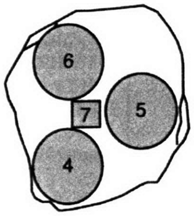

4) 1735.8 ± 9.4
5) 1741.2 ± 11.1
6) 1740.0 ± 12.0
7) 1729.9 ± 20.8

mean:
1737.9 ± 12.6
(± .73%)
MSWD = 0.43

Analyses 4-7, 12/10/04 (M/F gain of 60);
Pt #4: 285 µm, 20 Hz, 3000 bursts
clean with 10 bursts
Pt #5: 285 µm, 20 Hz, 4000 bursts
clean with 10 bursts
Pt #6: 285 µm, 20 Hz, 4000 bursts
clean with 10 bursts
Pt #7: 182 µm, 20 Hz, 4000 bursts
clean with 10 bursts

J97-c, 02M23B msc (pos HB)

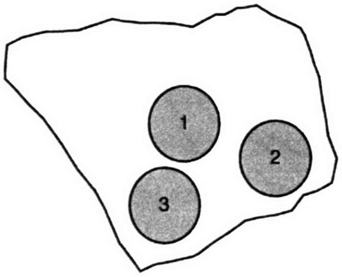

1) 1748.0 ± 11.9
2) 1734.8 ± 12.7
3) 1733.6 ± 10.9

mean:
1738.5 ± 13.1
(± .75%)
MSWD = 1.84

Analyses 1-3, 12/11/04 (M/F gain of 60);
Pt #1: 285 µm, 20 Hz, 4000 bursts
clean with 6 bursts
Pt #2: 285 µm, 20 Hz, 5000 bursts
did not clean
Pt #3: 285 µm, 20 Hz, 5000 bursts
clean with 6 bursts

Final reduction 12/16/04: Final blanks, irradiation parameters, fractionation, J-values, error on J 0.5%

Figure C14

500 µm

02M23B, Biotite, Filename BF4X024G (75% of 1.5x scale)
Charlebois Lake two-mica granite

All analyses (N = 8): 1738.1 ± 12.5 (± .72%), MSWD = 0.22

J97-a, 02M23B bt (pos HC)

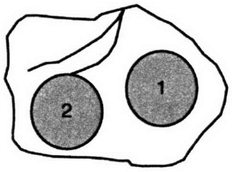

1) 1734.9 ± 16.4
2) 1738.7 ± 14.2

mean:
1737.1 ± 15.5
(± .89%)
MSWD = 0.13

Analyses 1-2, 12/11/04 (M/F gain of 60);
Pt #1: 256 µm, 20 Hz, 4000 bursts
clean with 5 bursts
Pt #2: 256 µm, 20 Hz, 4000 bursts
clean with 5 bursts

J97-b, 02M23B bt (pos HC)

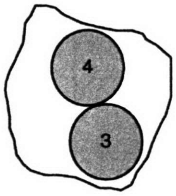

3) 1732.1 ± 19.4
4) 1741.5 ± 18.3

mean:
1737.1 ± 17.3
(± 1.00%)
MSWD = 0.50

Analyses 3-4, 12/11/04 (M/F gain of 60);
Pt #3: 256 µm, 20 Hz, 4000 bursts
clean with 5 bursts
Pt #4: 256 µm, 20 Hz, 4000 bursts
clean with 5 bursts

J97-c, 02M23B bt (pos HD)

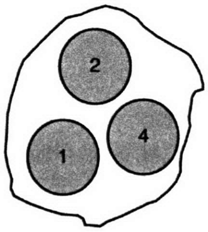

1)1745.8 ± 17.1
2) 1736.3 ± 15.1
4) 1736.7 ± 18.3

mean:
1739.4 ± 14.7
(± .41%)
MSWD = 0.41

Analyses 1-2, 4, 12/11/04 (M/F gain of 60);
Pt #1: 256 µm, 20 Hz, 4000 bursts
clean with 5 bursts
Pt #2: 256 µm, 20 Hz, 4000 bursts
clean with 5 bursts
Pt #4: 256 µm, 20 Hz, 4000 bursts
clean with 5 bursts

J97-d, 02M23B bt (pos HD)

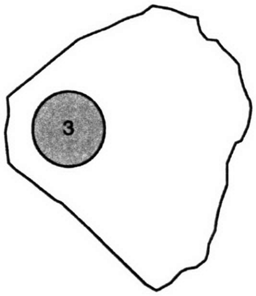

3) 1738.2 ± 11.7

Analysis #3, 12/11/04 (M/F gain of 60);
Pt #3: 256 µm, 20 Hz, 4000 bursts
clean with 5 bursts
After 1st point, the grain was loose and wouldn't stay put

Final reduction 12/16/04: Final blanks, irradiation parameters, fractionation, J-values, error on J 0.5%

Figure C15

500 μm

01M127B, Muscovite, Filename BF4X032A (75% of 1.0x scale)
Balliet Lake, msc-gt pegmatite

All analyses (N = 10): 1748.0 ± 11.84 (± .65%), MSWD = 2.84

J95-a, 01M127B msc, 4X032Aa (pos 2)

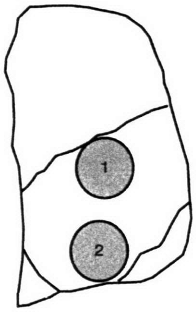

1) 1751.6 ± 6.2
2) 1737.5 ± 5.8

mean:
1744.0 ± 12.1
(± .69%)
MSWD = 11.17

Analyses 1-2, 12/17/04 (M/F gain of 60);
Pt #1: 285 μm, 20 Hz, 2500 bursts (hole through)
clean with 10 bursts
Pt #2: 285 μm, 20 Hz, 2500 bursts (hole through)
clean with 10 bursts

J95-b, 01M127B msc, 4X032Ab (pos 2)

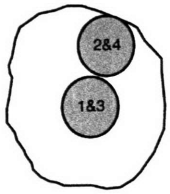

3) 1756.2 ± 8.4
4) 1750.1 ± 8.3

mean:
1753.1 ± 12.7
(± .72%)
MSWD = 1.07

Analyses 1-2, 12/15/04 (M/F gain of 60);
MP ran before realized viewport did not transmit UV,
poor ablation
Pt #1: 285 μm, 20 Hz, 2000 bursts (clean 5)
Pt #2: 285 μm, 20 Hz, 5000 bursts (clean 5)

Analyses 3-4, 12/17/04 (M/F gain of 60); Different viewport
Pt #3: 256 μm, 20 Hz, 2000 bursts (hole through)
Pt #4: 256 μm, 20 Hz, 2000 bursts (hole through)

J95-c, 01M127B msc, 4X032Ac (pos 2)

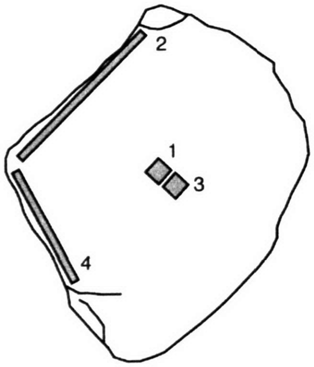

1) 1754.6 ± 7.3
2) 1745.6 ± 6.9
3) 1746.0 ± 6.0
4) 1753.6 ± 8.0

mean:
1749.3 ± 11.7
(± .67%)
MSWD = 1.87

Analyses 1-4, 12/17/04 (M/F gain of 60);
Pt #1: 182 μm, 20 Hz, 4000 bursts (hole through?)
clean with 5 bursts
Scan #2: 87 μm, 20 Hz, 3 passes, ~ 5 min (no clean)
Pt #3: 182 μm, 20 Hz, 4000 bursts (hole through?)
clean with 10 bursts
Scan #4: 106 μm, 20 Hz, 3 passes, ~ 6 min (no clean)

J95-d, 01M127B msc, 4X032Ad (pos 2)

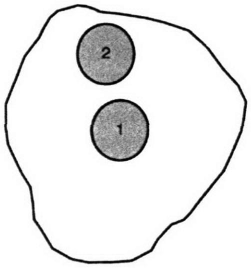

1) 1748.9 ± 7.2
2) 1744.5 ± 8.8

mean:
1747.1 ± 12.5
(± .71%)
MSWD = 0.60

Analyses 1-2, 12/17/04 (M/F gain of 60);
Pt #1: 285 μm, 20 Hz, 1500 bursts (hole through)
clean with 5 bursts
Pt #2: 285 μm, 20 Hz, 2000 bursts (hole through)
clean with 5 bursts

Final reduction 12/21/04: Final blanks, irradiation parameters, fractionation, J-values, error on J 0.5%

Figure C16

500 µm

01M127B, Biotite, Filename BF4X032B (75% of 1.5x scale)
Balliet Lake, msc-gt pegmatite

All analyses (N = 14): 1739.5 ± 11.5 (± .66%), MSWD = 1.14

J95-a, 01M127B bt, 4X032Ba (pos 2)

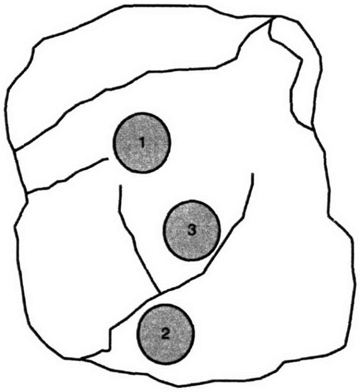

1) 1740.0 ± 15.2
2) 1734.1 ± 6.2
3) 1740.8 ± 6.9

mean:
1737.4 ± 12.0
(± .69%)
MSWD = 1.12

Analyses 1-3, 12/17/04 (M/F gain of 60);
Pt #1: 285 µm, 20 Hz, 2500 bursts (clean 10) (hole through)
Pt #2: 285 µm, 20 Hz, 2000 bursts (clean 10)
Pt #3: 285 µm, 20 Hz, 2000 bursts (clean 5)

J95-b, 01M127B bt, 4X032Bb (pos 2)

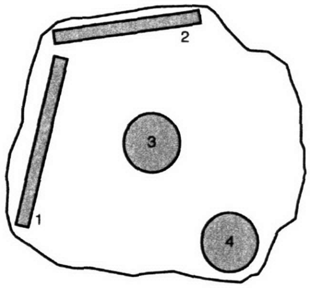

1) 1754.8 ± 17.6
2) 1731.5 ± 16.2
3) 1748.7 ± 48.4
4) 1733.1 ± 33.1

mean:
1741.5 ± 15.6
(± .90%)
MSWD = 1.38

Analyses 1-4, 12/15/04 (M/F gain of 60);
MP ran before realized viewport did not transmit UV,
poor ablation
Scan #1: 145 µm, 20 Hz, 6 min manual
Scan #2: 145 µm, 20 Hz, 5 scans for 5:50 total
Pt #3: 256 µm, 20 Hz, 5000 bursts (clean 5)
Pt #4: 256 µm, 20 Hz, 5000 bursts (clean 5)

J95-c, 01M127B bt, 4X032Bc (pos 2)

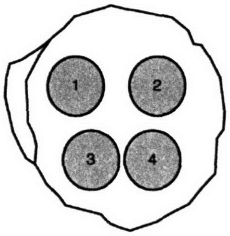

1) 1747.2 ± 9.5
2) 1738.6 ± 14.9
3) 1741.8 ± 13.7
4) 1743.7 ± 14.9

mean:
1743.9 ± 12.8
(± .73%)
MSWD = 0.37

Analyses 1-4, 12/15/04 (M/F gain of 60);
MP ran before realized viewport did not transmit UV,
poor ablation
Pt #1: 285 µm, 20 Hz, 3000 bursts (clean 5)
Pt #2: 285 µm, 20 Hz, 3000 bursts (clean 5)
Pt #3: 256 µm, 20 Hz, 4000 bursts (clean 5)
Pt #4: 256 µm, 20 Hz, 4000 bursts (clean 5)

J95-d, 01M127B bt, 4X032Bd (pos 2)

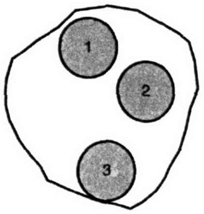

1) 1745.5 ± 8.6
2) 1739.4 ± 8.8
3) 1733.5 ± 7.8

Analyses 1-3, 12/17/04 (M/F gain of 60);
Pt #1: 285 µm, 20 Hz, 2000 bursts (clean 5) (hole through)
Pt #2: 285 µm, 20 Hz, 2000 bursts (clean 5) (hole through)
Pt #3: 285 µm, 20 Hz, 2000 bursts (clean 5) (hole through)

Final reduction 12/21/04: Final blanks, irradiation parameters, fractionation, J-values, error on J 0.5%

Figure C17

Appendix C

APPENDIX D. ^{40}AR/^{39}AR LASER INCREMENTAL HEATING BIOTITE DATA

Table D1. Chipman Domain ^{40}Ar/^{39}Ar Biotite Laser Incremental Heating Data[a]

	36Ar(a)	39Ar(k)	40Ar(r)	40Ar(r) (%)	39Ar(k) (%)	Age ± 2s (Ma)	
02-76B							
5A005K01	0.00131	0.04043	1.76361	82.01	3.79	1398.31	± 12.00
5A005K02	0.00152	0.09383	5.70228	92.68	8.79	1745.24	± 7.65
5A005K03	0.00051	0.11499	7.04639	97.93	10.78	1754.56	± 6.17
5A005K04	0.00040	0.14076	8.64349	98.65	13.19	1756.92	± 5.96
5A005K05	0.00014	0.08704	5.43202	99.25	8.16	1775.19	± 6.61
5A005K06	0.00010	0.08593	5.34729	99.44	8.05	1771.88	± 6.65
5A005K07	0.00007	0.07045	4.40121	99.52	6.60	1776.24	± 7.12
5A005K08	0.00008	0.06391	3.99960	99.41	5.99	1778.24	± 7.51
5A005K09	0.00012	0.10083	6.31938	99.46	9.45	1779.97	± 6.50
5A005K10	0.00008	0.07919	4.96006	99.54	7.42	1779.23	± 7.07
5A005K11	0.00003	0.07001	4.40016	99.79	6.56	1783.06	± 6.96
5A005K12	0.00006	0.07499	4.65003	99.61	7.03	1767.91	± 7.24
5A005K14	0.00000	0.01367	0.84841	100.00	1.28	1768.93	± 20.49
5A005K15	0.00003	0.03088	1.92229	99.60	2.89	1772.41	± 13.58

[a] Percentages of radiogenic 40Ar and K-derived 39Ar are reported for each analysis. Uncertainties are quoted at 2 sigma and do not include the propagated errors in irradiation parameter J.

Table D2. Southern Domain ^{40}Ar/^{39}Ar Biotite Laser Incremental Heating Data for sample 01SZ78[a]

	36Ar(a)	39Ar(k)	40Ar(r)	40Ar(r) (%)	39Ar(k) (%)	Age (Ma)	± 2s
01SZ78-5							
5A005A@1	0.00027	0.03650	1.34849	94.49	6.71	1242.82	± 53.76
5A005A@2	0.00005	0.02278	1.35816	98.88	4.19	1723.93	± 22.10
5A005A@3	0.00008	0.05272	3.23582	99.32	9.69	1756.44	± 10.57
5A005A04	0.00004	0.06307	3.96273	99.67	11.59	1782.84	± 8.93
5A005A05	0.00002	0.07870	5.01073	99.90	14.47	1797.87	± 8.94
5A005A06	0.00002	0.16410	10.61270	99.93	30.17	1815.64	± 5.98
5A005A07	0.00003	0.12605	7.99226	99.87	23.17	1793.12	± 6.64
01SZ78-9							
5A005C01	0.00005	0.00673	0.17138	92.72	0.85	939.52	± 89.45
5A005C02	0.00015	0.02479	1.54066	97.25	3.13	1770.47	± 22.35
5A005C03	0.00012	0.04624	3.10428	98.84	5.84	1858.81	± 12.67
5A005C04	0.00007	0.04126	2.74998	99.30	5.21	1850.45	± 13.31
5A005C05	0.00010	0.09181	6.13040	99.50	11.59	1852.43	± 9.12
5A005C06	0.00004	0.06886	4.60526	99.76	8.69	1854.32	± 11.47
5A005C07	0.00022	0.16543	10.90023	99.42	20.89	1837.09	± 8.92
5A005C08	0.00000	0.05549	3.66906	100.00	7.01	1841.06	± 10.69
5A005C09	0.00003	0.09238	6.11078	99.86	11.66	1841.57	± 8.95
5A005C10	0.00002	0.11538	7.56712	99.93	14.57	1831.78	± 9.01
5A005C11	0.00000	0.07679	5.03253	100.00	9.69	1830.88	± 8.47
5A005C12	0.00003	0.00509	0.31838	97.47	0.64	1777.19	± 81.02
5A005C13	0.00000	0.00185	0.11795	100.00	0.23	1801.99	± 143.91
01SZ78 Pan 8							
5A005F01	0.00002	0.00006	0.00296	30.49	0.03	1572.83	± 7169.57
5A005F02	0.00000	0.00045	0.03263	100.00	0.22	1946.08	± 502.44
5A005F03	0.00003	0.00601	0.39609	97.47	2.95	1836.67	± 65.09
5A005F04	0.00000	0.02941	1.92381	99.93	14.43	1828.65	± 14.36
5A005F05	0.00002	0.03377	2.21543	99.80	16.57	1832.21	± 13.08
5A005F06	0.00000	0.03407	2.22960	100.00	16.72	1829.19	± 8.86
5A005F07	0.00003	0.02768	1.77898	99.46	13.58	1808.71	± 15.41
5A005F08	0.00000	0.07233	4.72790	100.00	35.49	1827.92	± 8.59
01SZ78 Pan 7							
5A005G01	0.00003	0.00327	0.10928	92.07	1.19	1156.03	± 122.05
5A005G02	0.00012	0.13090	8.37357	99.57	47.82	1803.19	± 5.74
5A005G03	0.00005	0.02543	1.61853	99.16	9.29	1797.33	± 15.47
5A005G04	0.00000	0.03086	2.03705	100.00	11.27	1839.17	± 11.87
5A005G05	0.00000	0.02518	1.65341	99.96	9.20	1832.98	± 15.34
5A005G06	0.00000	0.02447	1.58652	99.92	8.94	1818.60	± 15.88
5A005G07	0.00000	0.01213	0.78809	100.00	4.43	1821.40	± 19.50
5A005G08	0.00000	0.02152	1.39349	100.00	7.86	1817.18	± 11.95

[a] See notes in Table D1.

Table D3. Southern Domain ^{40}Ar/^{39}Ar Biotite Laser Incremental Heating Data for sample 01SZ122B[a]

	36Ar(a)	39Ar(k)	40Ar(r)	40Ar(r)	39Ar(k)	Age	± 2s
				(%)	(%)	(Ma)	
01SZ122B -4							
5A005D01	0.00082	0.05643	1.17016	82.93	9.11	798.22	± 8.70
5A005D02	0.00035	0.01352	0.70527	87.21	2.18	1579.22	± 54.50
5A005D03	0.00159	0.13677	8.66899	94.85	22.08	1792.76	± 8.01
5A005D04	0.00020	0.11088	7.10229	99.16	17.90	1804.74	± 7.43
5A005D05	0.00006	0.07606	4.92558	99.63	12.28	1817.21	± 9.46
5A005D06	0.00008	0.08748	5.79551	99.57	14.12	1843.37	± 9.90
5A005D07	0.00008	0.09404	6.33094	99.63	15.18	1861.90	± 9.10
5A005D08	0.00000	0.04422	2.88773	99.99	7.14	1826.92	± 7.95
01SZ122B -3							
5A005E01	0.00075	0.04989	2.10196	90.41	6.17	1364.84	± 18.14
5A005E02	0.00029	0.04561	3.01218	97.22	5.64	1839.75	± 15.22
5A005E03	0.00022	0.08161	5.44624	98.84	10.09	1851.79	± 9.20
5A005E04	0.00005	0.06093	4.07039	99.62	7.54	1852.93	± 13.05
5A005E05	0.00008	0.06069	4.06538	99.41	7.51	1856.22	± 8.09
5A005E06	0.00007	0.08007	5.36320	99.59	9.90	1856.07	± 7.17
5A005E07	0.00002	0.08976	6.05379	99.88	11.10	1864.03	± 6.44
5A005E08	0.00005	0.12180	8.19638	99.80	15.07	1861.49	± 6.14
5A005E09	0.00003	0.11485	7.72254	99.89	14.21	1860.59	± 6.54
5A005E10	0.00001	0.04450	2.88217	99.89	5.50	1817.37	± 11.30
5A005E11	0.00002	0.05873	3.19832	99.83	7.26	1625.24	± 9.25
01SZ122B Pan 2							
5A005H01	0.00044	0.02707	1.28834	90.75	4.11	1484.79	± 14.37
5A005H02	0.00051	0.06177	4.08170	96.41	9.39	1840.36	± 8.04
5A005H03	0.00024	0.14836	9.80876	99.27	22.54	1840.99	± 5.69
5A005H04	0.00005	0.05960	3.93845	99.60	9.05	1840.46	± 8.27
5A005H05	0.00000	0.06179	4.12368	99.98	9.39	1851.80	± 7.74
5A005H06	0.00004	0.10751	7.14543	99.85	16.33	1847.05	± 6.26
5A005H07	0.00002	0.07811	5.19630	99.87	11.87	1848.11	± 7.20
5A005H08	0.00004	0.10876	7.24914	99.85	16.52	1850.42	± 6.47
5A005H09	0.00005	0.00521	0.33536	95.51	0.79	1809.49	± 69.37

[a]See notes in Table D1.

Table D4. Rae Domain ^{40}Ar/^{39}Ar Biotite Laser Incremental Heating Data[a]

	36Ar(a)	39Ar(k)	40Ar(r)	40Ar(r) (%)	39Ar(k) (%)	Age ± 2s (Ma)	
96W23E Pan 18							
5A005J01	0.00003	0.00268	0.10240	91.00	0.49	1275.22	± 167.20
5A005J02	0.00001	0.01553	1.02854	99.68	2.82	1847.13	± 23.91
5A005J03	0.00002	0.01768	1.18882	99.40	3.21	1864.87	± 21.60
5A005J04	0.00003	0.04333	2.96573	99.69	7.86	1885.63	± 10.46
5A005J05	0.00001	0.04464	3.02896	99.90	8.10	1875.32	± 11.28
5A005J06	0.00000	0.05294	3.56807	99.97	9.60	1867.72	± 9.30
5A005J07	0.00000	0.06105	4.16799	99.99	11.07	1882.70	± 8.53
5A005J08	0.00003	0.06146	4.15760	99.82	11.15	1871.90	± 8.35
5A005J09	0.00001	0.04417	3.02741	99.89	8.01	1887.09	± 11.07
5A005J10	0.00002	0.07900	5.33806	99.89	14.33	1870.64	± 6.86
5A005J11	0.00001	0.09350	6.30432	99.95	16.96	1868.09	± 6.74
5A005J12	0.00004	0.02488	1.66851	99.38	4.51	1861.90	± 15.33
5A005J13	0.00000	0.01049	0.72148	99.80	1.90	1890.86	± 34.86

[a]See notes in Table D1.

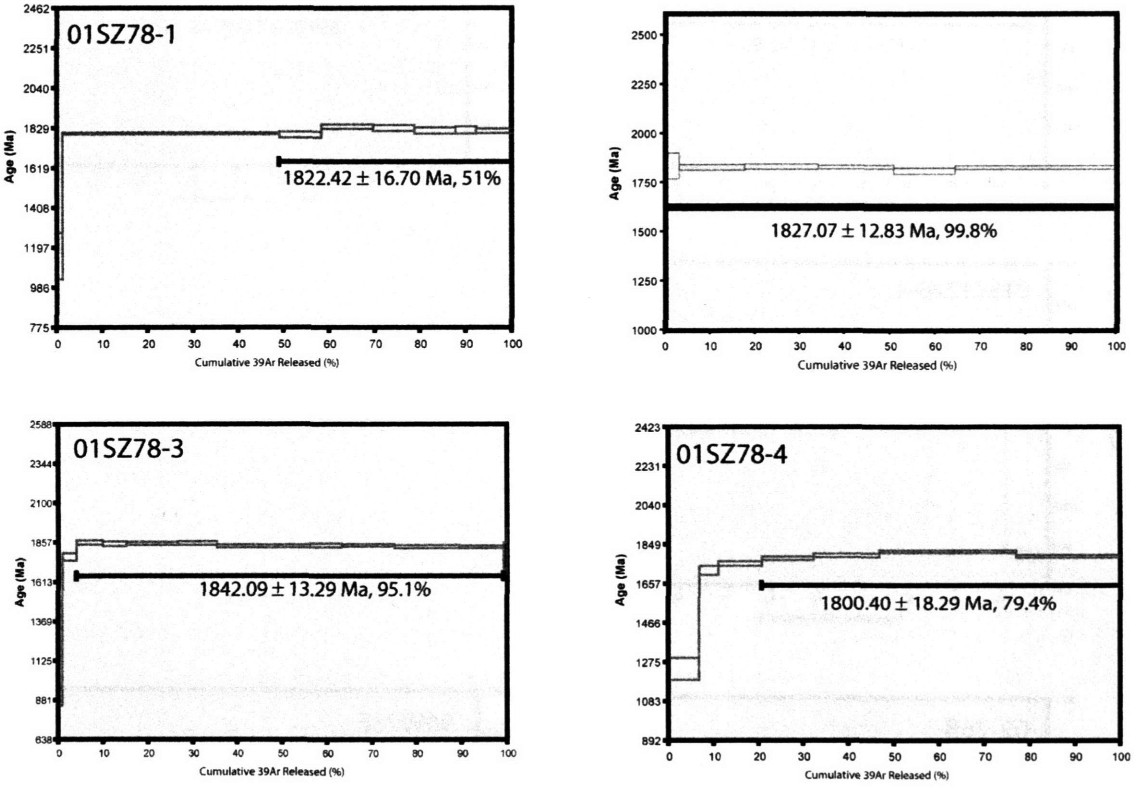
01SZ78-1
1822.42 ± 16.70 Ma, 51%
Age (Ma)
2462
2251
2040
1829
1619
1408
1197
986
775
Cumulative 39Ar Released (%)
0 10 20 30 40 50 60 70 80 90 100
1827.07 ± 12.83 Ma, 99.8%
2500
2250
2000
1750
1500
1250
1000
01SZ78-3
1842.09 ± 13.29 Ma, 95.1%
2588
2344
2100
1857
1613
1369
1125
881
638
01SZ78-4
1800.40 ± 18.29 Ma, 79.4%
2423
2231
2040
1849
1657
1466
1275
1083
892

Figure D1

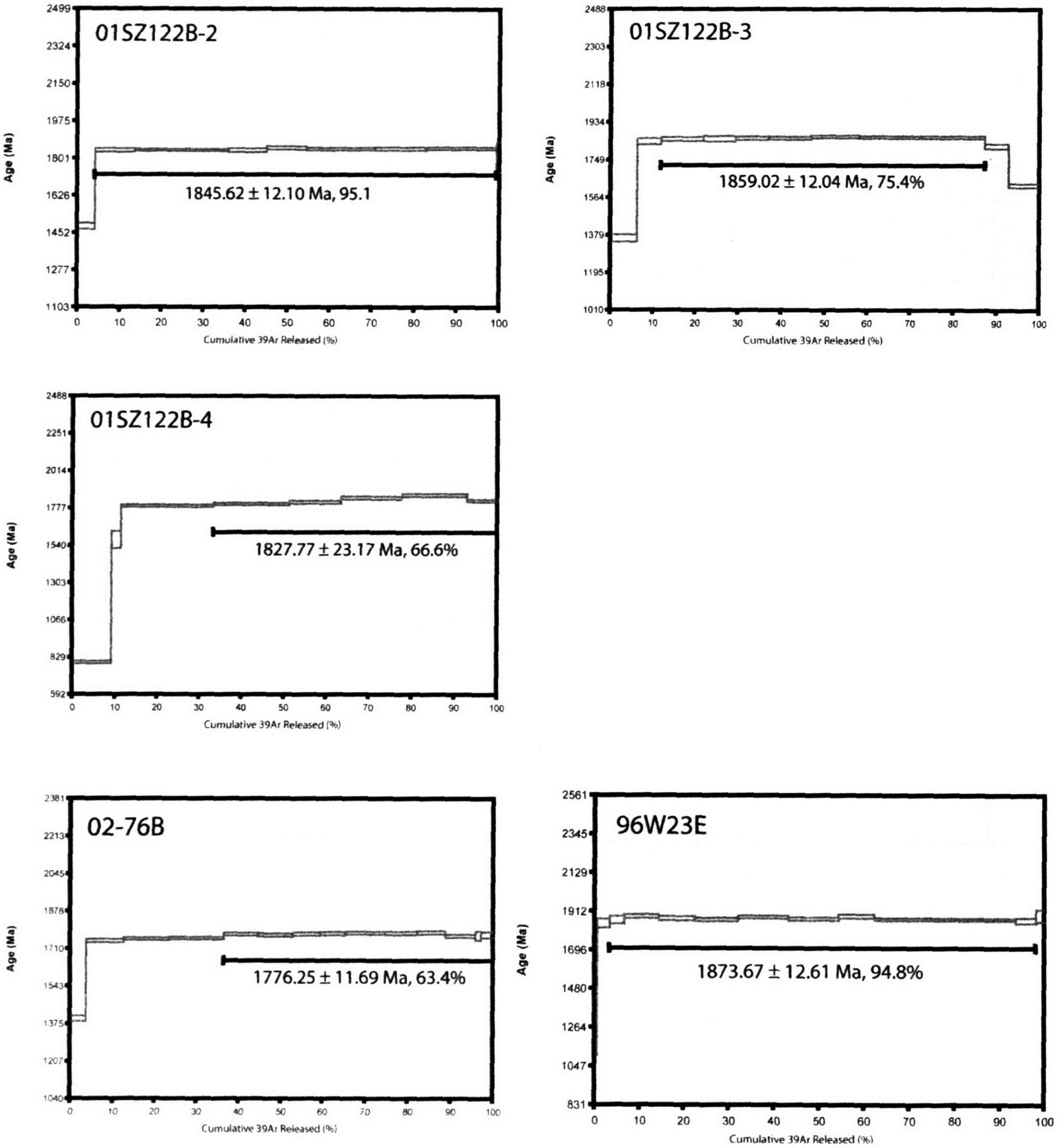

Figure D2

3205-45